LBL-5262

Energy and Environment Division

Preliminary Open File Report Geological and Geophysical Studies in Grass Valley, Nevada

H. Beyer, A. Dey, A. Liaw, E. Majer, T. V. McEvilly, H. F. Morrison, and H. Wollenberg

September 1976

Lawrence Berkeley Laboratory University of California/Berkeley

Prepared for the U.S. Energy Research and Development Administration under Contract No. W-7405-ENG-48

LBL-5262

DISCLAIMER

LBL-5262

PRELIMINARY OPEN FILE REPORT

GEOLOGICAL AND GEOPHYSICAL STUDIES IN GRASS VALLEY, NEVADA

H. Beyer, A. Dey, A. Liaw, E. Majer, T. V. McEvilly,
H. F. Morrison and H. Wollenberg

University of California
Lawrence Berkeley Laboratory
Berkeley, California 94720

September 1, 1976

This work was done with support from the U.S.
Energy Research and Development Administration

CONTENTS

Preliminary Open File Report

Geological and Geophysical Studies in Grass Valley, Nevada

INTRODUCTION

The Lawrence Berkeley Laboratory program for assessment of geothermal reservoirs has had three main goals:

1) To evaluate, on the basis of detailed geological, geochemical and geophysical data, the geothermal reservoirs in the mid Basin and Range geologic province.
2) To compare and evaluate geophysical techniques used in the exploration and delineation of these reservoirs.
3) To develop new techniques, and the instrumentation required, specifically for the deep penetration desired in geothermal investigations.

Four areas in north central Nevada were chosen for this study; Whirlwind Valley (Beowawe), Buffalo Valley, Grass Valley (Leach Hot Springs), and Buena Vista Valley (Kyle Hot Springs). These areas lie within an area of higher than normal heat flow, the Battle Mountain high heat flow area (Sass et al. 1971) shown on Fig. 1. Temperatures at depth in some hot springs in this area, determined by chemical geothermometers (Mariner et al. 1974) exceed 150-170°C and total dissolved solids in the surface waters are less than 5000 ppm. These systems are thus in the medium temperature, high quality category.

The Buffalo, Leach and Kyle sites were chosen because of favorable indications of geothermal potential, they were primarily composed of Federal land, and offered easy access and terrain amenable to equipment transportation. This latter was an important consideration since many geophysical techniques were to be evaluated and rugged terrain would have been a handicap to this

aspect of the program. Beowawe was chosen for some preliminary studies because some earlier geophysical data and drilling information was available. However, complicated land access problems prevented more than some reconnaissance electric and seismic studies. These, and the data from Buffalo Valley, have been reported by Wollenberg et al. (1975).

This report presents the results of the geological, geochemical and geophysical studies in the Leach Hot Springs area in Grass Valley. The data presented were taken between the Summer of 1974 and early Summer 1976. Analysis and overall interpretation of the data is still continuing, as are several field experiments, and the synthesis of all this information into the desired subsurface model is not complete. However, since the Leach Hot Springs KGRA in Grass Valley is soon to become available for geothermal leasing it is important that the data upon which evaluations of economic potential are based be released in preliminary form.

This report presents a brief summary of geological and geochemical studies of the Leach Hot Springs area. The geophysical techniques used are described in some detail and the results of the various surveys are presented. Detailed studies of these techniques are the subjects of reports presently in preparation as are details of equipment or instrumentation developed in the course of the study. This report thus presents only the data that pertain to the format of the overall program goals listed at the start of this introduction. The data in this preliminary report is, unfortunately, not on a uniform scale. This was dictated by the necessity to reproduce the Figures on 8 1/2 x 11 pages.

GEOLOGIC SETTING OF THE LEACH HOT SPRINGS AREA

Active hot springs areas in the Great Basin are in almost all cases associated with steeply dipping basin and range faults (Hose & Taylor (1974)), often at the intersection of two major orientations of faulting. A possible model for the numerous hot springs in the area is simply that surface waters descend along permeable zones associated with these faults, become heated at depths of only a few kilometers by the higher than normal gradients in this region, and ascend to the surface. Renner, et al. (1975), in their summary of hydrothermal convection systems in the U.S., are however, "skeptical that geothermal gradient alone can sustain high temperatures for the long durations of time indicated for these systems."

Certainly, if the only conduit for geothermal waters is along such permeable fault zones, or at the intersection of two such zones, the volume of the zone would have to be large to constitute a reservoir. The successful model of an economic reservoir must consist of a source of heat, a suitable transport mechanism, and a volume of sufficient porosity and permeability to be exploitable as a reservoir of hot water. Because of lack of definitive geologic information on most hot spring areas, the basis on which the estimates by Renner, et al. (1975) of heat content are made involve rather arbitrary assignments of volume. For example, for Leach Hot Springs, a subsurface reservoir of an areal extent of 4 square kilometers and a thickness of 2.5 km has been assumed. However, in the absence of direct, or for that matter indirect, information, a simple fault zone model could explain the surface hot spring activity and would entail no appreciable reservoir volume at all.

The Leach Hot Springs area is located in Grass Valley, Nevada approximately 50 km south of Winnemucca. The Sonoma and Tobin Ranges bound the valley on the east, while the valley is constricted south of the hot springs

by the Goldbanks Hills, locus of earlier mercury mining. Grass Valley is bounded on the west by the basalt-capped East Range. The distribution of major lithologic units in the region is illustrated on the geologic map (Fig. 2) and their stratigraphic relationships on the cross section, (Fig. 3). The intricate fault and lineament pattern, based strongly on photo interpretation, (Noble, 1975) is shown on a separate map, (Fig. 4). Paleozoic siliceous clastic rocks and greenstones are the oldest bedrock types in the region. In places in the Sonoma and Tobin Ranges, the Paleozoics are in thrust-fault contact with Triassic siliceous clastic and carbonate rocks. The Paleozoic and Triassic rocks have been intruded by granitic rocks of probable Triassic age in the Goldbanks Hills; elsewhere the granitics are probably of Cretaceous age. Though not exposed in the Leach Hot Springs area, Oligocene-Miocene rhyolitic tuffaceous rocks are probably present in the subsurface. They are overlain by a sequence of interbedded sandstone, fresh water limestone and altered tuffs, which are in turn overlain by coarser conglomeratic sediments (fanglomerates) derived from mountain range fronts steepened by the onset of basin and range faulting. The fanglomerates are opalized in places by siliceous hydrothermal activity associated with fault zones; occasionally the locus of mercury mineralization. Opalization of mercury deposits in the Goldbanks Hills and East Range closely resembles the opalized sinter at Leach Hot Springs. The Tertiary sedimentary sequence is overcapped by predominantly basaltic volcanic rocks whose ages, dated by the potassium-argon method, range from 14.5 to 11.5 million years.

Characteristic of the hot spring systems observed in northern Nevada, Leach Hot Springs is located on a fault, strongly expressed by a 10 to 15 m high scarp trending NE. Normal faulting since mid-Tertiary has offset rock units vertically several tens to several hundred meters (idealized cross section, Fig. 3). As shown on the fault and lineament map (Fig. 4)

the present-day hot springs occur at the zone of intersection of the NE trending fault and the NNW-SSE trending lineaments.

Total surface flow from the Leach Hot Springs system has been measured at 130 ℓ min^{-1} (Olmsted, et al., 1975). Surface temperatures of the springs reach 94° C, boiling at their altitude, and water temperatures at depth are estimated to be 155 to 170° C, based on silica and alkali-element geothermometers (Mariner, et al., 1974). Application of mixing-model equations (Fournier, et al., 1974), based on silica contents and temperatures of warm and cold spring waters, indicates that the temperature of hot water at depth within the Leach Hot Springs system may exceed 200°C. Material deposited by Leach Hot Springs, presently and in the past, is predominantly SiO_2.

GEOCHEMISTRY

In addition to the geochemical data provided by Mariner, et al. (1974, 1975) three pools were sampled at Leach Hot Springs, and their trace-element contents analyzed by neutron-activation methods (Bowman, et al., 1975). Results are illustrated on Fig. 5, and show considerable variation. The hottest pool had the lowest abundances of Na, Cl, W, Br, Cs, and Rb. The variations observed here do not appear to be related to mixing of ground water with the hot water system. For comparison, elemental abundances from a cold spring in this area are: Na (29 ± 1 ppm), Cl (56 ± 2 ppm), W (<3 ppb), Br (118 ± 2 ppb), Cs (.23 ±.02 ppb), Rb (3.7 ±.6 ppb), Ba (75 ± 10 ppb), Mo (<2 ppb), and Sb (<0.2 ppb).

Field radioactivity and radioelement contents of water and spring-deposit material were measured at Leach Hot Springs (Wollenberg, 1974). As with other spring systems dominated by SiO_2, field gamma radioactivity was low, ranging from 5 to 7.5 μ Rh^{-1} over the spring area. This was corroborated by the low

radioelement content of the sinter: Thorium 1.08 ppm, equivalent uranium 0.72 ppm, and 0.35% potassium. Hot spring water had contents of Radon-222 and Uranium-238 below detectability limits. This is in contrast to spring systems dominated by $CaCO_3$, where relatively high radioactivities and uranium daughter radioelement contents were observed.

HEAT FLOW

In a joint LBL-USGS project, seven 150-200 m heat flow holes were drilled in Grass Valley in the spring of 1975. Results of this study and earlier shallow holes drilled by Olmsted et al. (1975) are reported by Sass et al. (1976). As illustrated on Fig. 6, conductive heat flows exceed 9 HFU in a hole ~1 km NNE of the hot springs, and are of the order of 5 HFU at two locations, 5 km SW, and 9 Km SSE of the springs. Between the hot springs and these two locations, heat flow appears to be at or below the average for the Battle Mountain high heat flow region. Presently (late summer, 1976), cooperative LBL-USGS heat flow drilling is in progress in Grass Valley, detailing the conductive heat flow pattern within the area emcompassed by the seven holes drilled in 1975.

GEOPHYSICAL DATA

The geophysical data which have been obtained in Grass Valley, Nevada as part of the UCB-LBL geothermal project include gravity, magnetics, self-potential, electric field ratio tellurics, magnetotellurics, bipole-dipole resistivity, dipole-dipole resistivity, P-wave delay, microearthquake monitoring, seismic ground noise, and active seismic refraction/reflection.

Survey Lines

In most cases the geophysical data were obtained along the survey lines shown in Figure 7, although not all methods were employed along every line. The location of each line was determined on the basis of various factors; these are discussed below.

Most of Line A-A' lies along Grass Valley Road making access particularly

easy. It is roughly parallel to the strike of the range-front fault system, and serves as a tie line for the many other survey lines which cross it.

Lines B-B' and E-E' were laid out to be normal to the NE-SW trending faults which appear to control Leach Hot Springs, while skirting Hot Springs Ranch, privately owned property for which there were access permitting difficulties. Conveniently, the NW-SE direction of these lines is parallel to the major axis of the highly polarized long period (0.01-0.2 Hz) telluric field, making for high amplitude signals when E-field ratio telluric data were obtained.

Lines F-F', G-G', H-H', J-J', and K-K' were located approximately parallel to Lines B-B' and E-E' to provide a system of survey lines in the direction of the major telluric field axis for reconnaissance E-field ratio surveying.

Line C-C' was located to tie several lines together, while making use of good access along an existing road.

Lines D-D', P-P', Q-Q' and R-R' were laid out to be roughly perpendicular to the axis of Grass Valley, while avoiding private property. Additionally, Line R-R' was located to extend well into the Sonoma Range at Panther Canyon.

Line L-L' is a tie line along the western side of Grass Valley.

Lines M-M', N-N' and T-T' were located to correlate anomalous geophysical features seen in data collected along lines which they intersect.

Line S-S' was laid out after permission to traverse Hot Springs Ranch was obtained to gather data across Leach Hot Springs at a direction normal to the range front fault system.

Presentation of Data

Contour maps have been drawn for the gravity, magnetic, P-wave delay, bipole-dipole apparent resistivity and apparent conductance, and seismic ground noise data.

To facilitate the comparison of data from the various exploration techniques, Appendix A (Figures A1 through A17) shows most of the data collected along each survey line presented in profile form with a common distance abscissa. These profile data composites are in alphabetical order by survey line designation. Depending on the particular geophysical methods employed along a survey line, the data composite may include gravity, magnetic, self-potential, bipole-dipole apparent resistivity, E-field ratio telluric , and 1 km dipole length dipole-dipole apparent resistivity data. Also included in the data composites is the topography along the profile line, as well as faults and lithologic contacts as shown in Figures 2 and 4.

Dipole-dipole apparent resistivity pseudo-sections for dipole lengths of 250 meters and 500 meters are shown as separate figures in the text.

Gravity Survey

Gravity data were obtained with a Lacoste-Romberg gravimeter at 340 stations, covering about 200 square kilometers of Grass Valley, with most of the data taken at 0.5 km intervals along most of the survey lines. Along portions of Line E-E' the data density increased to 0.25 km intervals. Additional stations were obtained in the vicinity of Leach Hot Springs, in the Sonoma and Tobin Ranges to the east of Grass Valley, and in the East Range to the west of Grass Valley. The elevations of gravity stations along the profile lines were surveyed to within $\pm$ 0.03 meter. Remote stations in the mountain ranges were located at elevations known to $\pm$ 0.3 meter. The elevations of other stations have been estimated from topographic map contours to within $\pm$ 0.3 meter in the valley and $\pm$ 1.0 meter in the rugged terrain.

The complete Bouguer Anomaly has been calculated using a Bouguer density of 2.67 g/cm^3. The data are contoured in Figure 8 and presented in profile form in the composites of Appendix A. It is estimated that nearly all the values

are accurate to better than ± 0.1 milligal. Station locations are shown as dots on the map, Figure 8.

The first-order effect seen in the Bouguer Anomaly map is the thickness of valley sediments between the Paleozoic rocks of the Sonoma Range and the East Range (which is west of Grass Valley). The gravity low axis of the valley near the eastern side clearly indicates the greatest thickness of sediments, with the steep gradient east of this indicating a significant fault steeply downthrown to the west. From here the basement surface slopes more gently up to the west.

Seen by closer inspection of the Bouguer Anomaly map, and clearly demonstrated in the Line E-E' profile data, is a regional gradient of about 0.6 mGal per kilometer increasing to the northwest.

The gravity profile along Line E-E' across the major fault in the vicinity of Leach Hot Springs shows an anomaly of -17 mGals. Basin and Range alluvial valley fill varies widely in density, and can become very tightly compacted, as we have learned from shallow heat flow drilling. If an average density contrast of 0.4 to 0.3 g/cm^3 between the sediments and the bedrock is assumed, the maximum sedimentary section thickness will be in the range of 1.0 to 1.4 kilometer.

From preliminary reduction of gravity data too recent to be included in Figure 8, it appears that there is a closure of the gravity low anomaly which extends NW from the vicinity of Leach Hot Springs and is shown as open ended to the NW. Several new gravity stations taken along a line starting at the lowest region of this anomaly and extending to the NW to the windmill in T.33N., R. 38E., Section 32, suggest about 5 mGals of closure. If this is the case it suggests that, in spite of the valley broadening to the NW, with the hydrologic flow in this direction, either the depth to bedrock decreases or there is a densification in the geologic section.

A second anomaly of interest is the westward bulge of the steep gradient contours at Leach Hot Springs. Not only is this feature dense, but from other data it was found to have a high P-wave velocity and to be very resistive. There is sinter deposition in the vicinity of the Hot Springs, which is the obvious cause of this anomaly.

In the southeasternmost part of Grass Valley east of the Goldbanks Hills is a somewhat confined gravity low of interest. It appears that about 8-10 mGals of this anomaly is due to low density valley fill, suggesting that the sedimentary section may be 0.5 to 0.7 kilometer thick. This gravity anomaly is adjacent to three high heat flow wells (Q-3, BM37 and BM3 on Fig. 6), low resistivity, and microearthquake activity in Panther Canyon.

A gravity anomaly of possibly lesser interest is the high at 6 km W on Line D-D'. This coincides with relatively high heat flow at hole QH3 as shown on Figure 6.

Magnetic Survey

A Geometrics Model G816 proton precession magnetometer with 1 gamma accuracy was used for the magnetic survey of about 155 square kilometers of Grass Valley. Stations were obtained at 0.5 km intervals along most survey lines. Considering magnetic field fluctuations between base station readings, the relative accuracy of readings is assumed to be better than 10 gammas. A contour map of the magnetic data based on 274 stations is shown in Figure 9. Again the station readings are indicated by dots on the map.

The most striking aspect of the data from the ground magnetometer survey, shown in Figure 9, is the lack of relief: there is a range of only 200 gammas.

There is a low amplitude semicircular high extending westward from the Sonoma Range and centered on Leach Hot Springs. This feature is presently unexplained and does not appear to correlate with other data.

An aeromagnetic survey flown at 9000 feet barometric altitude (U.S. Geological Survey Open File Report) shows very low relief with a maximum range of 200 gammas over the entire Leach Hot Springs quadrangle.

Self-Potential

Theoretical analyses and some limited field data have suggested that geothermal activity might result in an associated dc field. The source for such a field is either the motion of conducting fluids in a porous medium or the result of thermoelectric effects. Due to the great variation of the fluid flow properties of rocks, it is difficult to make quantitative estimates of the streaming potentials in given geologic situations. However, self-potential anomalies of several hundred millivolts for known subsurface flow have been observed, and anomalies of 50 to 100 millivolts are often observed in areas of active flow, especially along faults. Thus the flow regime in a geothermal area may have good self-potential expression.

Thermoelectric potentials for a large hot buried sphere, representative of a geothermal reservoir, have been calculated for the site delineation study in Nevada (Corwin, 1975). This study showed that values of self-potential, negative over the center of the reservoir, as great as 60 mV might be expected; therefore, direct detection of a hot volume at depth might be possible.

Analysis of self-potential surveys in Buffalo and Grass Valleys has been accomplished by Corwin (1975). In general these preliminary surveys have revealed that:

i. Distinct self-potential anomalies are associated with the geothermal activity. Strong anomalies, believed to be associated with upwelling thermal fluids along a prominent fault (Olmsted, 1975) passing through the hot springs, were discovered.

ii. Electrode response to changes in soil chemistry and moisture content appears to be the major source of irreproducibility and background noise in self-potential surveys.

iii. Long wavelength anomalies associated with deep seated thermoelectric sources would almost certainly be concealed within the noise sources described in ii, and by survey procedure which, in traversing large distances using short electrode spread, accumulates significant error.

Bipole-Dipole Apparent Resistivity and Apparent Conductance

The bipole-dipole resistivity method (also called dipole mapping; see Keller et al. (1975) for a thorough treatment of the method) has been used as a reconnaissance exploration technique. Two sources were used: 60 kilowatt and 25-kilowatt motor-generator sets capable of forcing a long period (10 second) current square wave (maximum peak-to-peak amplitude of 200 amperes) into the ground between two shallow grounded electrodes separated by 1.5 to 2.5 km. At receiver stations located along the survey lines the resultant potential field gradient was measured over 100-meter long dipoles oriented parallel and perpendicular to the transmitting bipole in an L-shaped array. Copper-copper sulfate porous pots were used to ground the receiver dipoles, and Esterline Angus T171B strip chart recorders were used to monitor the receiver voltage.

The apparent resistivity, ρ_a, has been calculated as the homogeneous half-space resistivity necessary to produce the observed total electric field amplitude (regardless of direction) at the centroid of the receiver array due to the transmitter bipole moment. Similarly, the apparent conductance, S_a, has been calculated as the conductance (conductivity-thickness product) of a layer over an infinitely resistive half space required to produce the observed total electric field amplitude at the centroid of the receiver array due to the transmitted current. These

quantitites can be calculated from

$$\rho_a = 2\pi \frac{E_T}{I} \left[\frac{R_1 R_2}{\left(R_1^4 + R_2^4 + R_1 R_2 \left[Tx^2 - R_1^2 - R_2^2 \right] \right)^{1/2}} \right]$$

and

$$S_a = \frac{I\, Tx}{2\pi R_1 R_2 E_T}$$

where, as is shown in Figure 10,

$E_T = (E_{11}^2 + E_1^2)^{1/2}$ = the total electric field amplitude at the receiver array.

I = the transmitter current.

Tx = the transmitter length.

R_1 and R_2 = the distances from the transmitter electrodes to the centroid of the receiver array.

Figures 11 through 20 are apparent resistivity and apparent conductance contour maps for the five bipole-dipole transmitter locations occupied in Grass Valley. The transmitters are indicated by a pair of X's connected by a double line. A total of 333 receiver stations were occupied for the five transmitter positions.

To be able to compare two electrical reconnaissance methods LBL performed both bipole-dipole resistivity (controlled source) and electric field ratio tellurics (natural field source). Bipole-dipole resistivity has been widely used for geothermal exploration in the past five years, but has more recently become controversial due to difficulties with interpretation (McNitt, 1975). As the LBL field exploration program progressed more reliance was placed on anomalies located and detailed with E-field ratio tellurics and dipole-dipole resistivity (both of which are discussed below). While a two dimensional finite element modelling program has been

developed at UCB-LBL to aid in the interpretation of the bipole-dipole method, the data have not as yet been fully analyzed. However, on the basis of the data presented in Figures 11 through 20, and the comparison of the bipole-dipole data with that from other exploration techniques as seen in the profile data composites (Appendix A), some observations can be made.

For a given transmitter location the bipole-dipole method inherently suffers from a lack of ability to discriminate between shallow and deep anomalies. To circumvent this, multiple transmitter locations are required, but then the method becomes as time consuming as other resistivity surveys such as dipole-dipole or Schlumberger, and can no longer be considered as a reconnaissance method. Furthermore, the apparent resistivity (or apparent conductance) values calculated at a given receiver station are very sensitive to the transmitter location, and even to the transmitter orientation at a particular location. For the five transmitter locations used in Grass Valley the apparent resistivity maps shown in Figures 11 through 15 (or apparent conductance maps shown in Figures 16 through 20) are in many areas significantly different. For transmitter numbers 1, 2 and 3 the transmitter location is nearly the same; only the orientation is different. An example of this is displayed in profile form in Figure A5 in Appendix A showing the bipole-dipole apparent resistivity along the eastern end of Line E-E'. For transmitter numbers 1 and 4 the valley sediments appear to become increasing conductive to the west from the vicinity of Leach Hot Springs (at approximately 1 km E). For transmitter numbers 2 and 5 the data suggest that the sediments become more resistive.

These profile data also show the resistive anomaly associated with the sinter spring deposits at 0.5 to 2.5 km E. The transmitter number 5 bipole-dipole data do not show this feature at all.

As is quite reasonably the case, the resistivity structure in the immediate vicinity of the transmitter has a marked effect upon the received data, yet the method provides no means of accessing this structure short of including in the survey for each transmitter many receiver stations at the site of all other transmitters. These transmitter sites would not ordinarily be in the area of interest for receiver stations and therefore, increase the time for the survey.

The comparison of apparent conductance with apparent resistivity data should allow a discrimination of layered models with a resistive basement from more nearly uniform models. However, almost without exception, when the Grass Valley resistivity and conductance maps are compared for a particular transmitter location (Figure 11 versus Figure 16, Figure 12 versus Figure 17, etc.) the anomaly patterns are nearly identical. (High resistivity features have low conductance, and vice versus.)

Electric Field Ratio Tellurics

The electric (E) field ratio telluric method discussed here is an abbreviated version of the conventional telluric current method in which the natural electric field of the earth is measured at a roving station and referenced to that at a base station. At both locations an orthogonal array of grounded electric dipoles is used to measure the horizontal electric field vector. The apparent resistivities under the two locations are proprotional to the areas of correlated closures traced out by the E-field vector.

The need for a more rapid, less expensive, reconnaissance electrical method than bipole-dipole resistivity led UCB-LBL to experimentation with a telluric current technique described by Neuenschwander and Metcalf (1942), Dahlberg (1945), and Yungul (1973). For this E-field ratio telluric method (Beyer, et al., 1975) the ratio of a particular component of the telluric

field is measured as is seen by two co-linear consecutive electric dipoles along a survey line; dipole lengths of 500 meters, and occasionally 250 meters were used in Grass Valley. As shown in Figure 21 three equispaced electrodes are emplaced in the ground along the line. The signals from the two electric dipoles (using the central electrode as common) are bandpass filtered and used, respectively, as inputs to the X and Y channels of an X-Y plotter. The phase difference between the signals seen by the two dipoles is small for the long period(20 second) data recorded in Nevada unless a high contrast near surface lateral resistivity discontinuity exists within the span of the array. For in-phase signals the X-Y plotter will draw a straight line with a slope equal to the ratio of the electric fields observed along the dipoles. The array is leap-frogged along the survey line to obtain a continuous set of electric field intensity ratios. When successively multiplied together these ratios yield a profile of the component of the relative electric field strength in the direction of the survey line.

Exploration depth is an inverse function of the frequency of the incident electromagnetic field. In using the E-field ratio telluric method for reconnaissance two frequencies which are peaks in the natural electromagnetic spectrum have been used: 0.05 Hz (filters banded at 0.03-0.06 Hz) for deep probing and the 8 Hz Schumann resonance band (filters set at 6-10 Hz) for investigating shallow features.

The 8 Hz signals could not be handled in quite the same manner as the long period tellurics due to two considerations: considerable phase shift was observed between the signals seen by the two in-line dipoles, and the X-Y plotter which was used (the Simpson Model No. 2745 X-Y, Y-T Recorder) has a maximum frequency response of 2 Hz. For these reasons each of the two incoming telluric signals was rectified and integrated - stored capacitively with a slow discharge rate. The capacitor voltages were read into the

X and Y channels of the plotter to produce a line whose slope represents the ratio of the average amplitudes of the telluric signals in the profile direction. As with the 0.05 Hz data, these ratios are successively multiplied along the survey line.

The E-field ratio telluric method at 0.05 and 8 Hz has been used as a reconnaissance method to traverse 152 line-kilometers in Grass Valley. The data are plotted with the other profile data in Appendix A.

Quantitative interpretation of the E-field ratio in terms of earth resistivity is straightforward for simple models. For example, at a semi-infinite vertical contact the current density normal to the contact must be continuous, so the ratio of the normal components of the electric field at the contact must be proportional to the resistivity ratio, whereas away from the contact over a homogeneous half space the electric field is proportional to the square root of the resistivity.

E-field ratio telluric response over two-dimensional resistivity structures can be calculated with arbitrary profile line angle with respect to strike (α), arbitrary incident magnetic field polarization angle with respect to strike (β), and arbitrary incident magnetic field ellipticity (ϵ). Figure 22 shows such a model for the eastern end of Line E-E' in Grass Valley. The parameters $\alpha = -45$, $\beta = +45$ were selected to approximate the field conditions of incident magnetic field polarization direction and profile line direction with respect to strike. For these values of α and β the incident magnetic field ellipticity, ϵ , has little influence on the data. Since the E-field ratio data is expressed in relative amplitude it can be shifted along the ordinate to yield a moderately good fit between the field data and the computer model generated data. The resistivity model structure shown in Figure 22 was developed as a preliminary interpretation of dipole-dipole resistivity data to be discussed below.

The E-field ratio telluric survey has proved to be quite valuable for locating several anomalies. Along Line E-E' (see Figure A5) the 0.05 Hz data clearly demark resistive spring deposits from 0 km to 2 km E, as do the telluric profiles along Lines A-A' (Figure A1) and S-S' (Figure A17). From the 8 Hz telluric data it appears that this resistive feature is overlain by a conductive anomaly, possibly saturated alluvium from the spring activity. At 3 km E on Line E-E' the E-field ratio increases sharply to the east indicating which fault of several in this vicinity offers a significant lateral resistivity contrast. At the western end of Line E-E' between 11 km and 14 km W the 8 Hz tellurics indicates somewhat higher resistivity than over the rest of the valley, while the deeper penetrating 0.05 Hz data suggest a conductive anomaly in an area where the gravity and P-wave delay data indicate only a thin layer of alluvium.

The telluric survey along the eastern end of Line H-H' (see Figure A8) proved to be of particular value in finding the low resistivity anomaly in the southeastern part of Grass Valley near Panther Canyon.

Dipole-Dipole Resistivity

To determine the detailed electrical resistivity structure of the subsurface in areas of interest (possibly located by E-field ratio tellurics or bipole-dipole resistivity) the d.c. resistivity method has been used. To probe to the depths required for geothermal exploration, electrode separations of ten kilometers or more is often required. For such surveys the polar dipole-dipole array holds considerable logistical advantage over arrays such as Schlumberger or Wenner in that the whole distance need not be spanned with wire. Constant transmitter and receiver dipole lengths, a, are employed, with increased depth of penetration being achieved by increasing the separation between the transmitter and receiver dipoles at unit intervals of $N \times a$, where $N = 1,2,3...$ The upper limit on N is determined by the maximum depth of interest or the separation at which the signal at the receiver is lost in the

telluric or instrumental noise. Using the current, I, injected into the ground at the transmitter dipole, and the resulting voltage, V, observed at the receiver dipole, an apparent resistivity, ρ_a, is calculated assuming a homogeneous half space:

$$\rho_a = \frac{V}{I} \pi a N(N+1)(N+2)$$

As depicted in Figure 23 the calculated values of ρ_a are conventionally plotted at the intersection of lines angling down at 45 degrees from the centers of the transmitting and receiving dipoles to produce an apparent resistivity pseudo-section (Hallof, 1957, Marshall & Madden, 1959). (N.B. - For the uninitiated, the apparent resistivity values plotted in the pseudo-section cannot be construed as determinations of the resistivity of the earth at corresponding locations; the apparent resistivity pseudo-section is only a form of displaying the data.)

Depending upon the resolution and the depth of exploration desired to investigate a particular feature, dipole-dipole surveys using three different dipole lengths (a) were performed: a total of 70 line-kilometers was surveyed using 1 km dipoles; 26 line-kilometers using 500 meter dipoles; and 11 line-kilometers with 250 meter dipoles. In all cases the transmitter-receiver separations were carried to at least an N spacing of 10.

The equipment used to perform these surveys was the same as that used for bipole-dipole resistivity measurements, with the addition of clock synchronized signal averagers to increase the signal-to-noise ratio at the receivers. The synchronous detection resulted in increased data accuracy and increased depth of penetration because it permitted use of greater transmitter-receiver separations.

To interpret the dipole-dipole resistivity field data, a computer program using a finite difference technique has been developed in our laboratory to calculate dipole-dipole apparent resistivity pseudo-sections over complex two-dimensional models.

Line E-E' which trends NW-SE across Grass Valley just north of Leach Hot Springs has been surveyed using every geophysical technique applied by LBL as a means of comparing the interpretation of each method.

Figure 24 shows one attempt at modelling the 1 km dipole length dipole-dipole apparent resistivity pseudo-section for Line E-E'. The general configuration of the contact between the bedrock (shown as 200 Ω-m) and the overlying conductive material was determined primarily on the basis of the gravity, P-wave delay and reflection seismic data. The model represents moderately high near-surface resistivity (shown as 30 and 12 Ω-m) in the central portion of the valley, grading down into a massive conductive (1 Ω-m) zone in the region of thickest sedimentary section. At 1 km E is the near surface resistivity high which also shows up markedly in the E-field ratio telluric data, and is presumed to be the result of spring deposition as well as fault displacement. East of this is a somewhat thicker sedimentary section before the bedrock surface is faulted up to become the Sonoma Range. Gravity and P-wave delay data indicate a dense, high-velocity anomaly at 10 km W. This is included in the resistivity model as a thining of the conductive section to 250 meters in this region, but the result is an unacceptable increase of many values in the model generated pseudo-section. Between 11 and 15 km W is a somewhat thicker conductive (3-7 Ω -m) sedimentary section. While shallow apparent resistivity values were not found along this part of the line, the effects are definitely seen in apparent resistivities found for larger N-spacings for which receiver electrodes were placed between 11 and 15 km W. The tellurics also shows this to be a con-

ductive region.

Models for a conductive layer overlying a more resistive half-space can be rather insensitive to the resistivity of the half-space with the result that it can be difficult to determine bedrock resistivity. A model similar to that shown in Figure 24 has been calculated with the 200 Ω-m bedrock resistivity reduced to 20 Ω-m; only relatively subtle changes appeared in the pseudo-section.

A 500 meter dipole length dipole-dipole pseudo-section (Figure 25A) was obtained as a compromise between desires for greater resolution than that afforded by the 1 km dipole length data and for sufficient penetration to see the bottom of the deep conductive anomaly in the center of the valley. Figure 25b shows a moderately successful modelling attempt with one significant modification of the concept of Figure 24, which is based upon a model for the seismic reflection data (see Figure 80, which will be discussed in the seismic section of this report). The modification is the addition to the resistivity model of a thick moderately conductive (8 Ω-m) zone beneath the 12 Ω-m and 1 Ω-m layers to the west of 0 km in Figure 25b. Comparing this figure with Figures 3 and 80, the 12 Ω-m layer is interpreted as the Quaternary alluvium with a P-wave velocity of 1.8 km/sec., and the 1 Ω-m layer is seen as the Tertiary sediments and volcanics with a velocity of 2.9 km/sec. The 8 Ω-m section is then the older, complexly folded and faulted (resulting in high permeability and low resistivity) Paleozoic rock , which is part of a thrust sheet presumed to underlie the Tertiary section in the valley. Beneath this are younger Paleozoic formations with high resistivity (200 Ω-m) and velocity (5.0 km/sec.). An interpretation of this sort allows the deeper Paleozoic bedrock to be resistive while allowing a thick enough conductive section for low apparent resistivity values to appear in the pseudo-section at large N-spacings.

Figure 26 shows an excellent two-dimensional computer model fit to the 250 meter dipole length pseudo-section run on Line A-A'. Significant points displayed in the model are (1) the 30 Ω-m block from 3.0 to 3.5 km N, which represents resistive spring deposits, (2) the possibility of more extensive silicification to the north and northwest forming a thin near surface resistive layer, and (3) the 20 Ω-m "basement" beneath the 2 and 4 Ω-m alluvium. Models with a basement resistivity of 100 Ω-m would not fit the observed data.

The dipole-dipole pseudo-section and model for Line B-B', Figures 27a and b suggest that the Grass Valley sedimentary section becomes somewhat more resistive (2 Ω-m) at depth to the south and west of Leach Hot Springs than was found to the northwest of the hot springs along Line E-E'. Judging from topography the direction of hydrologic flow in the valley is to the northwest. The Line M-M' dipole-dipole resistivity data shown in Figure 28 bear out the increase of resistivity to the south. Line M-M' follows the gravity low axis of the valley, the region of thickest sedimentary section, and intersects Lines E-E' and B-B' at the centers of their 1 and 2 Ω-m anomalies.

Across Line D-D' the gravity and E-field ratio telluric data (see Figure A4) are of particular help in designing a model for the dipole-dipole resistivity (Figures 29a and b). Dense, resistive material (possibly a horst of basement rock, or hydrothermal deposition) occurs at 5.0 to 6.5 km W. It is interesting to note that the low resistivity anomaly in the dipole-dipole apparent resistivity pseudo-section is not the result of a conductive anomaly at 5 km W, but is rather due to low resistivity features on either side.

Low E-field ratio telluric anomalies at the eastern end of Line H-H' and on Lines P-P', Q-Q' and R-R' (Figures A8, A14, A15, A16) led to dipole-dipole resistivity surveys and modelling along Lines H-H' and T-T' (Figures 30a and b, and Figures 31 a and b, respectively). Two-dimensional modelling

has been used here for survey lines which are perpendicular to each other in a quite tightly confined portion of the valley, so agreement between the two models should not be expected to be perfect. The models do suggest however, that a very conductive (2-3 Ω-m) anomalous feature entends from near the surface down to the shallow (600-800 meters deep) basement, and possibly continues to the south at depth under resistive (10-30 Ω-m) surface material. There is no surface expression of the near surface portion of the conductive anomaly, but heat flow hole Q-3 (Figure 6) at this location yields 4.9 HFU.

Magnetotellurics

In the summer of 1974 preliminary tests of a magnetotelluric system incorporating a Josephson effect superconducting magnetometer for the magnetic field sensor were conducted. Problems with electronics and shielding of the sensor from high amplitude transients (SFERICS) prevented completion of a full magnetotelluric survey of the area.

By August 1975 these problems had been corrected and 17 stations were occupied in Grass Valley. These stations were located along the main geophysical traverse lines, Figure 7. Two Josephson effect magnetometers were used, a Devleco Model 8230 3 axis magnetometer and a 3 axis dc SQUID magnetometer developed by Prof. John Clarke under funding from the USGS (Clarke, 1976). Three components of the magnetic field and two horizontal electric components were amplified and filtered, and recorded on a Honeywell 5600 FM tape recorder. At many of the stations outputs from both magnetometers were recorded simultaneously for coherence studies on the magnetic field and for performance studies on the magnetometers. These experiments are being analyzed for a separate report.

A read-after-write head on the recorder was used to monitor the recorded signals on a paper chart recorder in the field.

Two basic recording bands were used to accommodate, with wide dynamic range of the signals, to the restricted range of the recorder (50 db): a low frequency band from .01 to 5 Hz and a high frequency band from 1 Hz to 40 Hz.

The electric fields were measured with orthogonal electrode arrays of 500 meter lengths. Copper-copper sulfate porous pots were used as receiver electrodes. The magnetometer axes were aligned with the electrode arms and the orientation (E_x:N59°W, E_y:N31°E) was the same at every station (Figure 32).

The data presented in this report were analyzed using conventional power spectral techniques (e.g. Vozoff, 1972, and Sims, et al., 1971). While other analysis methods are being developed in this program the resulting apparent resistivities using this conventional approach provide a useful picture of the subsurface conductivity distribution.

The electric and magnetic fields were played back and demodulated from the FM recorder. These data were fed directly to a multichannel A/D converter and placed on digital tape. The data were also monitored on a multichannel analog chart recorder and segments containing bad data were identified and listed for omission in the subsequent digital processing. The remaining data were divided into discrete time segments, each of which was Fourier transformed. All possible cross-spectra and auto-spectra for the components of the field were computed. The cross-spectra and auto-spectra were averaged over both the ensemble of time segments and over frequency intervals of constant Q. For frequencies between 0.01 Hz and 1 Hz, the ensemble averages typically contained ten 500 second long time sequences. For frequencies between 1 Hz and 40 Hz, the ensemble averages contained about thirty 8 second long time sequences.

An average two-dimensional impedence tensor was calculated for each frequency window using expressions for the tensor elements which are unbiased by noise in the electric field (Sims, et al., 1971). (We choose a form for the impedence tensor which is unbiased by electric field noise since we expect electric signals over a conductive body to be relatively smaller compared with the noise than are the magnetic signals.) The impedence tensors were rotated to find the principle (or strike) direction which minimized the magnitude of the sum of the off-diagonal tensor elements. Finally, the apparent resistivities ρ_x (parallel to strike) and ρ_y (perpendicular to strike) were calculated from the rotated impedence tensor. We assess the quality

of the resistivity data by computing the coherency, η, between the measured electric fields and the electric fields predicted by forming the product of the measured magnetic field and the unrotated impedence tensor. The low frequencies ($<$ 1 Hz) were rated as: good if $0.95 < \eta < 1$, fair if $0.89 < \eta < 0.95$, and poor if $\eta < 0.89$. For the high frequencies ($>$ 1 Hz) our ratings are as follows: good if $0.90 < \eta < 1$, fair if $0.72 < \eta < 0.90$, and poor if $\eta < 0.72$.

The rotated apparent resistivities for each station are plotted in Figures 33 to 48 as a function of $T^{1/2}$, where T is the period in seconds. ρ_x is obtained from the rotated pair E_x/H_y, ρ_y from the rotated pair E_y/H_x. Figures 33 to 39 are in order from West to East along line E-E'. Figures 40 to 46 are arranged in order of location from south to north along line A-A'. Figures 47 and 48 show the apparent resistivities obtained on lines M-M' and B-B' respectively. For almost all of Grass Valley the principle directions for the rotated values of ρ_a are nearly the same (Table 1), and the rotation angles are the same for all frequencies. These results indicate that the major range front-valley contact controls the regional current flow. While detailed interpretation requires numerical modelling of individual station data, a qualitative description of the electrical section is provided by the pseudo-sections of ρ_y values on lines E-E' and A-A' in Figures 49 and 50. These provide a graphical representation of apparent resistivity as a function of $T^{1/2}$ (which in turn is proportional to depth) and station location.

The very low values of apparent resistivity observed in the vicinity of Leach Hot Springs should be viewed with caution until detailed modelling is complete. This type of anomaly is characteristic of contacts between zones of differing resistivity where local electric fields perpendicular to the contact on the conductive side are attenuated. It should also be noted

that low values of apparent resistivity reflecting low levels of electric field are poorly determined since the signal to noise ratio is low.

Seismological Methods

Several techniques based on seismological observations have been suggested and applied, with varying and often controversial results, to the problem of detecting and delineating the geothermal reservoir. In keeping with the general goal of the LBL program, studies were undertaken of these applications which either showed promise scientifically or were in general use in the field. The aim of the research effort, the testing and evaluation of these seismic methods, involves a balanced approach with theoretical analysis, field studies, and model generation. The methods selected for study are:

1. Microearthquakes
    a. spatial/temporal distribution
    b. mechanisms
2. Wave Propagation Characteristics (Distant Sources)
    a. velocity distribution (p-delays)
    b. attenuation
3. Ambient Microseism Characteristics ("Ground Noise")
    a. spatial variation in field of -
        amplitude
        frequency
        wavenumber
    b. reservoir-generated signals
4. Reflection Survey
    a. structure
    b. velocity
    c. direct reservoir detection

5. Refraction Survey
    a. structure
    b. velocity

In developing the program it became clear that data either did not exist, or were not accessible, of a sufficient quality and coverage to evaluate the methods in a uniform manner. This prompted three lines of philosophy characteristic of the effort:

1. A prospect area was selected for comparative assessment technique studies.
2. Contractural data-gathering services were used when available.
3. Equipment was fabricated at LBL only when unique in design or not available elsewhere.

In keeping with this approach, evaluation of methods 1-3 required fabrication of a special-purpose, wide-bandwidth, multichannel field seismic data acquisition system; methods 4 and 5 were done by contract with a geophysical exploration company; and the area ultimately selected for the comparative methodology effort was Grass Valley, Nevada. Data presented later in this report represent the stage of the investigation and preliminary interpretation as of August 1976.

Seismic Data and Preliminary Interpretation

1. Microearthquakes

A. The microearthquake study was conducted in three parts. First was a reconnaissance period using 8 Sprengnether M.E.Q.-800 smoked paper recorders, with 4.5 Hz geophones. Initially a large array was set out covering the whole valley for 6 weeks to determine areas of activity. Based on this information, the instruments were moved to each area of activity. The

reconnaissance study indicated earthquakes occurring in a triangular area bounded by Leach Hot Springs, Panther Canyon, and the Goldbanks Hills (Figure 7). However, no activity was apparent in the immediate Hot Springs Area. Faulting mechanisms were inconclusive, indicating a complex faulting pattern. Over the period of recording the average occurrence of microearthquakes was 2-3/day, with magnitudes from -.5 to 1.0. No reliable depths were determined from the reconnaissance study. The second phase of study reoccupied the valley using a 12-station telemetered data system, with 4.5 Hz vertical and horizontal geophones, recording on FM analog tape (DC-80 Hz). This study confirmed the absence of microearthquakes around the Hot Springs area, and confirmed an active region to the south in Panther Canyon and the Goldbanks Hills. Also detailed was the complexity of faulting in this area, with no single throughgoing fault plane indicated as controlling the earthquakes. However, the epicenters seem to define a linear source region between the Goldbanks Hills and Panther Canyon. The rate of occurrence was still about 2-3 per day. Depths were determined from 3 to 5 km. Magnitudes ranged from -.5 to 1.0.

The final survey phase concentrated in the southern part of the valley as shown in Figure 51. Single-component, vertical, 4.5 Hz geophones were used normally, though for a period of time six stations included a horizontal component. The 3 shaded areas in Figure 51 correspond to zones of earthquake swarm activity, though no two areas were ever active simultaneously. The swarms characteristically consist of 20-30 earthquakes. Excluding these swarms, there is an average of one earthquake per day in the area. The magnitudes vary from -0.5 to 1.0. Focal depths are 5-8 km in the SW Swarm, 3-5 km in the central swarm, and 2-5 km in the NE swarm. Composite fault plane solutions are generally inconsistent, but for the SW swarm,

right lateral strike slip seems the controlling mechanism. Wadati diagrams show Poisson's ratio in the range 0.25 to 0.30 over the entire region, with no apparent anomalies.

2. Propagation Characteristics

The telemetry system provides relative timing between stations to ± 0.005 sec. An almost daily source of large explosions at a mine 45 km due east of the Hot Springs allowed a study of relative P-wave arrival times. Eighty sites were occupied in a grid with 1 km centers, bounded by survey lines E-E' and D-D' (see Figure 7). Around the Hot Springs, grid spacing was reduced to 0.5 km for a radius of 2 km. Relative P-wave arrival times, corrected for average velocity and referenced to bedrock (site 4.5E on E-E') are shown in Figure 52. The delay pattern, greatest in the center of the valley and minimum on the edges, reflects valley fill. However, around the Hot Springs the relative times are advanced; i.e. delays of up to -0.150 sec. This appears to be due to higher velocity silicified sediments extending to depth around the springs. The high gradient in delay to the north of the Hot Springs indicates a sharp boundary in the anomalous high velocity material.

Further evidence for a sinter deposit around the hot springs is seen in the variations of frequency content of records at different sites. Figure 52 shows the same distant explosion recorded at 3 different sites, all recorded with the same gain. The bedrock and valley sites are similar in frequency content with slightly differing amplitudes. The Hot Springs record, in contrast, shows a marked increase in the frequency content of the P-wave, with a slight increase in amplitude.

A more pronounced effect is seen in Figure 54 for a local microearthquake, affecting the S-wave. These observations indicate that the high velocity zone also has a very high Q relative to the surrounding areas. The

explosion arrivals came from almost due east, while the microearthquake occurred south of the station. Only stations near the Hot Springs show this effect indicating an inhomogeneity of small lateral extent but extending from the surface to appreciable depth. The effect decreases with distance from the Hot Springs, disappearing at approximately one kilometer distance.

3. Ambient Microseism Characteristics (Ground Noise).

The ground noise experiments were designed to investigate the spatial distribution of the ambient background microseisms, in amplitude and frequency, plus parameters such as the propagation direction and the apparent velocity. To study the spatial distribution, 24 locations were occupied from July 1 - 14, 1975; and 47 additional locations were occupied from October 12 - 24, 1975. Due to the limitation in the number of radio transmitters available in 1975, we were able to acquire data from only seven different locations simultaneously. A reference station was occupied throughout the experiment.

For processing, data were carefully selected from quiet recording periods. At least 28 simultaneous blocks of data were chosen from each of the seven stations, carefully avoiding transient signals or cultural noise. Each data block of 6.4 second length was filtered and digitized at 80 sps. The resulting 512-point records were tapered and transformed into the frequency domain by means of the FFT algorithm. The Fourier transform multiplied by its complex conjugate produced the power spectral density. The estimated power spectral density at each location is the average over at least 28 data blocks, to increase the statistical confidence. The velocity spectral density, VSD, in millimicron/sec/Hz, was obtained by taking square root of the power spectral density estimate and correcting for system responses. The noise level in dB for a particular frequency band at a station is obtained by

integrating the velocity spectral density over the frequency band and normalizing by the same quantity at the reference station. Data from four representative locations are presented to illustrate the characteristics of the seismic ground noise in Grass Valley. Figures 55 to 58 show the velocity spectral density (VSD) plots for each location; error bars indicate the 95% confidence limits. Figures 59 to 62 present contours of relative ground noise level in particular frequency bands; the values are given in dB with respect to the reference site REF.

At all frequencies the Hot Springs area shows background level. The valley center with thickest alluvium apparently enhances the microseism level uniformly in the 4-10 Hz range. However, at lower and higher frequencies, the effect is spotty, with some valley regions showing very low levels.

In order to study the propagation parameters of the microseisms, we fielded a 12-element roving array at 16 representative locations in the area from July 3 - 19, 1976. The array configuration and its response in wavenumber space are shown in Figure 63. Data acquisition equipment is identical to that used in the previous study, except that data were transmitted by cable for the short distances, instead of by radio. Twenty-four transient-free data blocks were selected simultaneously from each of the 12 elements of the array. High-resolution wavenumber analysis, based on the construction of complex weighting functions (maximumlikelihood filters) from the input data blocks for each array element, was used to estimate the power spectral density in two-dimensional wavenumber space at particular frequencies. The peak of the resulting three-dimensional (kx, ky, f) power spectral density function indicates the apparent velocity and direction of coherent seismic waves propagating across the array, i.e., the dominant horizontal wavenumber. The high-resolution technique minimizes the spurious

effects of the side lobes in the array response.

Figures 64 to 66 show representative wavenumber plots at specific frequencies for three sites. At valley sites the dominant energy propagates from the east at low velocity near 300 m/s; probably Rayleigh waves guided in the upper 10-20 m of alluvium. The dominant waves near the Hot Springs are considerably higher velocity, around 1 km/s. The method represents a powerful, objective, quantitative analysis technique for determining the propagation parameters of background noise and their spatial variations.

4. Reflection Survey

For structural control, a Vibroseis (registered trade name, Continental Oil Co.) reflection survey was conducted in the vicinity of the Hot Springs. Line E-E', from 5.25W to 2.25E, was surveyed, as was a cross line, E-X', centered at the Hot Springs. Fifty meter group intervals, 1200% stack and 16 58-12 Hz sweeps of 16 sec. length were used. Resulting sections—conventional, relative amplitude, and migrated—are shown in Figures 67 to 72. Data quality is generally quite good except in the immediate Hot Springs area where the fault-bounded silicified section is apparent in the lack of reflections. Faulting is evident, by reflection correlation and presence of diffractions, on section E-E'. Velocity analyses on E-E' were generally good and differentiated clearly the major lithologic units in the section, i.e., Qal (6000ft/s), Tertiary (9000ft/s), Paleozoic (13000ft/s), and deep basement (17000ft/s), approximately modelled as 1.8, 2.9, 4.0, and 5.0 km/s, respectively.

5. Refraction Survey

As a further study, a refraction line on E-E' and its extension southeast was surveyed, with a spread from 2.8W to 2.0E and 100 m group intervals. Seven shotpoints (up to 60 sweeps) from 7.6W (VP305) to 10.75E (VP-61) were used. Records are shown in Figures 73 to 79.

As an aid in interpretation, a generalized model, based on the preliminary reflection and refraction interpretation, was constructed for finite element computation of the equivalent refraction spread and shotpoint VP257. The initial model is shown in Figure 80 and the resulting second section in Figure 81. Agreement is generally good, although details differ. The outlook is encouraging for further use of the finite element technique in modeling.

SUMMARY

The detailed analysis and synthesis of all the geophysical data is not complete. Important heat flow data essential to the definition of a reservoir model are still being acquired, and many of the geophysical lines have yet to be interpreted in terms of detailed computer models of the subsurface resistivity. However, several important conclusions can be drawn from the data, and these focus attention on two main areas of geothermal potential.

In the vicinity of Leach Hot Springs there is evidence of a long history of silicic deposition from thermal waters. The seismic P-wave delay map, Figure 52, most clearly outlines an area of anomalously high velocity of at least 3 km^2 areal extent. The ground noise studies show this to be an area of low attenuation, high Q, and the reflection study verifies this conclusion. Further, an analysis of the velocities, P-delays and reflections indicates that the silicified zone must be at least 2 km thick and thus, at that point in the section, must extend well into the Paleozoic basement.

The densification accompanying the presumed silicification is evident in the "shoulder" on the Bouguer map of the area, Figure 8. The telluric reconnaissance profiles on lines A-A', E-E' and S-S' all showed a resistive picture in this area and the preliminary resistivity modelling for the dipole-dipole resistivity pseudo-section of Line A-A' (Figure 26) also requires a zone of higher resistivity in this area. None of the analyses to date has defined the shape of this silicified zone with depth.

Some further indication of the extent of the silicification and its possible fault control was found in hole QH1 (Figure 6) where the Hot Springs fault zone was drilled through and found to be highly silicic at a point about 1 km from Leach Hot Springs.

The geophysical data confirm the general geologic cross section (Figure 3), at least on Line E-E'. Further analysis will lead to some redefinition of the location, and possibly dip, of the faults and will also modify the vertical lithologic section. More cross sections can be drawn from the composite data of other lines that will lead to a better subsurface model of the geology. Tentatively, a vertical section at station 2W on Line E-E', drawn from both electrical and seismic data, is composed of the following layers:

Layer	Thickness	Resistivity	Velocity	Geology
1	.4 to .5 km	10-20 Ω-m	1.8 km/sec.	Recent Sed.
2	.8 to 1.0 km	1-5 Ω-m	2.9 km/sec.	Tertiary Sed.and Volc.
3	1.0	8-30 Ω-m	4.0 km/sec.	Paleozoic
4	∞	200 Ω-m	5.0 km/sec.	Paleozoic

The low resistivity zone, here identified with Tertiary sediments, is confined in areal extent to a region of roughly oval shape extending NW from the Springs to the intersection of line M-M' and F-F'. (See the composite profile for line M-M', Figure 12A in Appendix A).This low coincides well with the axis of the gravity low but is displaced slightly to the east of the center of the graben-like feature in the fault map, Figure 4. The heat flow value in this zone, Q1 is not high by Battle Mountain standards (2.24 HFU) suggesting that an accumulation of conductive sediments (e.g., ancient playa deposits) in the deepest portion of the valley is responsible for the resistivity anomaly.

Finally, it should be noted that the telluric profile and the dipole-dipole data on line E-E' show a zone of low resistivity at depth starting at about 10W and extending west. Apart from a small gravity high in this vicinity none of the other data extend to this point. Since the geologic

model suggests a steady thinning of the Quaternary and Tertiary cover in this area, the resistivity lows should be included in any further studies of the area.

The remaining area of obvious geothermal interest is that of Panther Canyon and the valley immediately west of it. This area is dominated by a strong NE trending gravity feature which offsets topography and the Bouguer contours (Figure 8). This trend matches a regional NE-SW lineament pattern observed on ERTS and high altitude photographs. It is also the only portion of the Grass Valley area that is seismically active (Figure 51). The seismic zone is one of complicated faulting and frequent microearthquakes. It is also located at the northern extreme of the Pleasant Valley fault, scene of the large Pleasant Valley earthquake in 1915 (M 7-8).

There is a strong electrical conductivity high on this area (see profile data for lines H, L and T in Appendix A and the dipole-dipole pseudosections, Figures 30 and 31) and the heat flow in Q3 is 4.9 HFU.

REFERENCES

Beyer, H., and Morrison, H. F., 1975, Electrical exploration of geothermal systems in Basin and Range valleys of Nevada: Abstract, Second U. N. Symposium on the Development and Use of Geothermal Resources, In Press.

Bowman, H., Hebert, A., Wollenberg, H., and Asaro, F., 1975, Trace, minor and major elements in geothermal waters and associated rock formations (north-central Nevada): Second U. N. Symposium on the Development and Use of Geothermal Resources, In Press.

Clarke, John, 1976, An improved low frequency electromagnetic prospecting system for geothermal exploration utilizing a dc squid magnetometer: Final report on USGS grant #14-08-0001-G-224, Univ. of Calif., Berkeley.

Corwin, R., 1975, Use of the self-potential method for geothermal exploration: Lawrence Berkeley Laboratory Report, LBL 3235, UCII, TID-4500-R62.

Dahlberg, R. A., Jr., 1945, An Investigation of natural earth currents: Geophysics, v. 10, no. 4, p. 494-506.

Fournier, R. O. et al., 1974, Geochemical indicators of subsurface temperature: U. S. Geol. Surv. Jour. of Res. 2 (3).

Hallof, P., 1957, On the interpretation of resistivity and induced polarization results: Ph.D. thesis, M.I.T. Dept. of Geology and Geophysics.

Hose, R. K. and Taylor, B. E., 1974, Geothermal systems of northern Nevada: U. S. Geol. Surv. Open File Report 74-271.

Keller, G. V., Furgerson, R., Lee, C. Y., Harthill, N., and Jacobson, J. J., 1975, The dipole mapping method: Geophysics, v. 40, no. 3, p. 451-472.

Marshall, D.J., and Madden, T. R., 1959, Induced polarization, a study of its causes: Geophysics, v. 24, no. 4, p. 790-816.

Mariner, R. H., et al., 1974, The chemical composition and estimated minimum thermal reservoir temperatures of the principal hot springs of northern and central Nevada, U. S. Geol. Surv. open file report.

Mariner, R. H., et al., 1975, The minor and trace elements, gas and isotope compositions of the principal hot springs of Nevada and Oregon: U. S. Geol. Surv. open file report.

McNitt, J. R., 1975, Summary of U. N. exploration experience, 1965-1975: Second U. N. Symposium on the development and use of geothermal resources, In Press.

Neuenschwander, E. F., and Metcalf, D. F., 1942, A study of electrical earth noise: Geophysics, v. 7, no. 1, p. 69-77.

Noble, D. C., 1975, Geologic history and geothermal potential of the Leach Hot Springs area, Pershing County, Nevada: a preliminary report to the Lawrence Berkeley Laboratory.

Olmsted, F. H., Glancy, P. A., Harrill, J. R., Rush, F. E., and Vandenburgh, A. S., 1975, Preliminary hydrogeologic appraisal of selected hydrothermal systems in northern and central Nevada: U. S. Geol. Surv. open file report. 75-56.

Renner, J. L., White, D. E., and Williams, D. L., 1975, Hydrothermal convection systems in: Assessment of Geothermal Resources of the United States-1975. D. E. White and D. L. Williams, Editors. Geological Survey Circular 726.

Sass, J. H., Lachenbruch, A. H., Monroe, R. J., Greene, G. W., and Moses, T. H., 1971, Heat flow in the Western United States: JGR, v. 76, n. 26, p. 6376-6413.

Sass, J. H., et al., 1976, Geothermal data from test wells drilled in Grass Valley and Buffalo Valley, Nevada: U. S. Geol. Surv. open file report 76-85, and Lawrence Berkeley Laboratory Report LBL 4489.

Sims, W. E., Bostick, F. X., and Smith, H. W., 1971, The estimation of magnetotelluric impedance tensor elements from measured data: Geophysics, v. 36, n. 5, p. 938-942.

Vozoff, Keeva, 1972, The magnetotelluric method in the exploration of sedimentary basins: Geophysics, v. 37, n. 1, p. 98-141.

Wollenberg, H. A., Asaro, F., Bowman, H., McEvilly, T., Morrison, H. F., and Witherspoon, P., 1975, Geothermal Energy Resource Assessment: Lawrence Berkeley Laboratory, Report UCID-3762.

Yungul, S. H., Hembree, M. R., and Greenhouse, J. P., 1973, Telluric anomalies associated with isolated reefs in the Midland Basin, Texas: Geophysics, v. 38, no. 3, p. 545-556.

TABLE I

MAGNETOTELLURIC APPARENT RESISTIVITY:

ROTATION OF AXES TO PRINCIPAL DIRECTIONS

STATION POSITION LINE	AXIS ROTATION in DEGREES (Clockwise is positive)
3.0 KM N. A-A'	$10^{\circ} \pm 10$
1.5 KM N. A-A'	$10^{\circ} \pm 10$
0.0 KM - A-A'	$15^{\circ} \pm 5$
1.5 KM S. A-A'	$10^{\circ} \pm 10$
4.0 KM A. A-A'	$0^{\circ} \pm 10$
6.0 KM S. A-A'	$10^{\circ} \pm 10$
8.0 KM S- A-A'	$20^{\circ} \pm 10$
3.5 KM E. E-E'	$15^{\circ} \pm 10$
2.0 KM E. E-E'	$7^{\circ} \pm 18$
1.0 KM E. E-E'	$0^{\circ} \pm 10$
0.0 KM - E-E'	$10^{\circ} \pm 10$
1.0 KM W. E-E'	$5^{\circ} \pm 10$
2.5 KM W. E-E'	$15^{\circ} \pm 5$
4.0 KM W. E-E'	$10^{\circ} \pm 5$ (low freq. only)
6.0 KM W. E-E'	$0^{\circ} \pm 10$
1.0 KM E. B-B'	$0^{\circ} \pm 10$
2.0 KM N. M-M'	$20^{\circ} \pm 10$

Note: Except at a few stations the amount of axis rotation is fairly constant over frequency, especially at the lower frequencies.

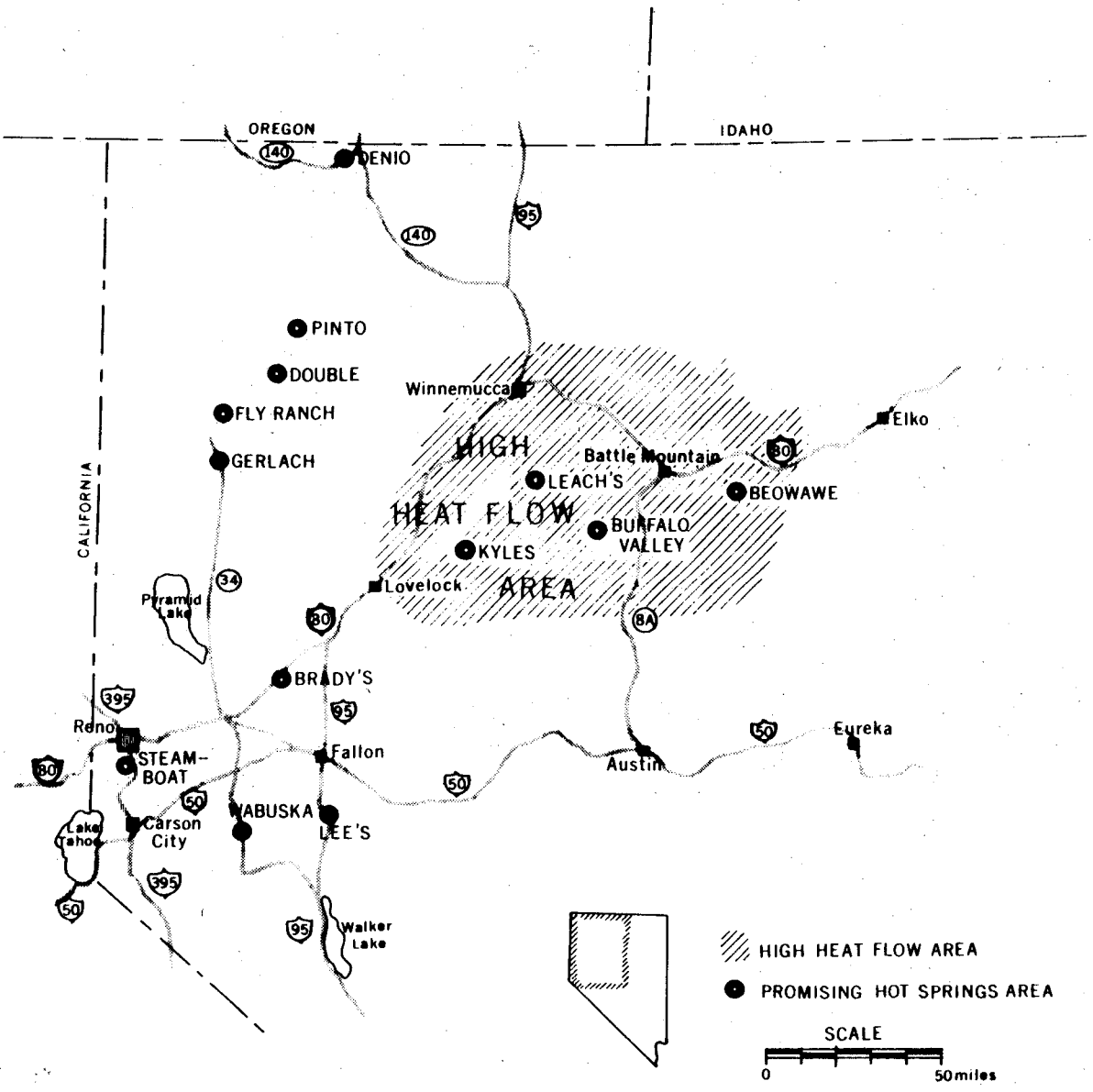

Hot Springs in Northwestern Nevada

XBL 735 676

Figure 1: Location map, northwestern Nevada, showing prominent thermal spring areas within and outside of the Battle Mountain high heat flow region.

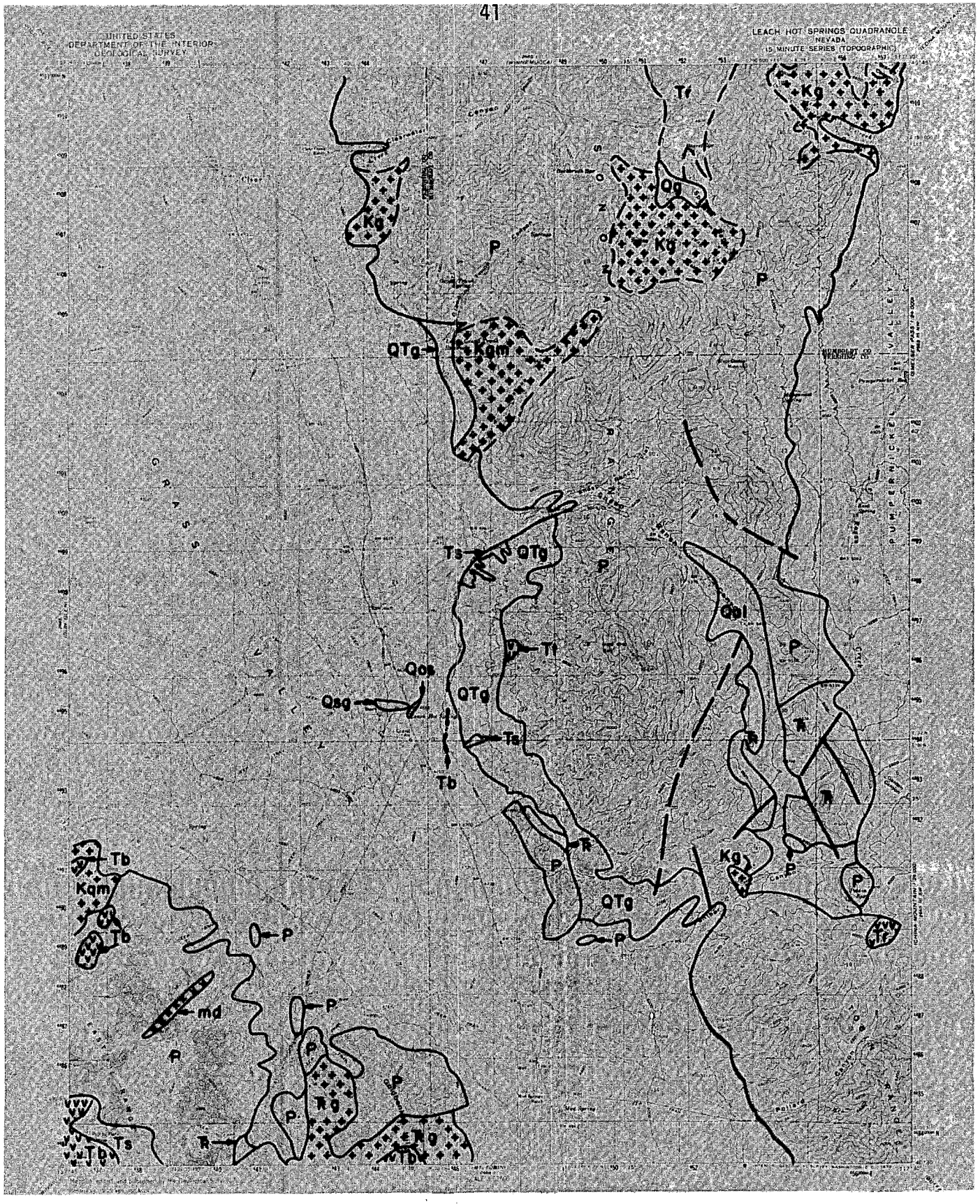

CBB 751-49

Figure 2: Lithologic map, Leach Hot Springs area. Qal: alluvium, Qos: older sinter deposits, Qsg: sinter gravels, QTg: Quaternary-Tertiary gravels and fanglomerates, Tb: Tertiary basalt, Tr: Tertiary rhyolite, Tt: tuff, Ts: Tertiary sedimentary rocks, Kqm: quartz monzonite, Kg: granitic rock, md: mafic dike, TRg: Triassic granitic rocks, TR: undifferentiated Triassic sedimentary rocks, P: undifferentiated Paleozoic sedimentary rocks.

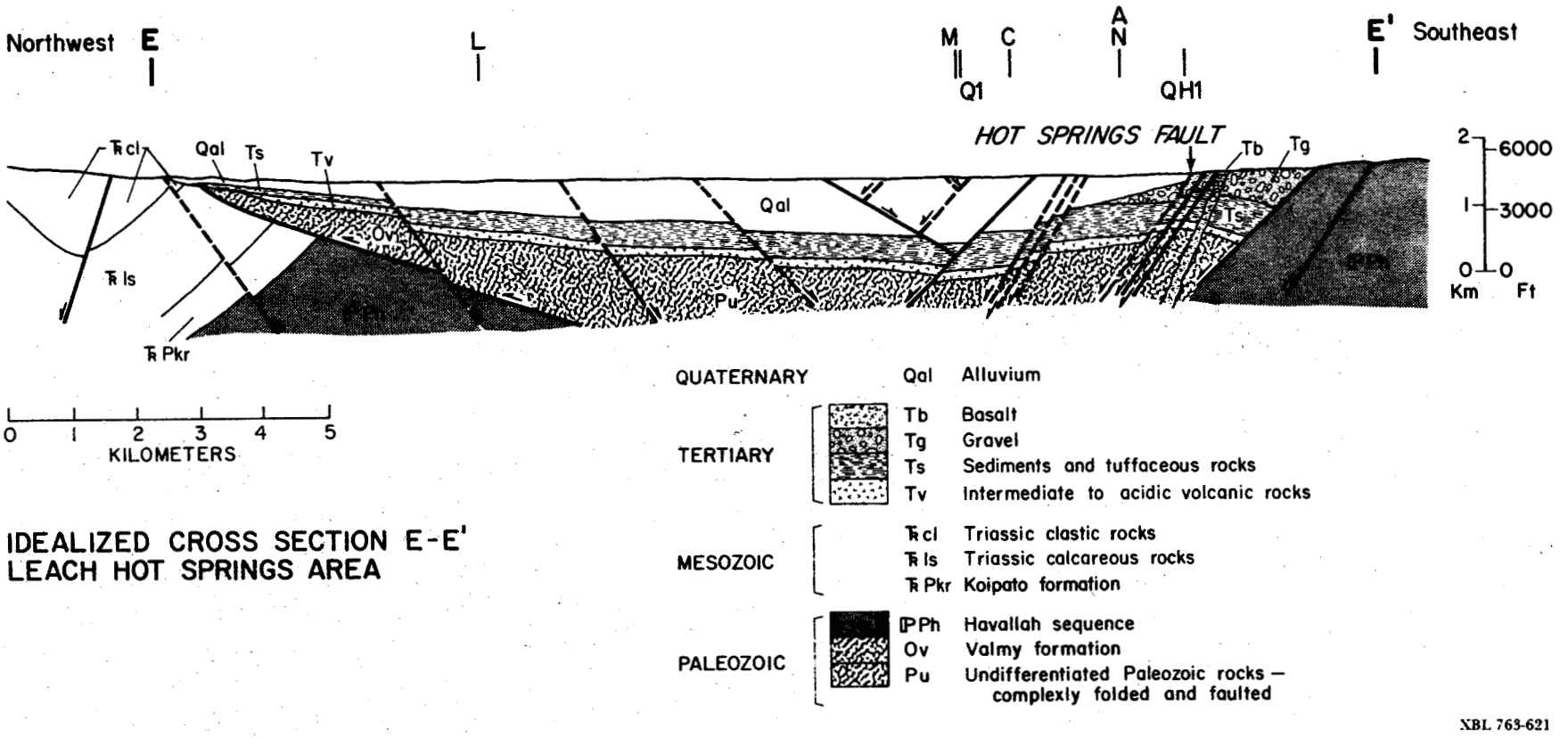

IDEALIZED CROSS SECTION E-E'
LEACH HOT SPRINGS AREA

Figure 3: Idealized geologic cross section along line E-E' (Figure 7).

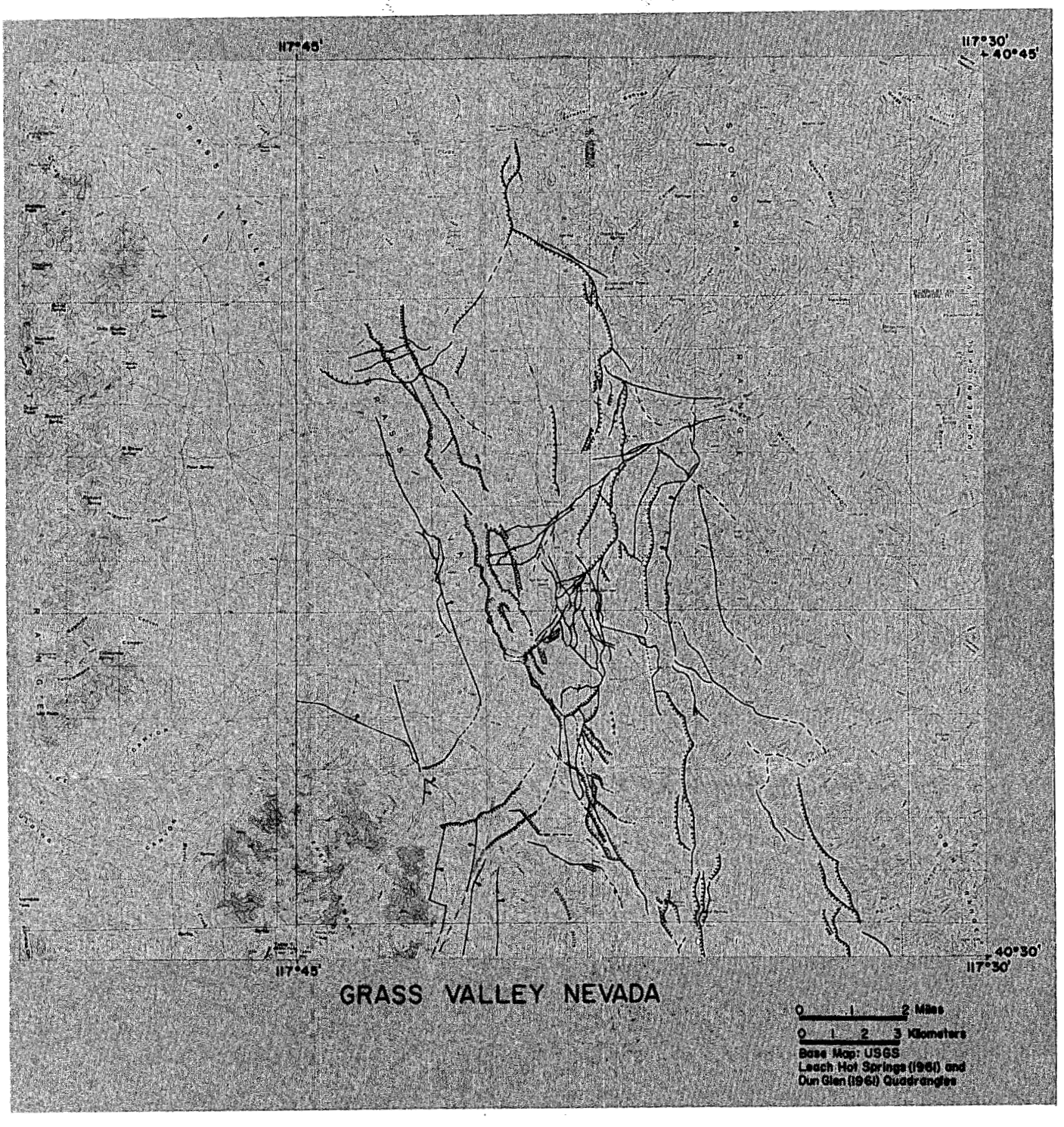

CBB 7410-7615

Figure 4: Fault map of the Leach Hot Springs area. Hachured lines indicate down-faulted sides of scarplets; ball symbol indicates downthrown side of other faults.

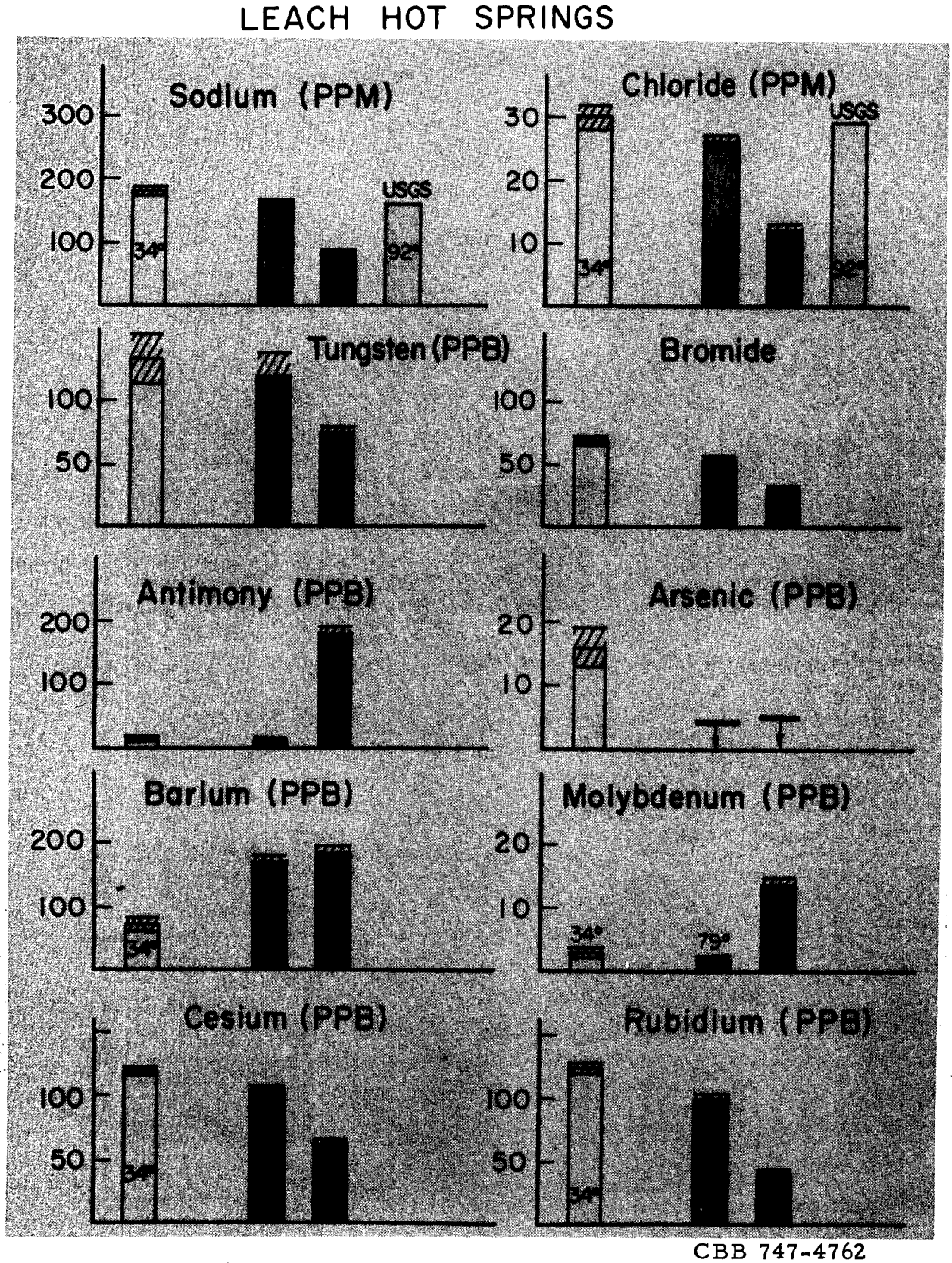

Figure 5: Abundances of prominent elements in three separate hot pools at Leach Hot Springs.

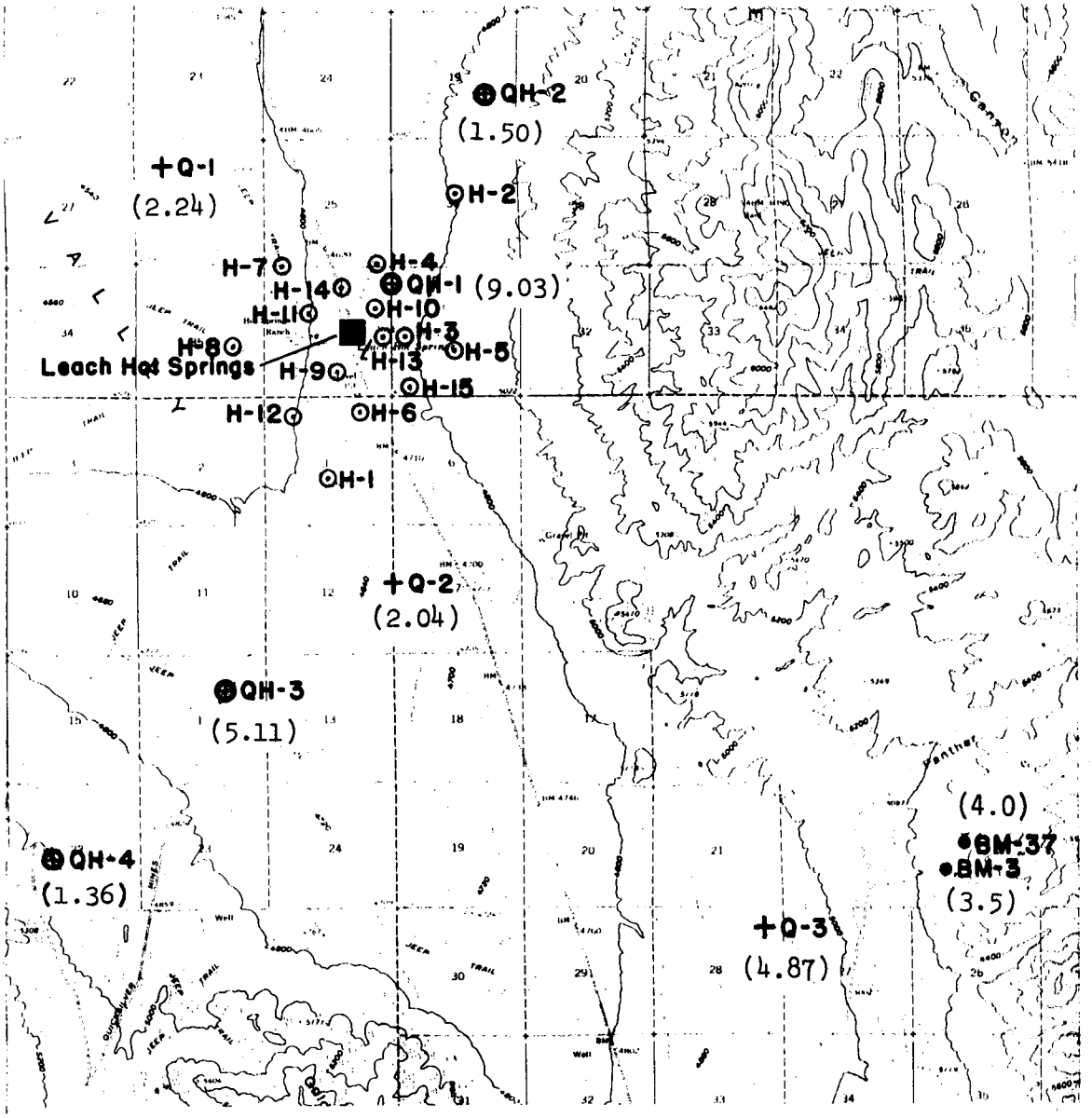

Figure 6: Locations of wells at Grass Valley (Heat-flow values are shown in parentheses)

+ Q, heat-flow holes
⊙ H, shallow hydrologic test wells
⊕ QH, heat flow - hydrologic test wells
• , heat-flow determinations from Sass and others, 1971

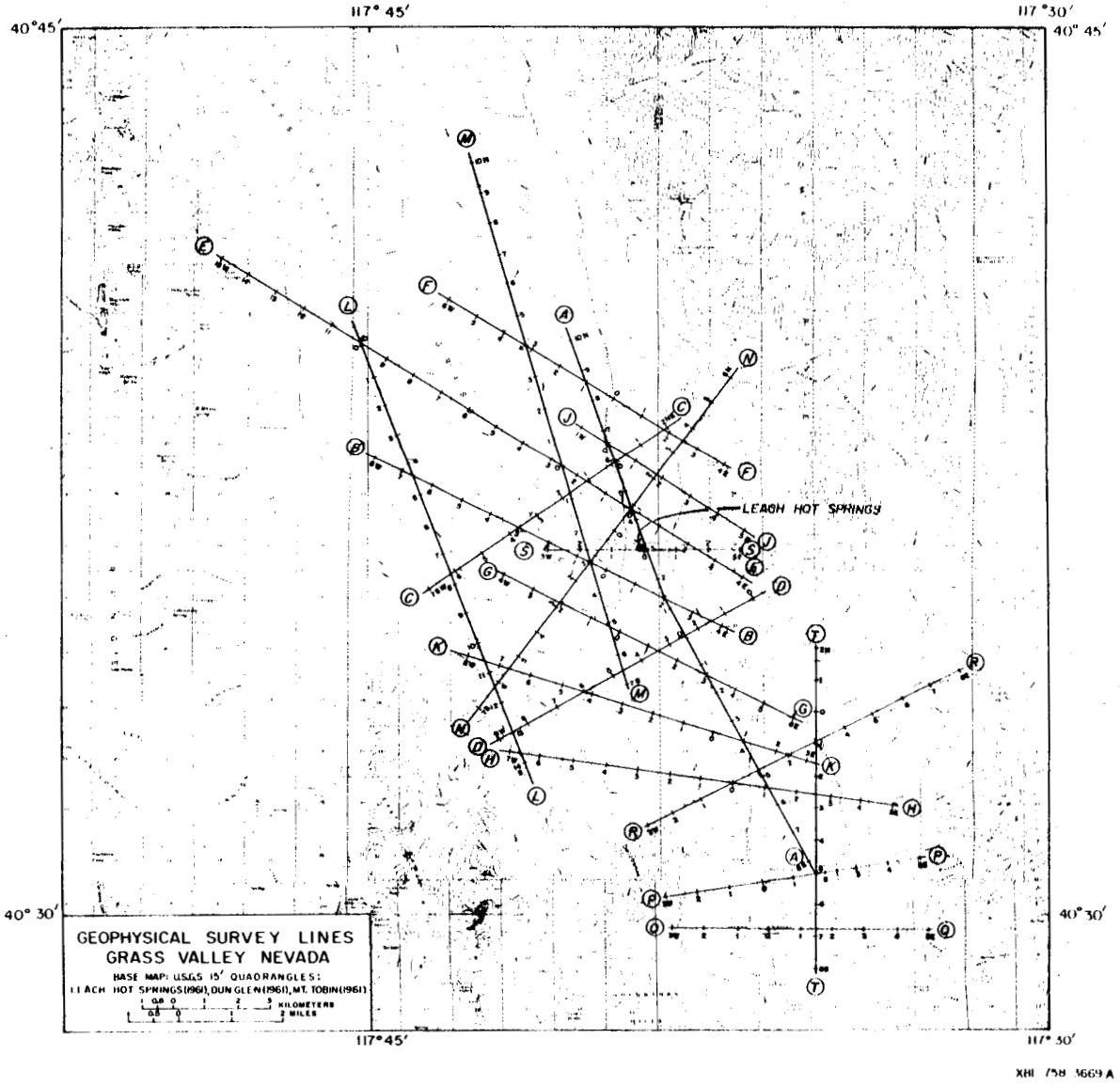

Figure 7: Geophysical Survey Lines in Grass Valley, Nevada.

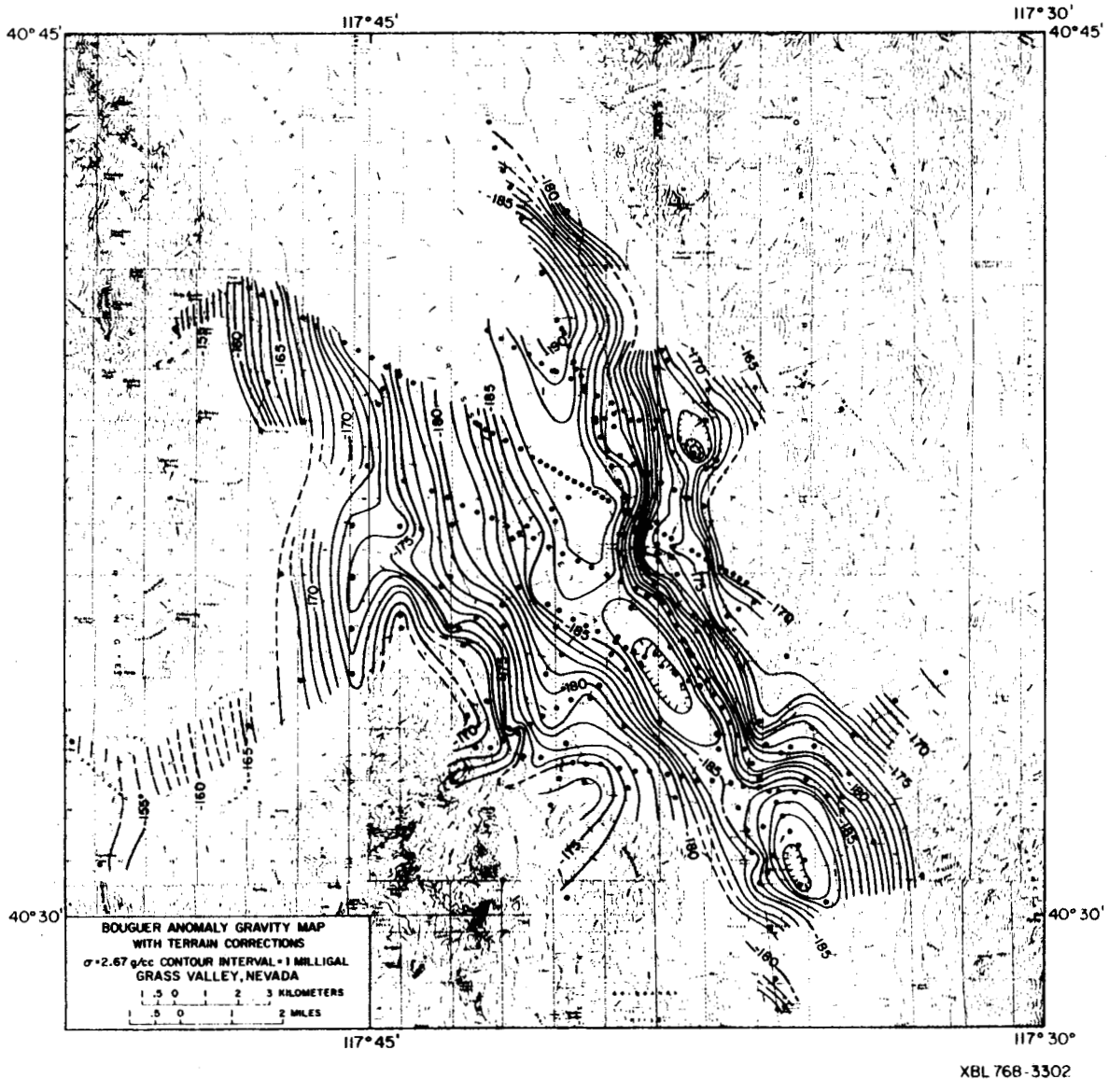

Figure 8: Bouguer anomaly gravity map, Grass Valley, Nevada.

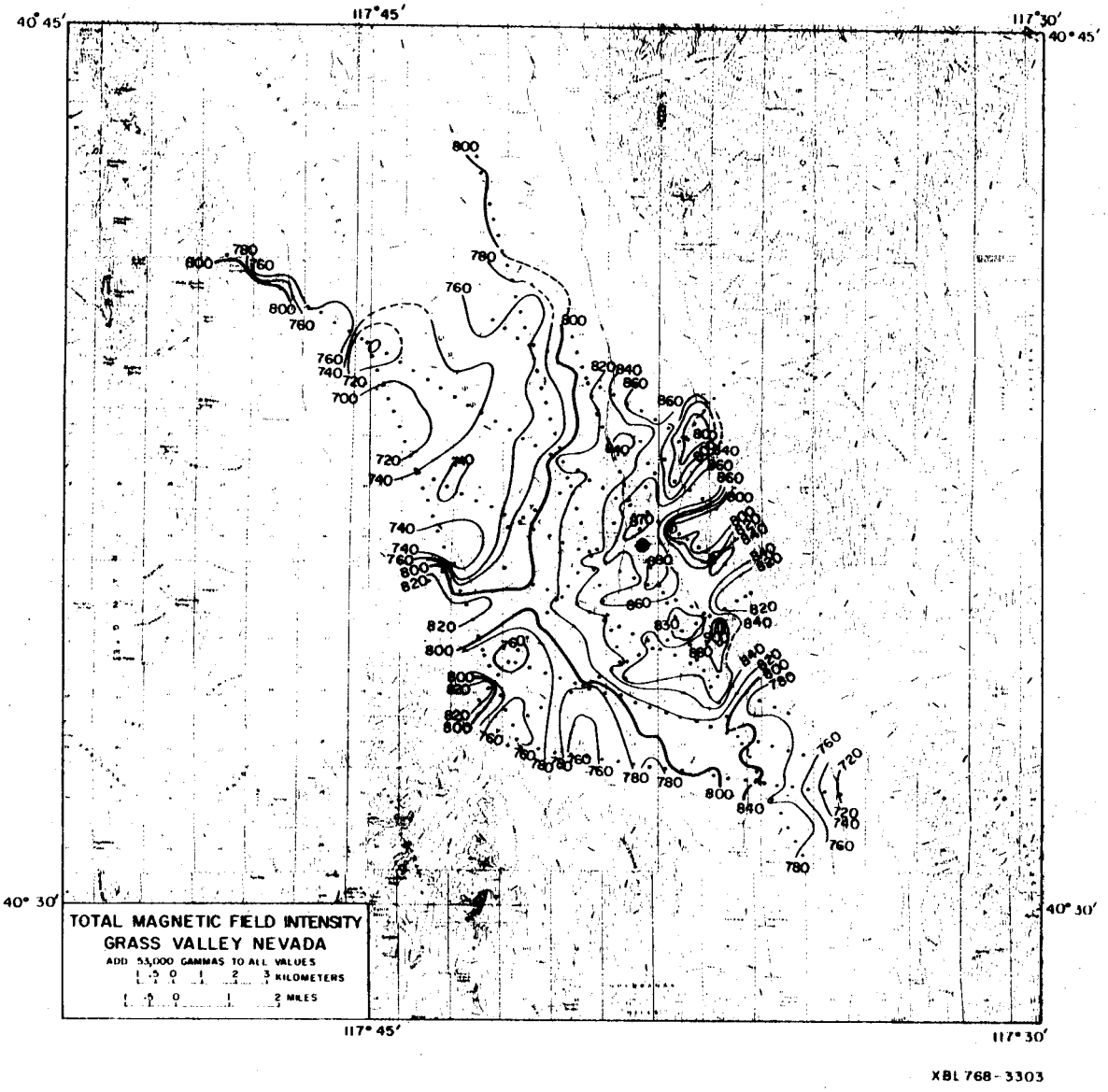

Figure 9: Ground magnetic field map, total intensity, Grass Valley, Nevada.

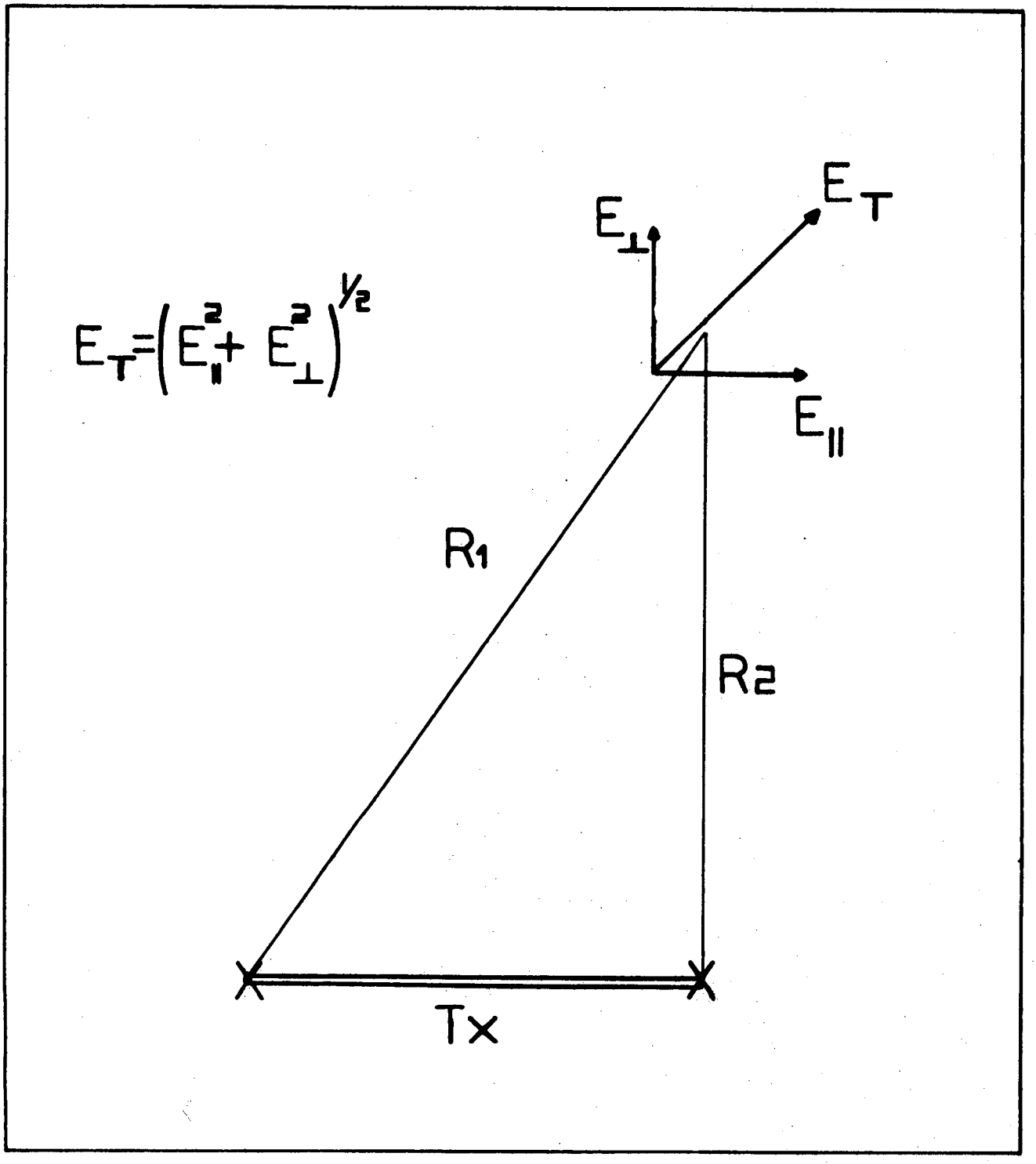

Figure 10: Bipole-dipole apparent resistivity and apparent conductance array.

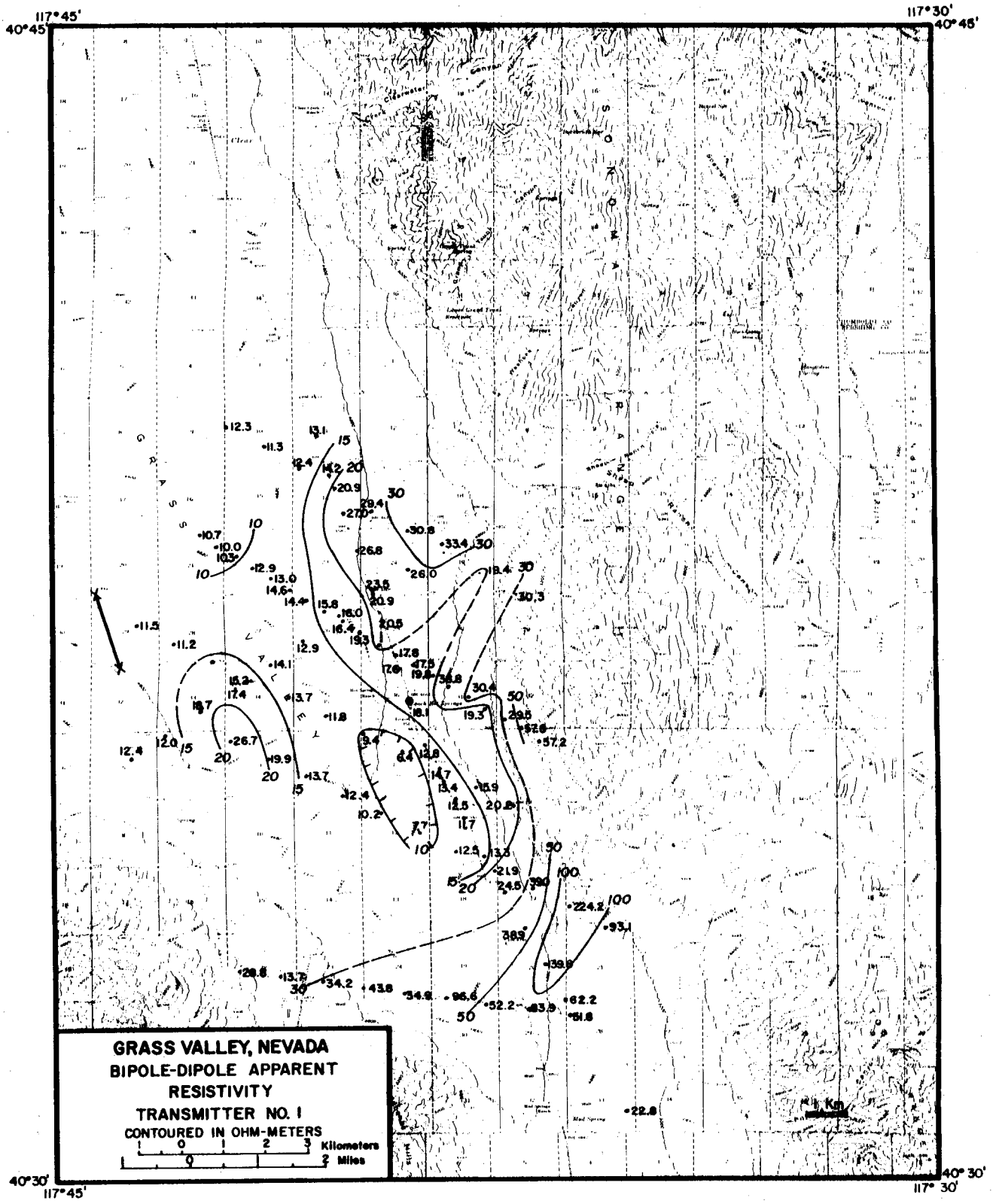

XBL 768-10090

Figure 11: Bipole-dipole apparent resistivity map for transmitter no. 1.

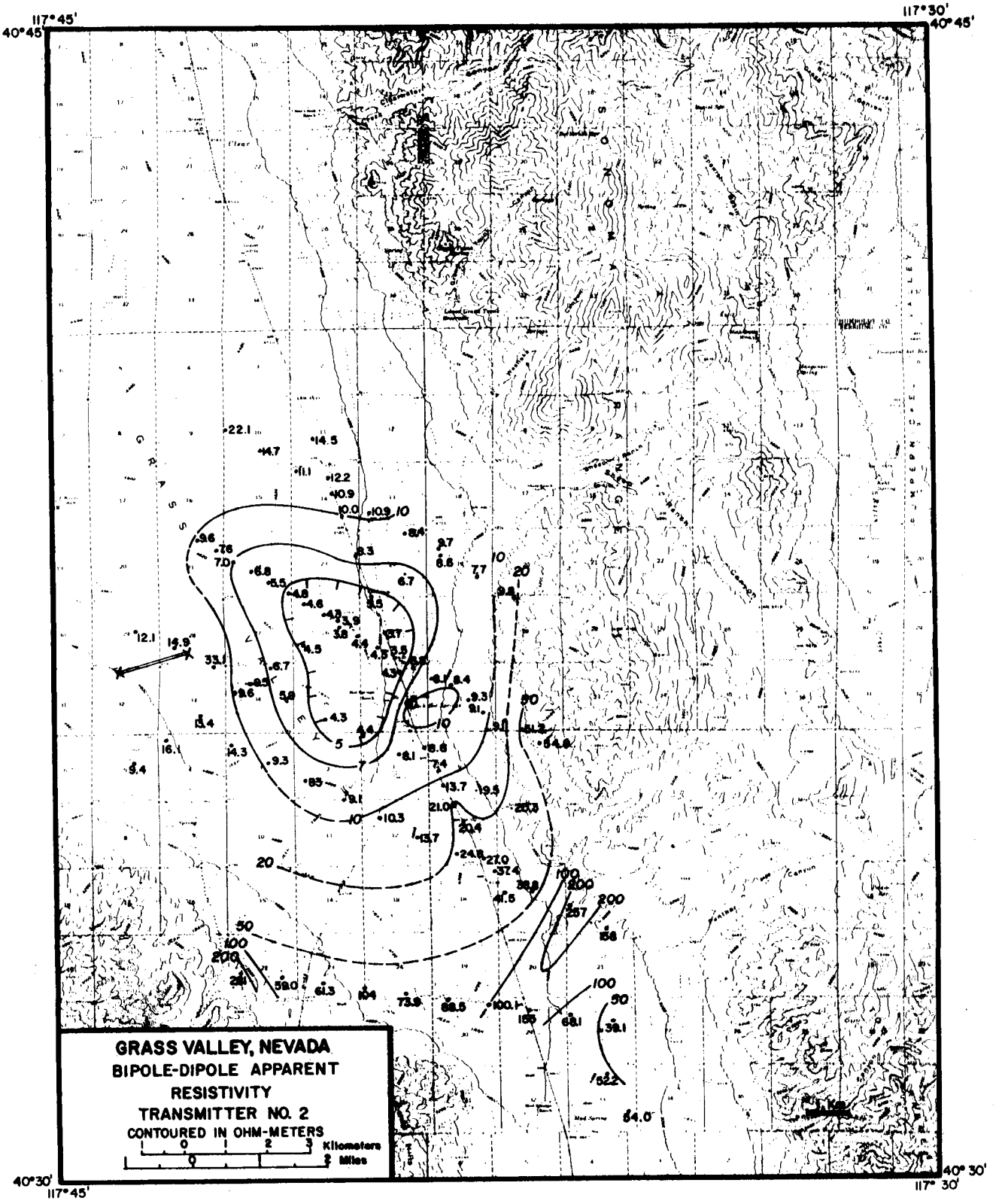

Figure 12: Bipole-dipole apparent resistivity map for transmitter no. 2.

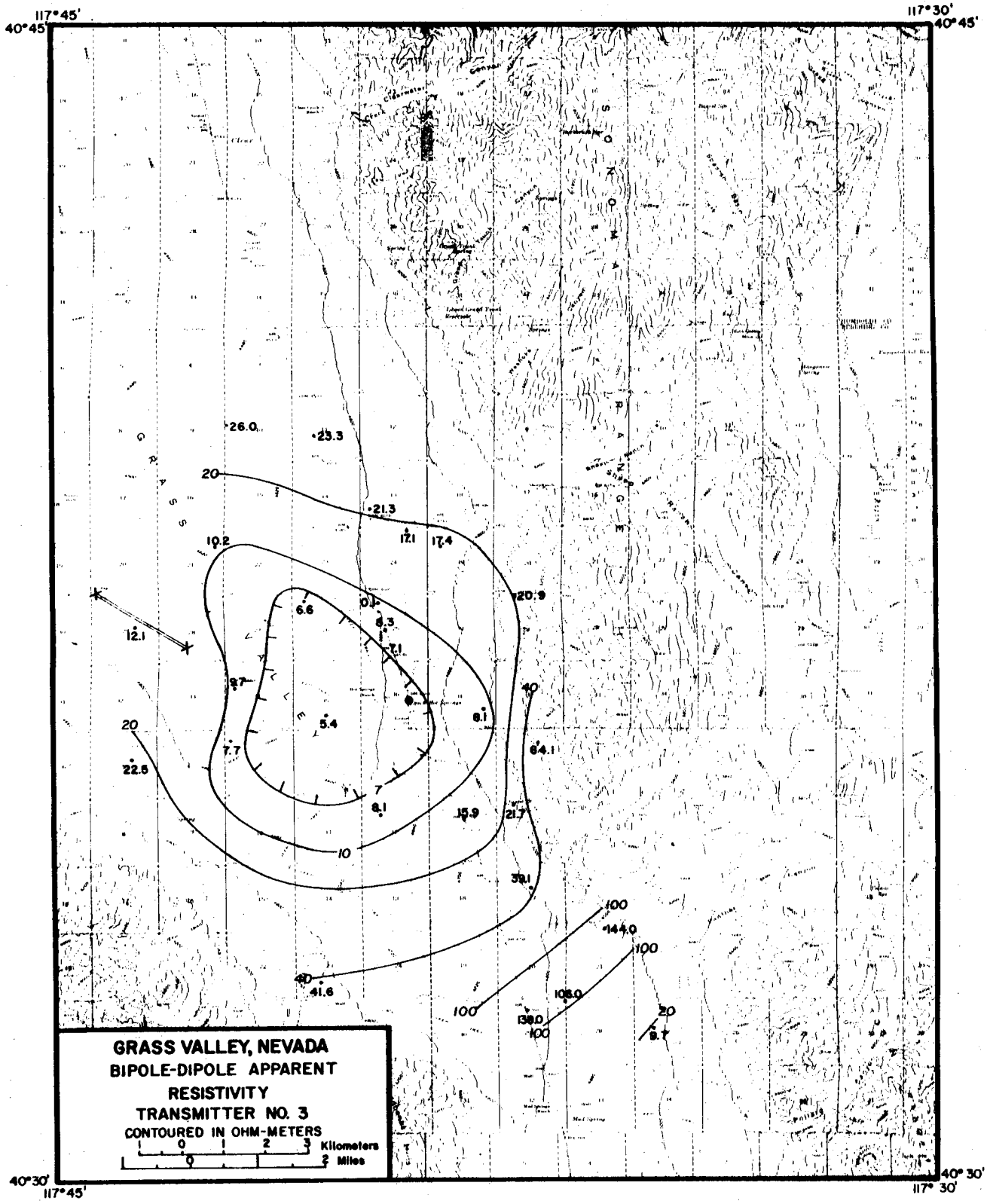

Figure 13: Bipole-dipole apparent resistivity map for transmitter no. 3.

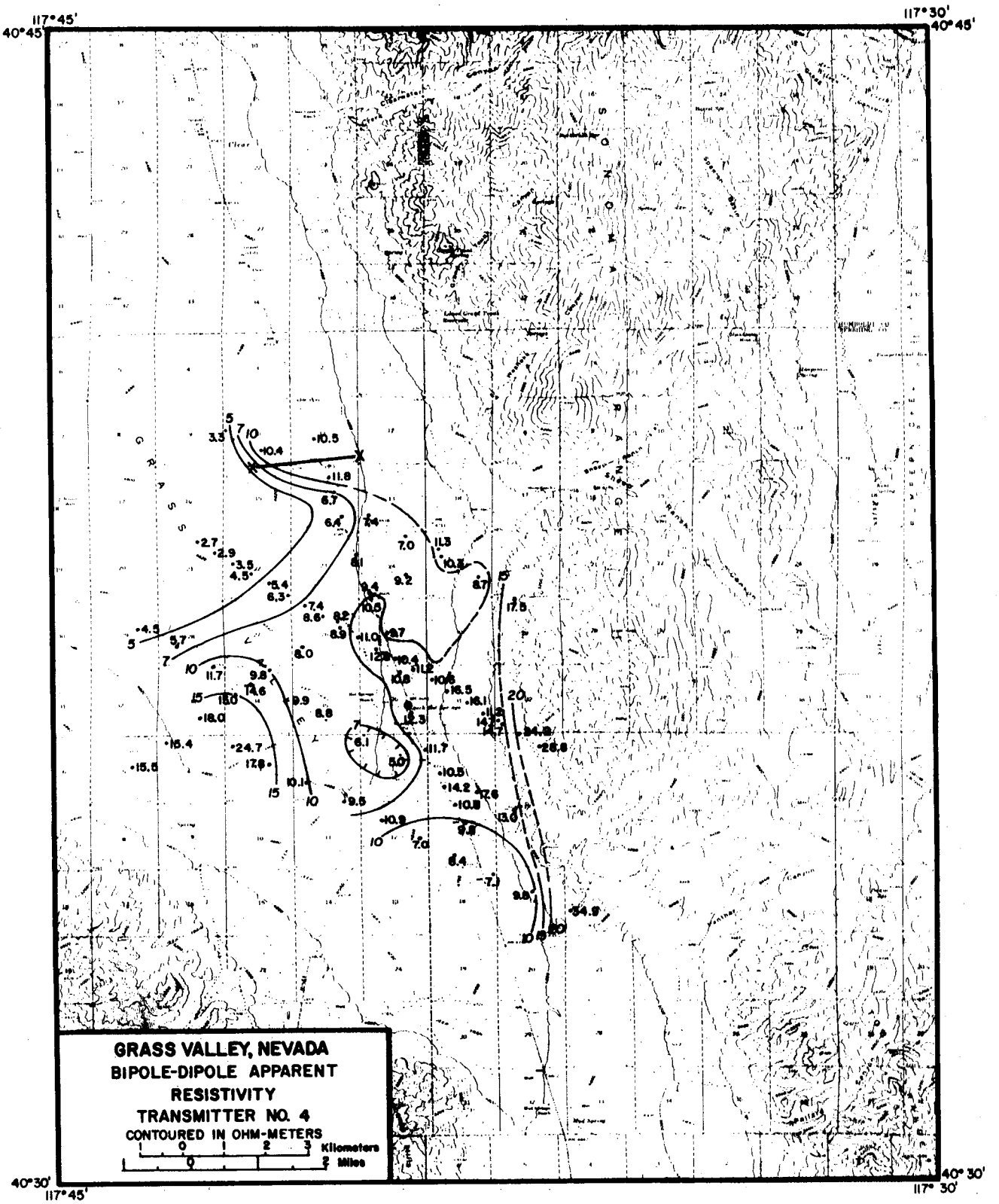

Figure 14: Bipole-dipole apparent resistivity map for transmitter no. 4.

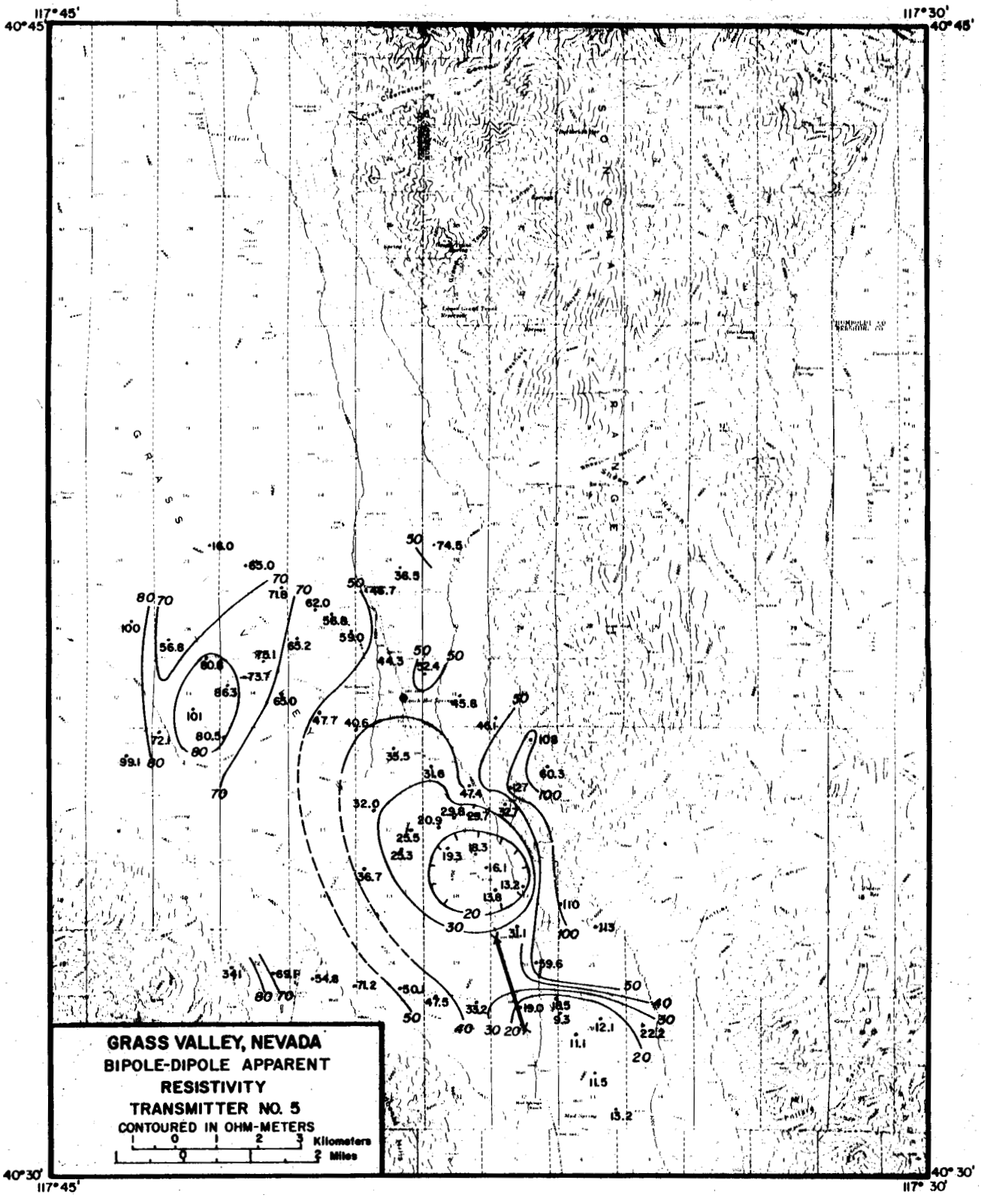

Figure 15: Bipole-dipole apparent resistivity map for transmitter no. 5.

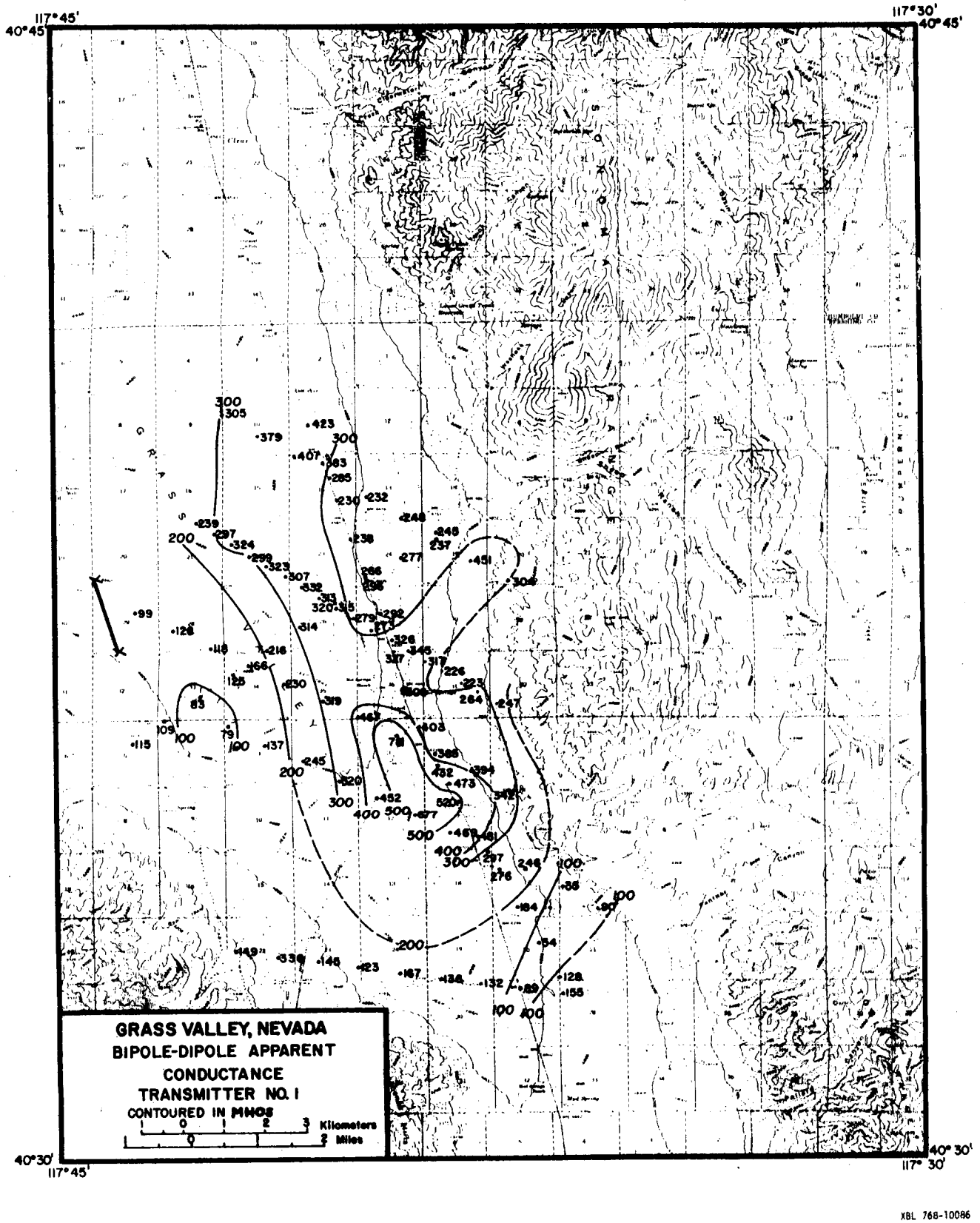

Figure 16: Bipole-dipole apparent conductance map for transmitter no. 1.

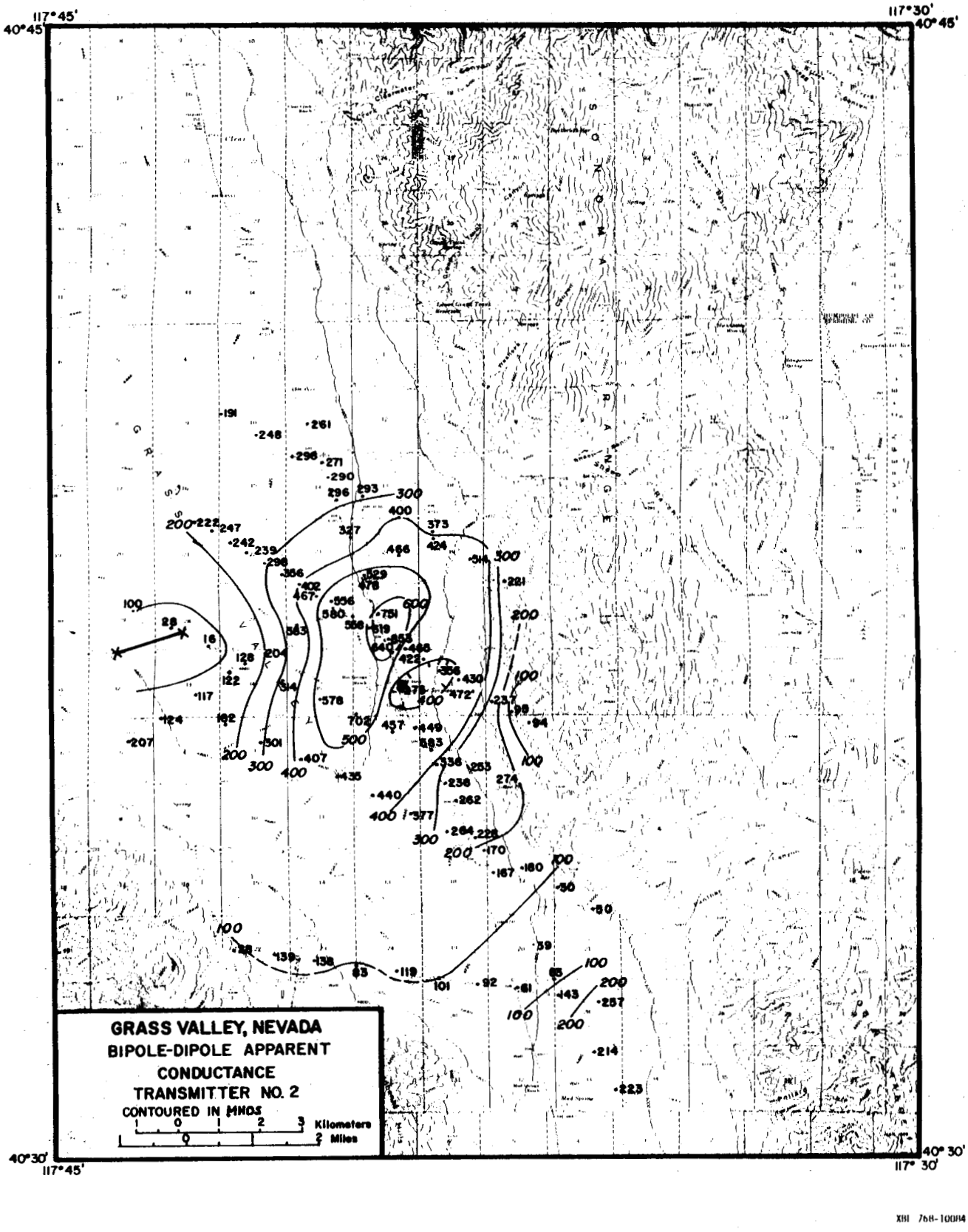

Figure 17: Bipole-dipole apparent conductance map for transmitter no. 2.

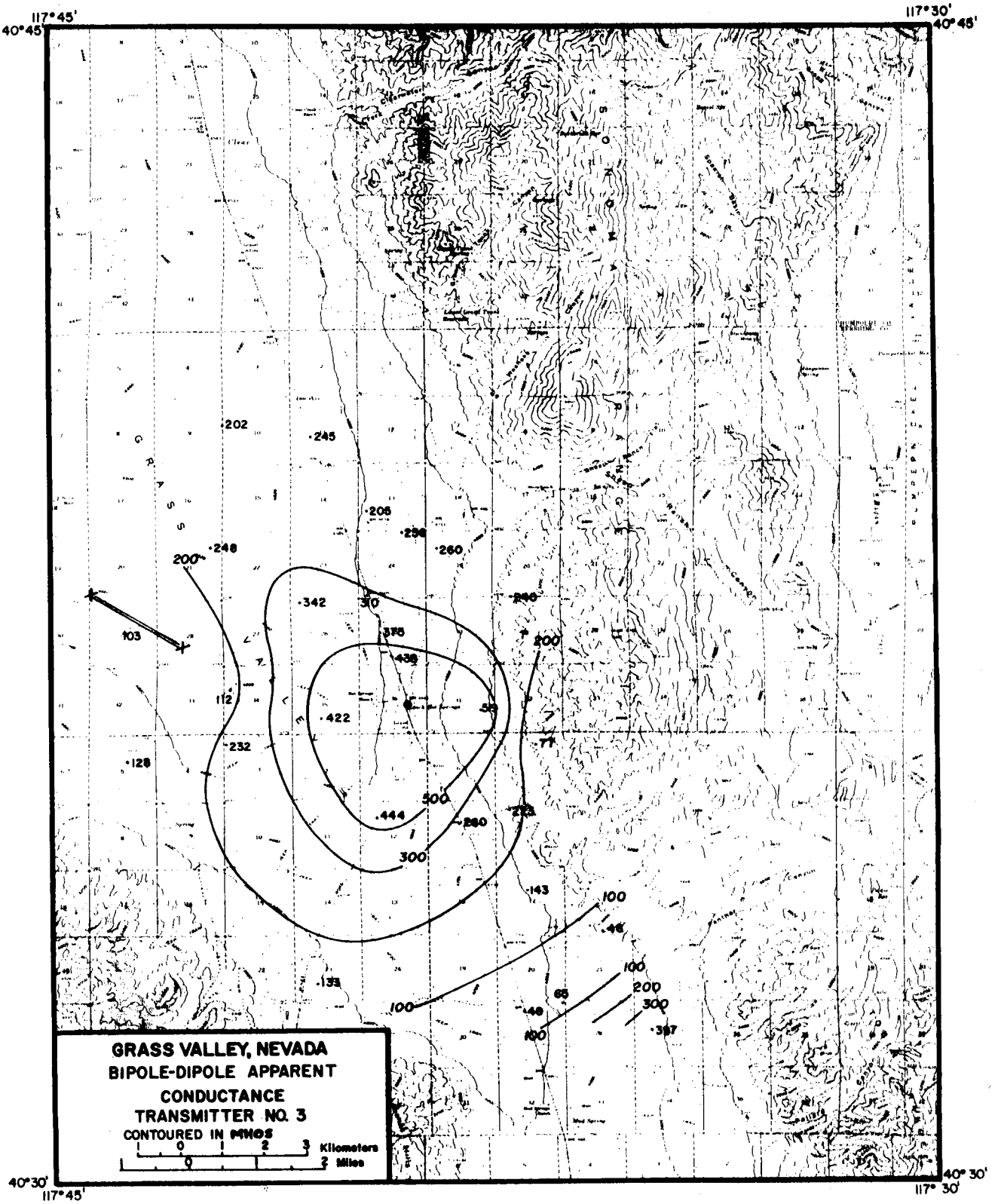

Figure 18: Bipole-dipole apparent conductance map for transmitter no. 3.

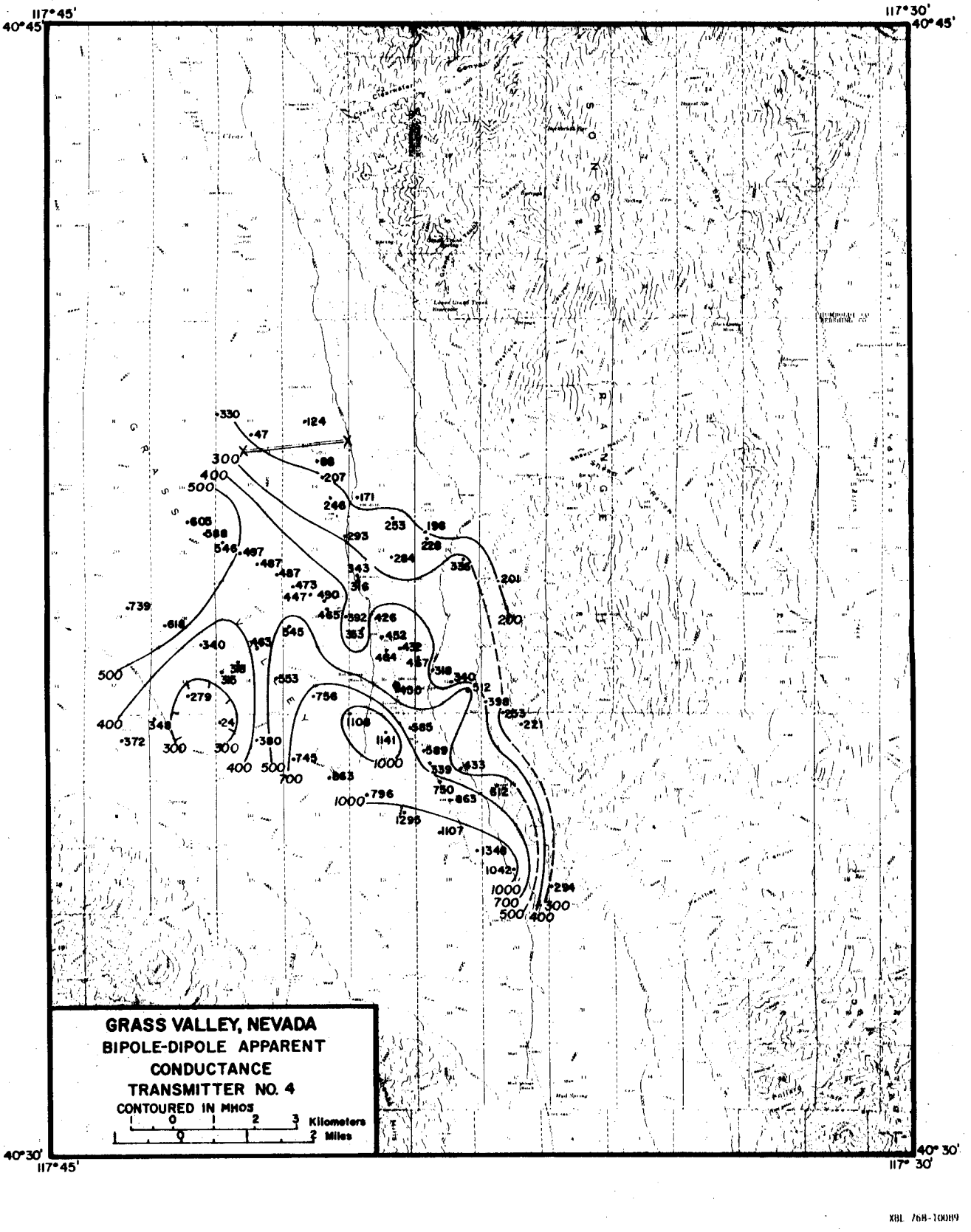

Figure 19: Bipole-dipole apparent conductance map for transmitter no. 4.

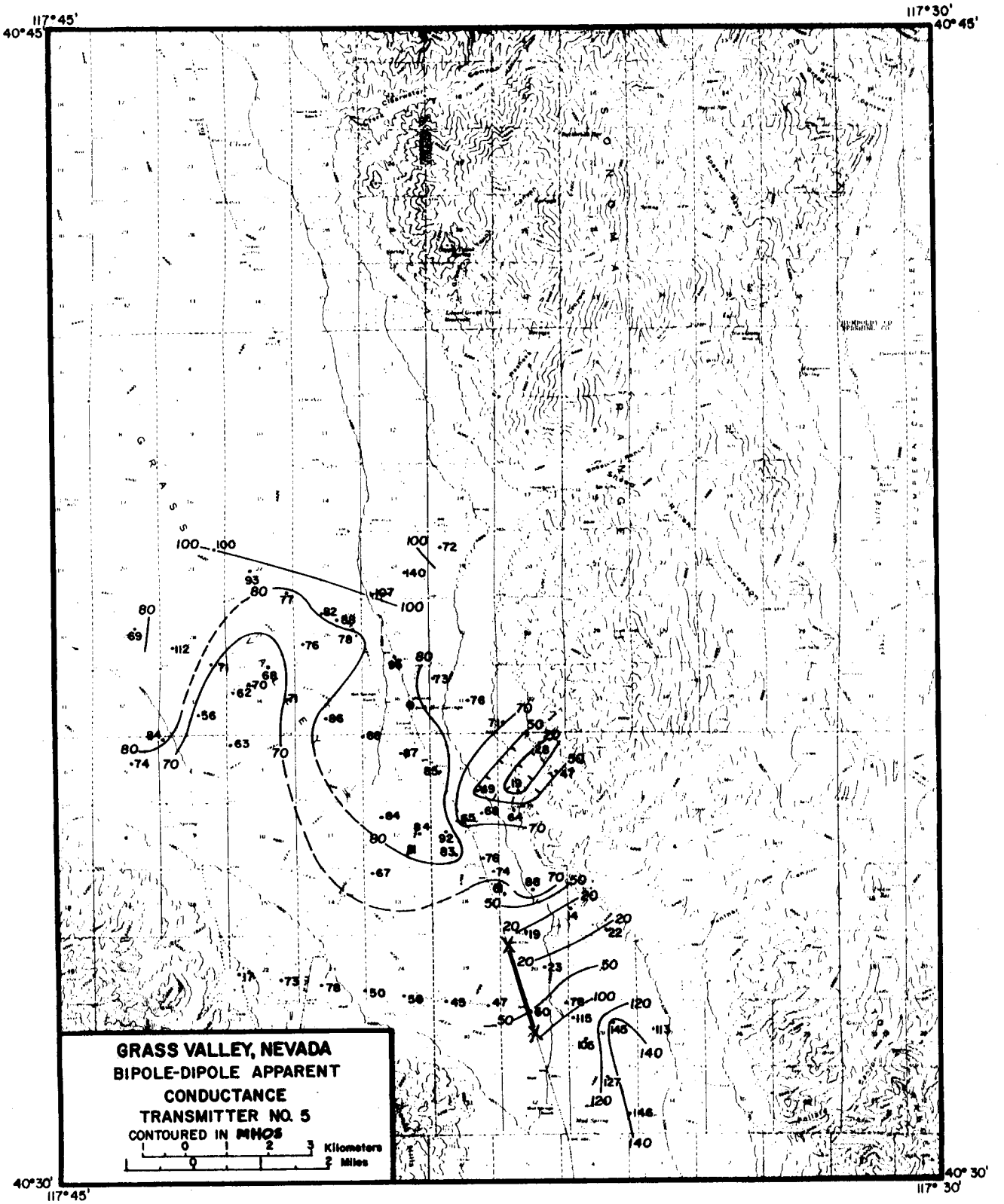

Figure 20: Bipole-dipole apparent conductance map for transmitter no. 5.

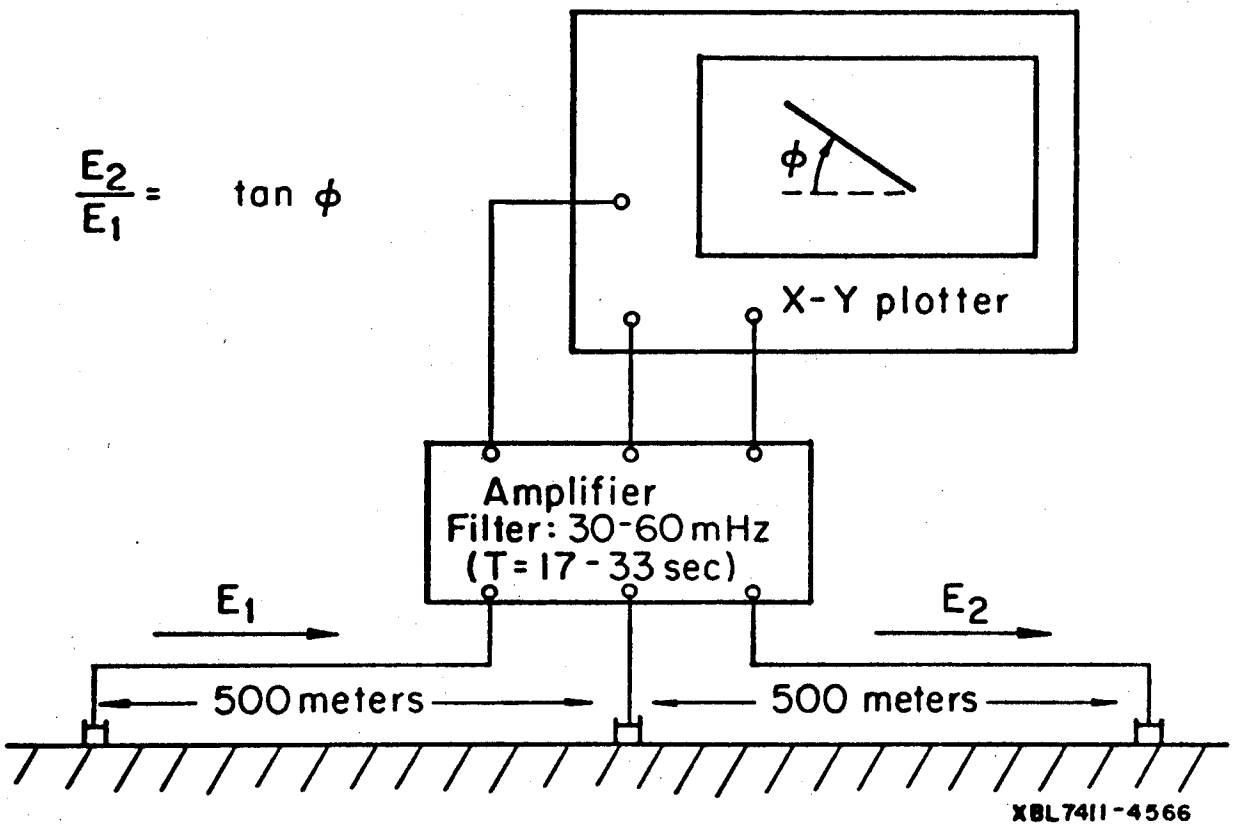

Figure 21: Schematic diagram of E-field ratio profiling system.

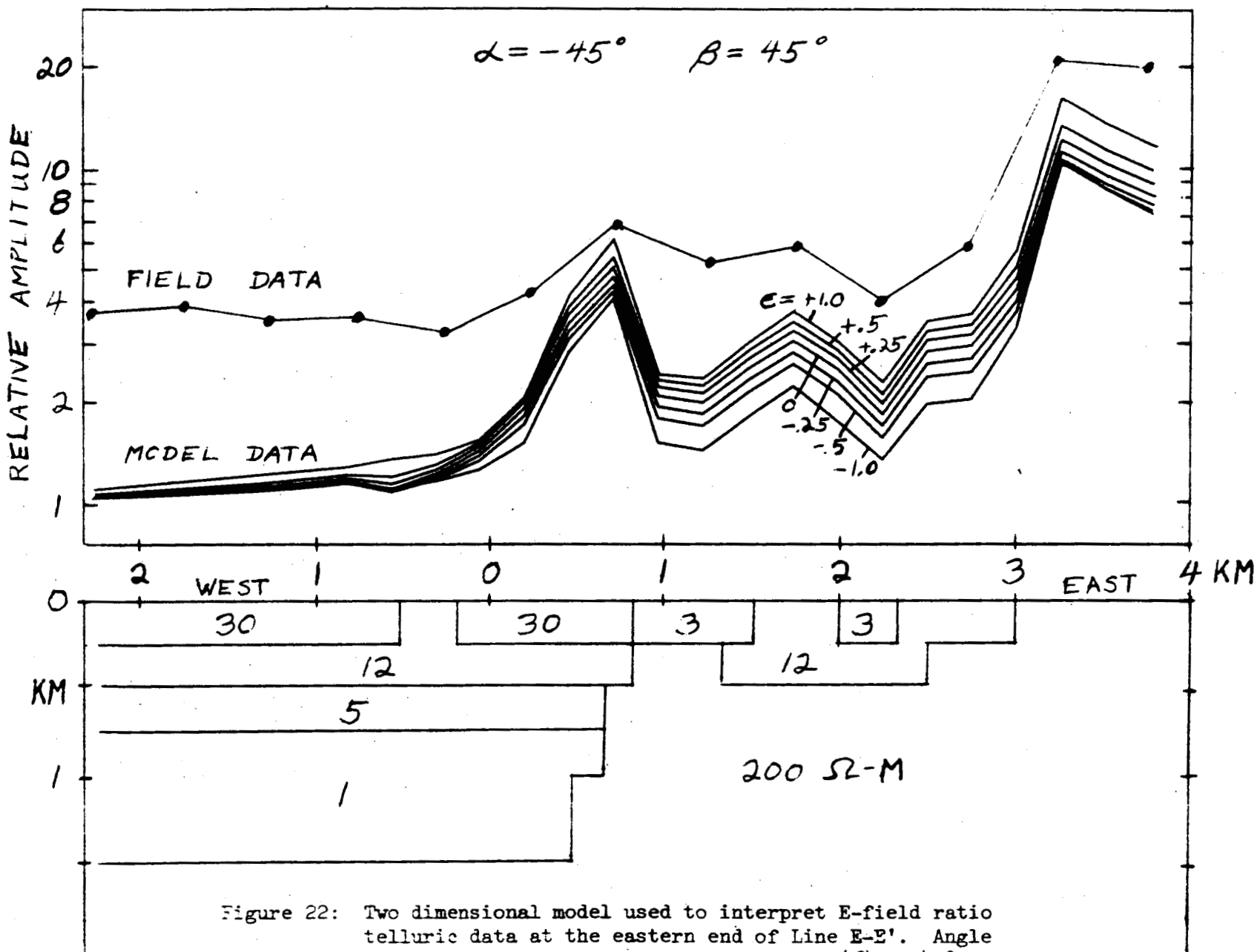

Figure 22: Two dimensional model used to interpret E-field ratio telluric data at the eastern end of Line E-E'. Angle of traverse line with respect to strike (β) is 45°: incident magnetic field polarization (α) at -45° to strike: magnetic field ellipticity (ϵ) is the variable.

DIPOLE-DIPOLE APPARENT RESISTIVITY PSEUDO-SECTION

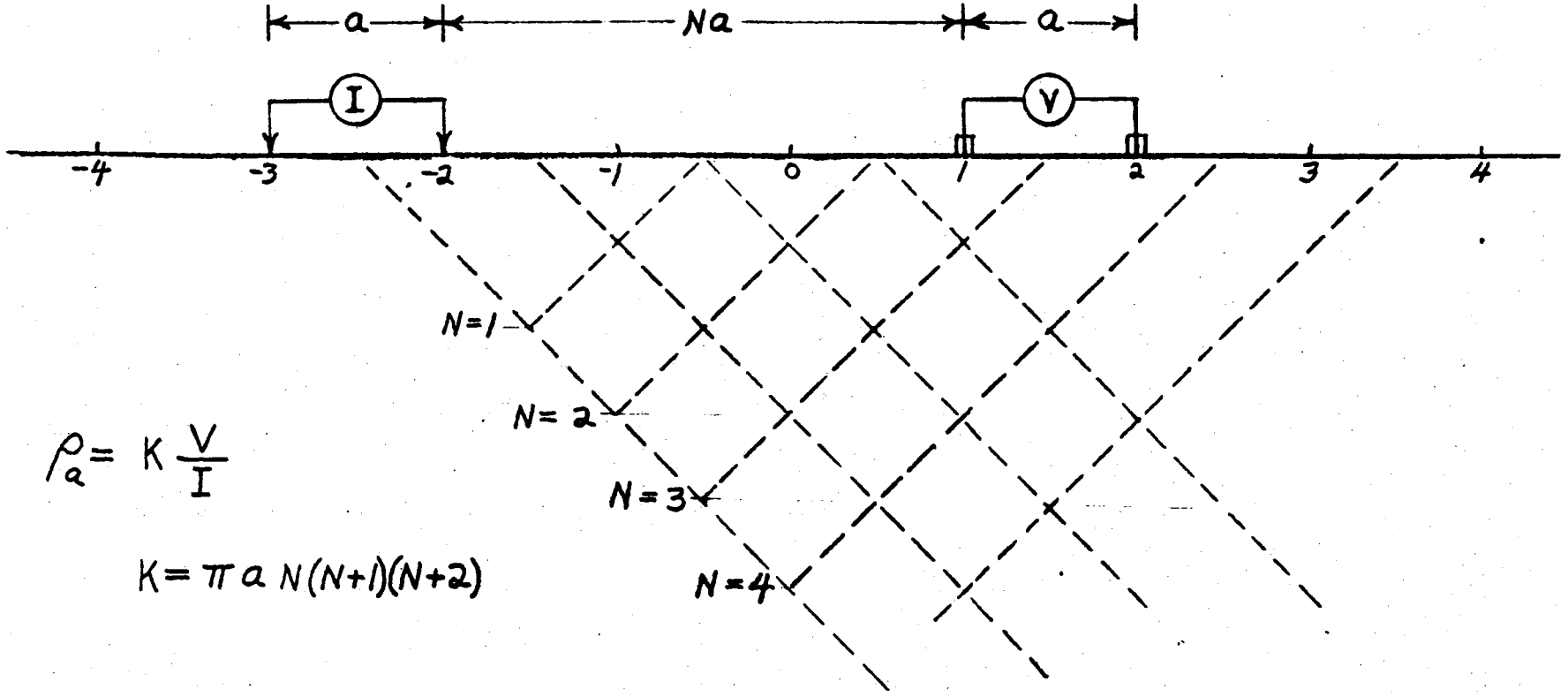

Figure 23: Schematic diagram of data presentation for dipole-dipole apparent resistivity.

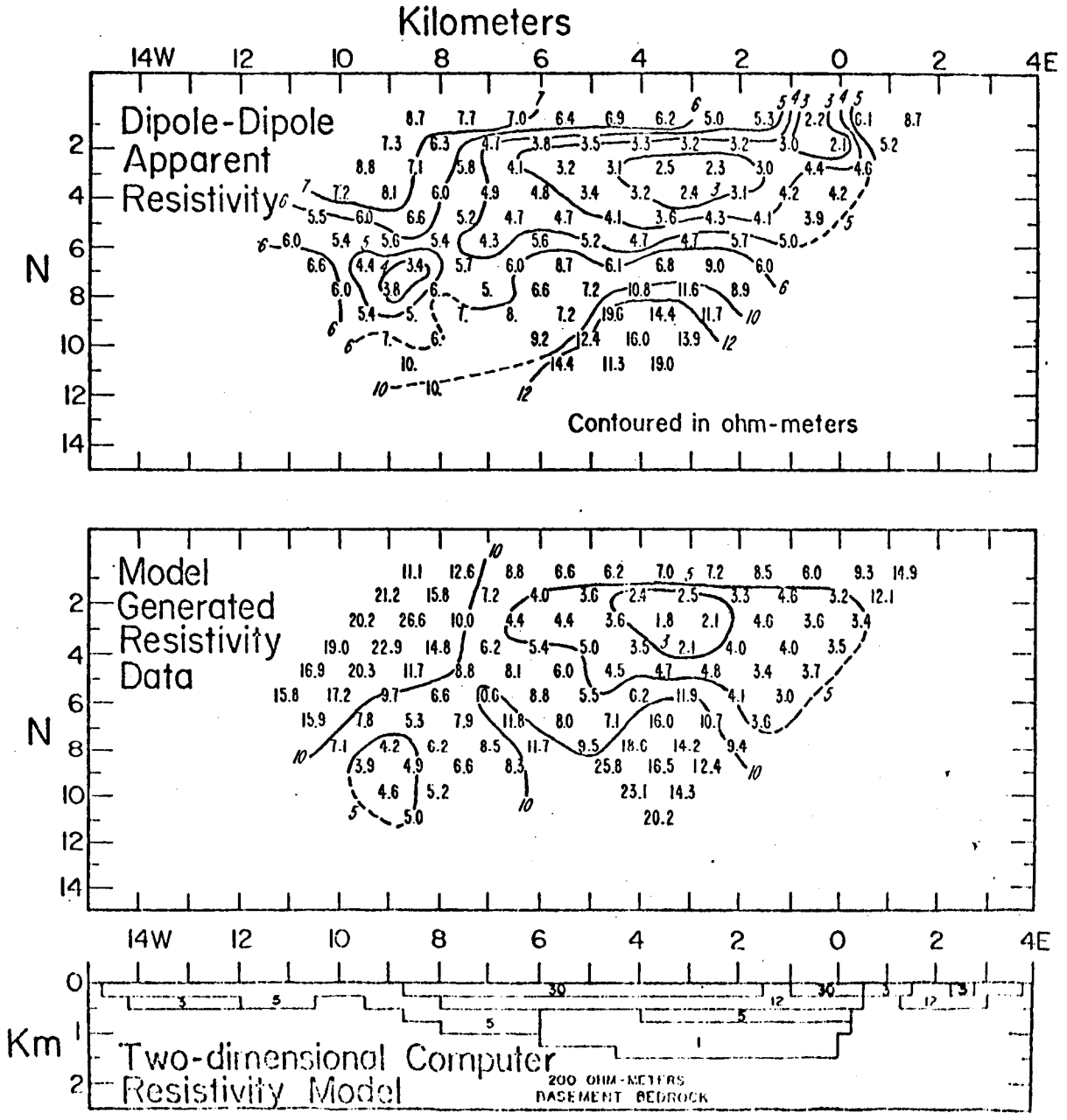

Figure 24: Dipole-dipole apparent resistivity pseudo-section and preliminary computer model interpretation on line E-E'. One kilometer dipoles.

GRASS VALLEY
Line E-E'

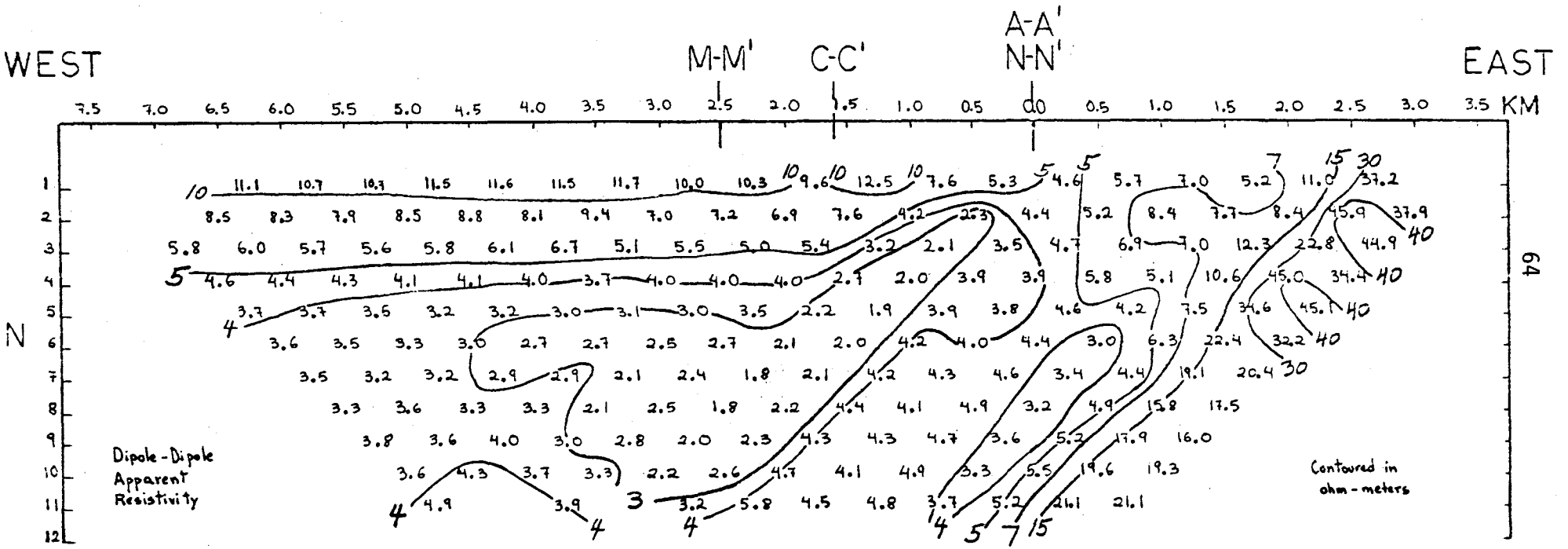

Figure 25a: Dipole-dipole apparent resistivity pseudo-section on line E-E', 500 m dipoles.

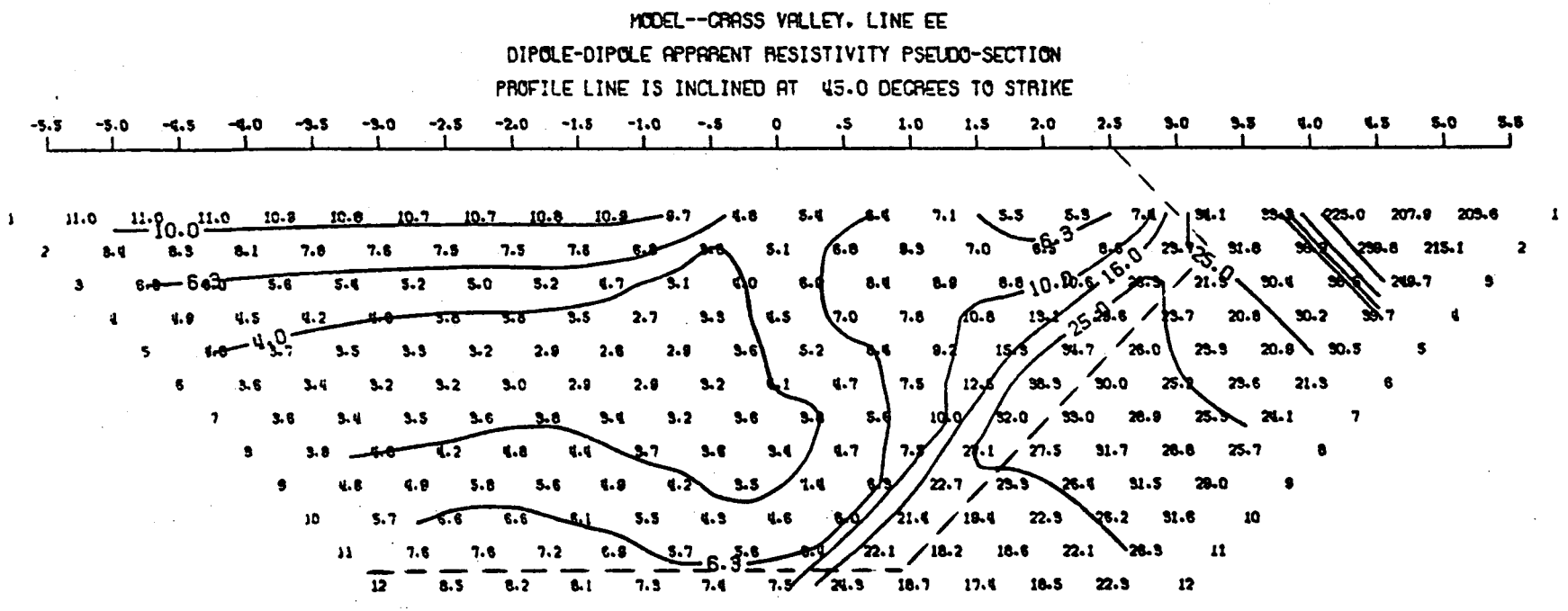

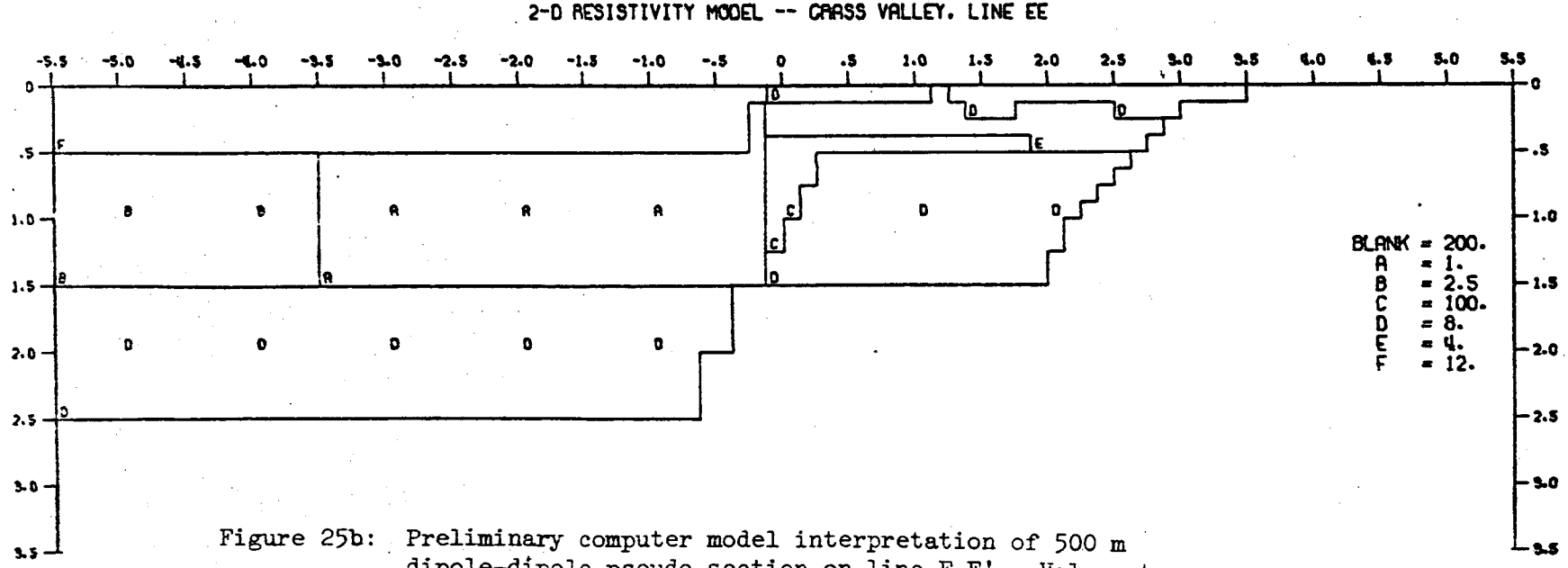

Figure 25b: Preliminary computer model interpretation of 500 m dipole-dipole pseudo-section on line E-E'. Values to the left of dashed line represent data coverage in Figure 25a.

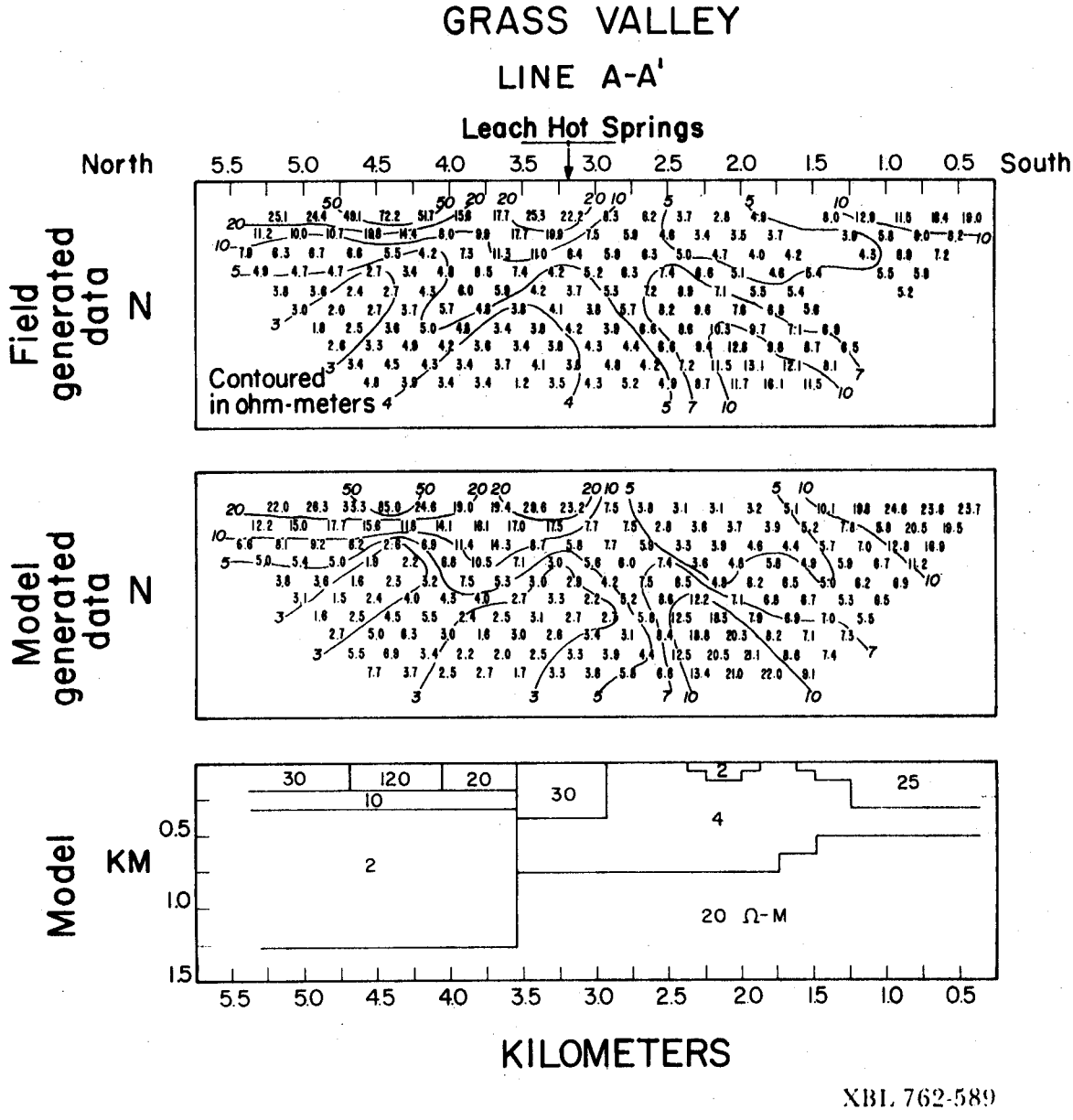

Figure 26: Dipole-dipole apparent resistivity pseudo-section on line A-A', 250 m dipoles and preliminary computer model interpretation on line A-A'.

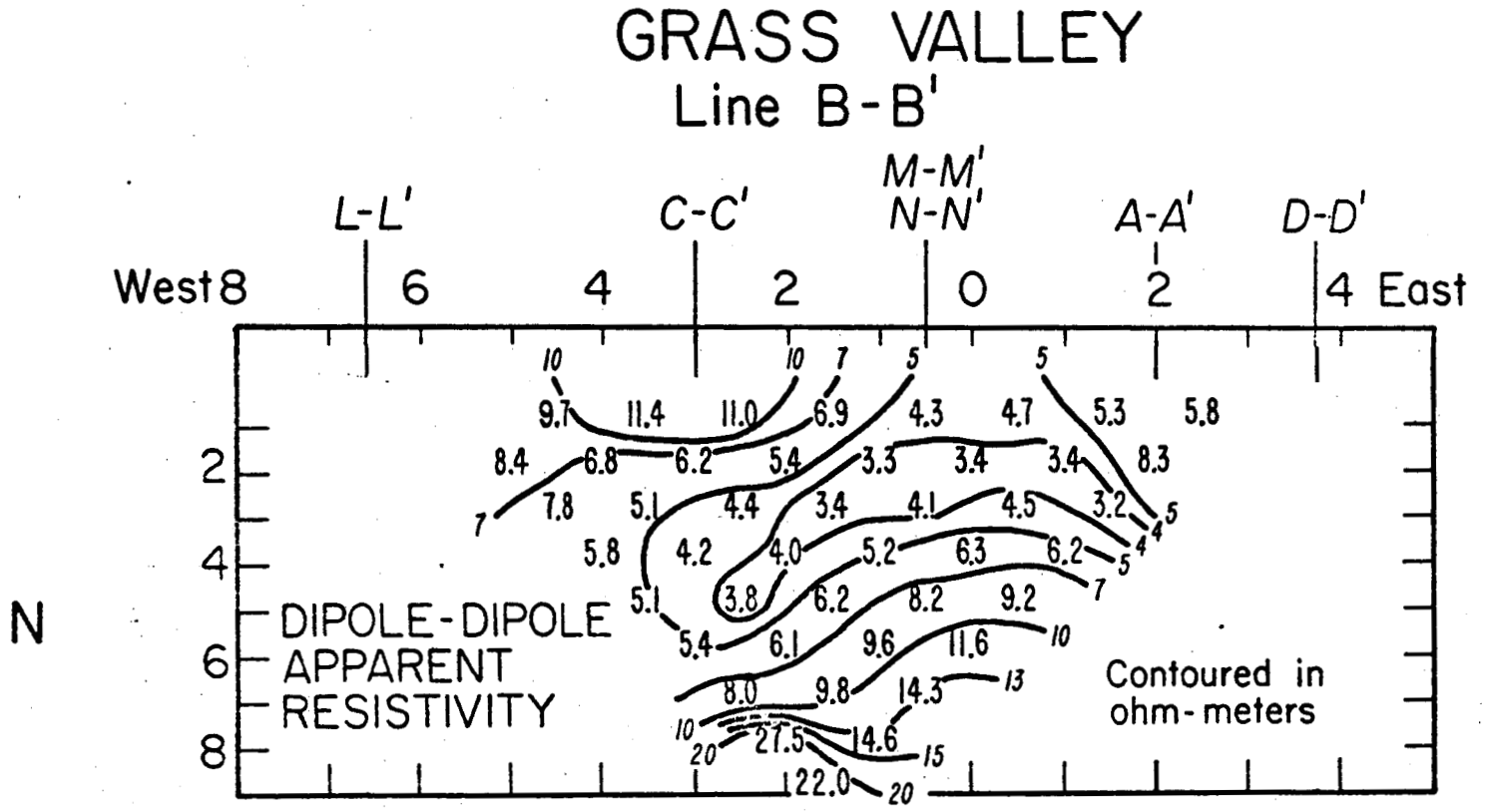

Figure 27a Dipole-dipole apparent resistivity pseudo-section on line B-B', 1 km dipoles.

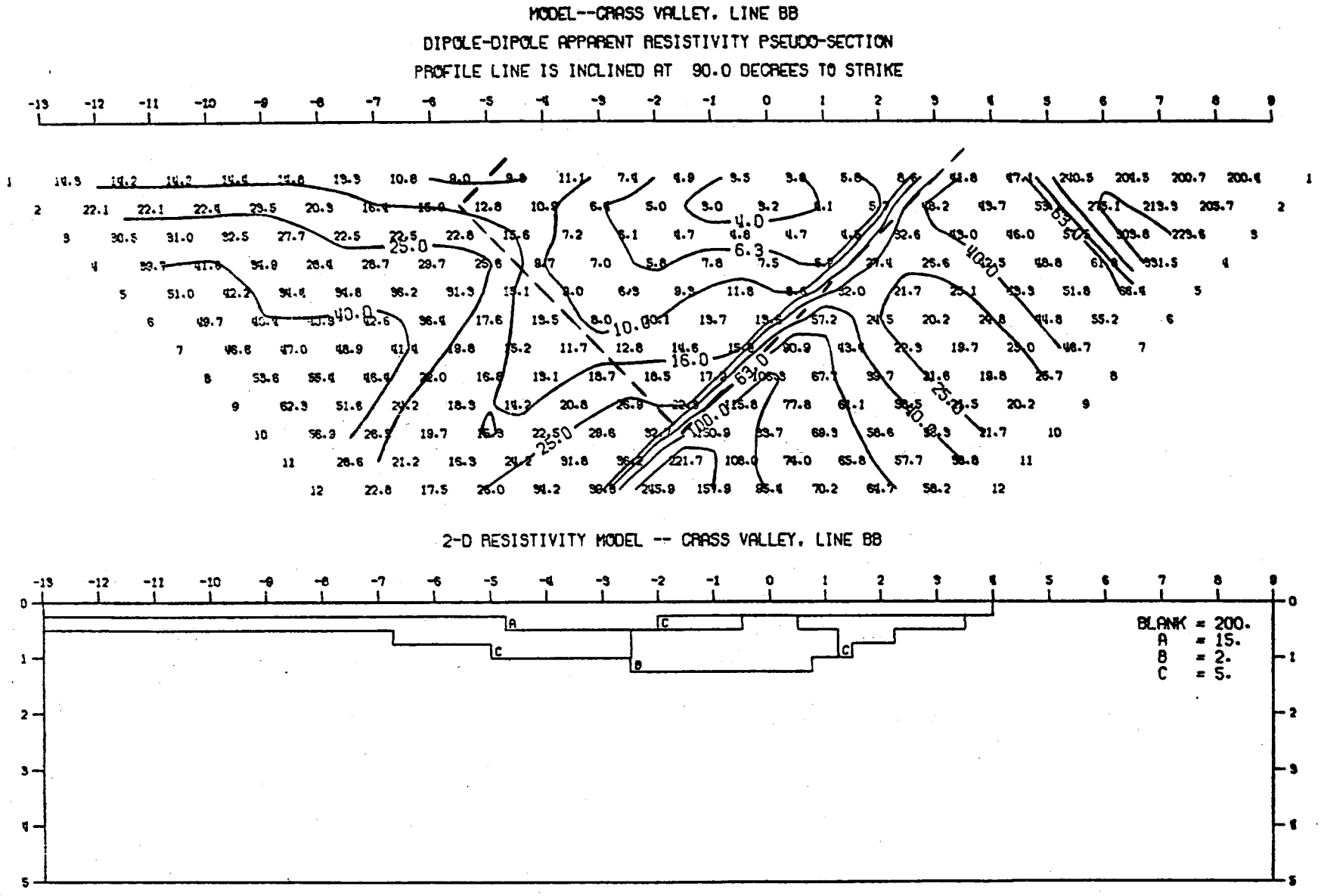

Figure 27b: Preliminary computer model interpretation of 1 km dipole-dipole pseudo-section on line B-B'. Values above dashed line represent data coverage in Figure 27a.

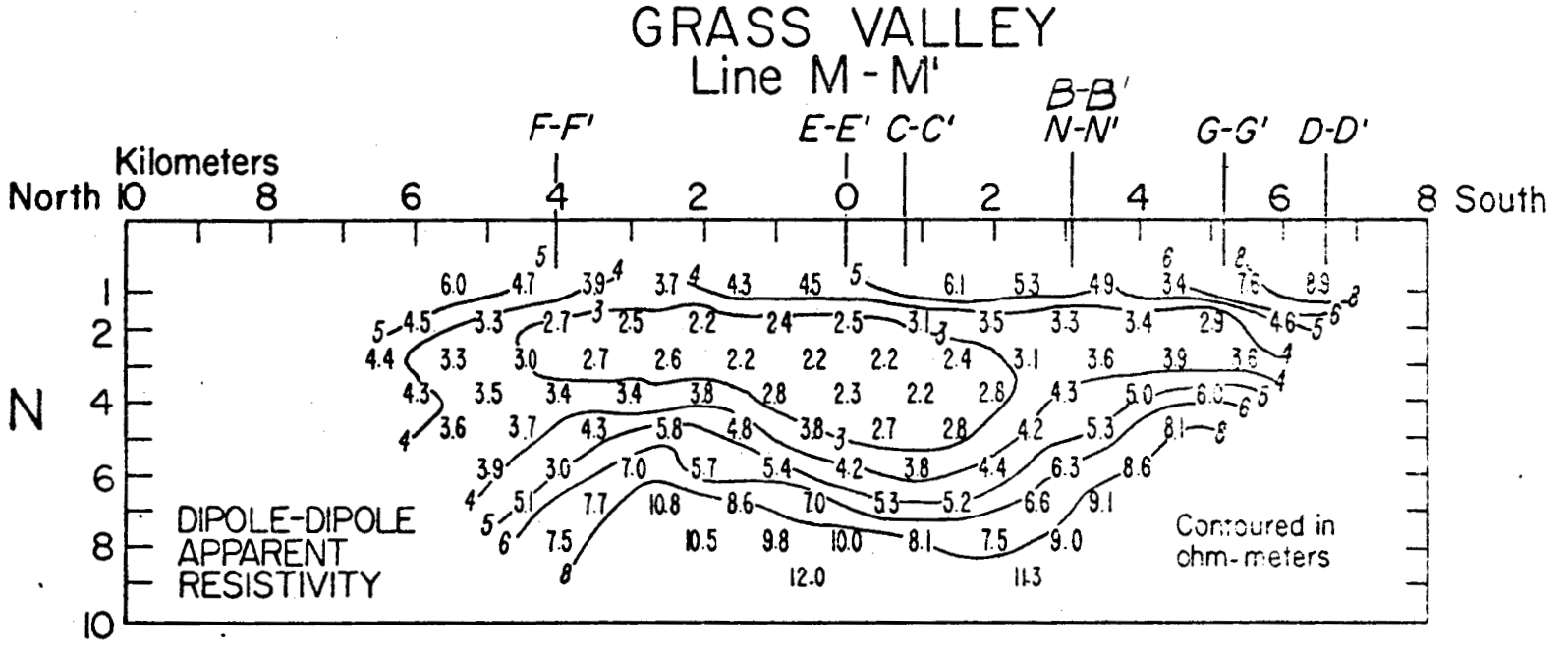

Figure 28: Dipole-dipole apparent resistivity pseudo-section on line M-M', 1 km dipoles.

GRASS VALLEY
Line D-D'

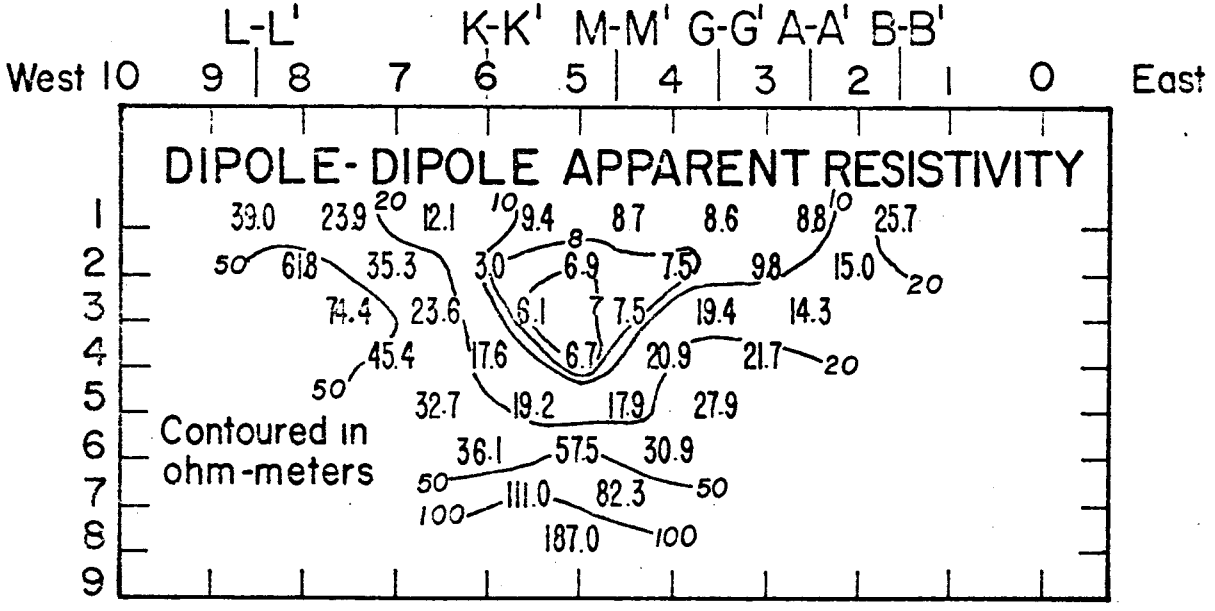

N

Kilometers

Figure 29a: Dipole-dipole apparent resistivity pseudo-section on line D-D', 1 km dipoles.

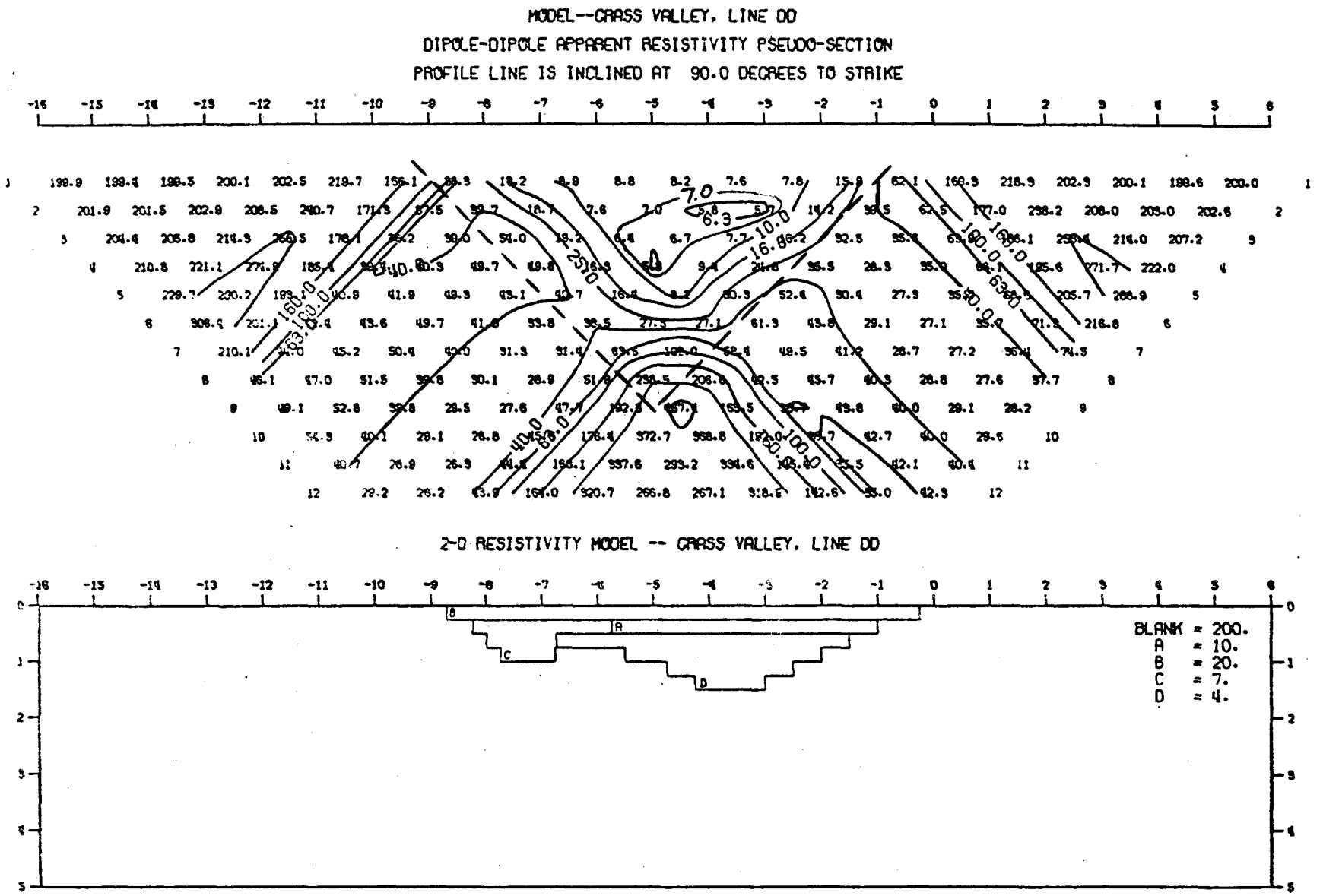

Figure 29b: Preliminary computer model interpretation of 1 km dipole-dipole pseudo-section on line D-D'. Values above dashed line represent data coverage in Figure 29a.

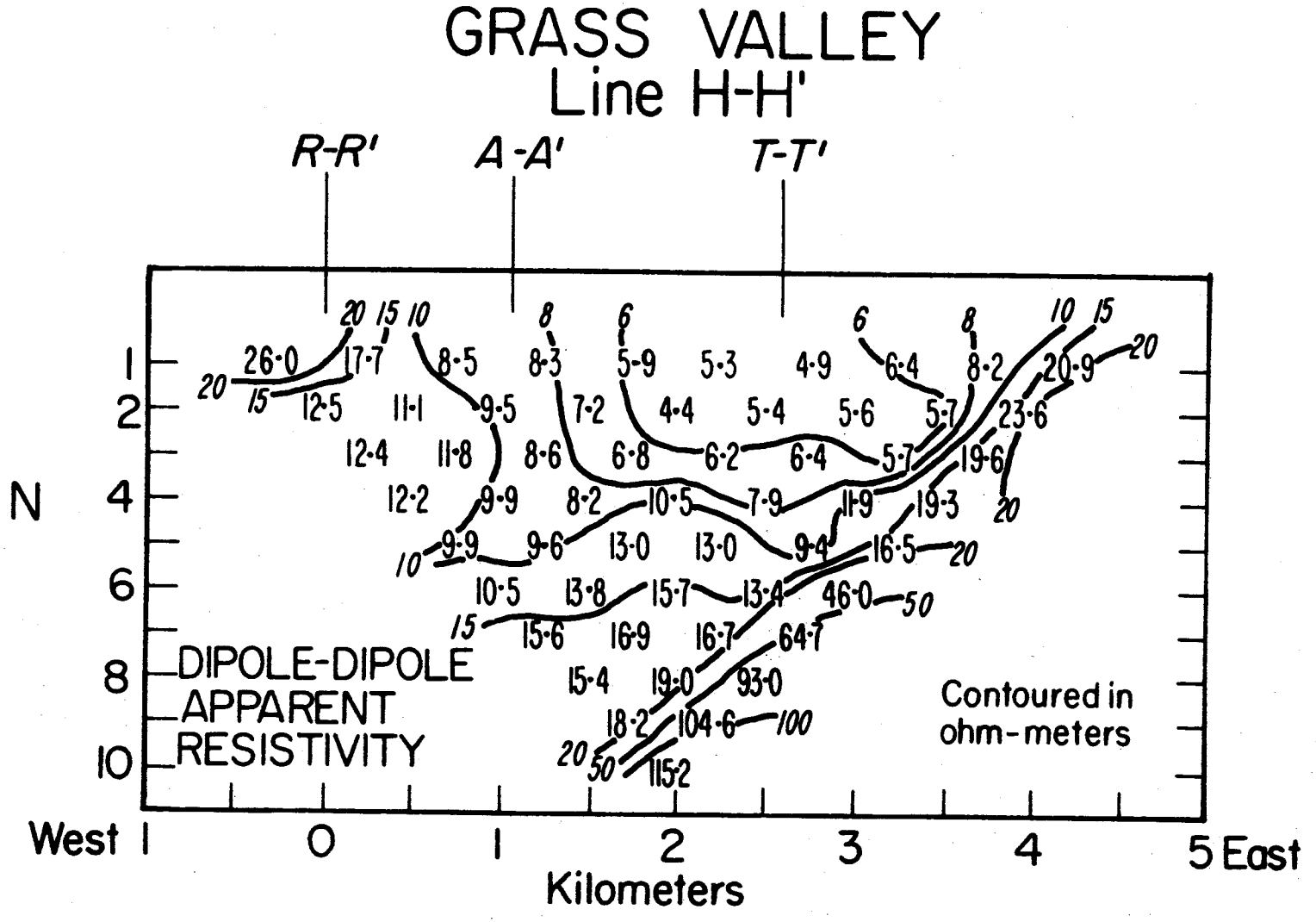

Figure 30a: Dipole-dipole apparent resistivity pseudo-section on line H-H', 500 m dipoles.

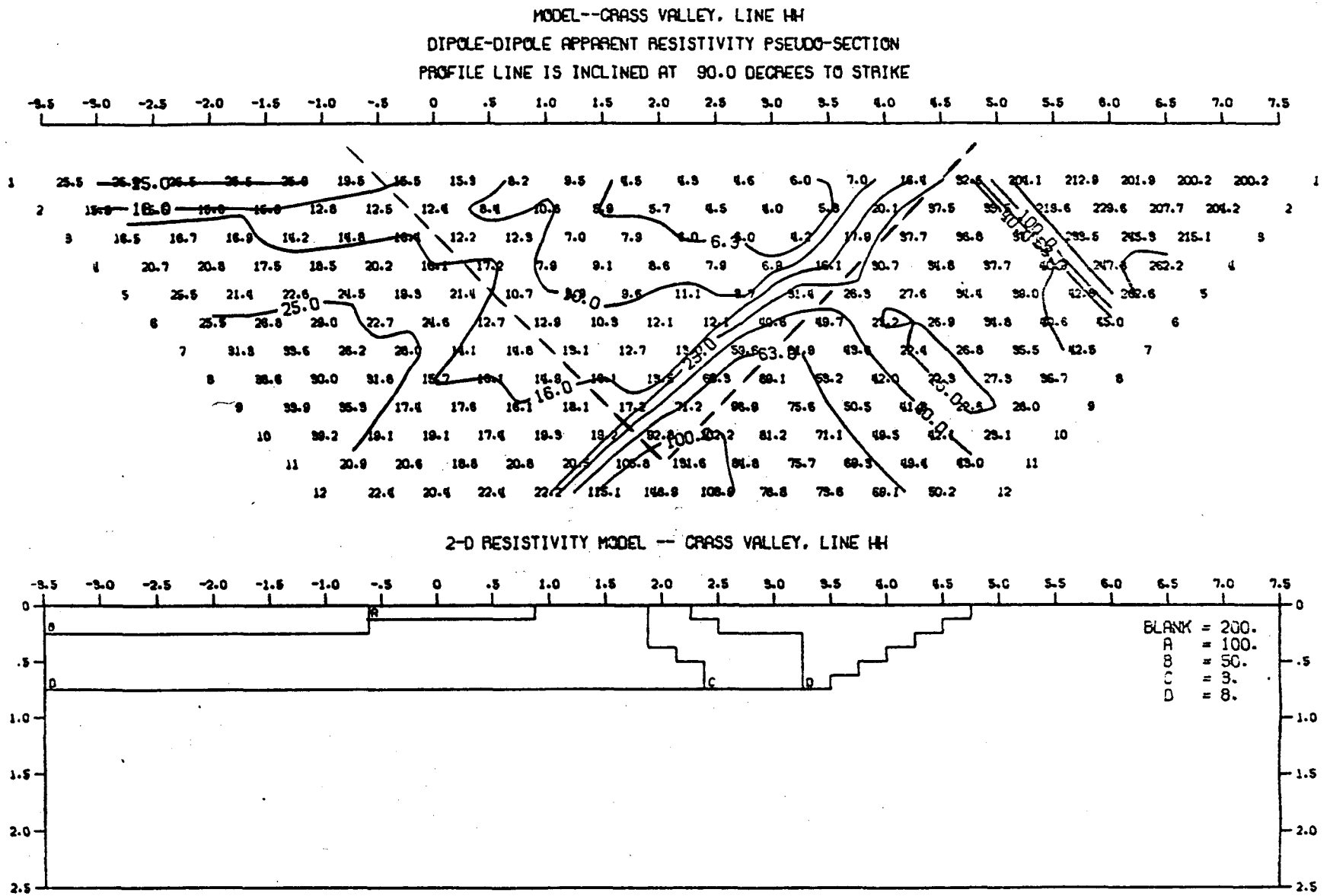

Figure 30b: Preliminary computer model interpretation of 500 m dipole-dipole pseudo-section on line H-H'. Values above dashed line represent data coverage in Figure 30a.

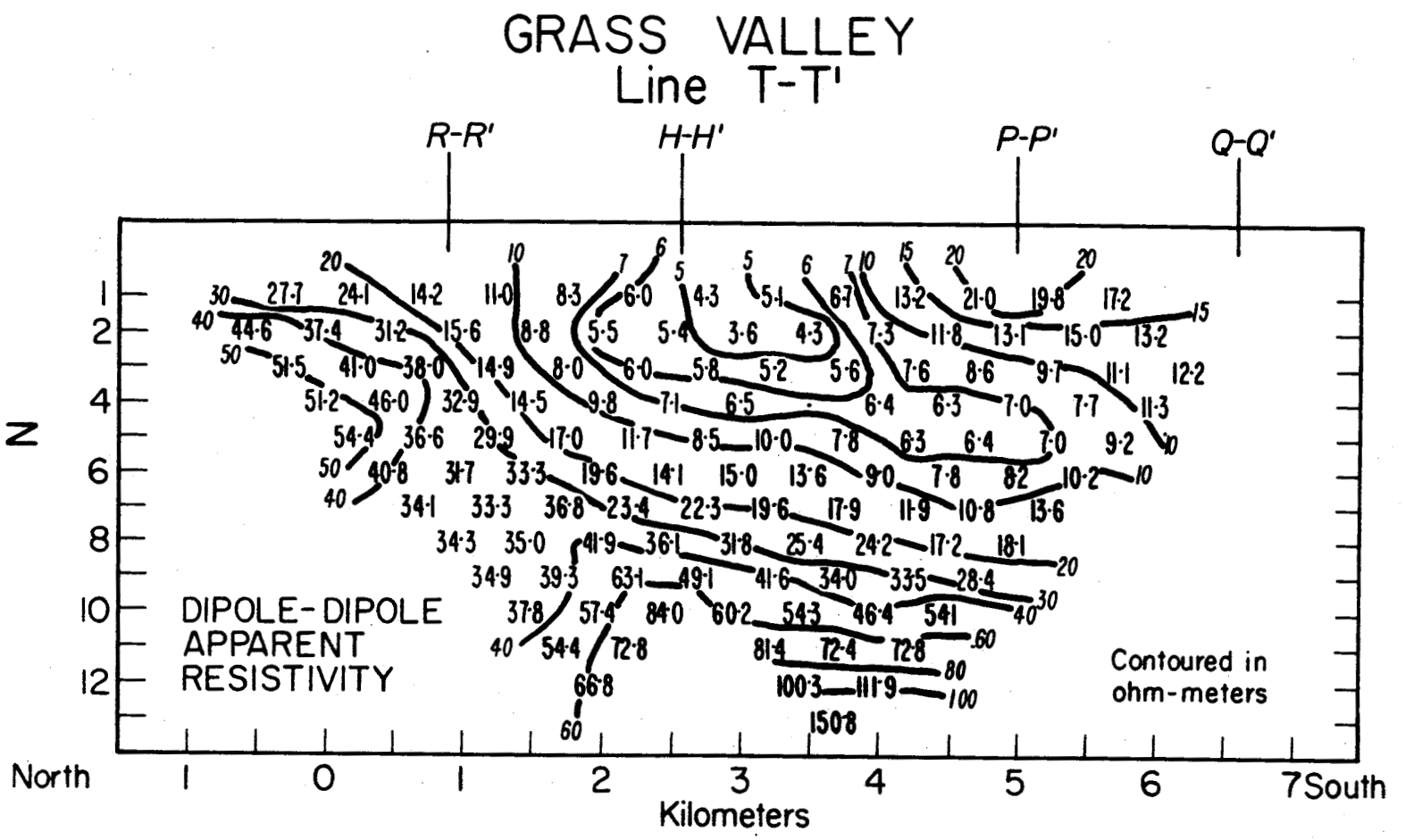

XBL 7512-9839

Figure 3la: Dipole-dipole apparent resistivity pseudo-section on line T-T', 500 m dipoles.

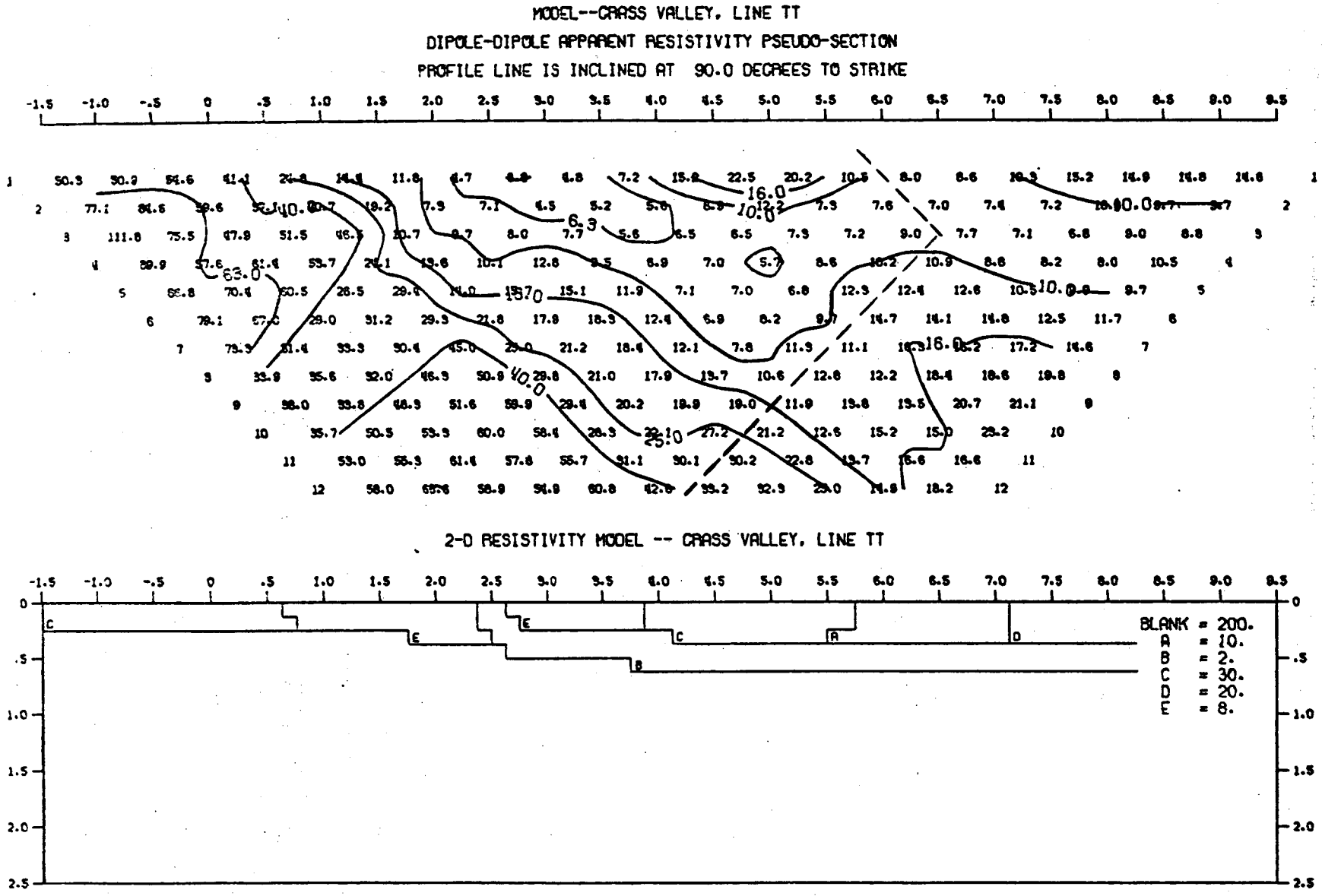

Figure 31b: Preliminary computer model interpretation of 500 m dipole-dipole pseudo-section on line T-T'. Values to the left of dashed line represent data coverage in Figure 31a.

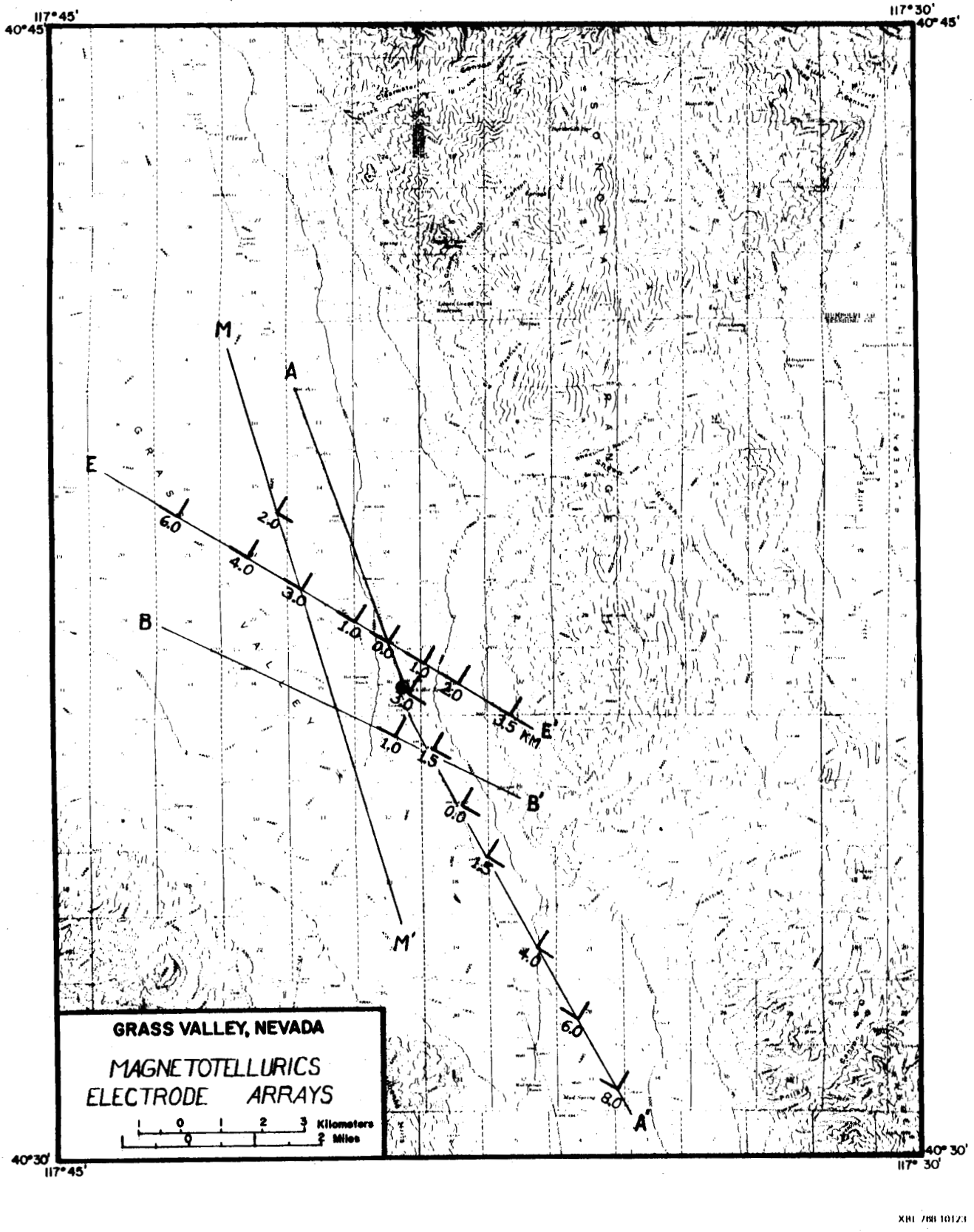

Figure 32: Location of magnetotelluric stations in Grass Valley, Nevada.

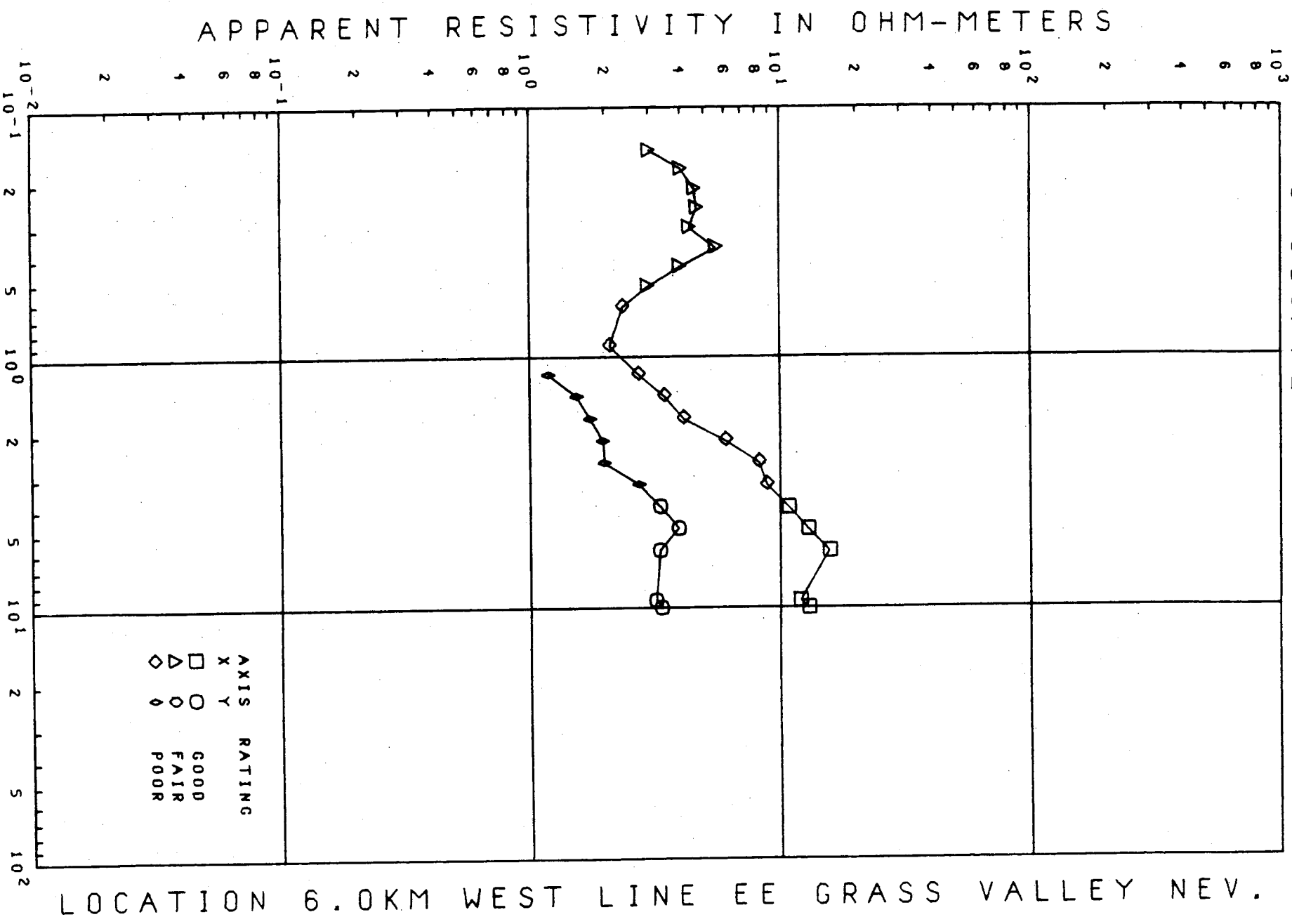

Figure 33: Principal apparent resistivity values. Station 6.0 km West Line E-E'

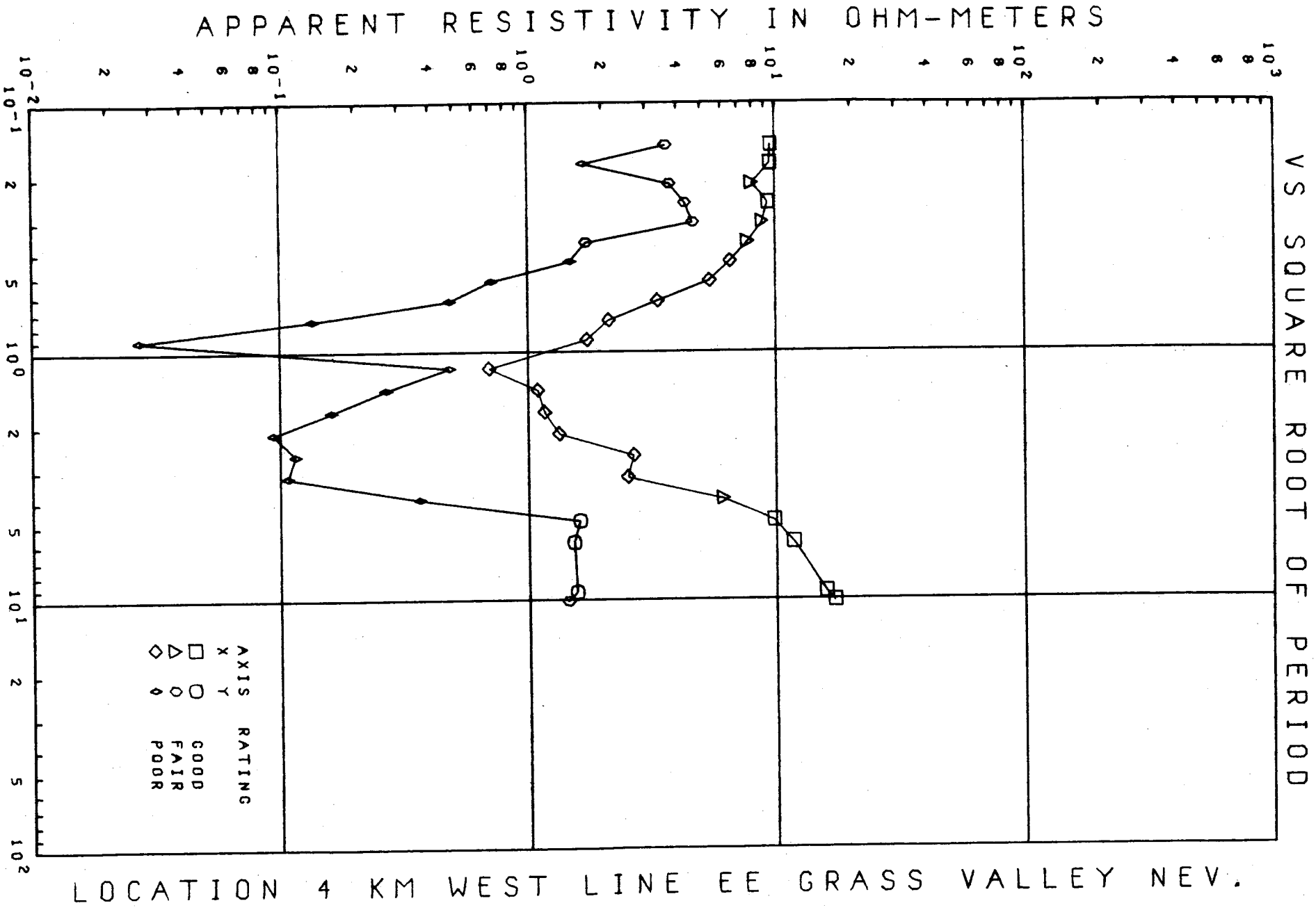

Figure 34: Principal apparent resistivity values. Station 4.0 km West Line E-E'

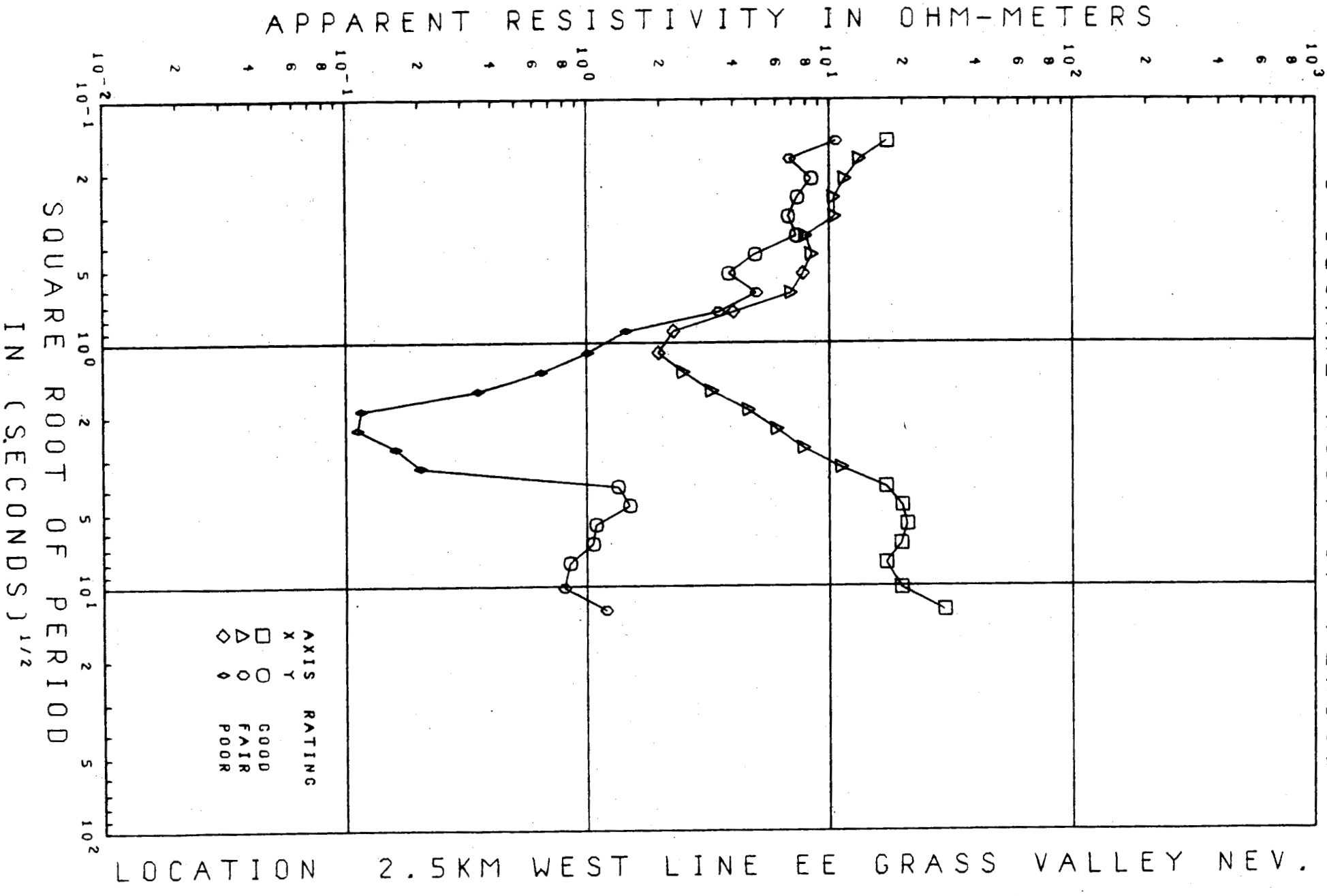

Figure 35: Principal apparent resistivity values. Station 2.5 km West Line E-E'

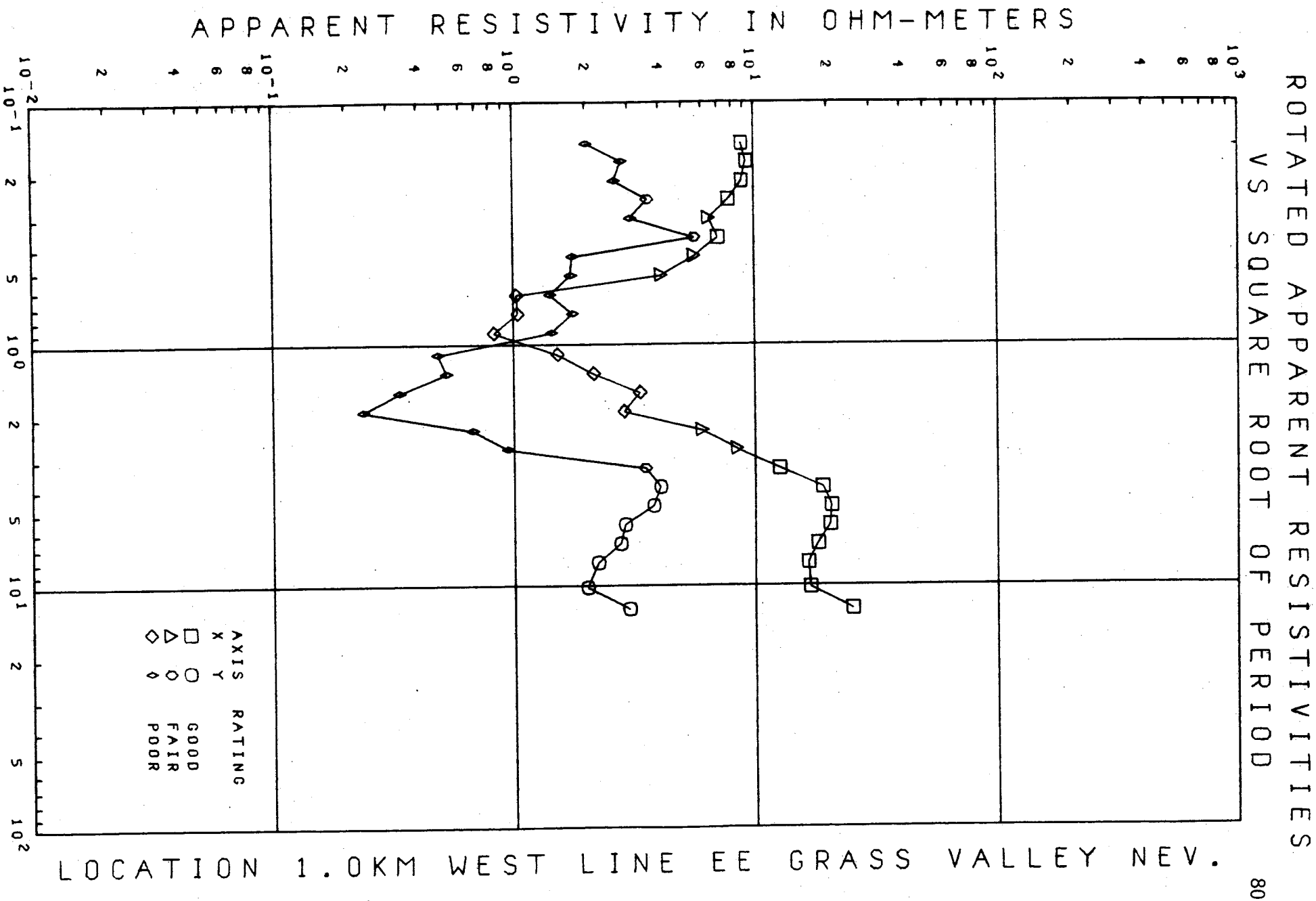

Figure 36: Principal apparent resistivity values. Station 1.0 km West Line E-E'

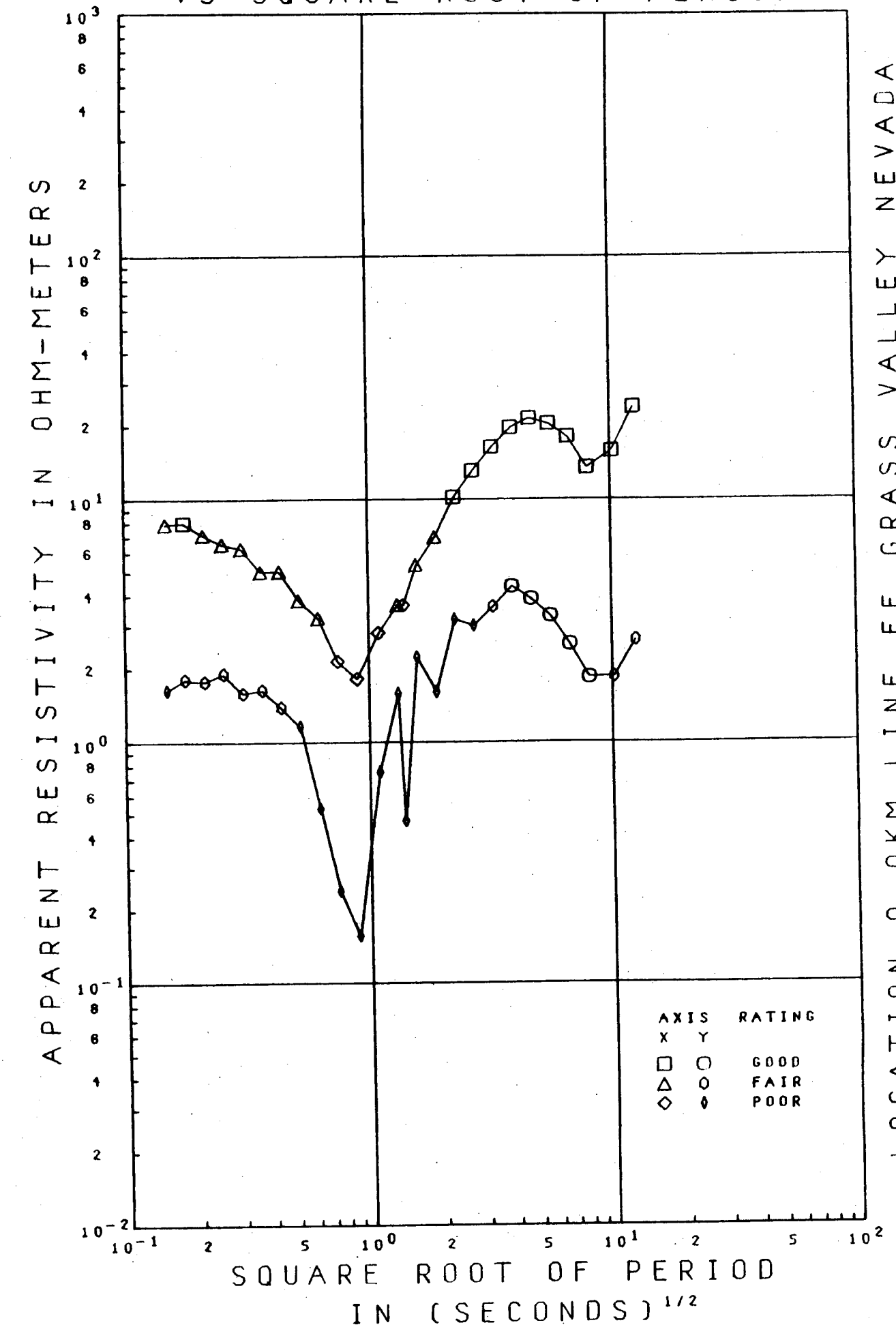

Figure 37: Principal apparent resistivity values. Station 0.0 km West Line E-E'

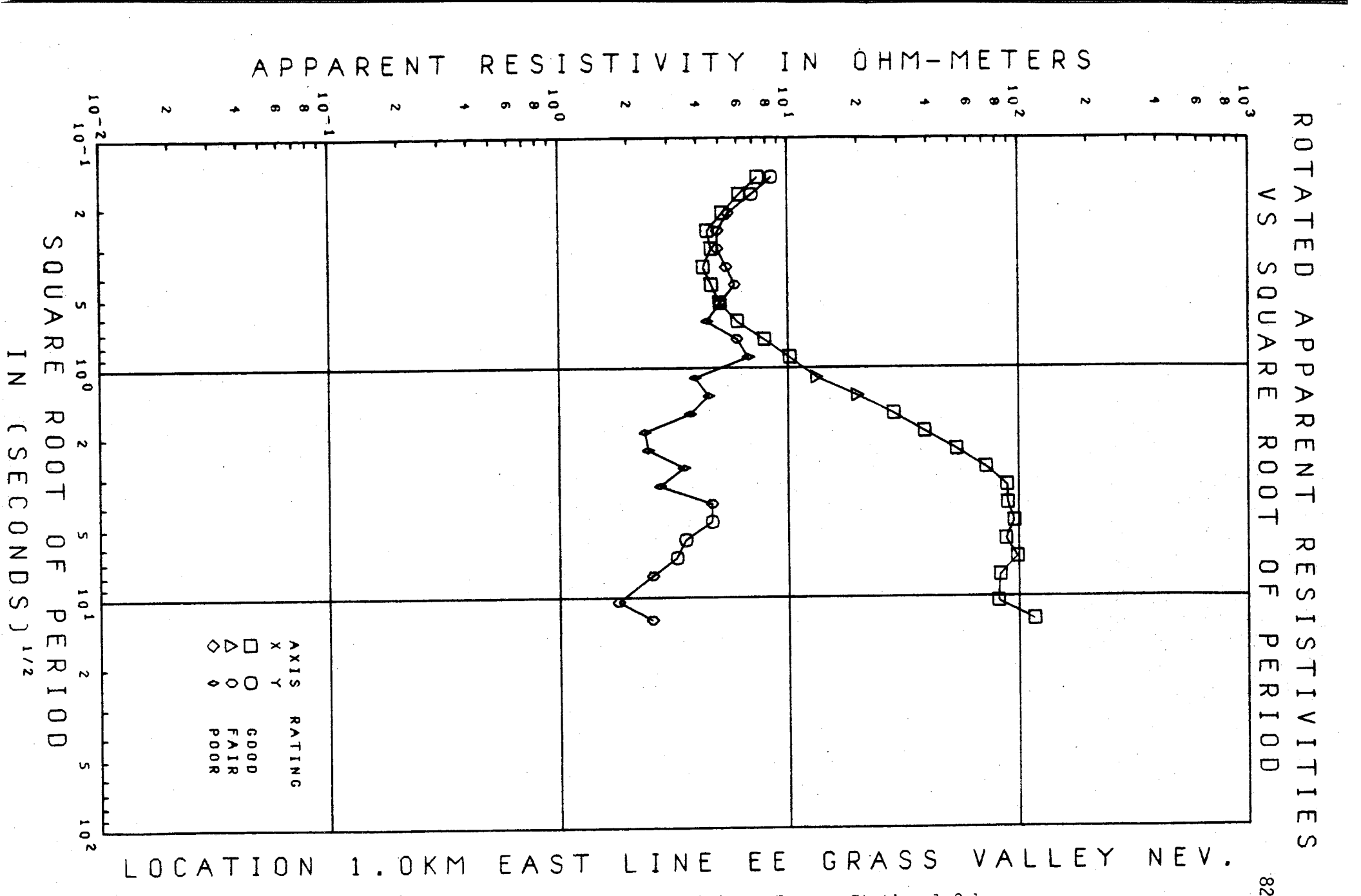

Figure 38: Principal apparent resistivity values. Station 1.0 km East Line E-E'

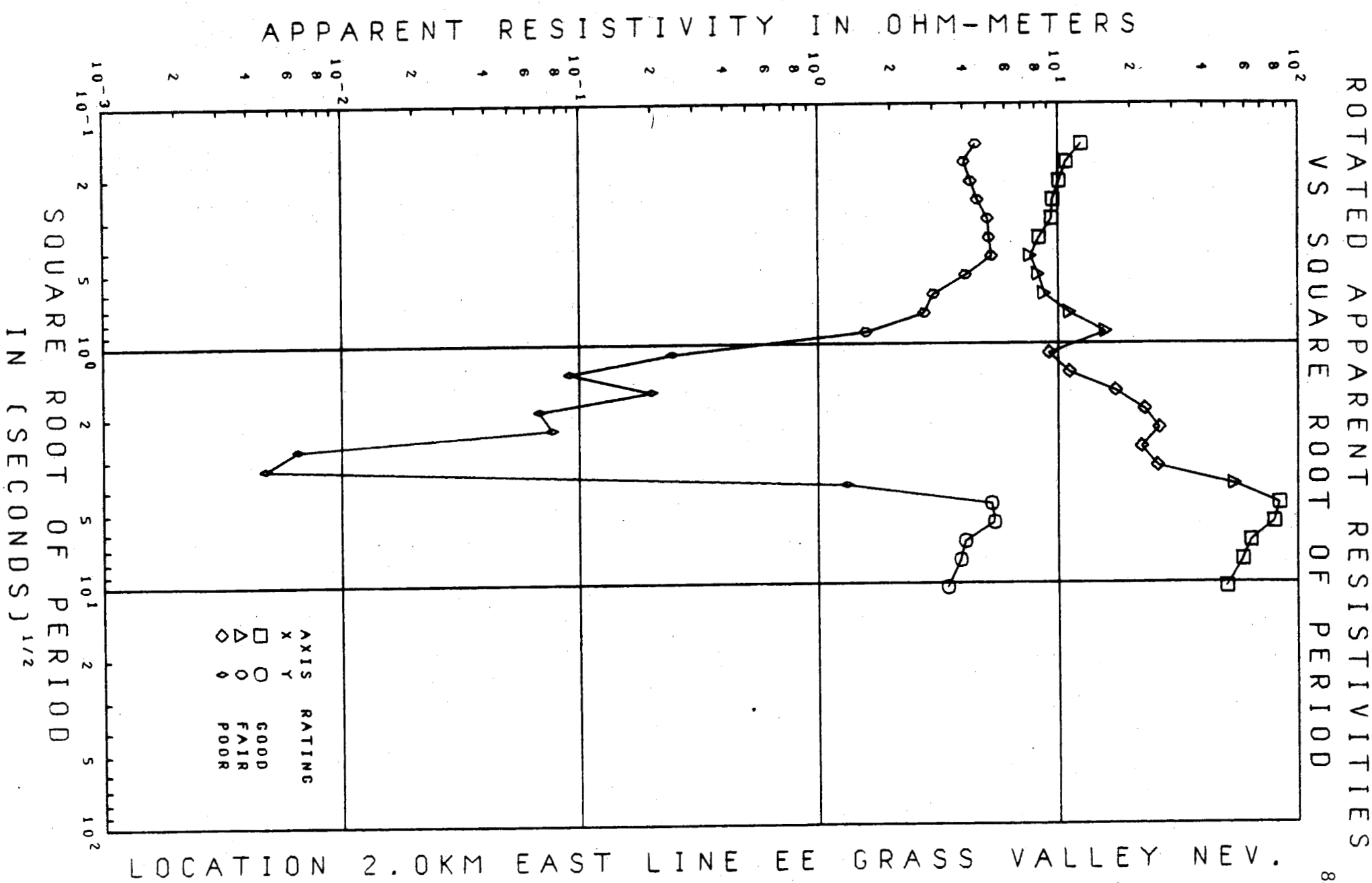

Figure 39: Principal apparent resistivity values. Station 2.0 km East Line E-E'

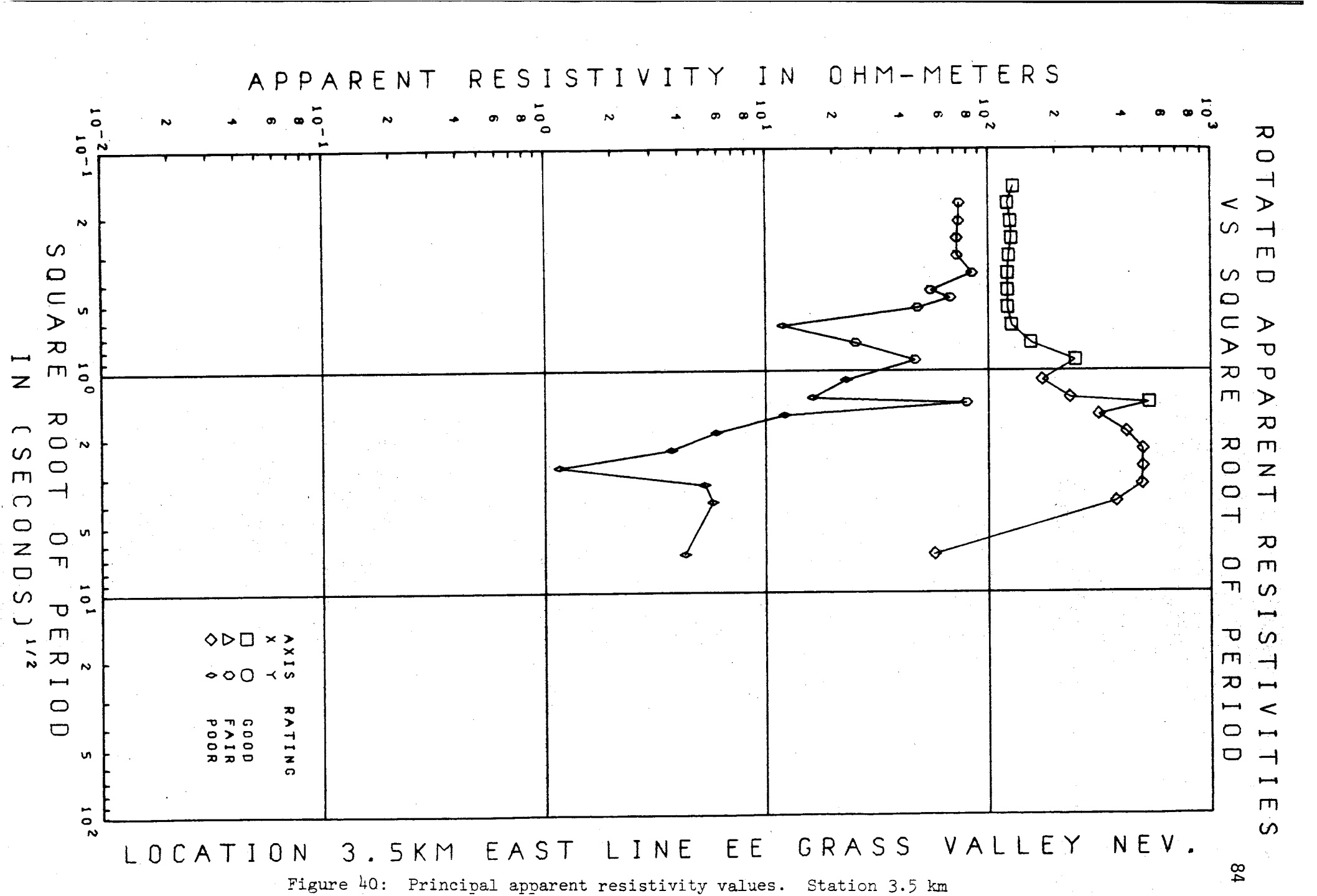

Figure 40: Principal apparent resistivity values. Station 3.5 km East Line E-E'

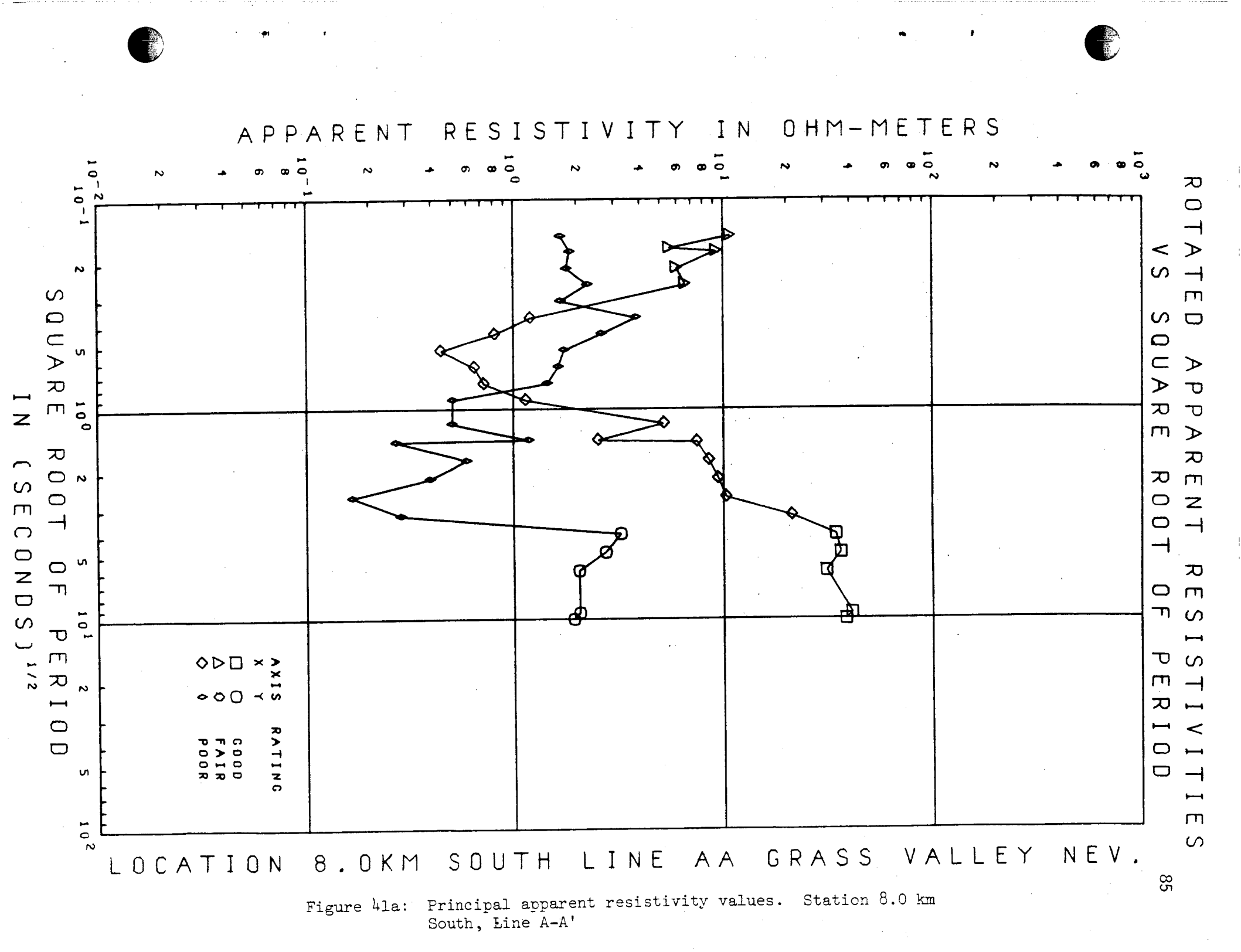

Figure 41a: Principal apparent resistivity values. Station 8.0 km South, Line A-A'

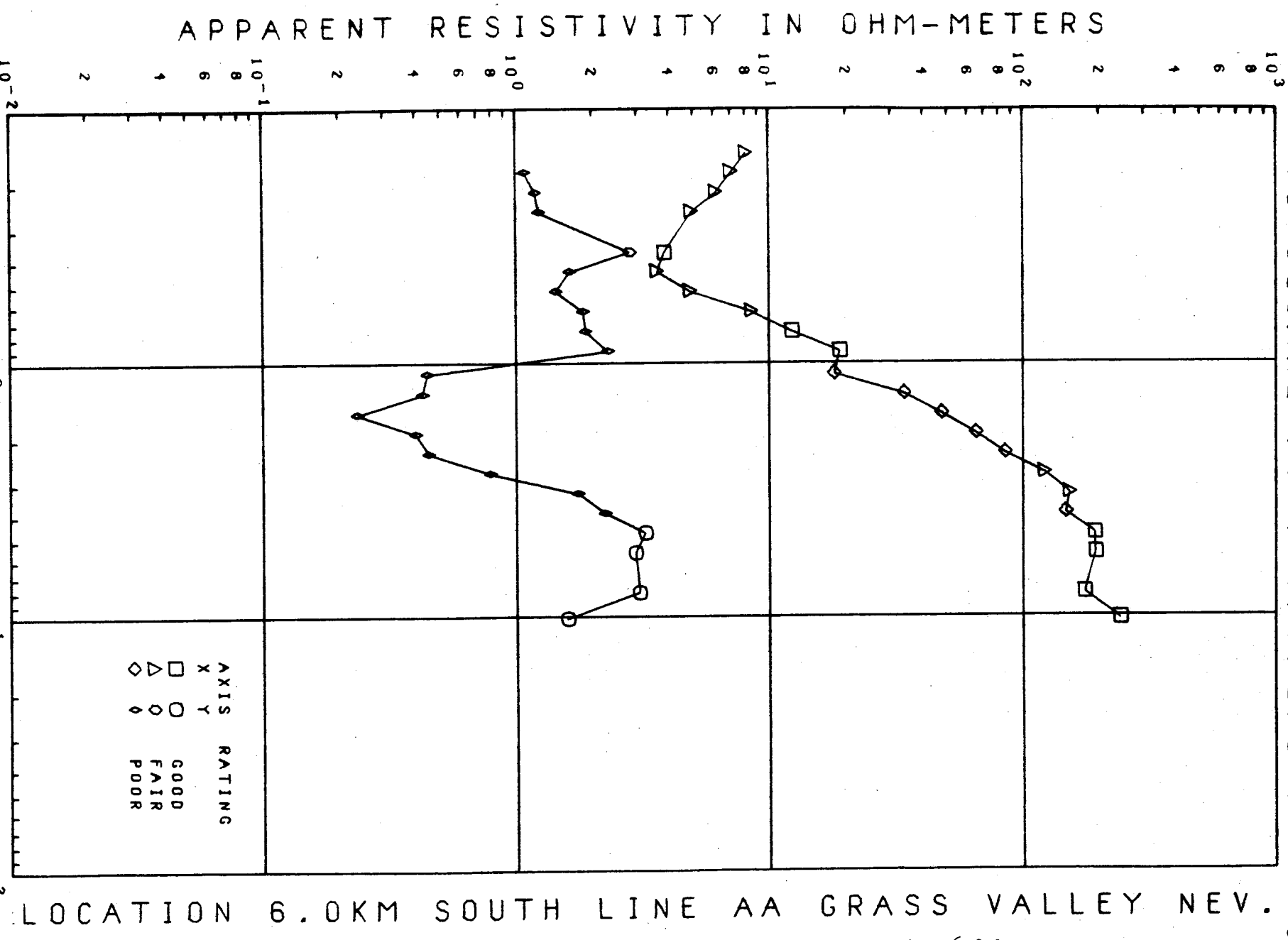

Figure 41b: Principal apparent resistivity values. Station 6.0 km South Line A-A'

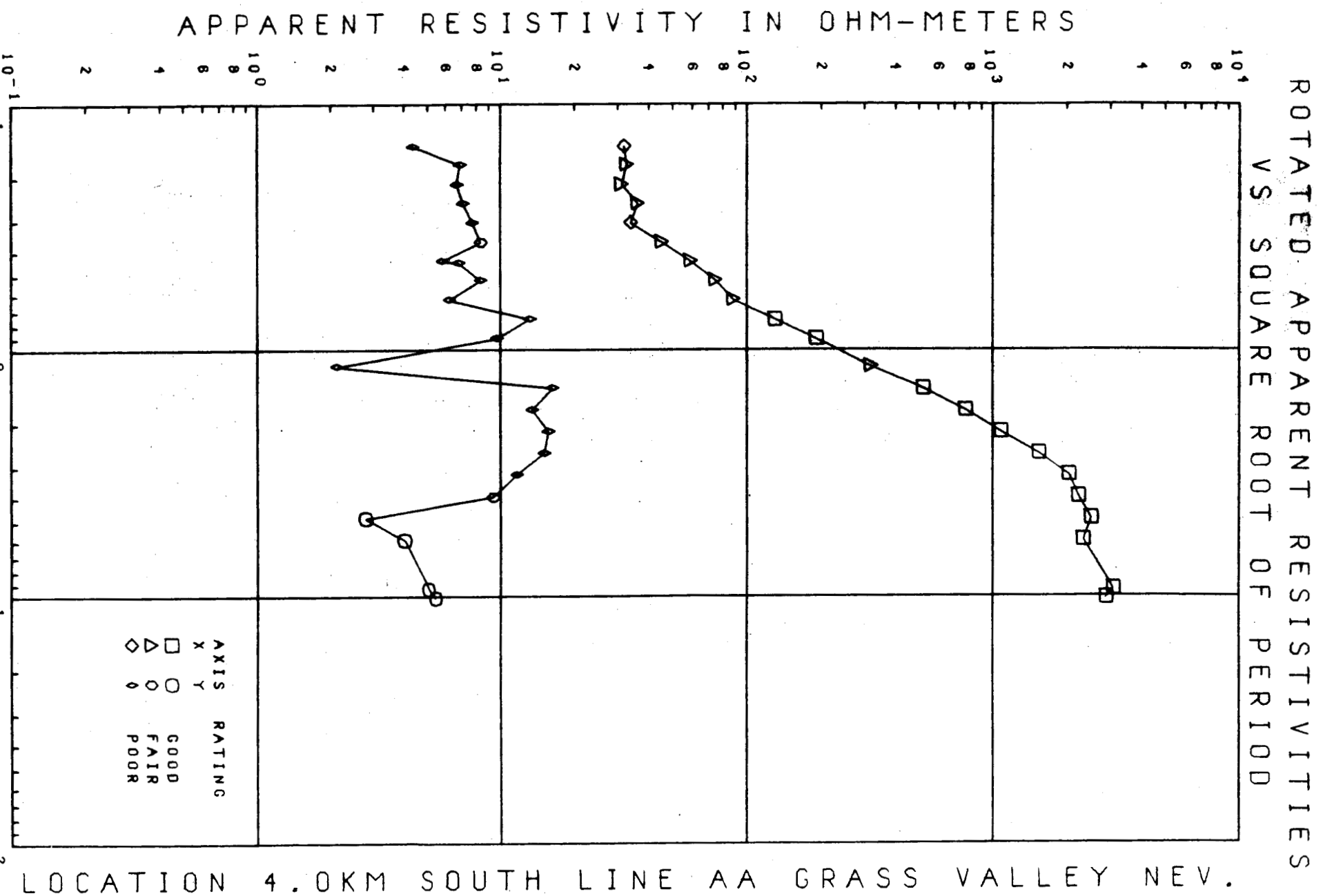

Figure 42: Principal apparent resistivity values. Station 4.0 km South Line A-A'

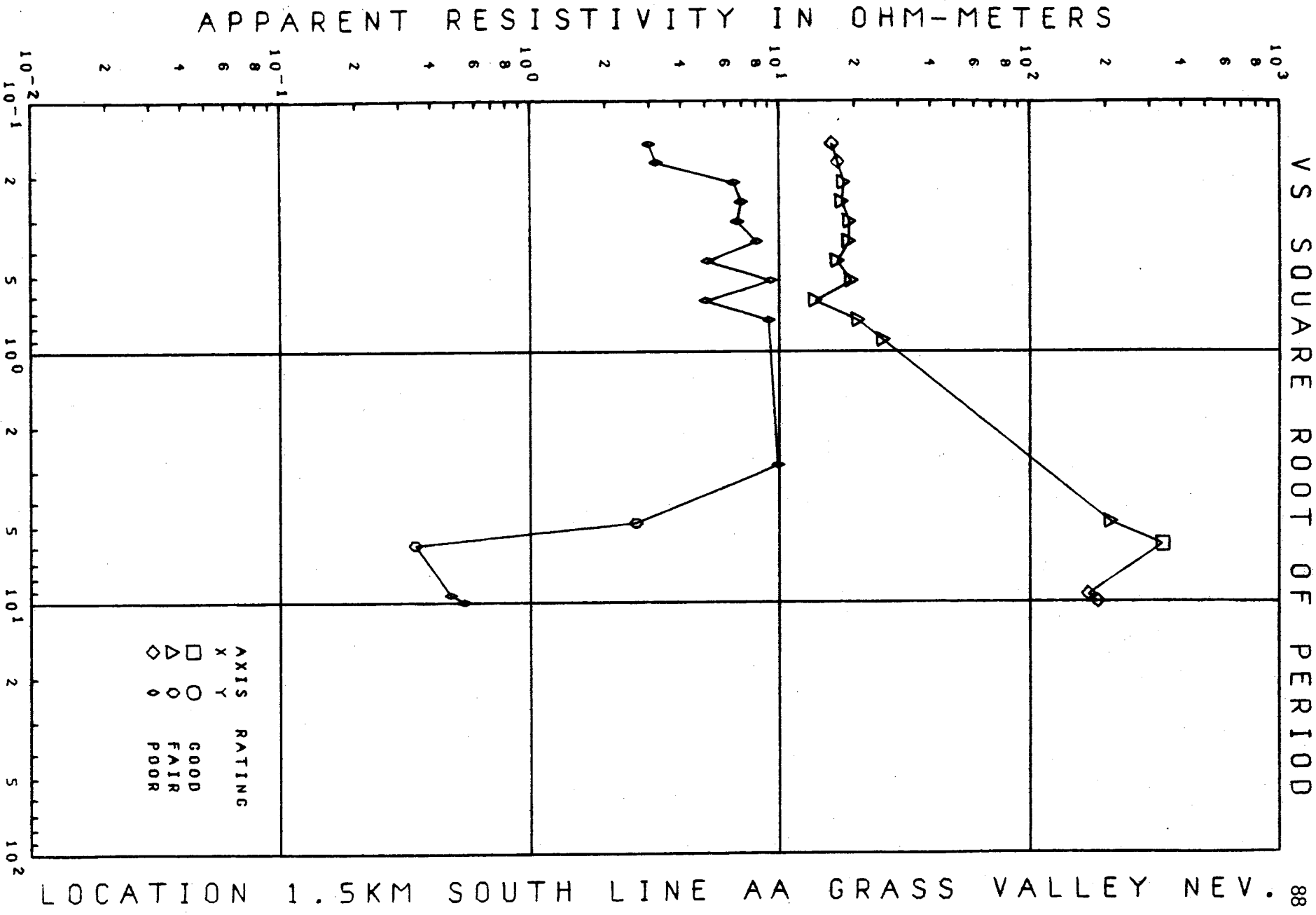

Figure 43: Principal apparent resistivity values. Station 1.5 km South Line A-A'

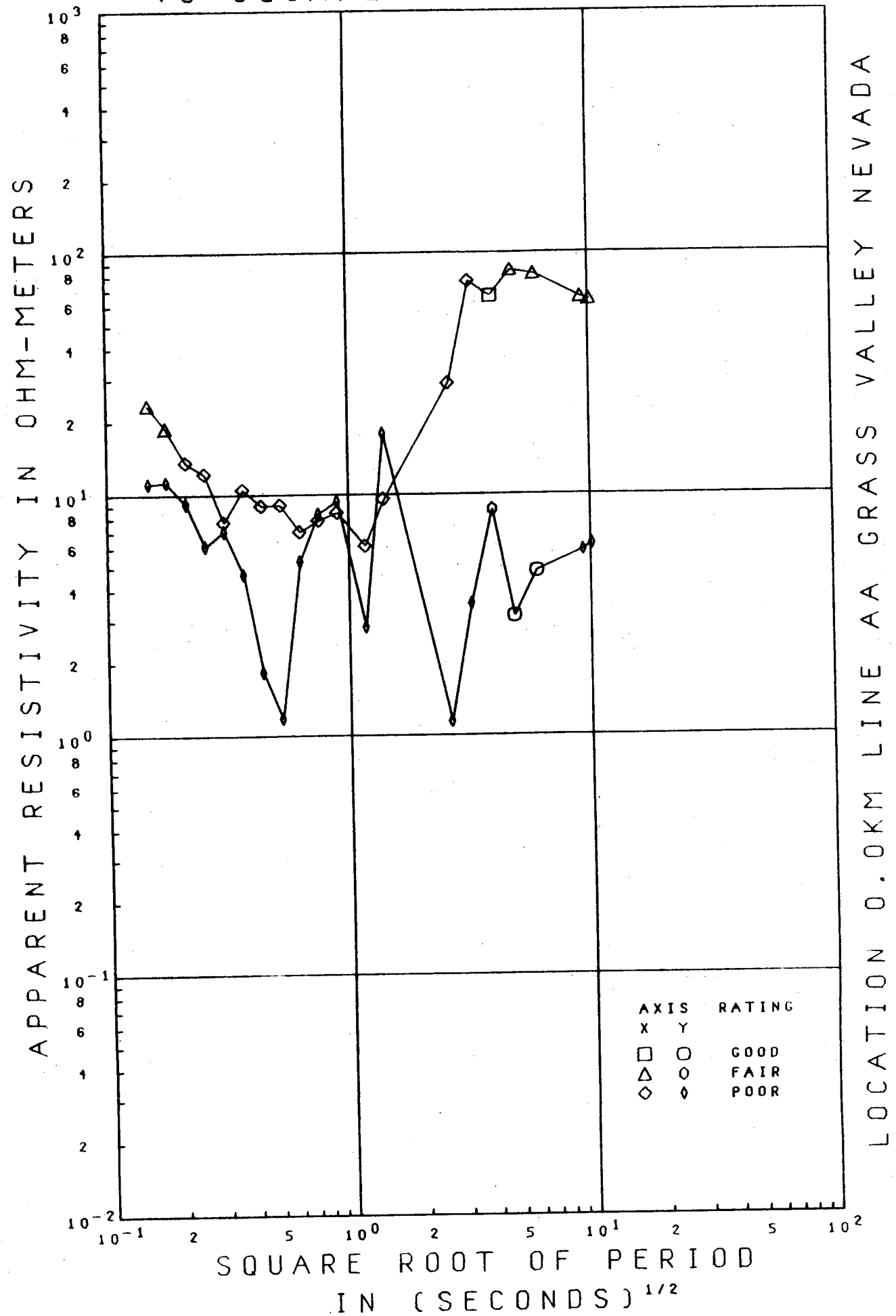

Figure 44: Principal apparent resistivity values. Station 0.0 km South Line A-A'

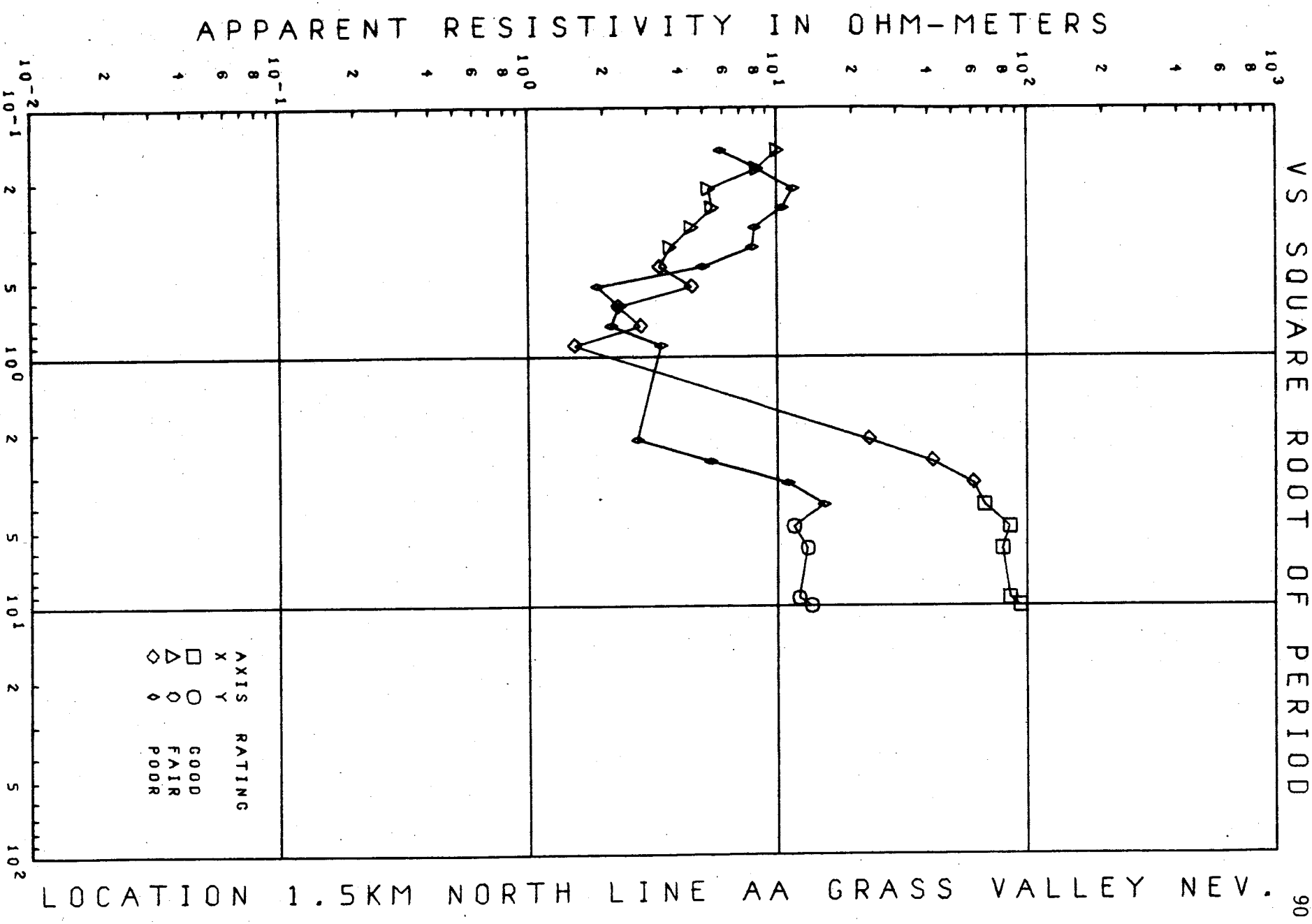

Figure 45: Principal apparent resistivity values. Station 1.5 km North Line A-A'

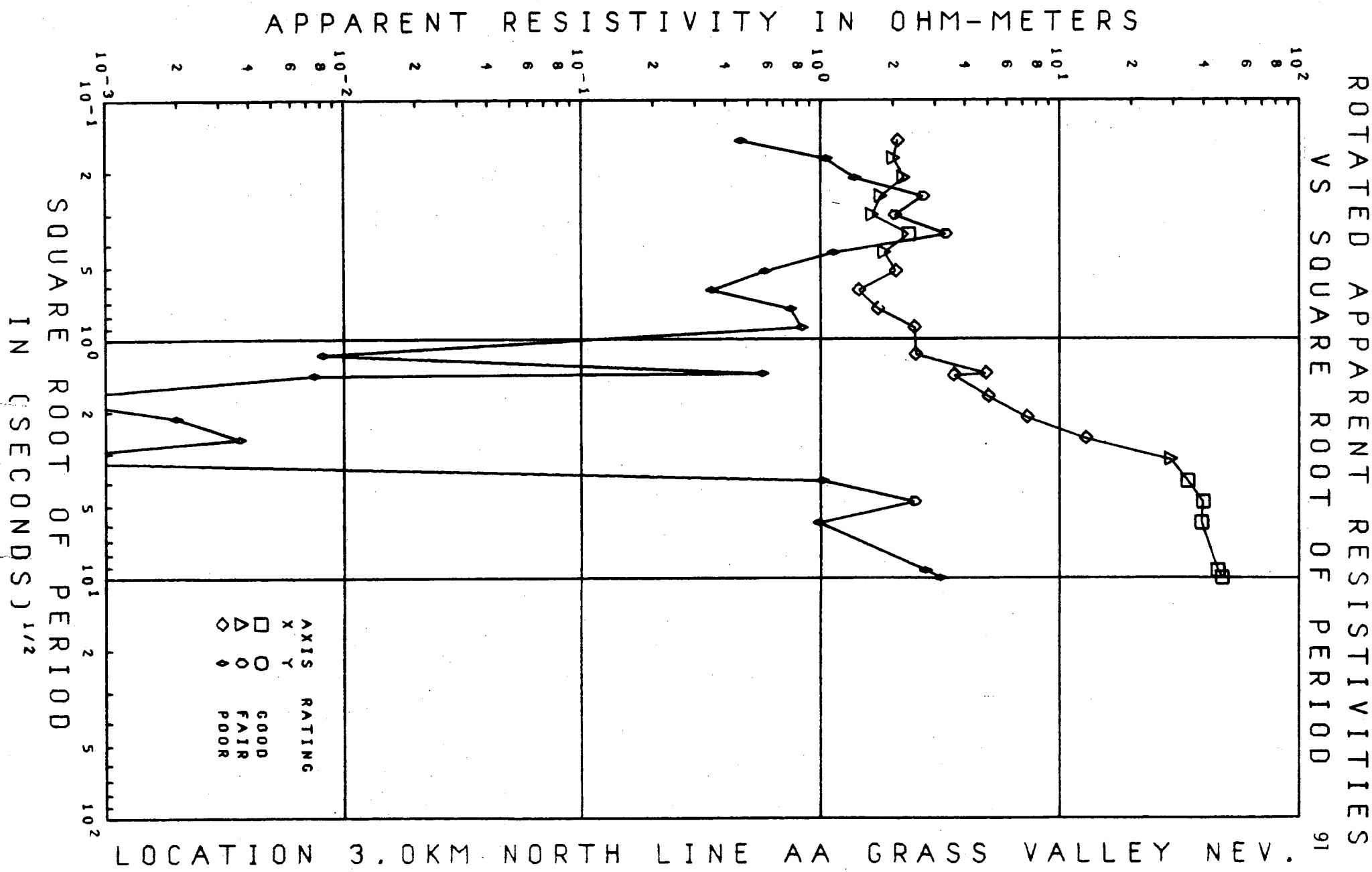

Figure 46: Principal apparent resistivity values. Station 3.0 km North Line A-A'

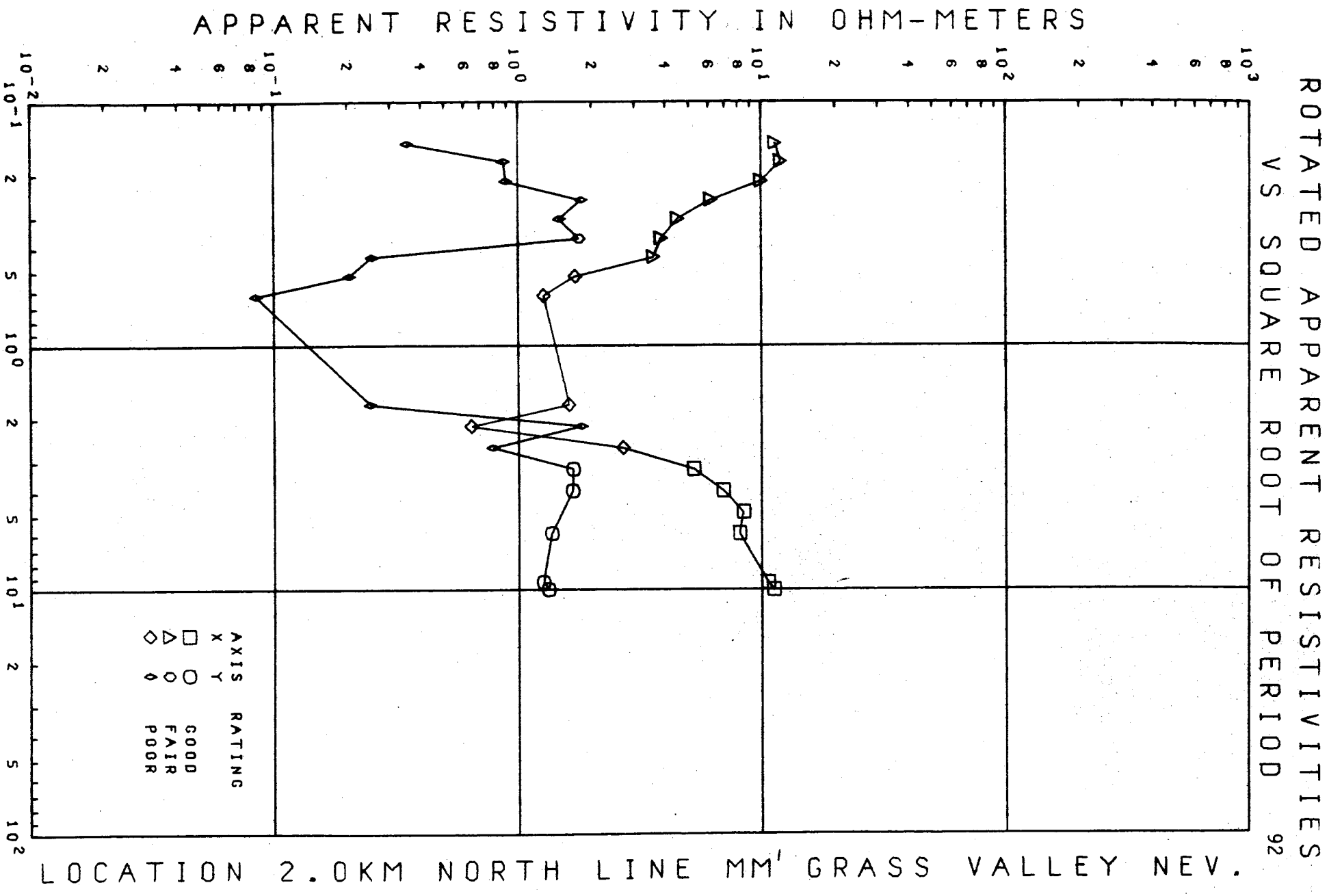

Figure 47: Principal apparent resistivity values. Station 2.0 km North Line M-M'

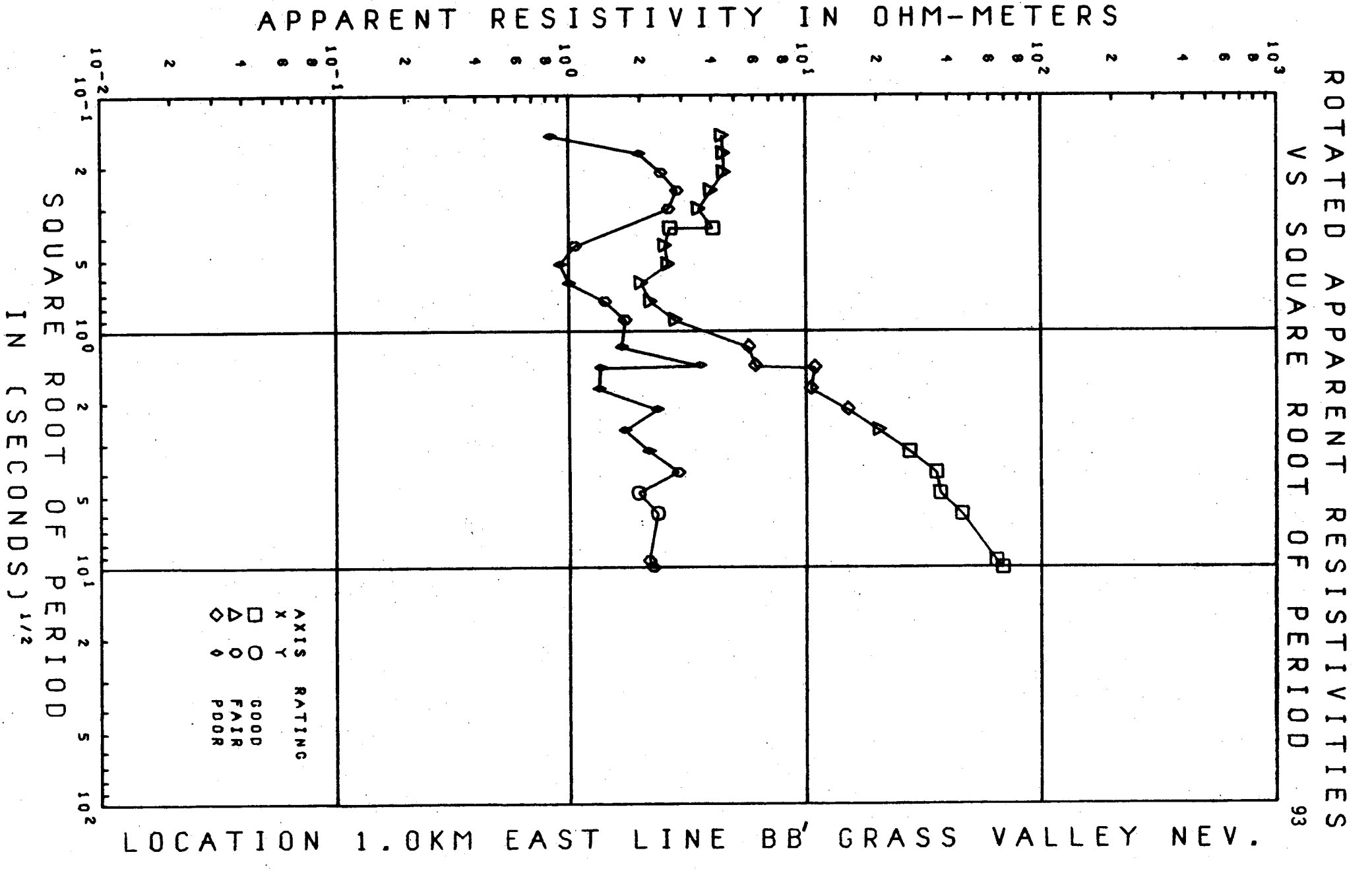

Figure 48: Principal apparent resistivity values. Station 1.0 km East Line B-B'

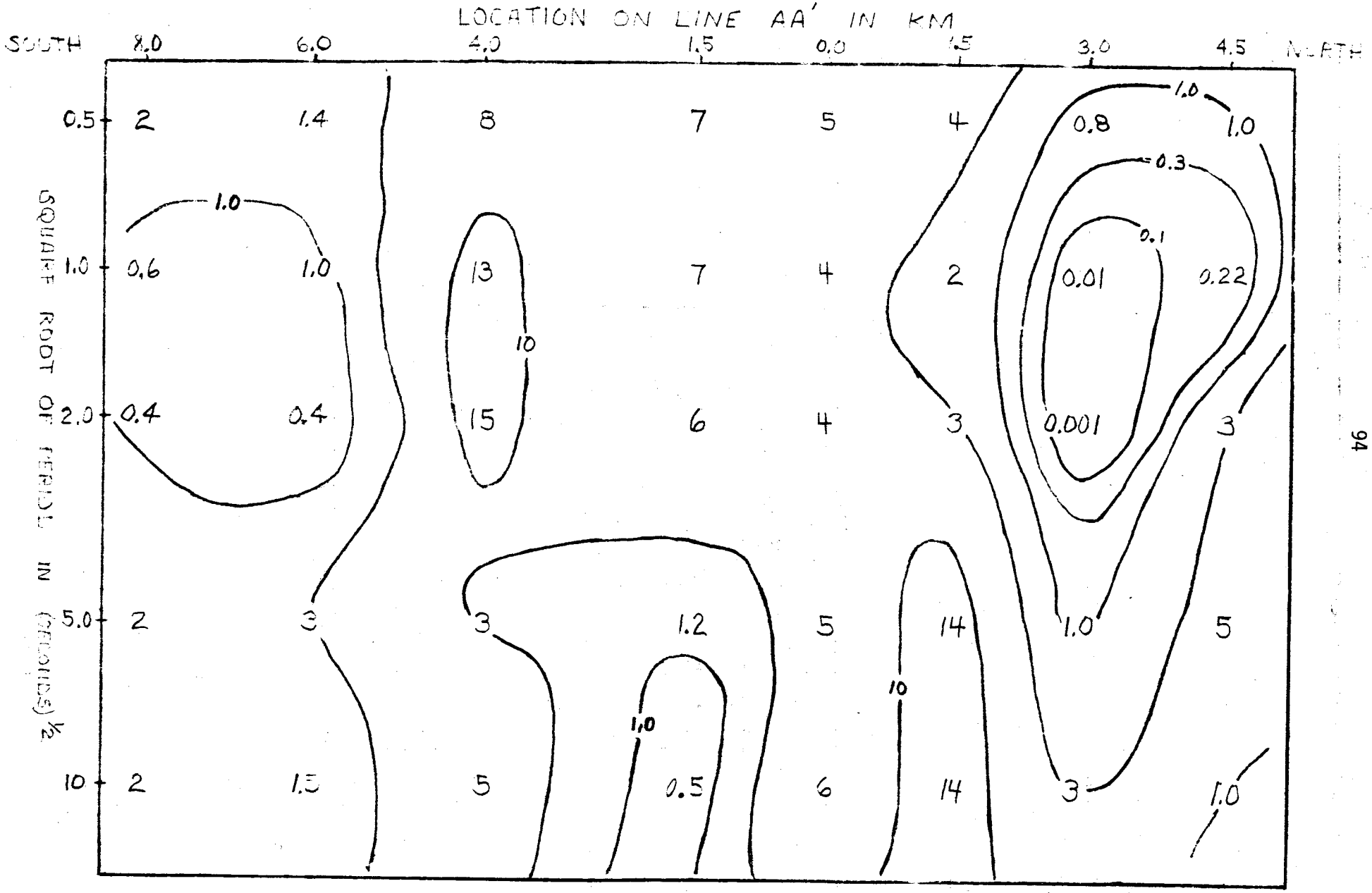

Figure 49: Pseudo-section of Y axis principal apparent resistivities on line A-A'

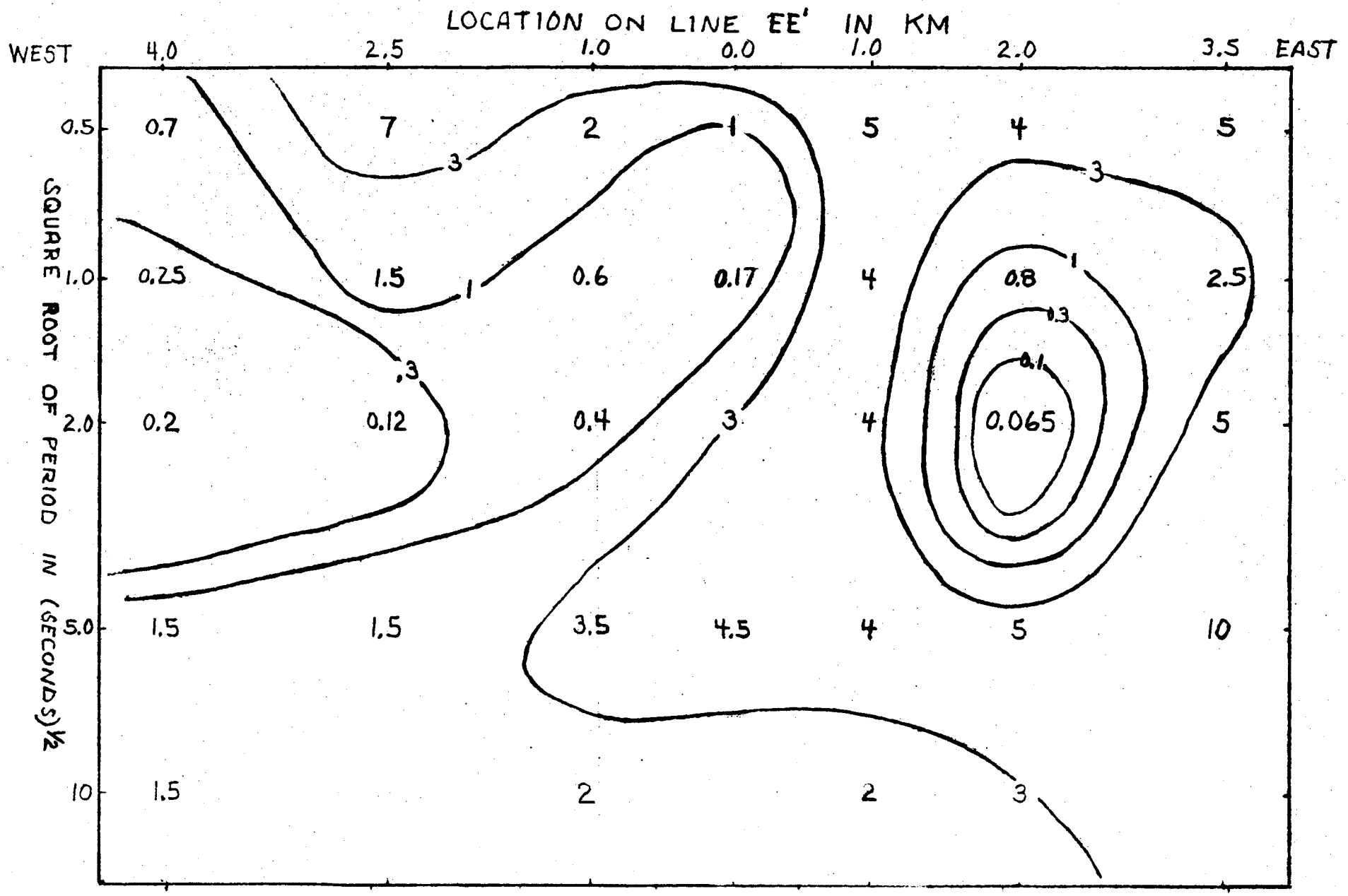

Figure 50: Pseudo section of Y axis principal apparent resistivities on line E-E'

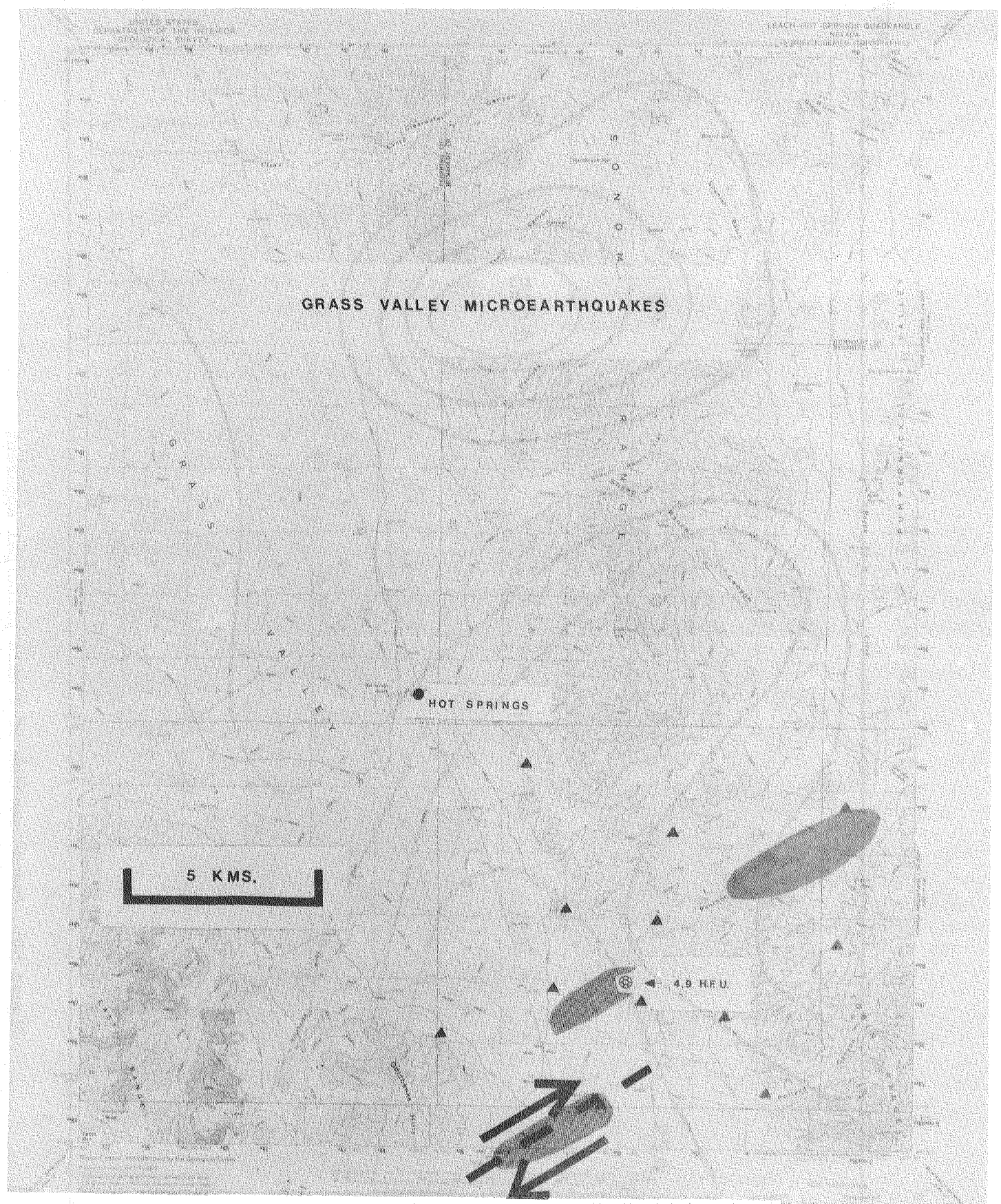

Figure 51: Grass Valley microearthquake survey results. Stations (triangles) shown in phase three configuration. Shaded areas are zones of earthquake swarm activity. Preferred faulting mechanism is indicated for SW swarm - others are complex faulting. Heat flow measurement is shown.

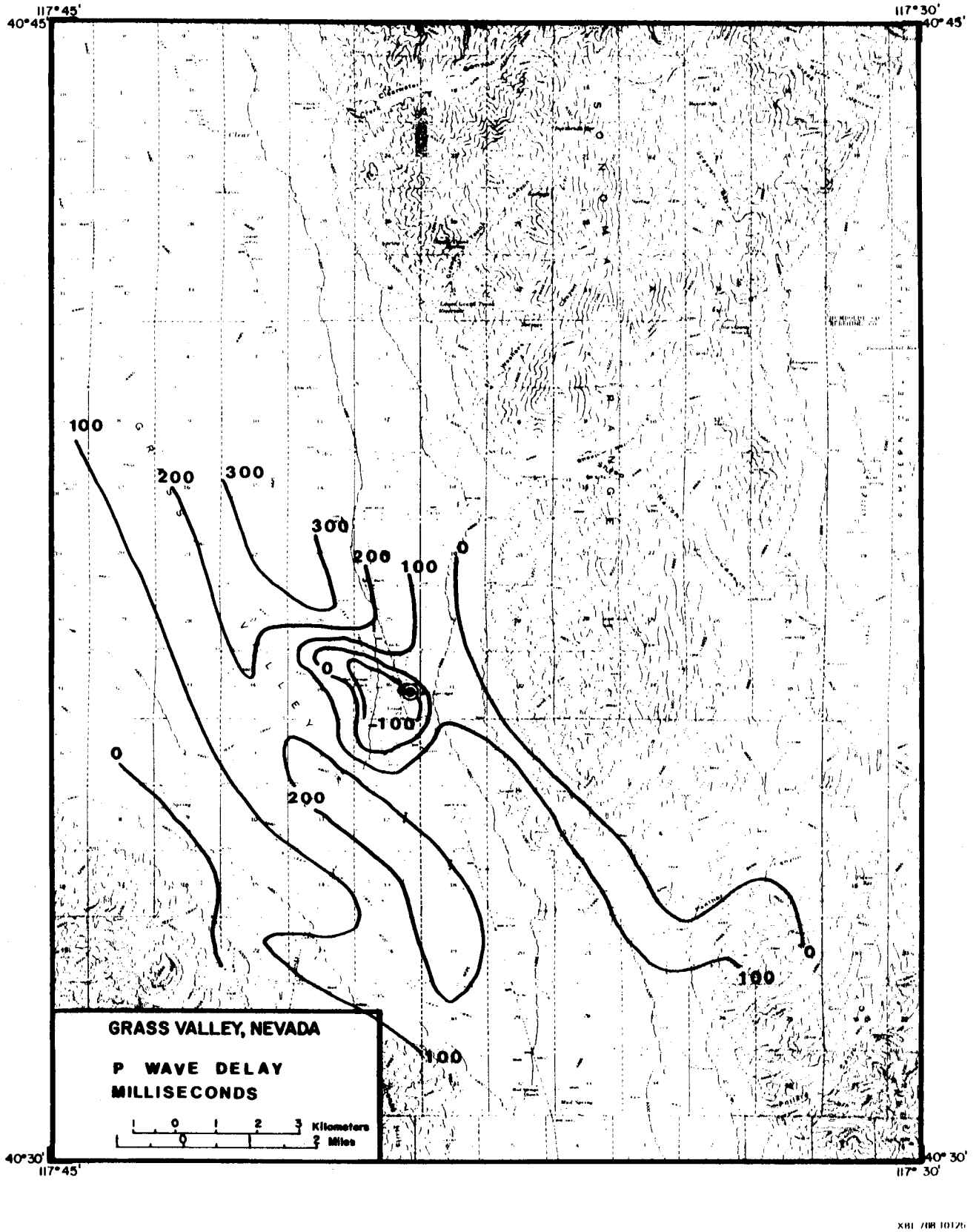

Figure 52: Normalized P-wave delay, in milliseconds, for southern Grass Valley. Symbol shows location of Leach Hot Springs, an area of strong negative delays.

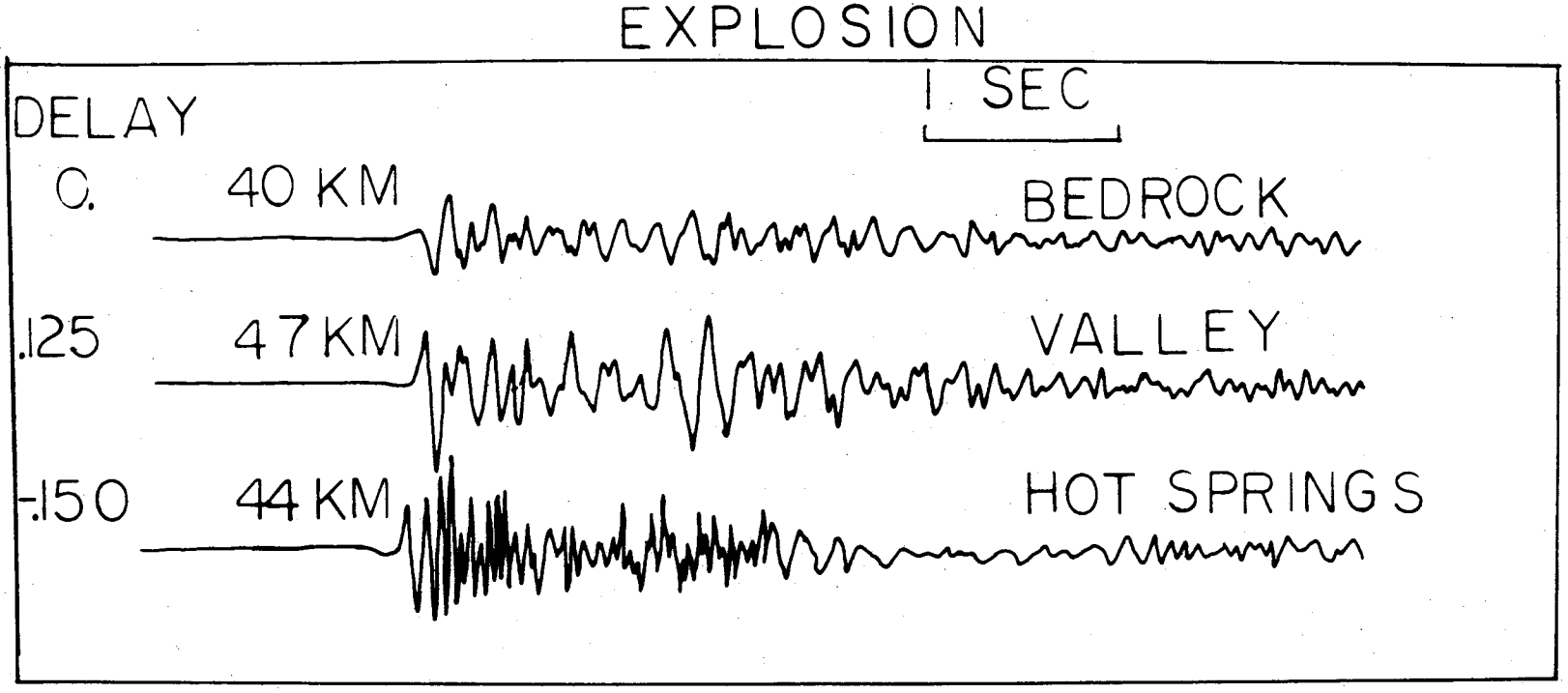

Figure 53: Comparison of seismograms from the same distant mine explosion, recorded at three sites.

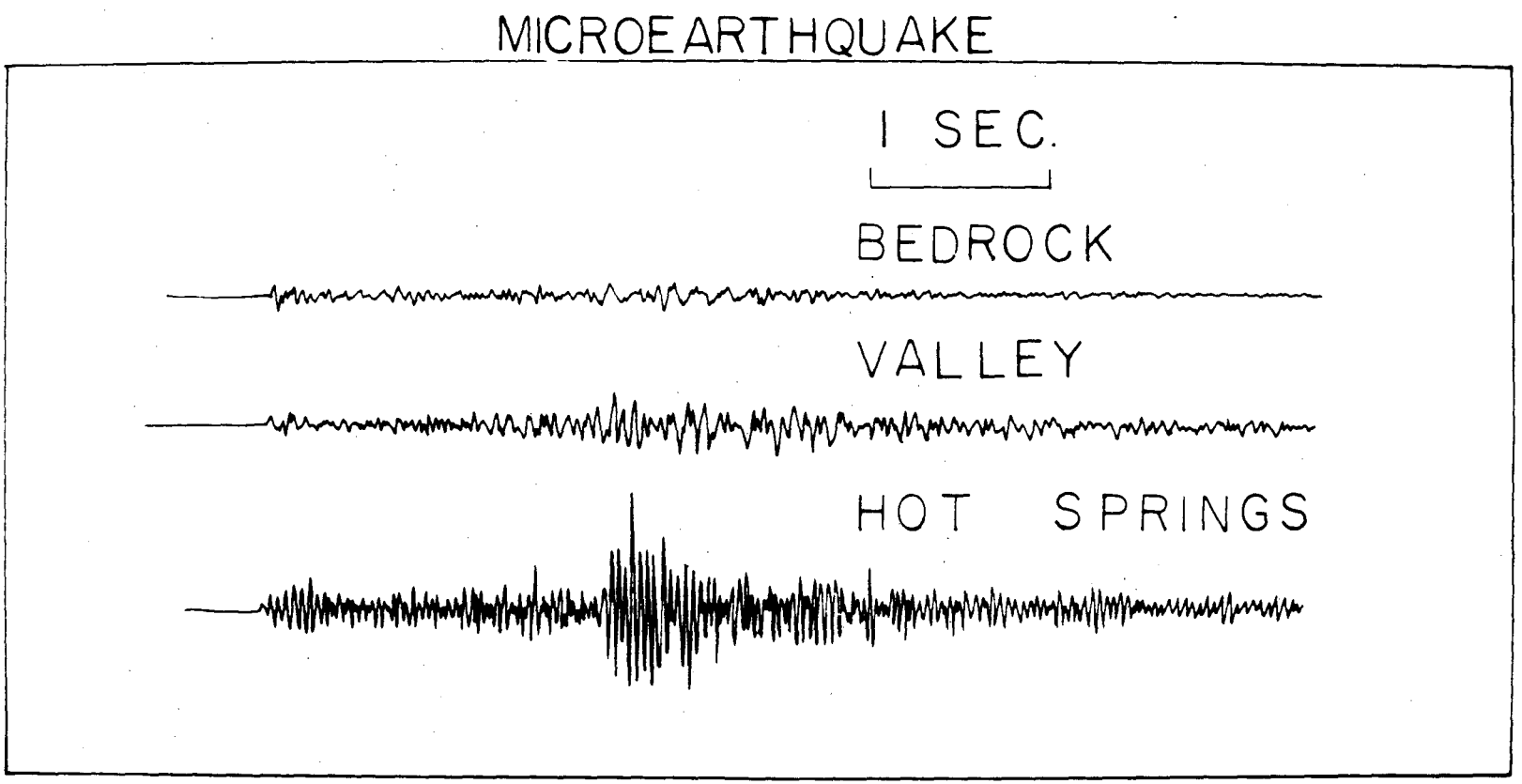

Figure 54: Comparison of seismograms from the same local micro-earthquake, recorded at three sites.

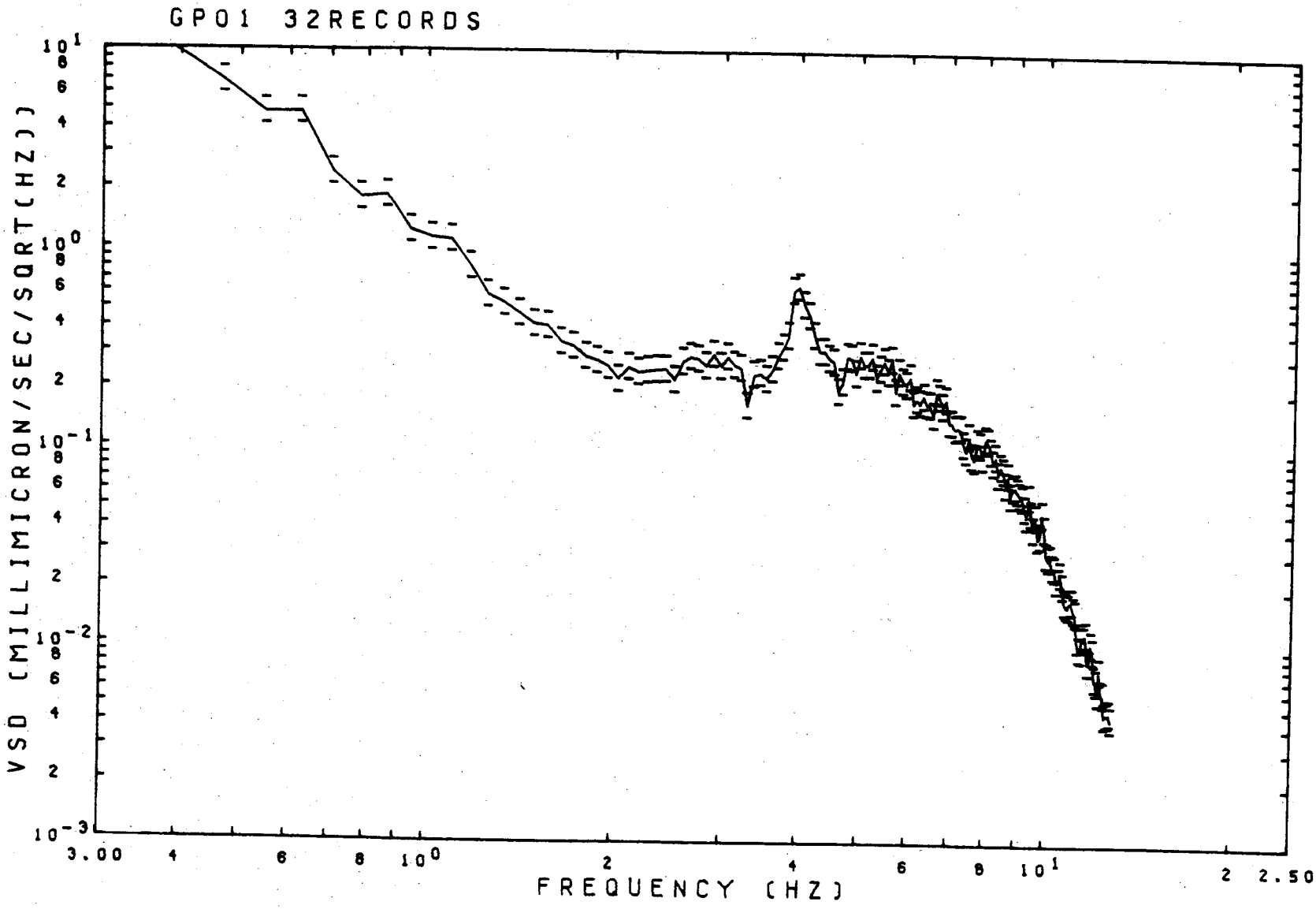

Figure 55: Averaged VSD for 32 samples at bedrock site GP. Bars give 95% confidence limits.

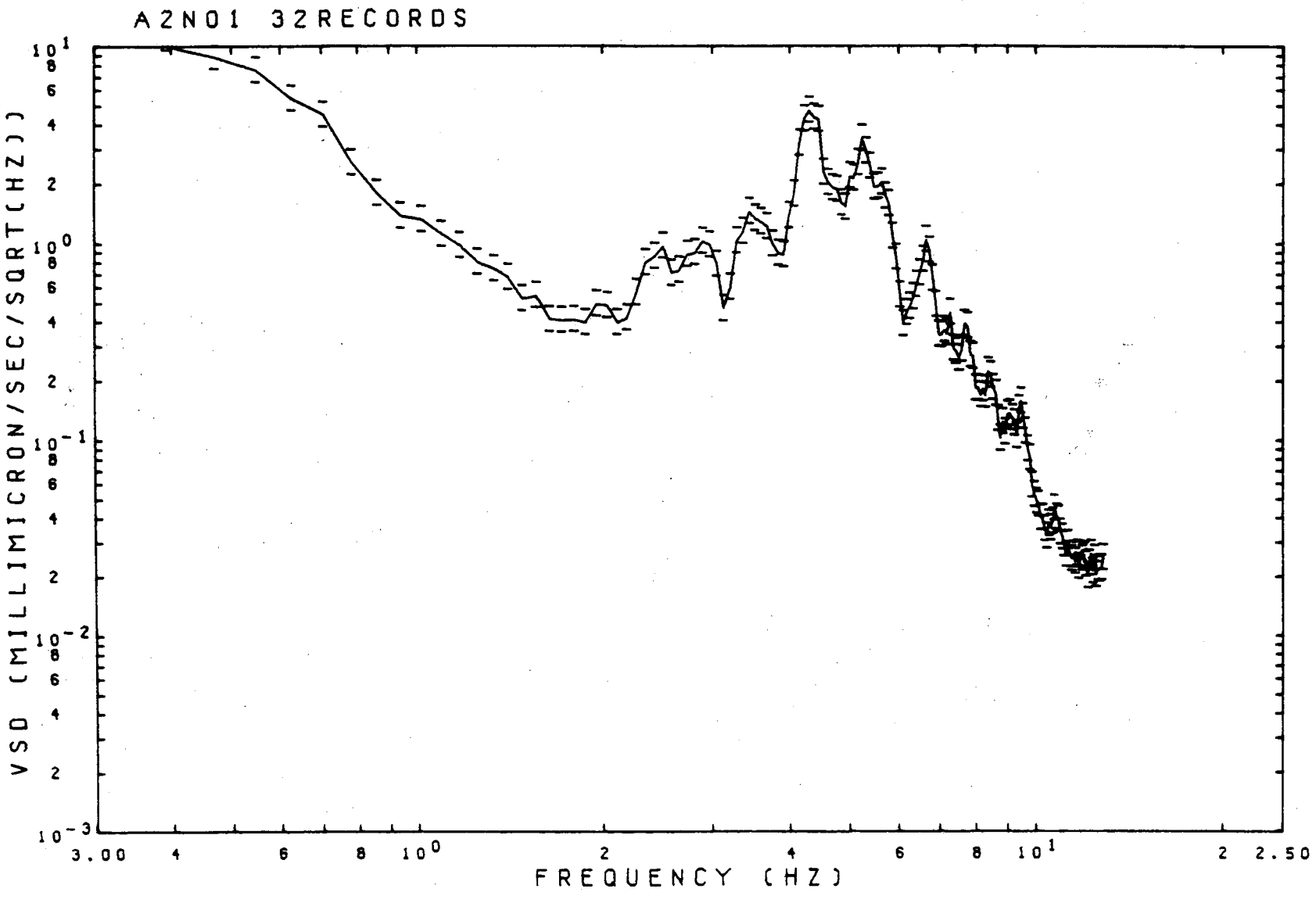

Figure 56: Averaged VSD for 32 samples at site A2N near the hot springs.

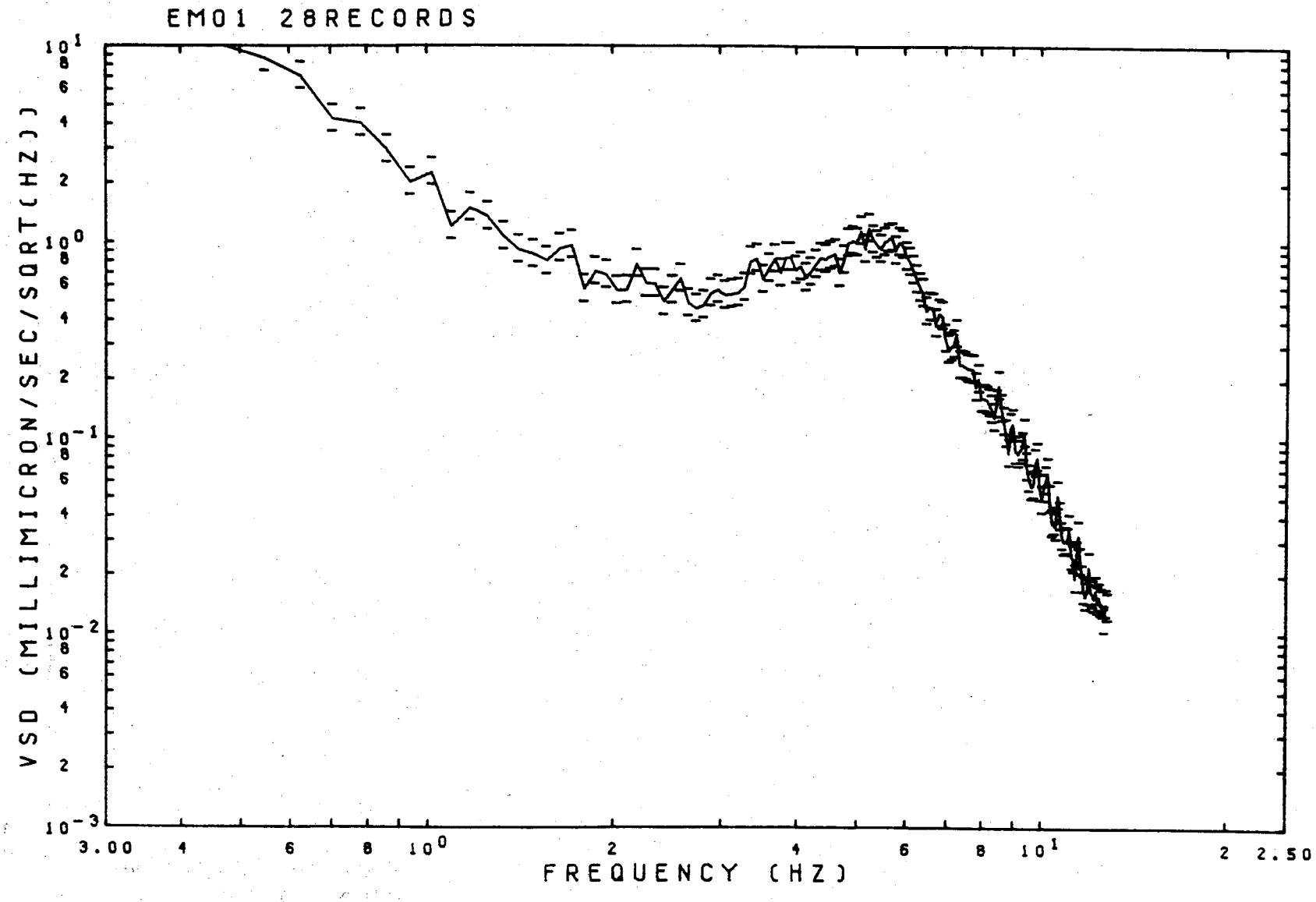

Figure 57: Averaged VSD for 28 samples at site EM in the valley.

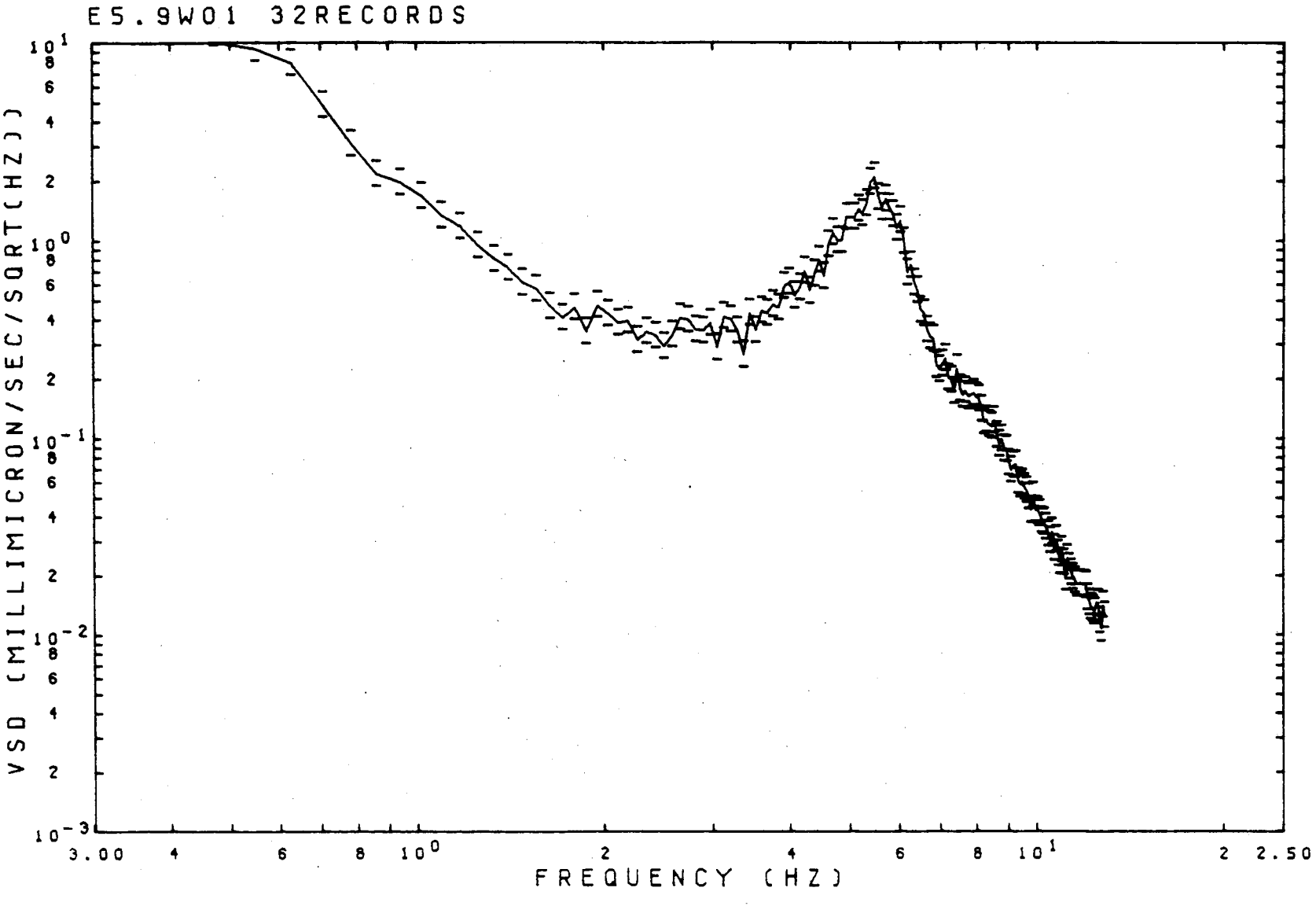

Figure 58: Averaged VSD for 32 samples at site E5.9 in the valley.

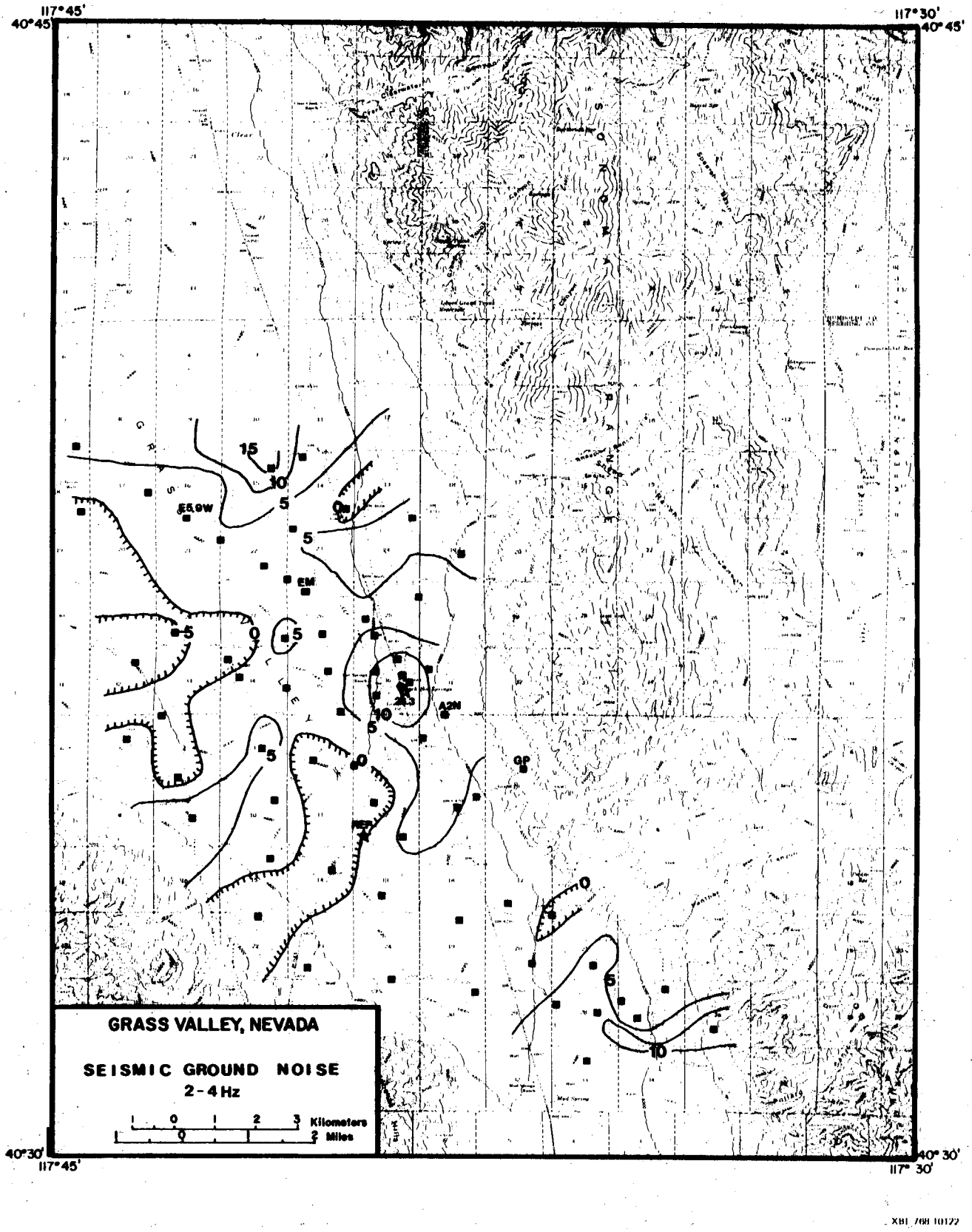

Figure 59: 2-4 Hz ground noise level with respect to station REF, contoured in dB.

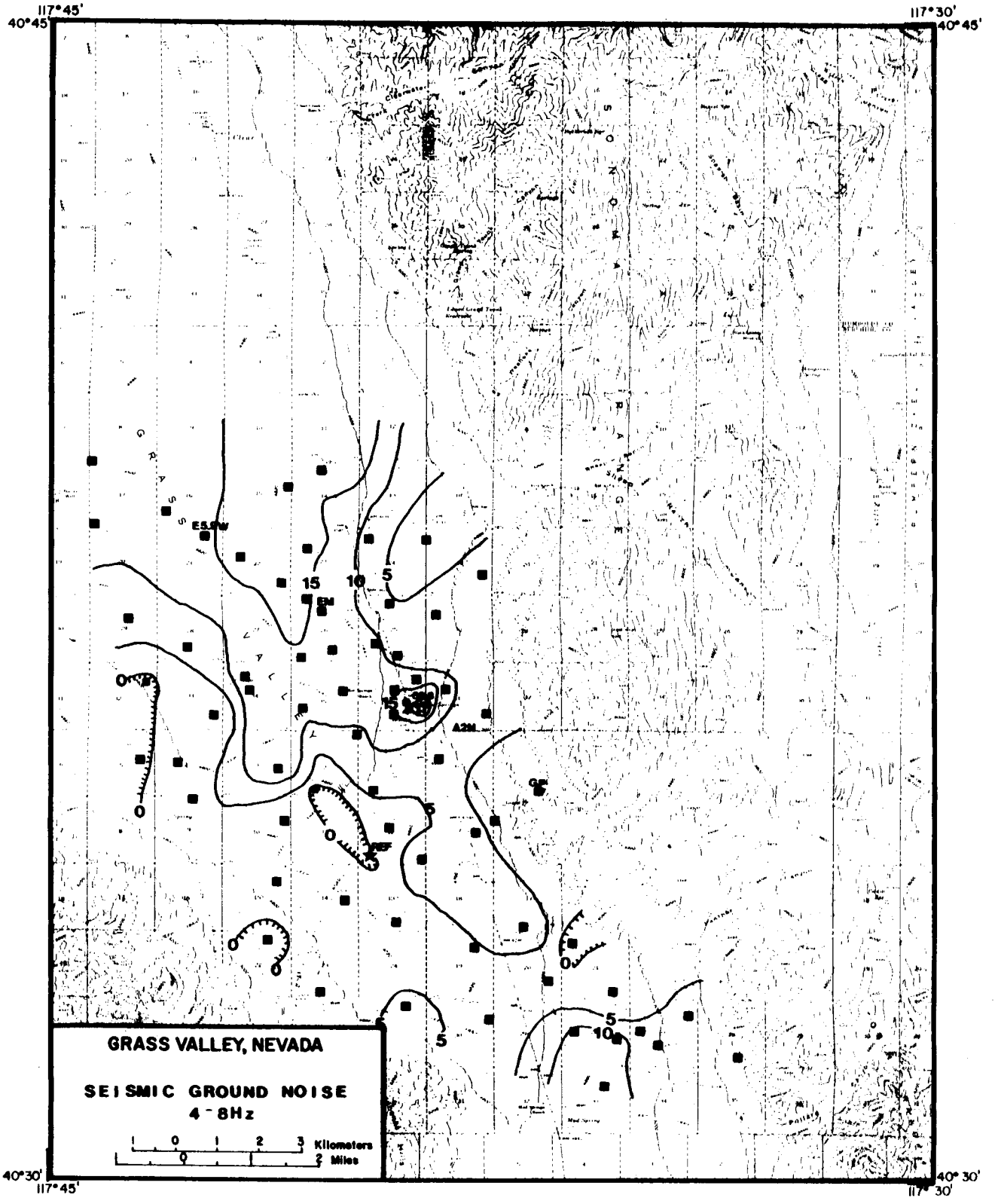

Figure 60: 4-8 Hz ground noise level with respect to station REF, contoured in dB.

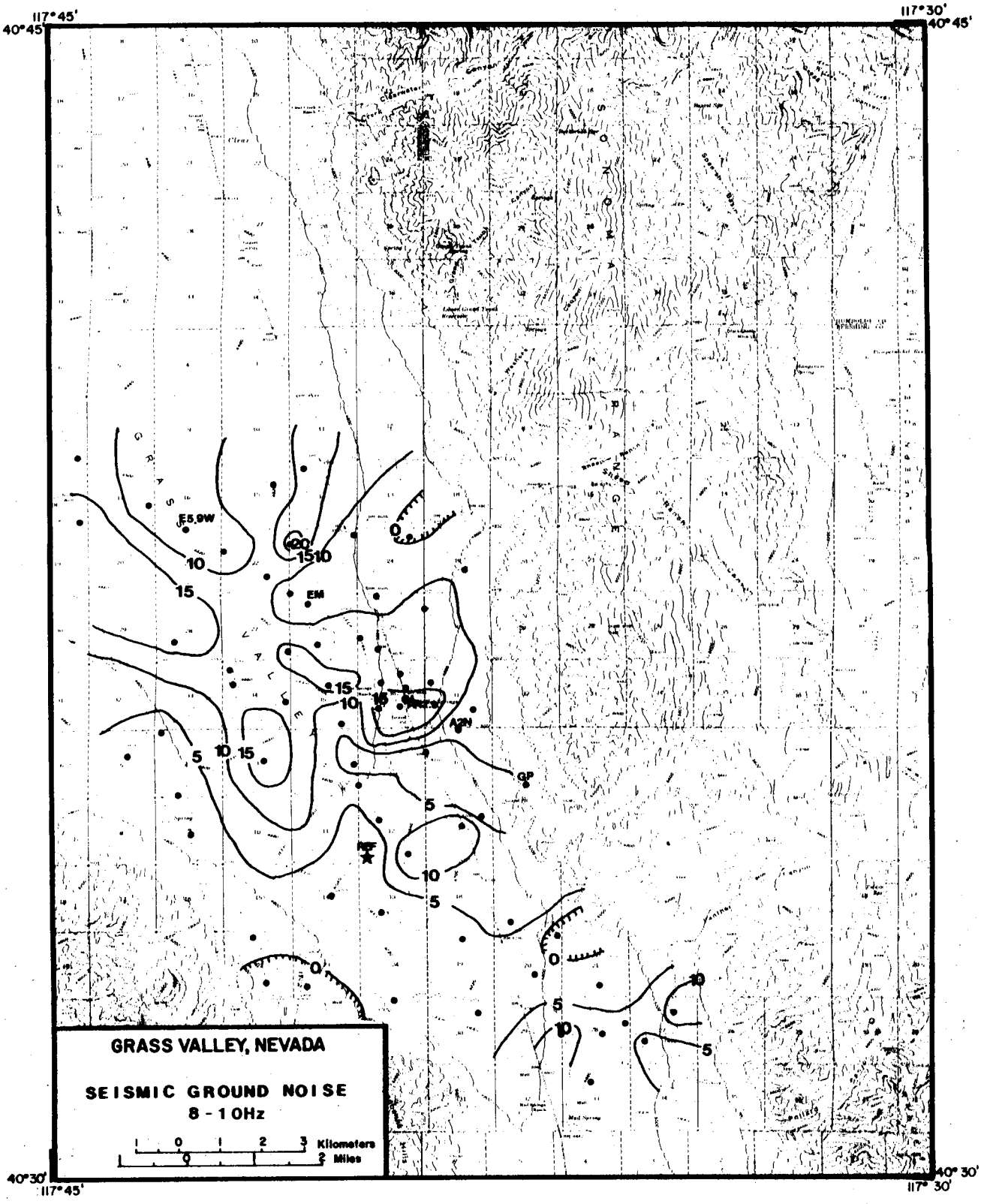

Figure 61: 8-10 Hz ground noise with respect to station REF, contoured in dB.

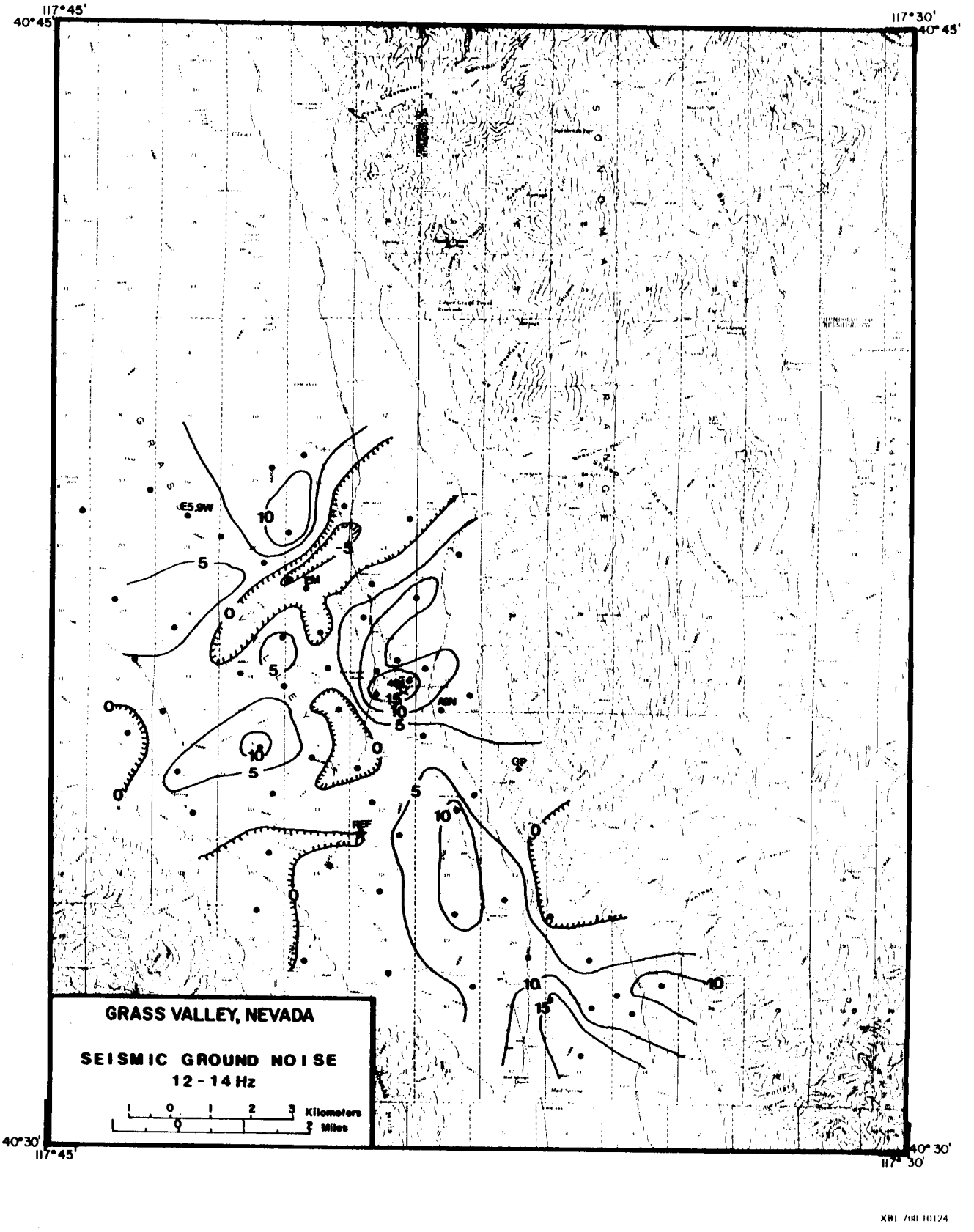

Figure 62: 12-14 Hz ground noise with respect to station REF, contoured in dB.

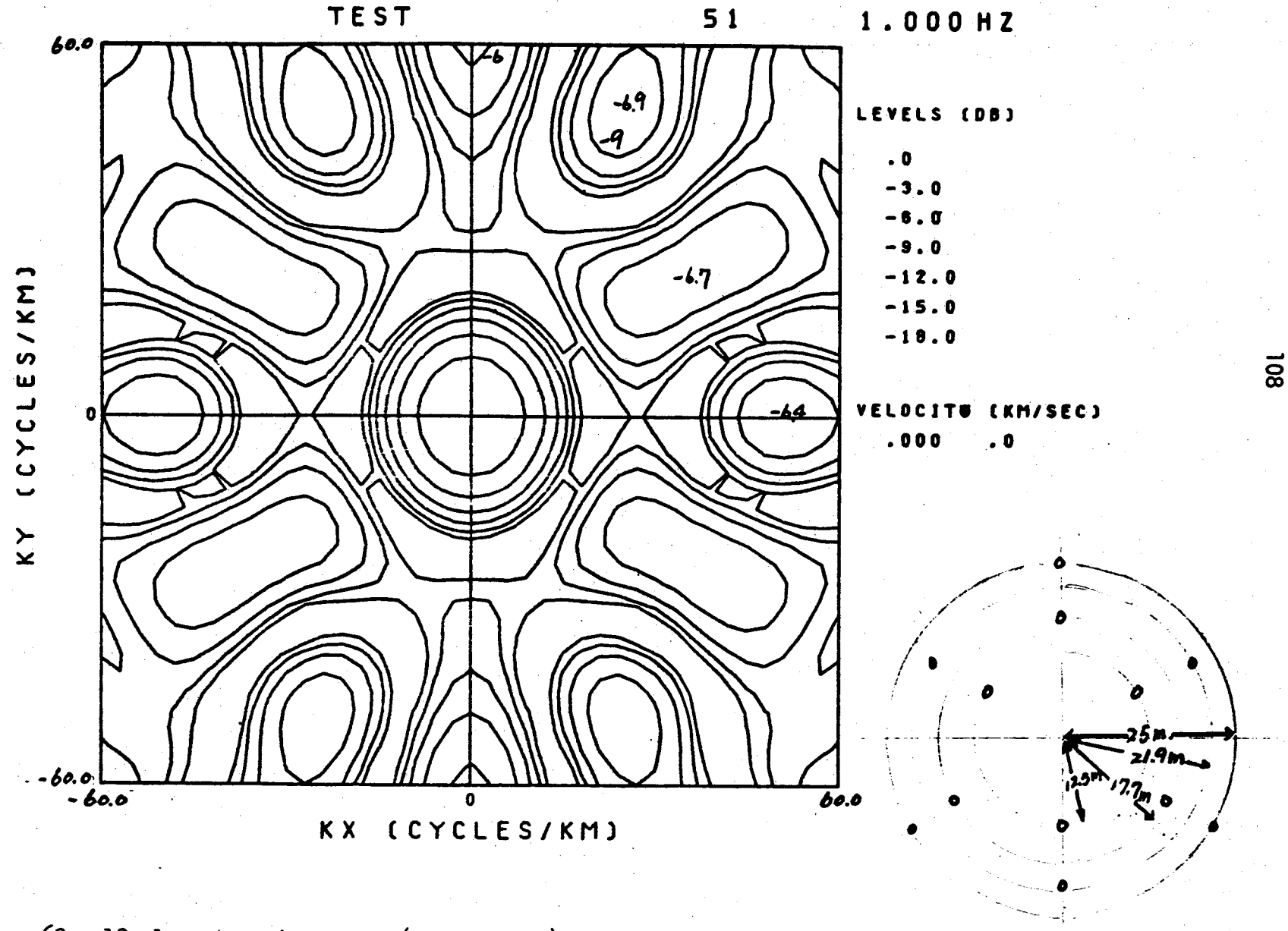

Figure 63: 12-element roving array (lower right) and array response in wavenumber space, contoured in dB at values shown in legend.

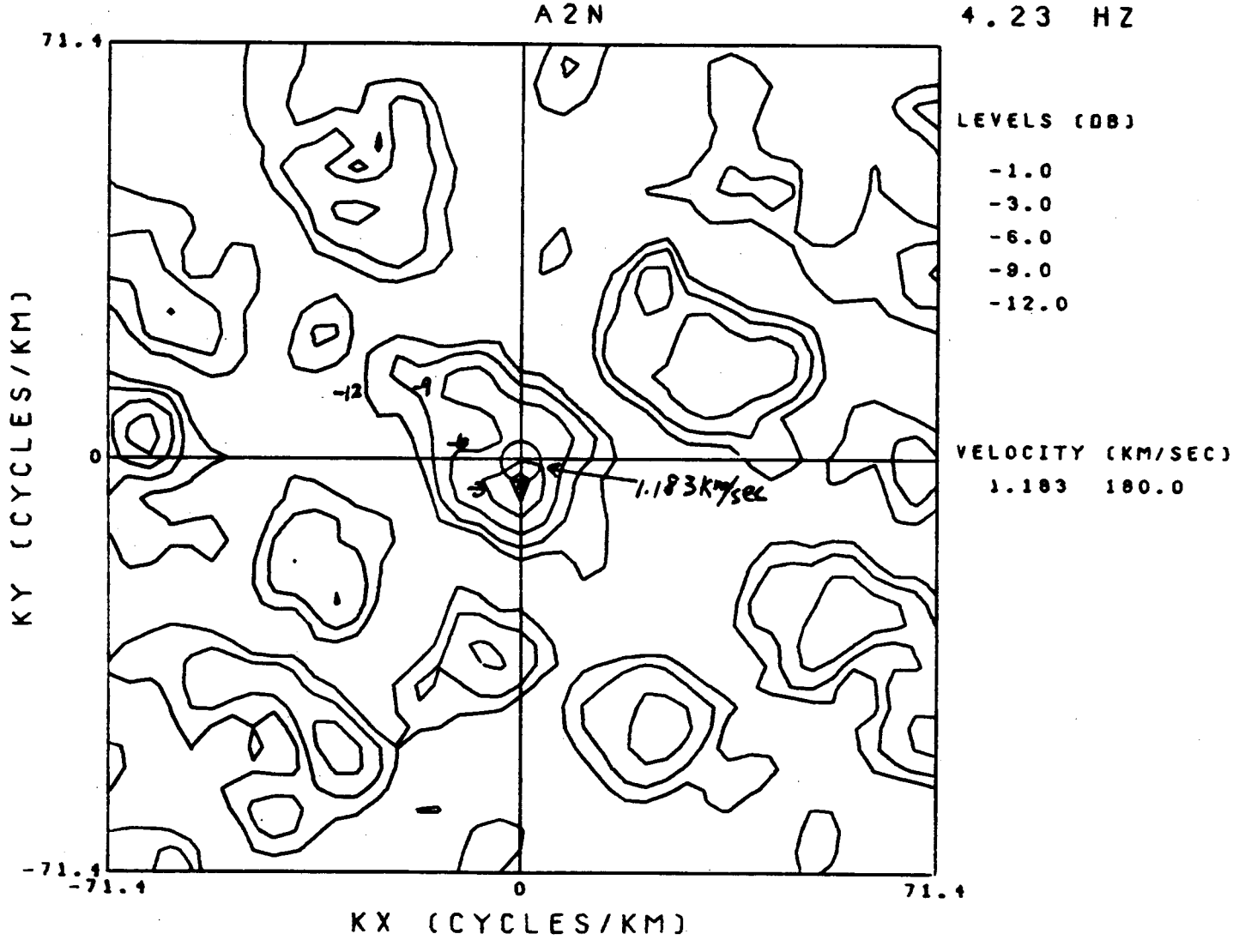

Figure 64: Wavenumber plot for site A2N near the hot springs. Contours at 4.32 Hz in dB as shown in legend. Peak velocity and azimuth given in legend.

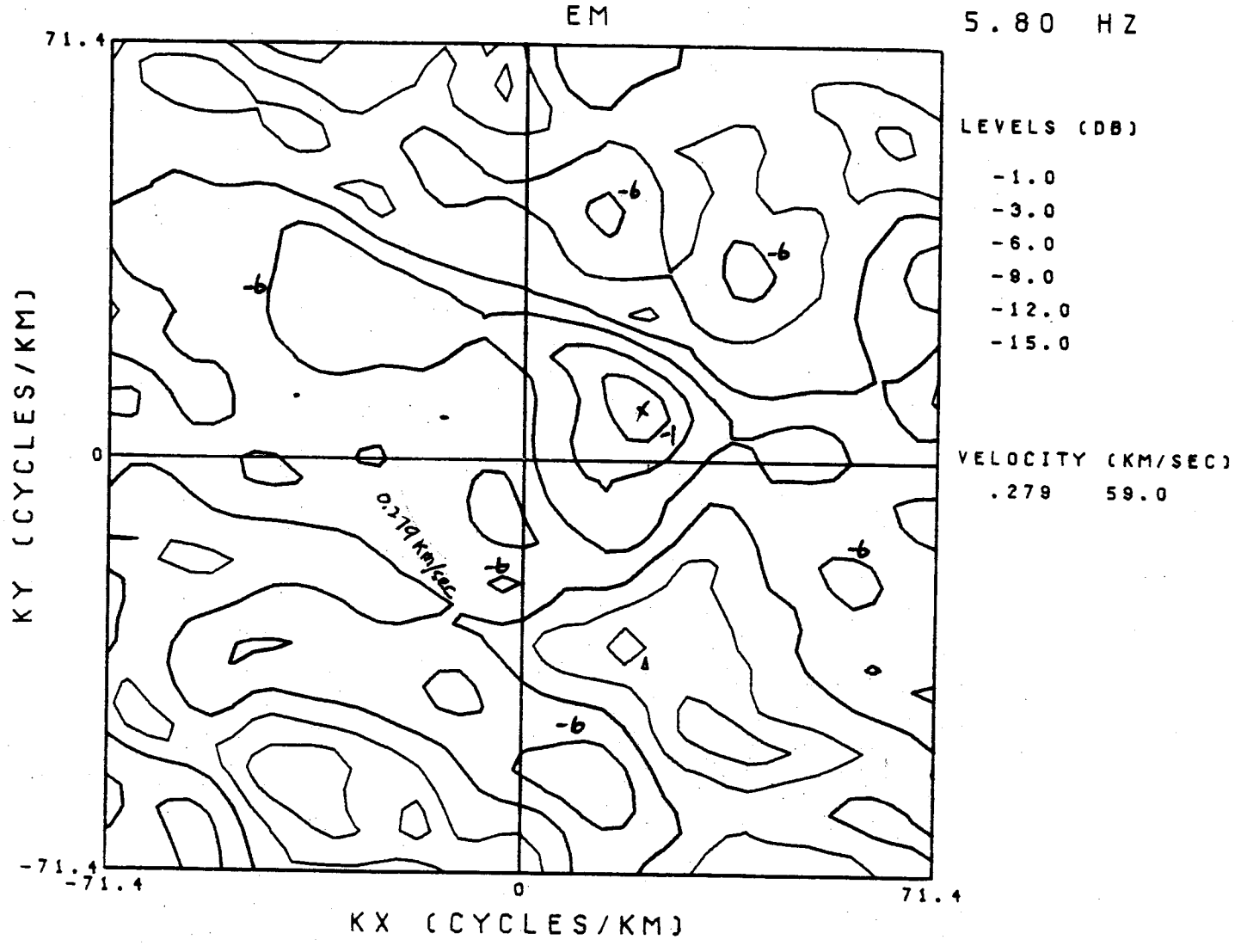

Figure 65: Wavenumber plot for valley site EM at 5.80 Hz.

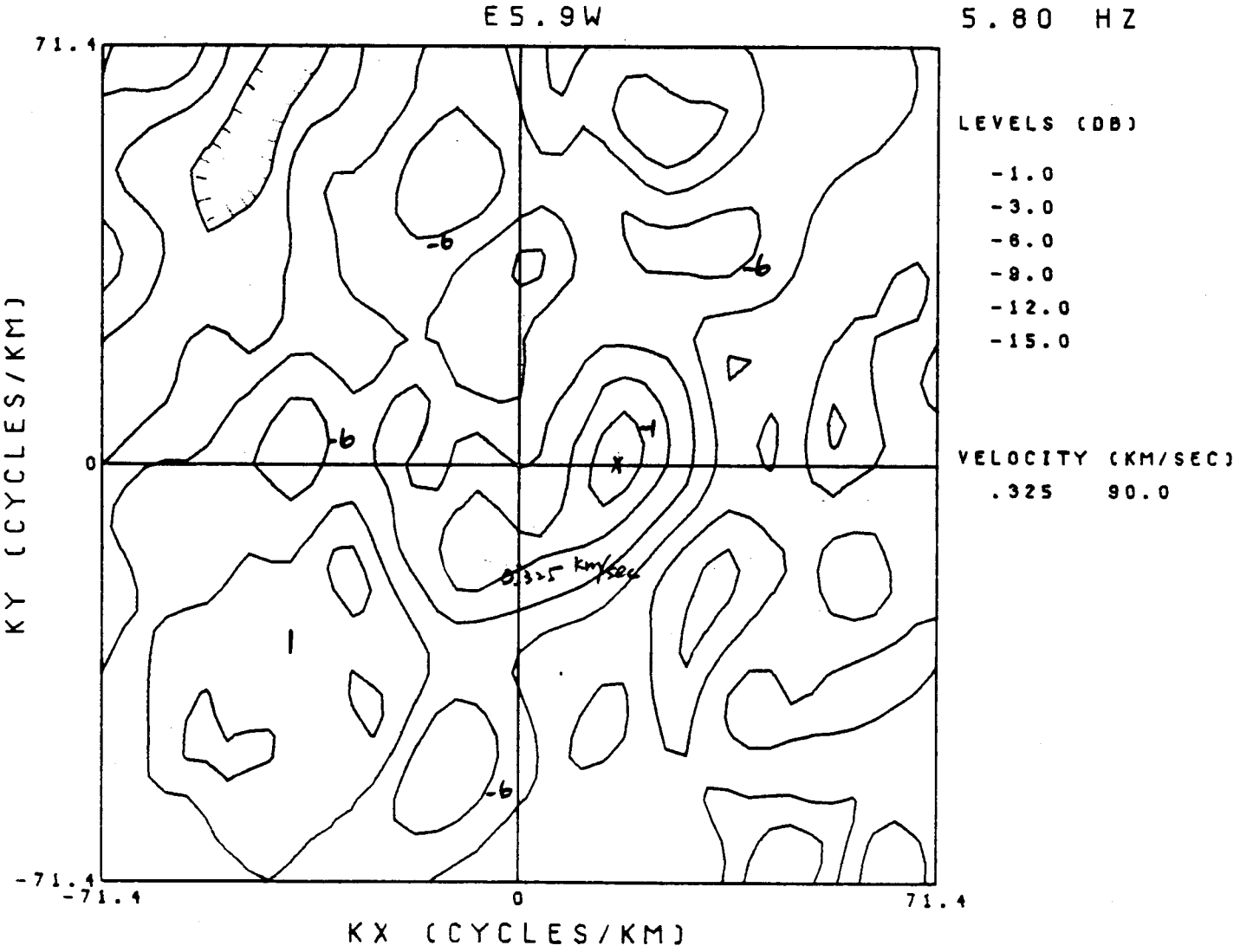

Figure 66: Wavenumber plot for valley site E5.9W at 5.80 Hz.

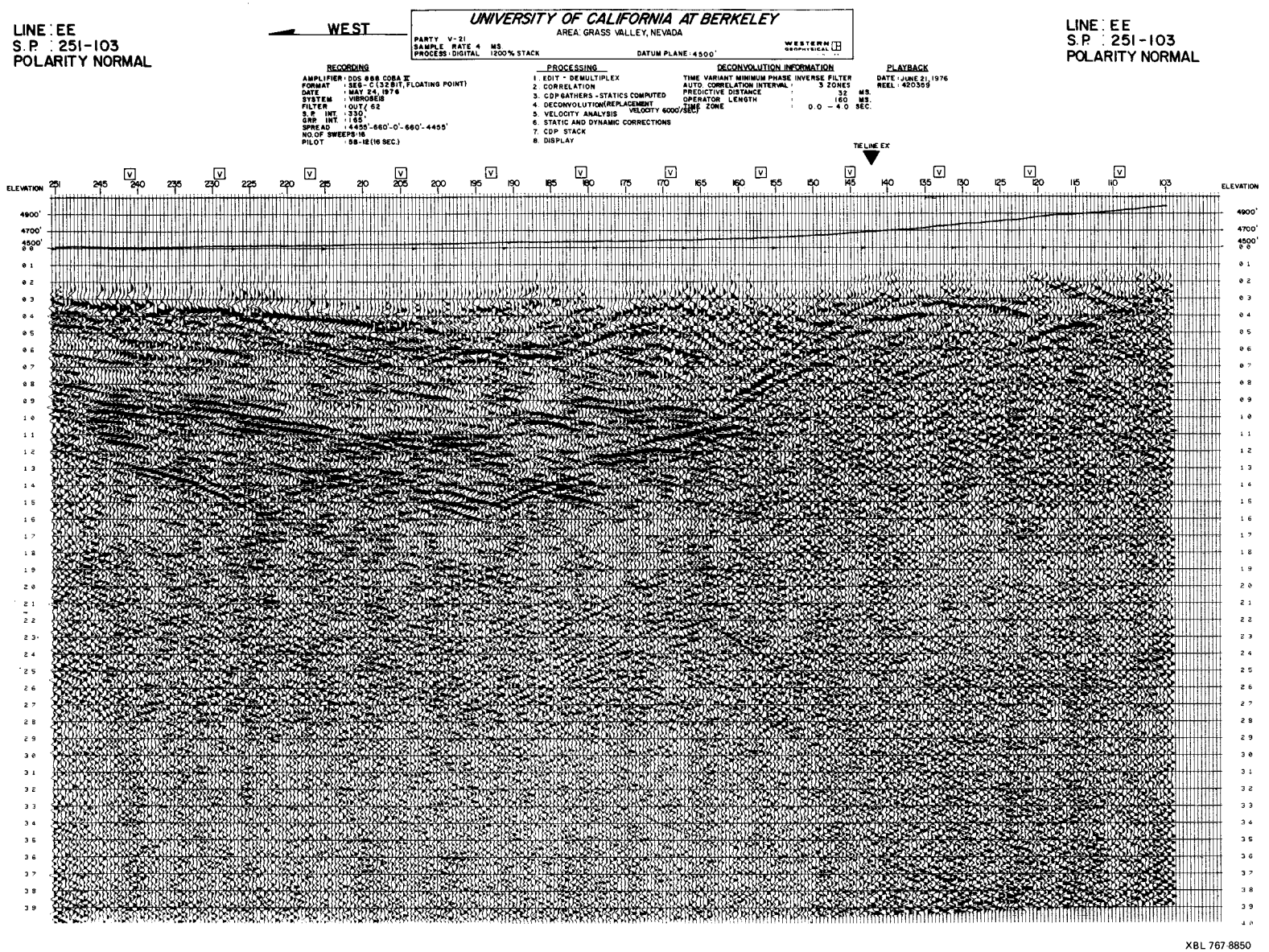

Figure 67: Line E-E', conventional section.

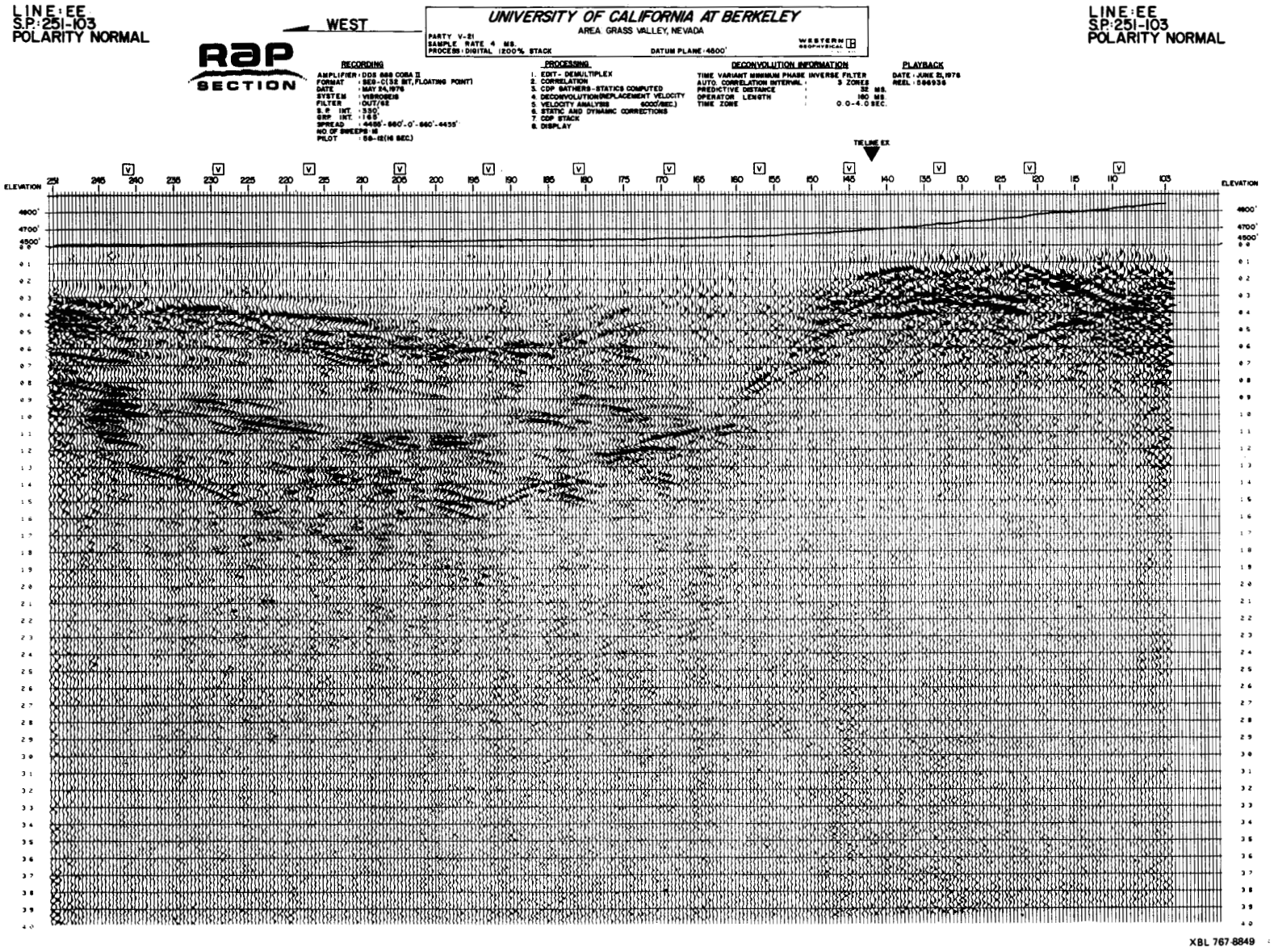

Figure 68: Line E-E', relative amplitude section.

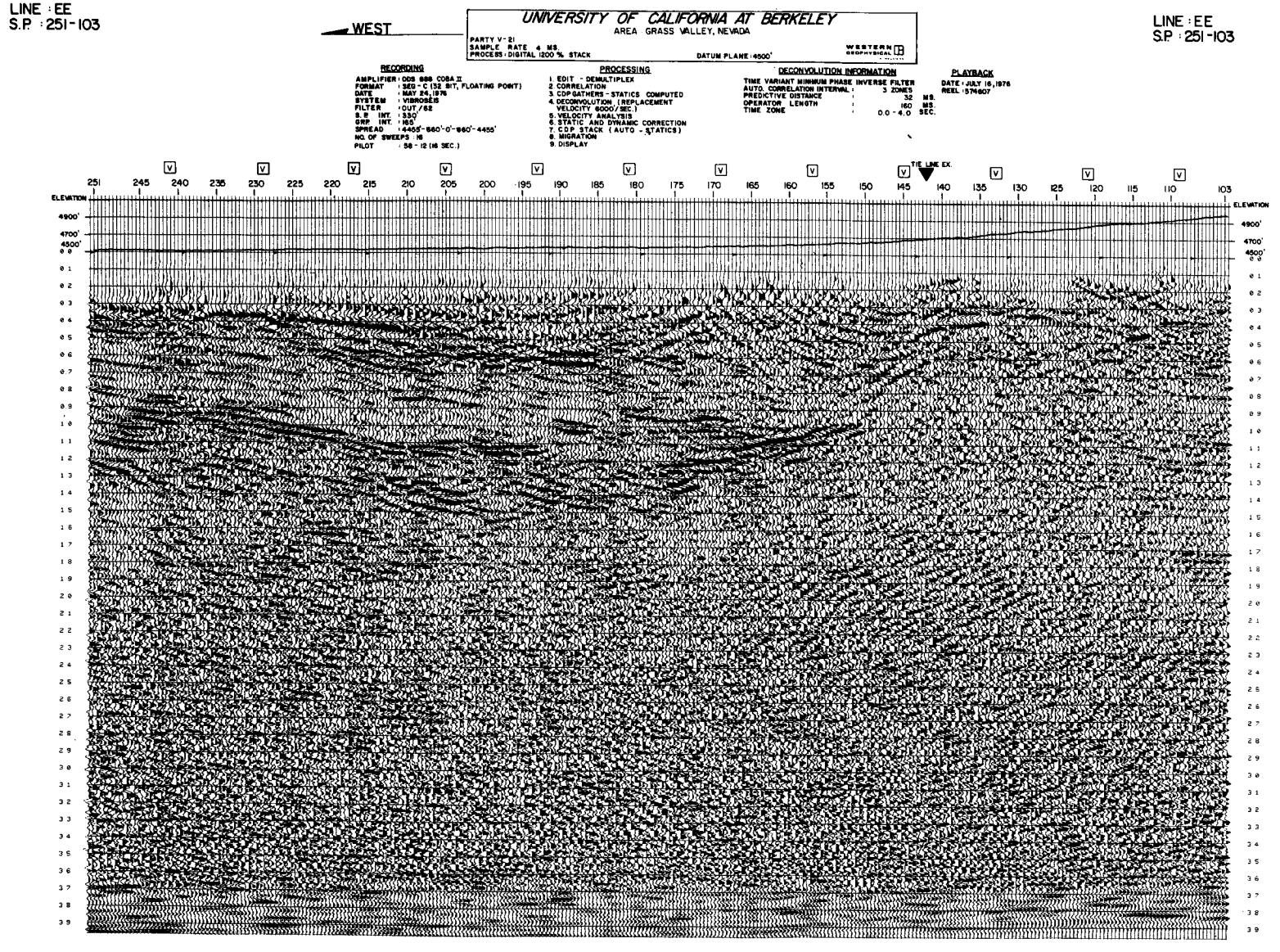

XBB 768-7630

Figure 69: Line E-E', migrated section.

LINE: EX
S.P191 -103
(POLARITY NORMAL)

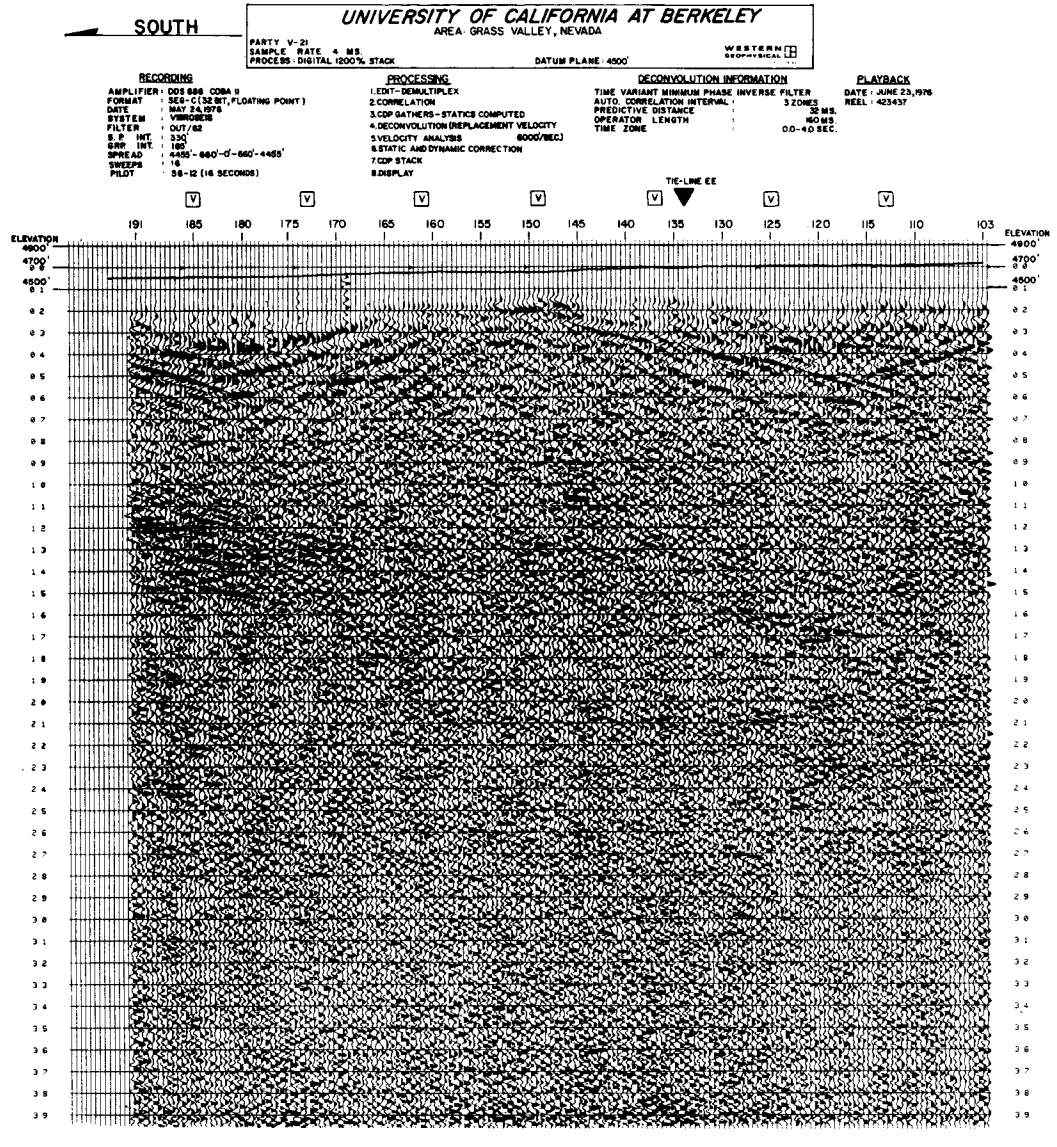

XBB 768-7628

LINE: EX
S.P. 191 -103
(POLARITY NORMAL)

Figure 70: Line E-X', conventional section.

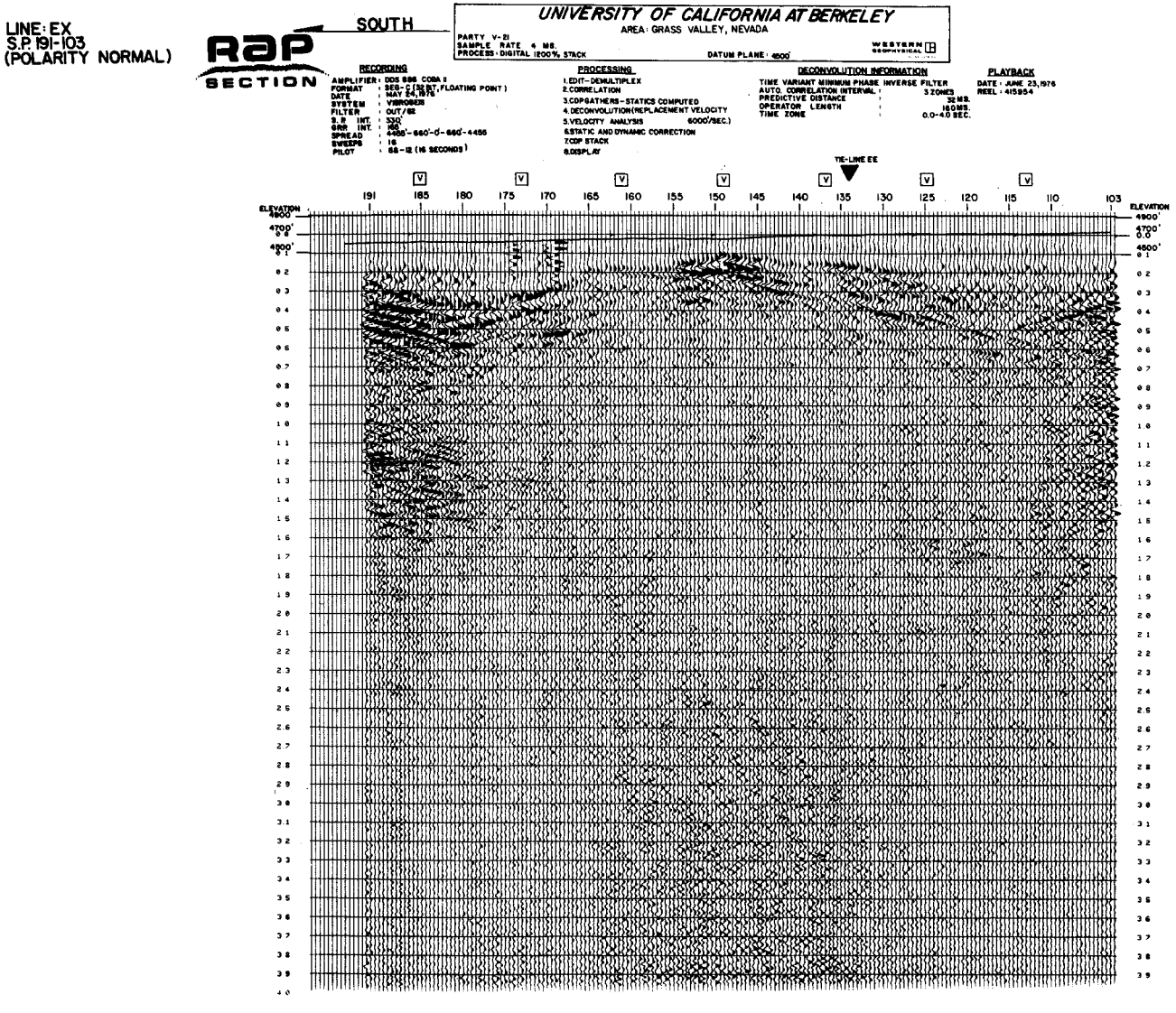

XBL 767-8848

Figure 71: Line E-X', relative amplitude section.

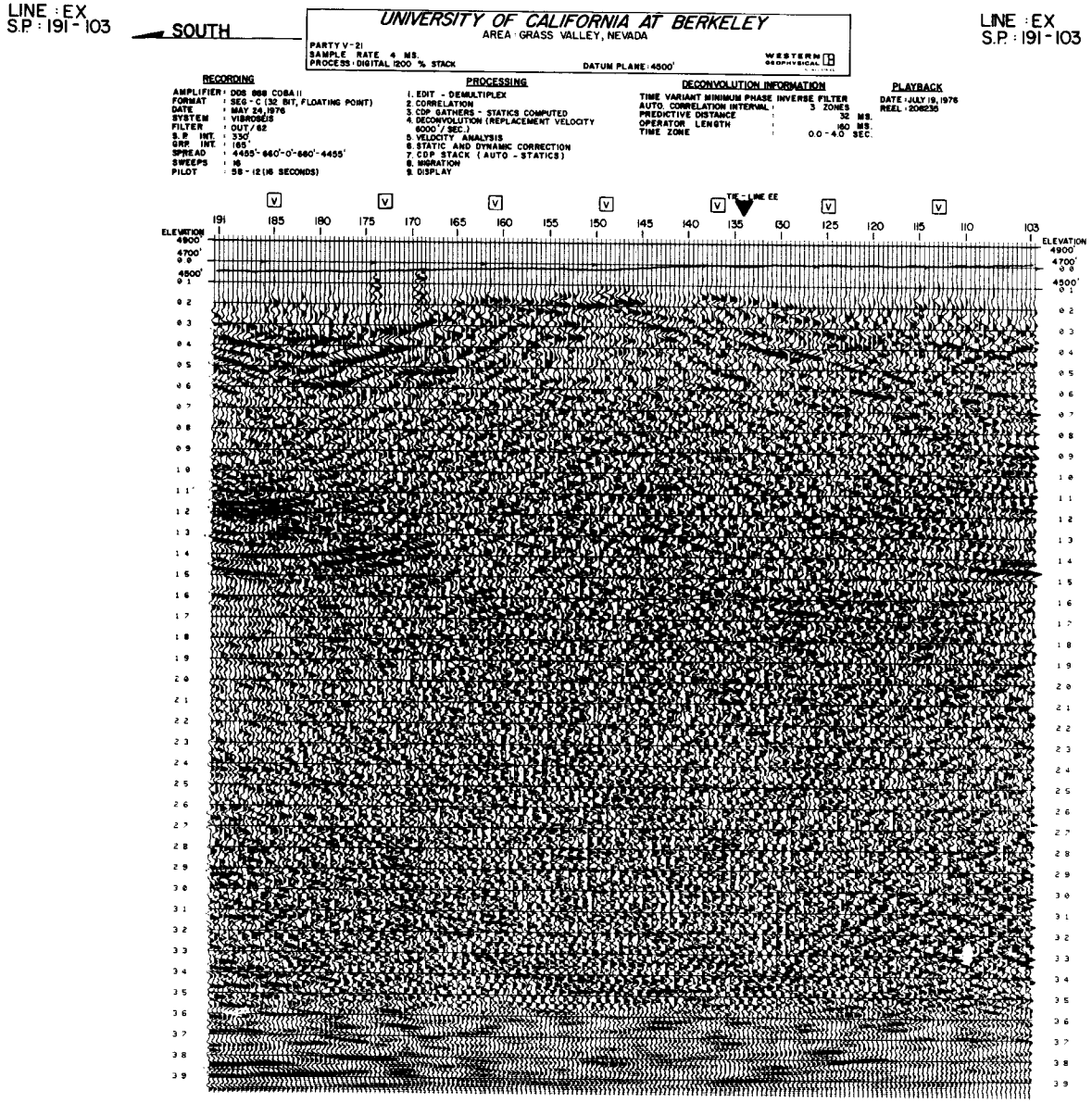

XBB 768-7629

Figure 72: Line E-X', migrated section.

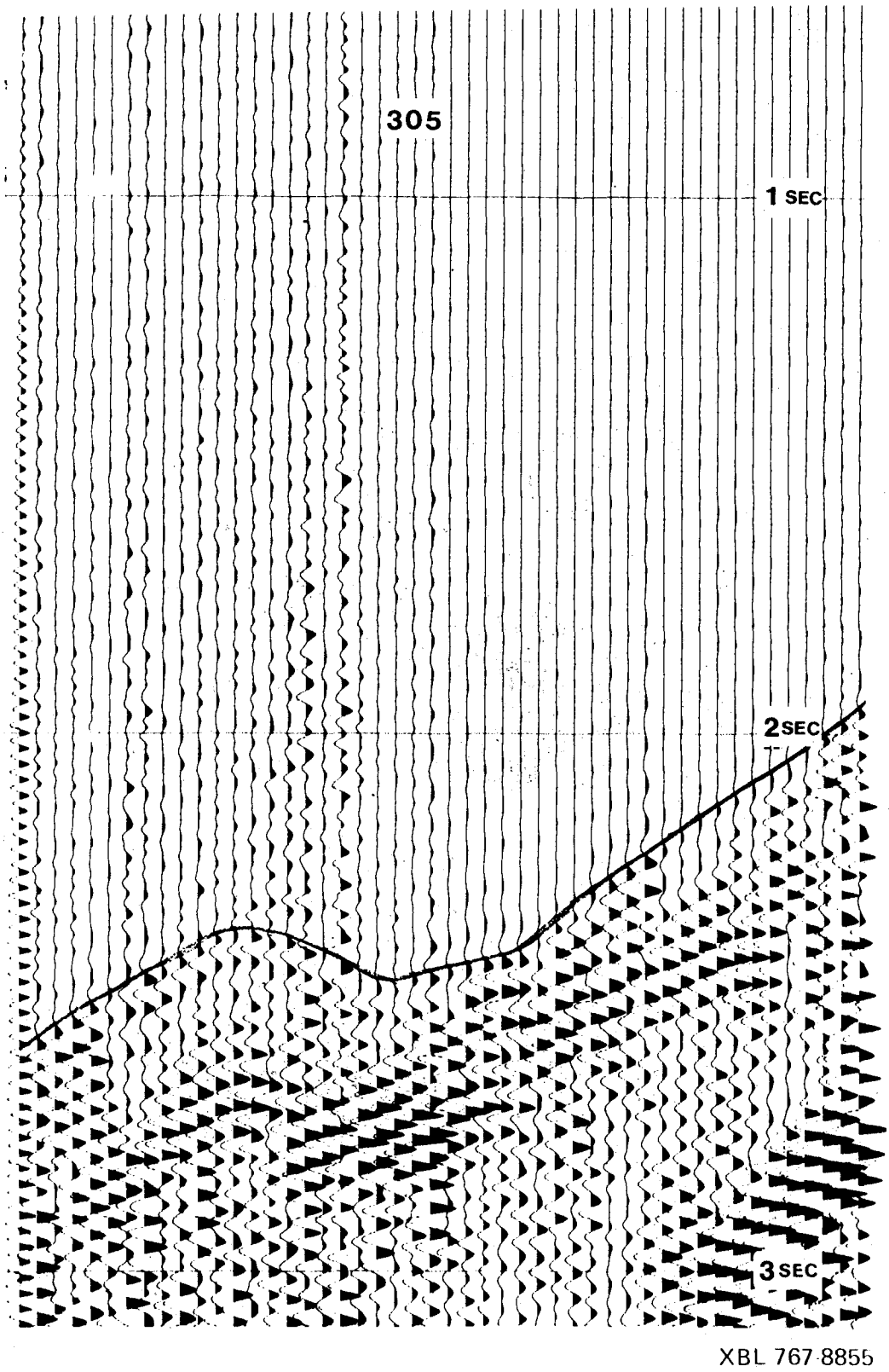

Figure 73: Refraction spread for SP at VP 305. Spread is from 2.0E (left) to 2.8W (right).

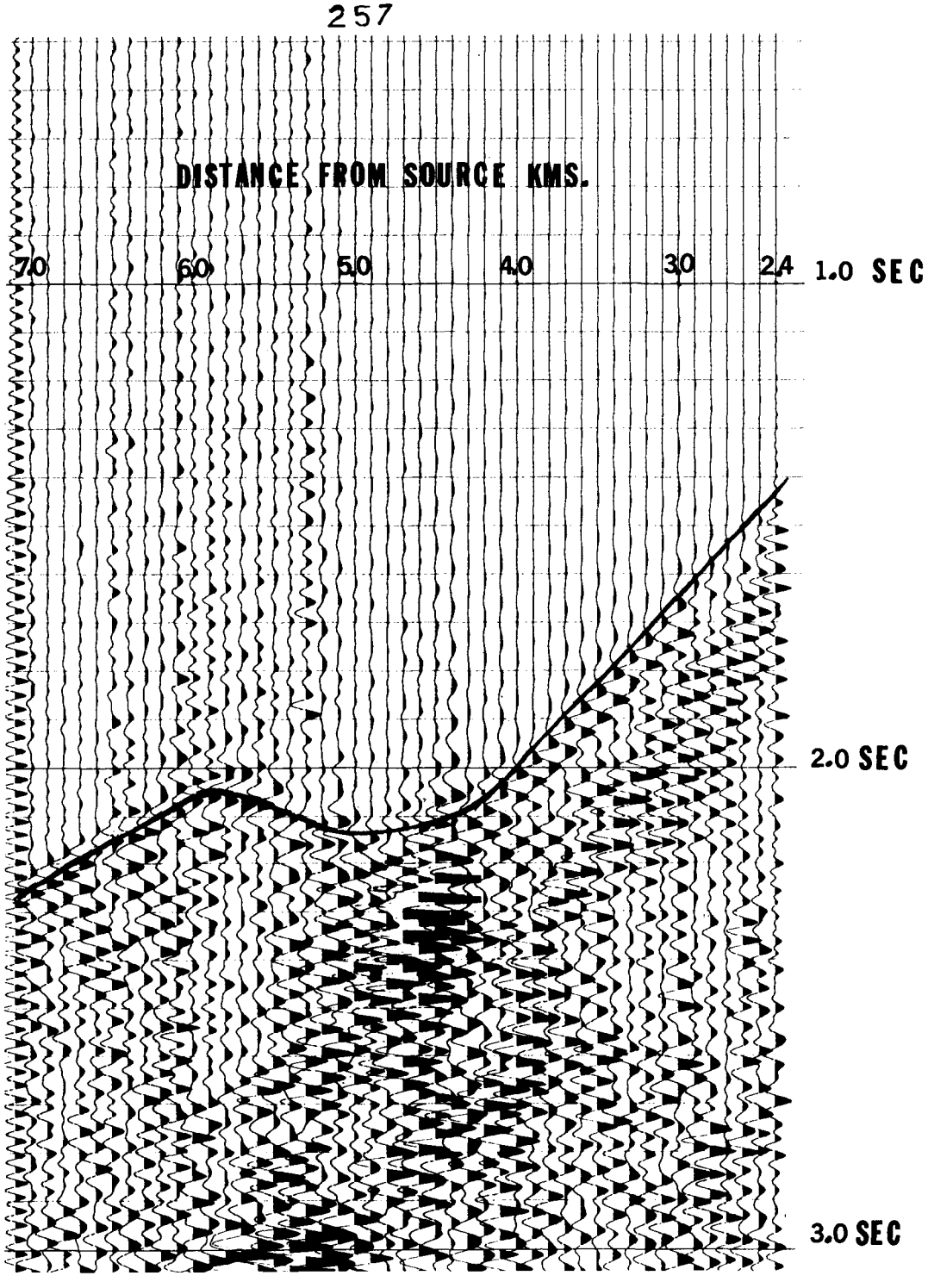

Figure 74: Refraction spread, VP 257.

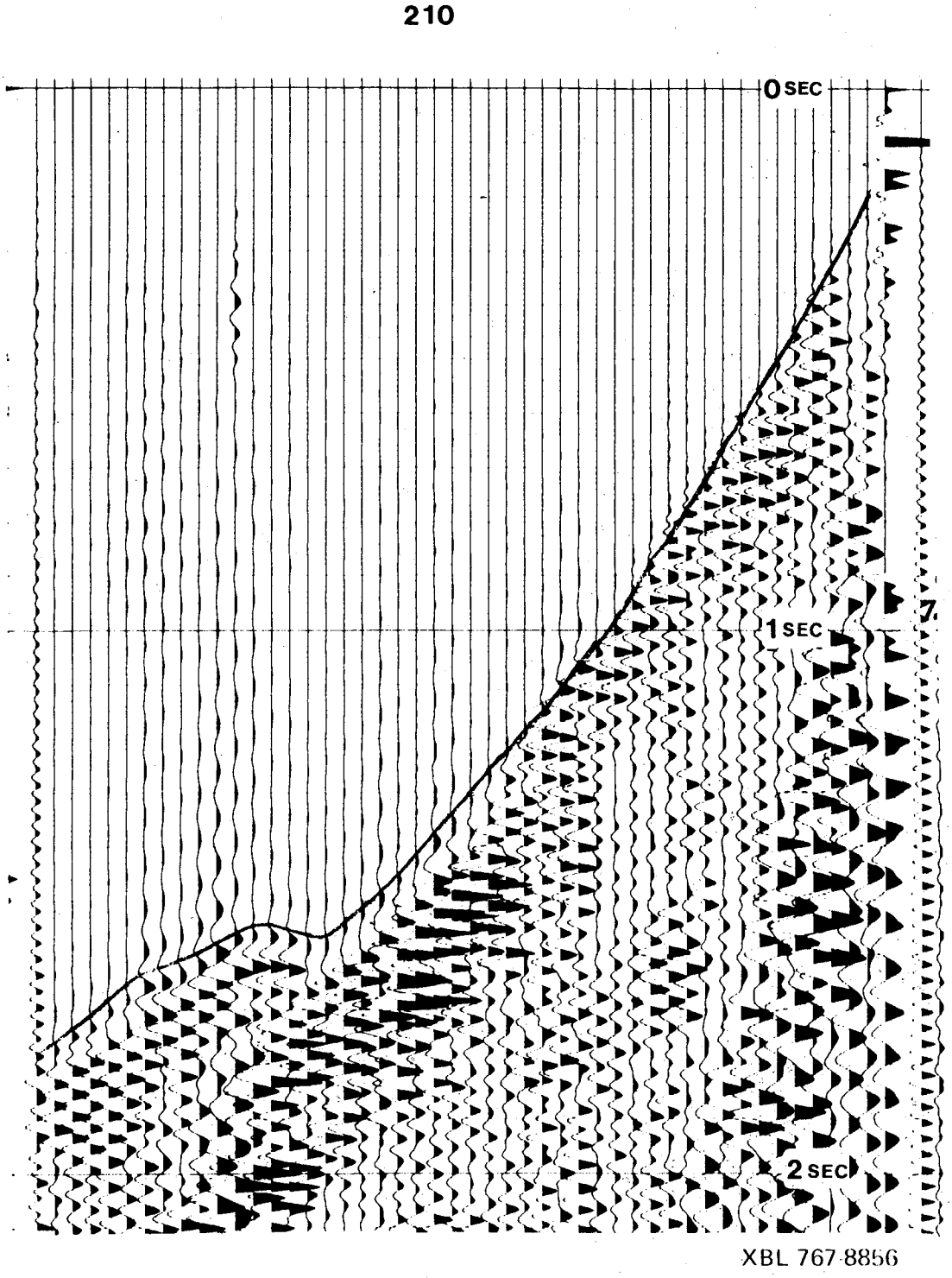

Figure 75: Refraction spread for VP 210.

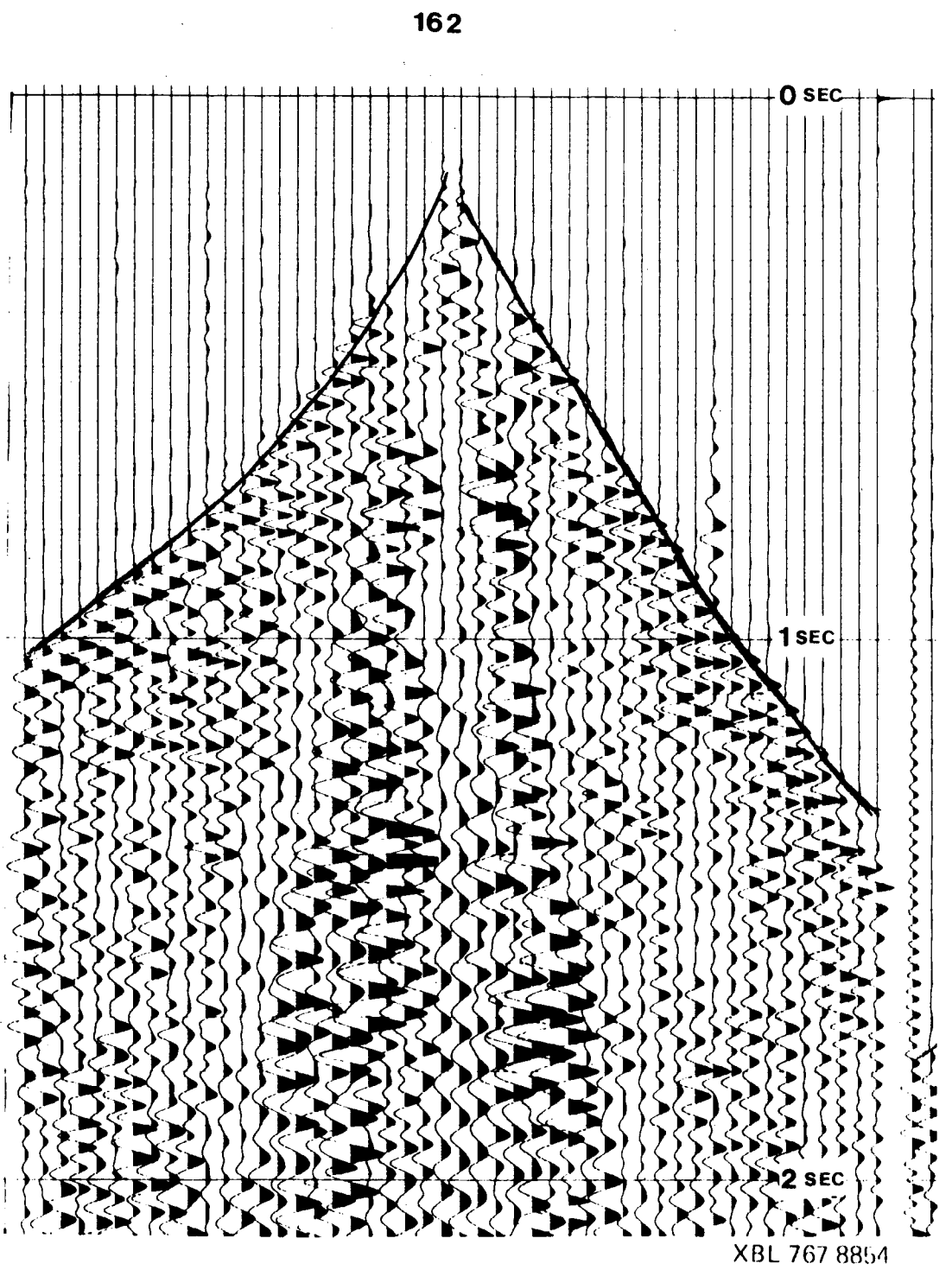

Figure 76: Refraction spread for VP 162.

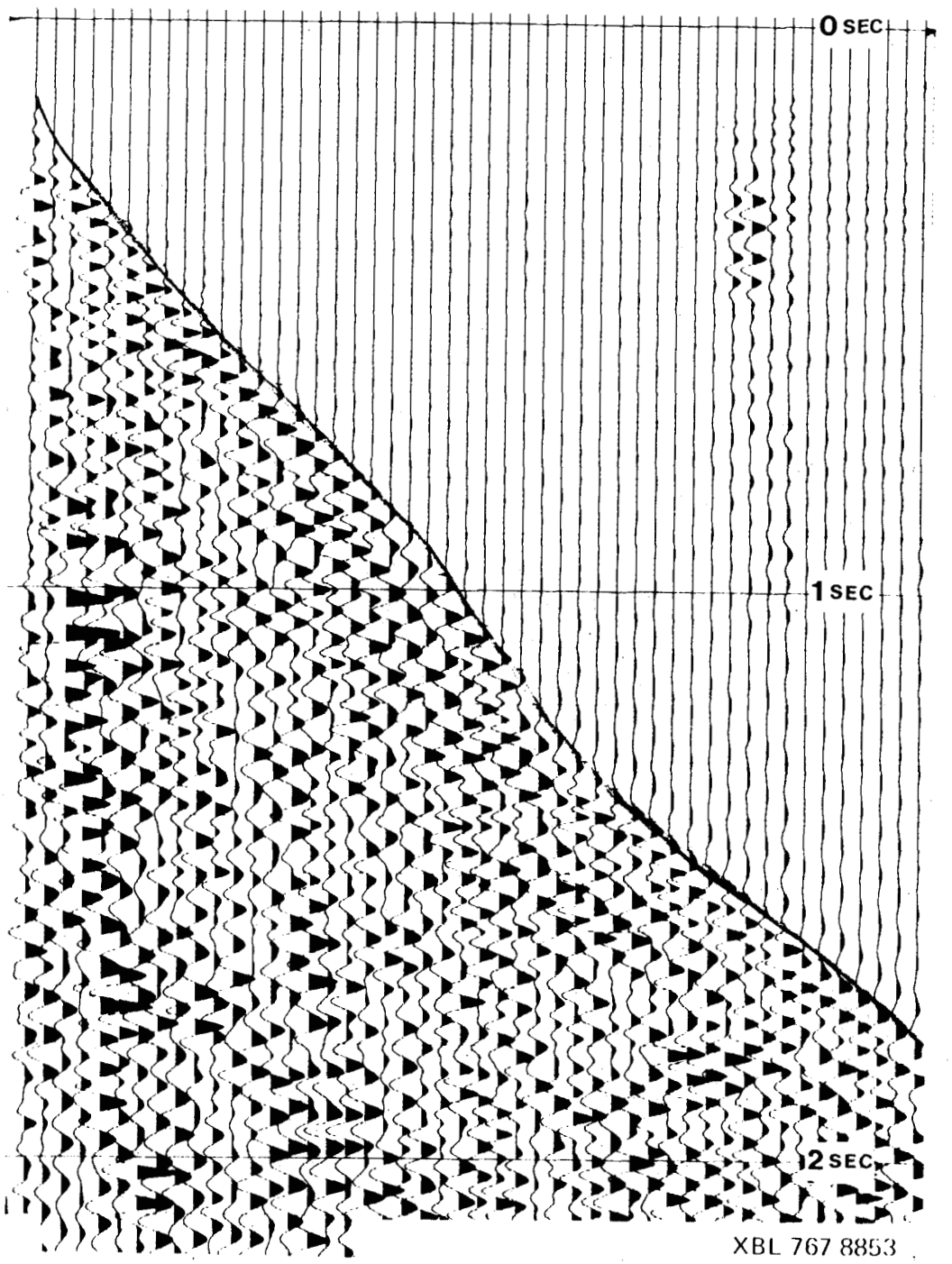

Figure 77: Refraction spread for VP 114.

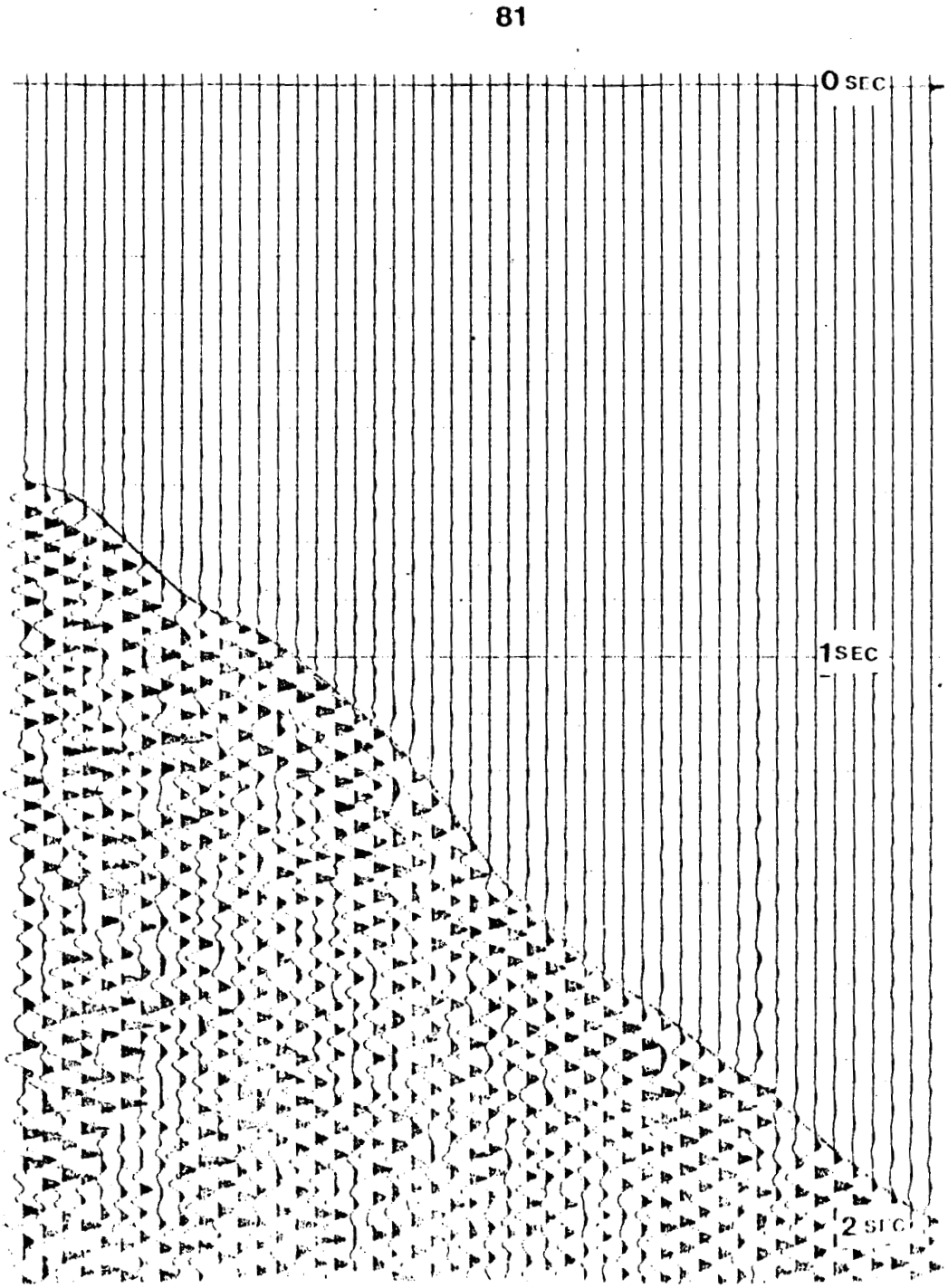

Figure 78: Refraction spread for VP 81.

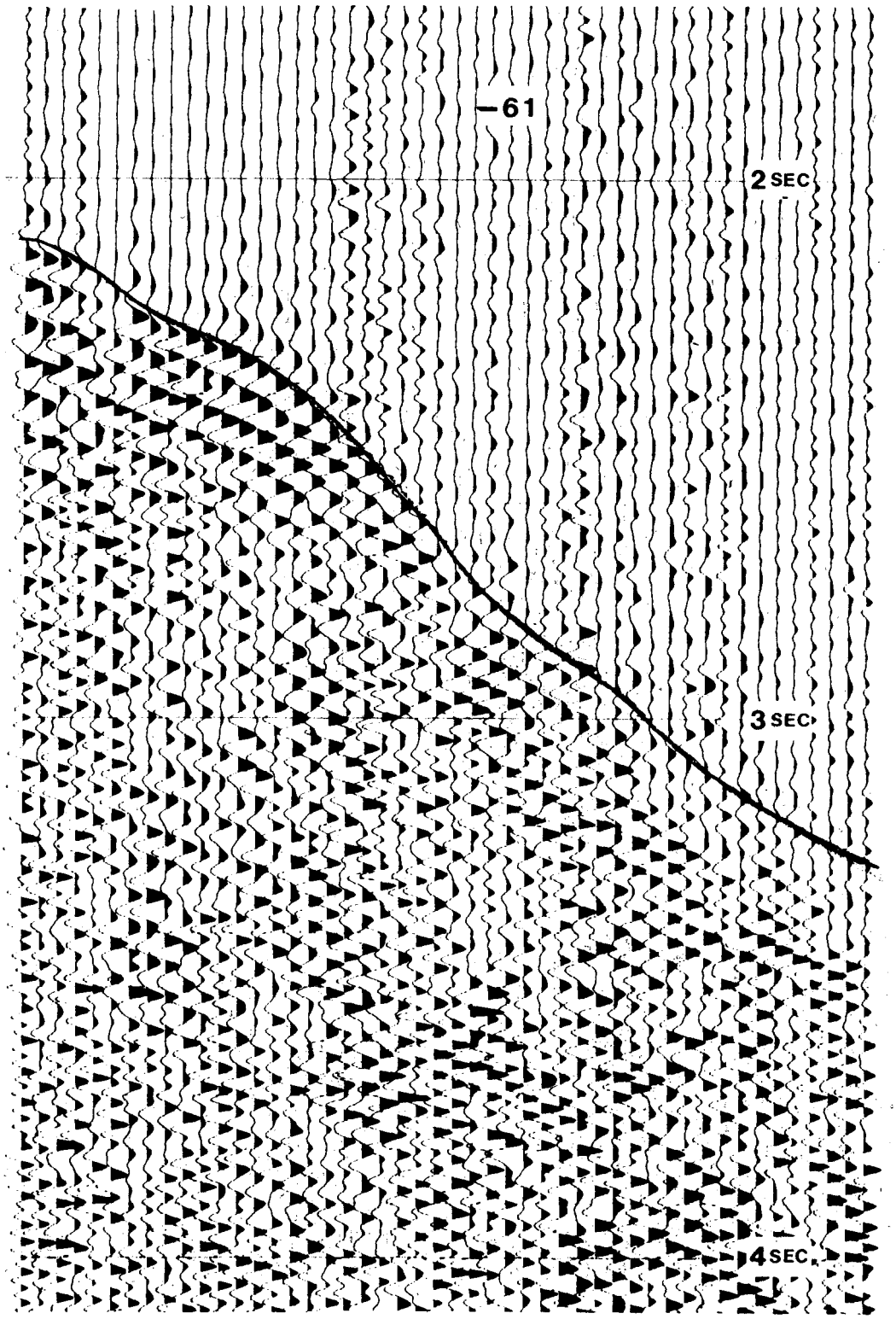

Figure 79: Refraction spread for VP 61.

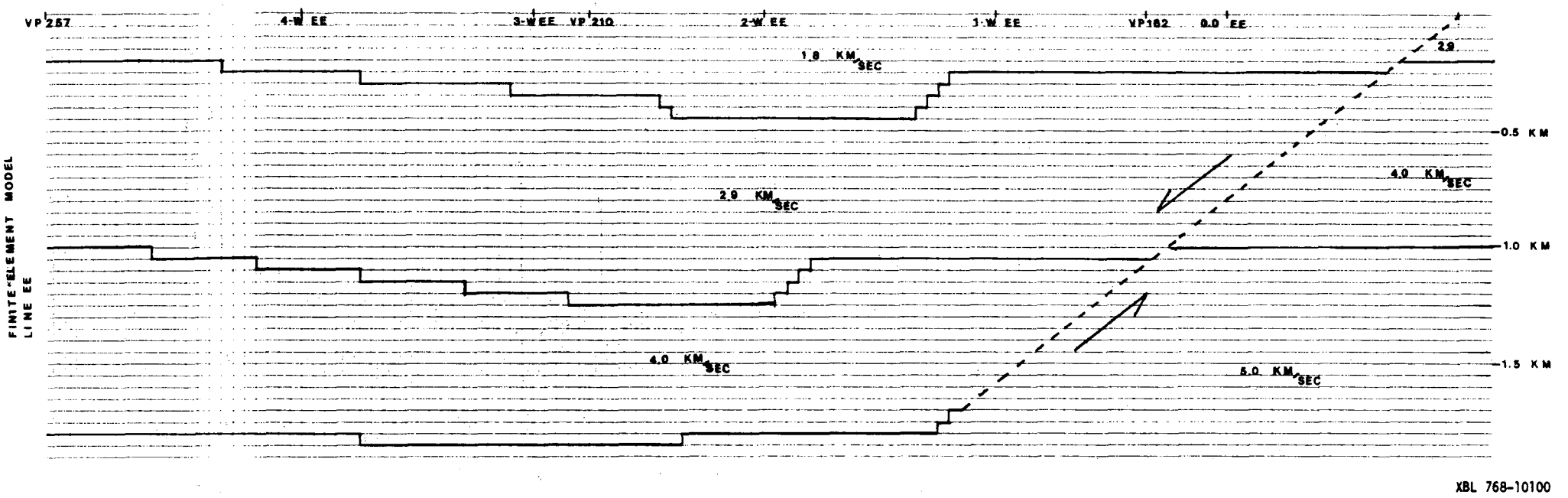

Figure 80: Generalized model for finite element computations.

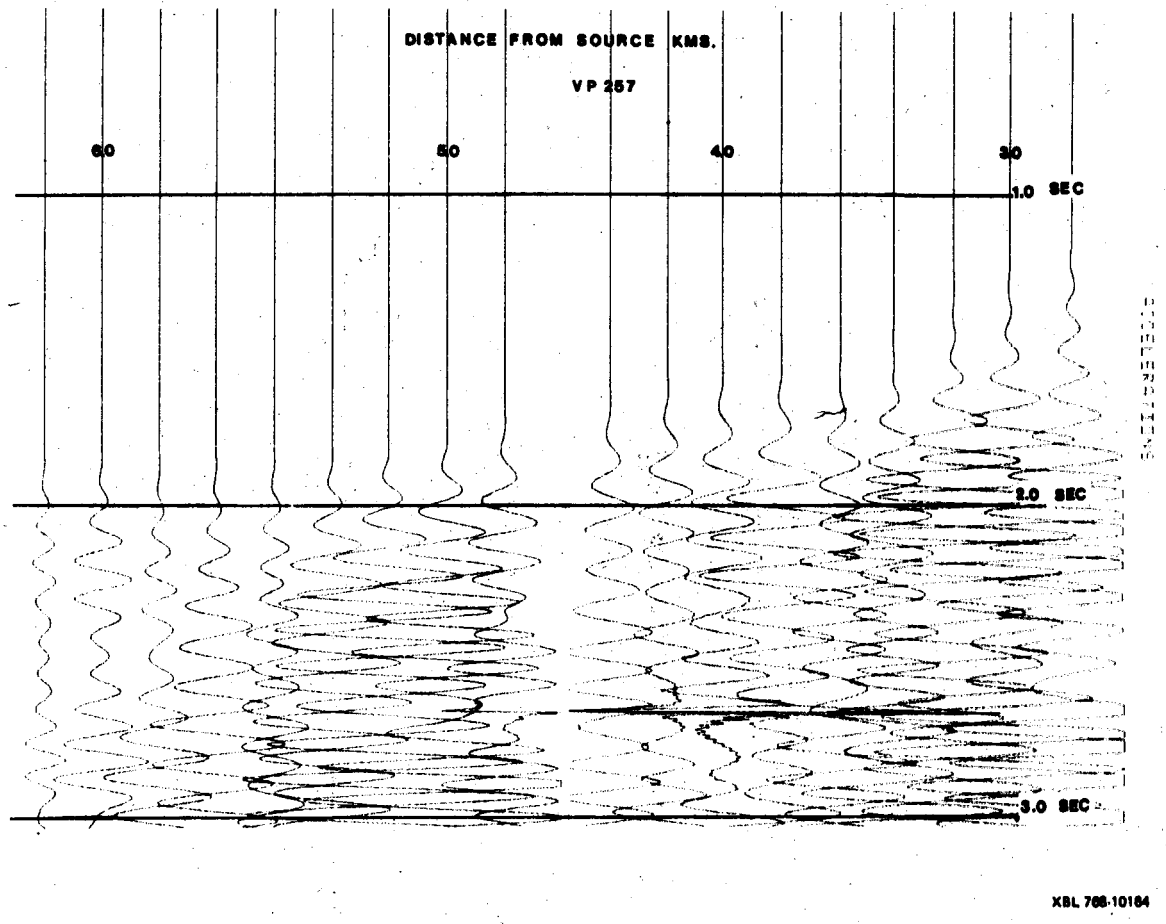

Figure 81: Synthetic re-fraction record section for VP 257, generated by finite element computation. Glitch at 2.7 sec is spurious.

APPENDIX A

GEOPHYSICAL DATA PROFILE COMPOSITES

Grass Valley, Nevada

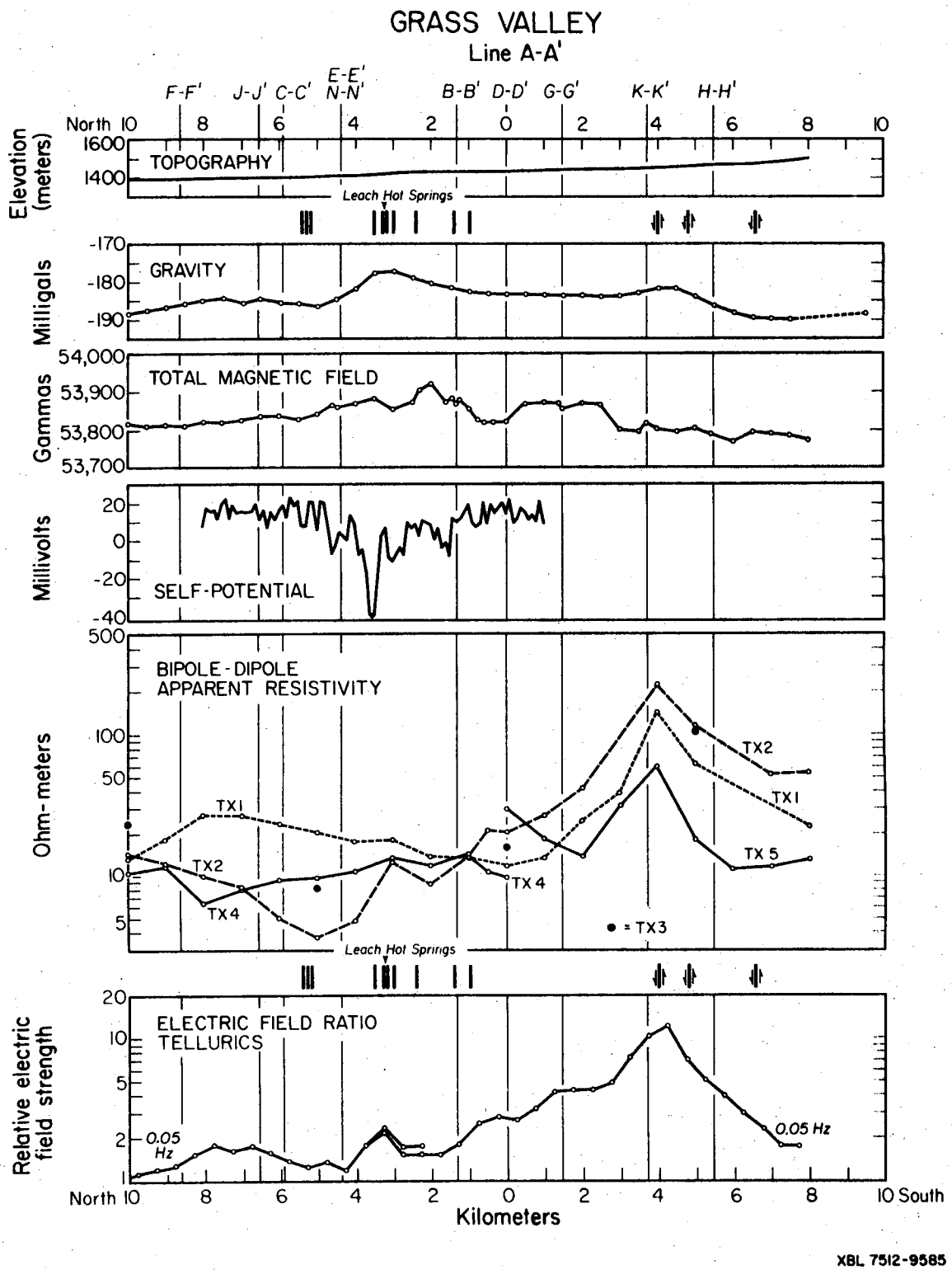

Figure A1: Geophysical Data Profile Composite for line A-A'

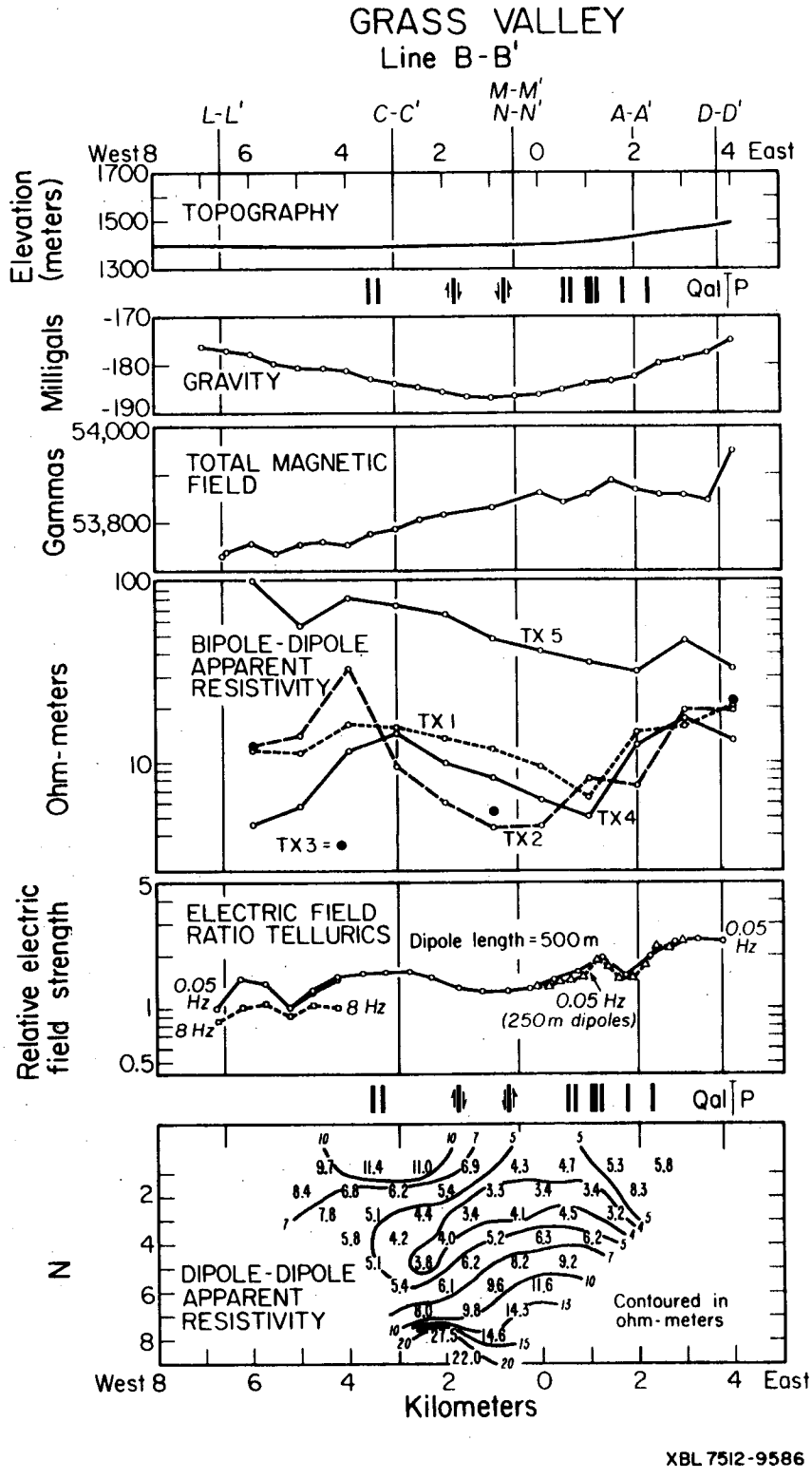

Figure A2: Geophysical Data Profile Composite for line B-B'

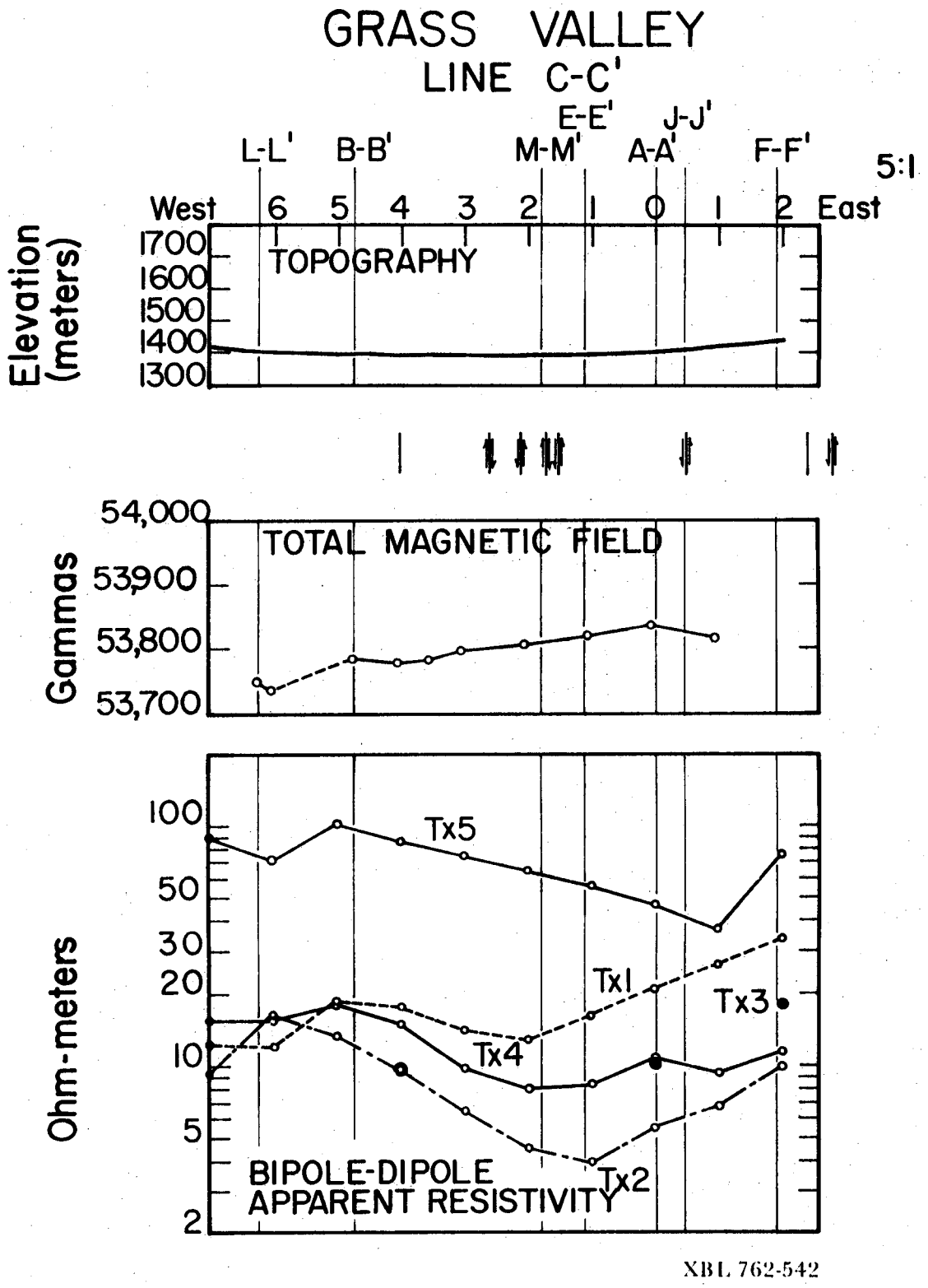

Figure A3: Geophysical Data Profile Composite for line C-C'

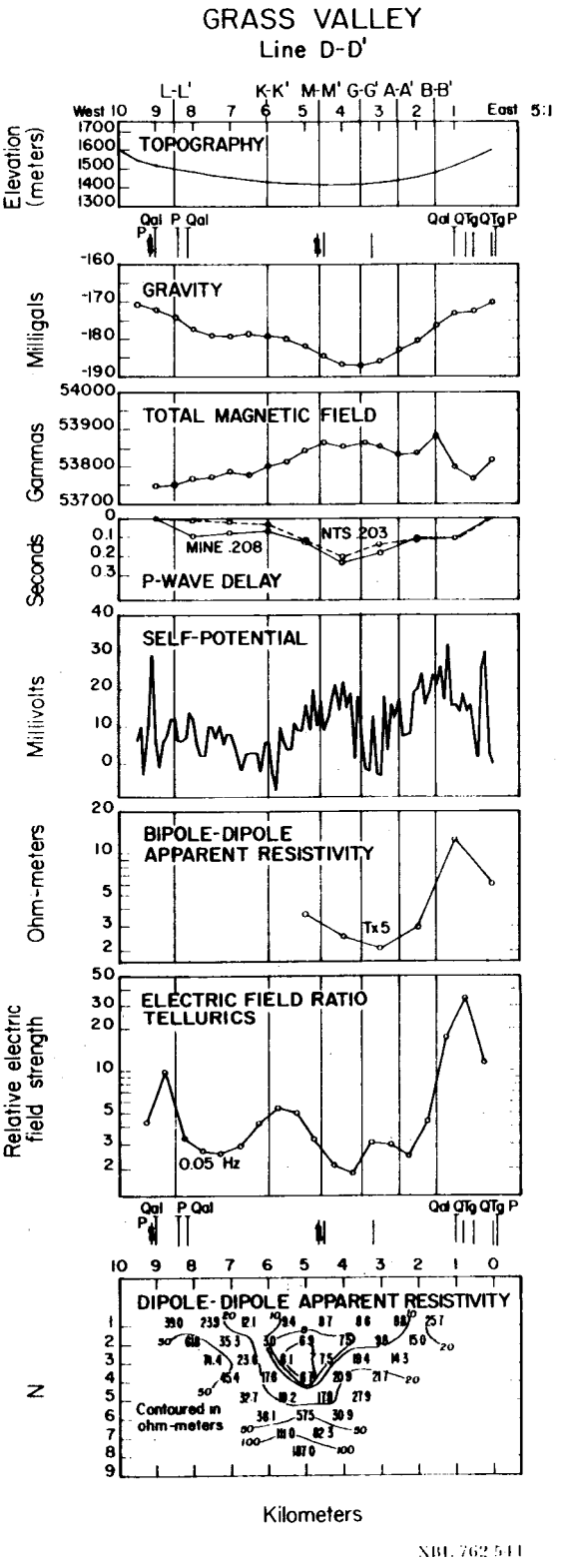

Figure A4: Geophysical Data Profile Composite for line D-D'

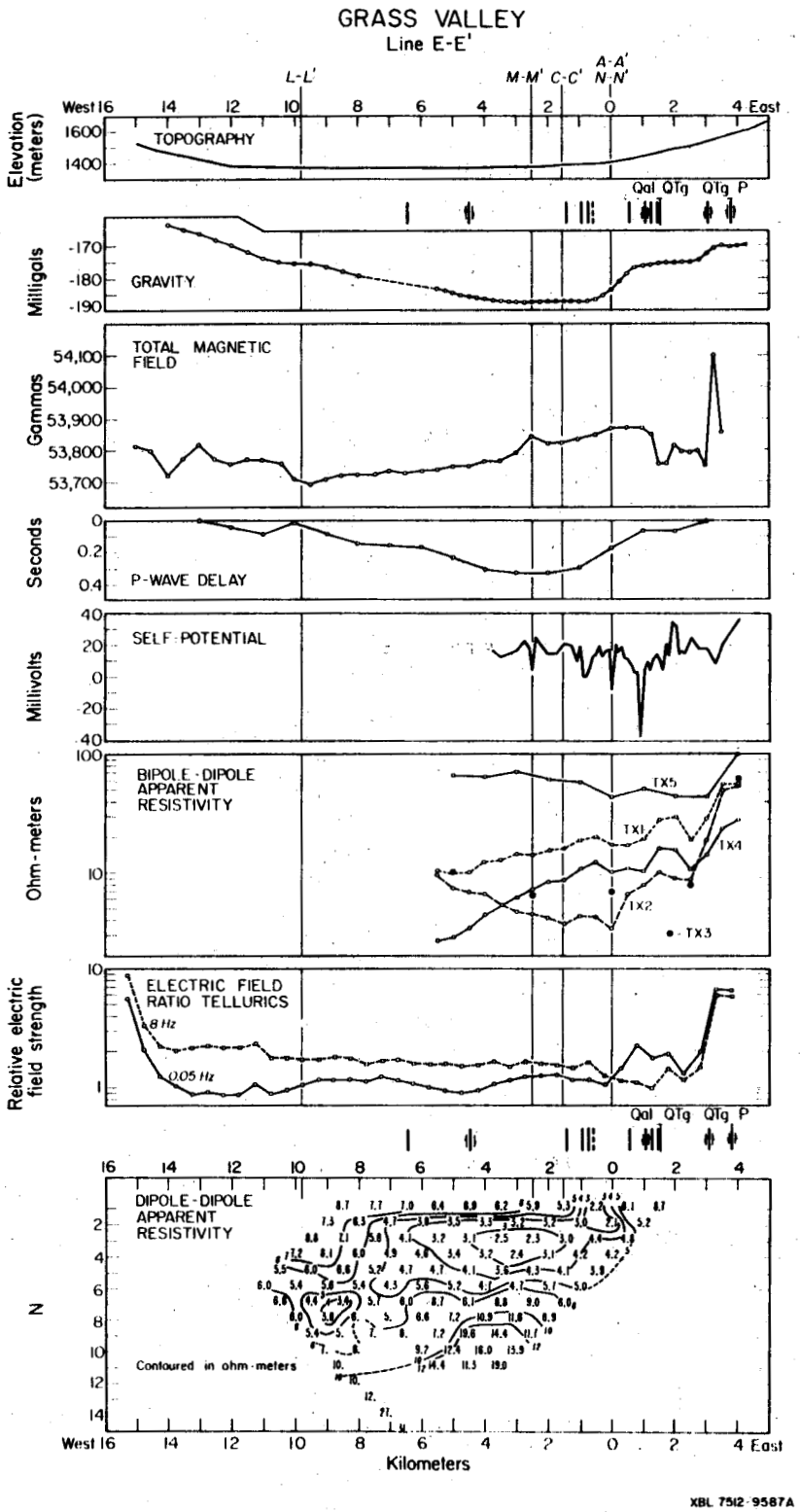

Figure A5: Geophysical Data Profile Composite for line E-E'

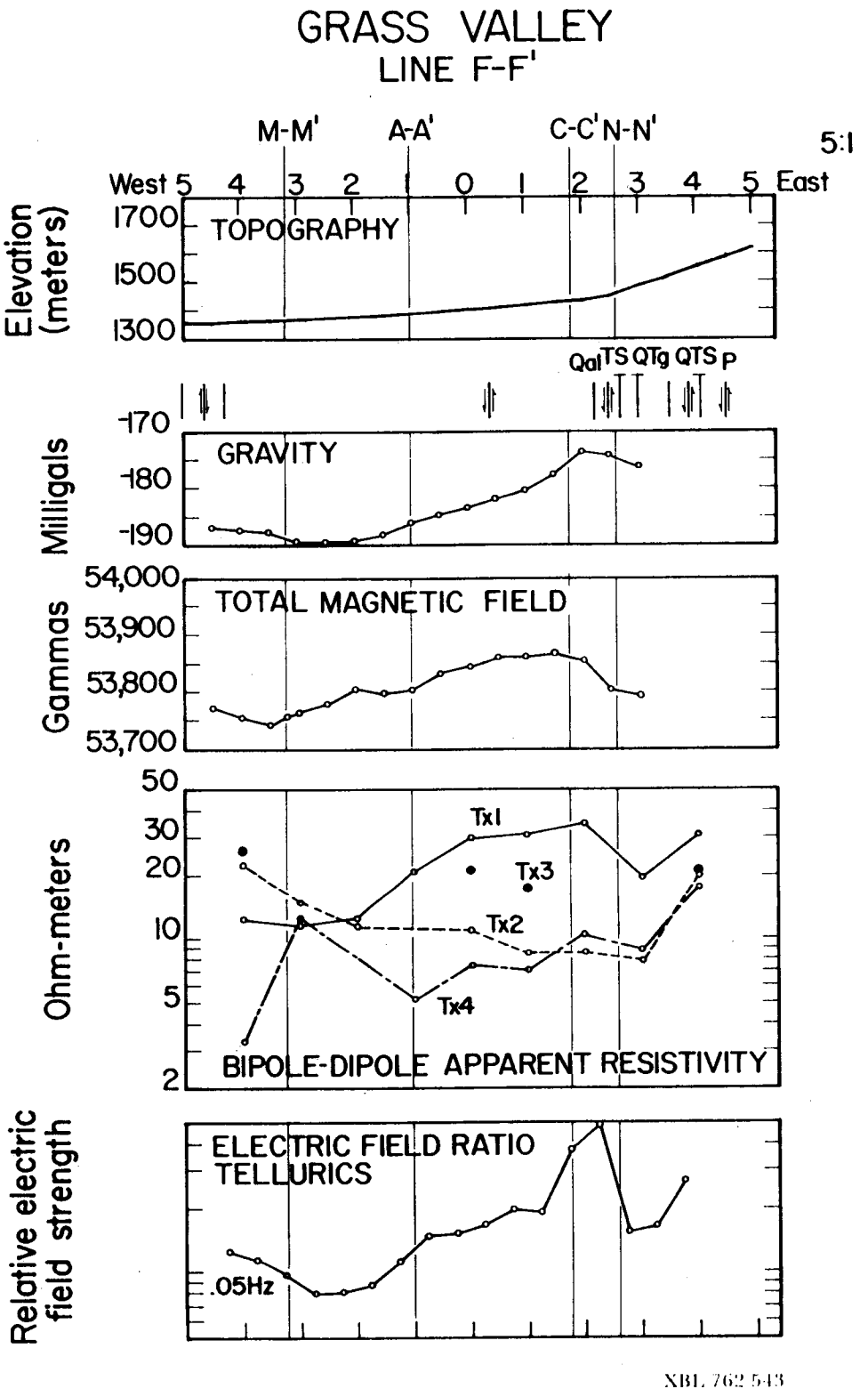

Figure A6: Geophysical Data Profile Composite for line F-F'

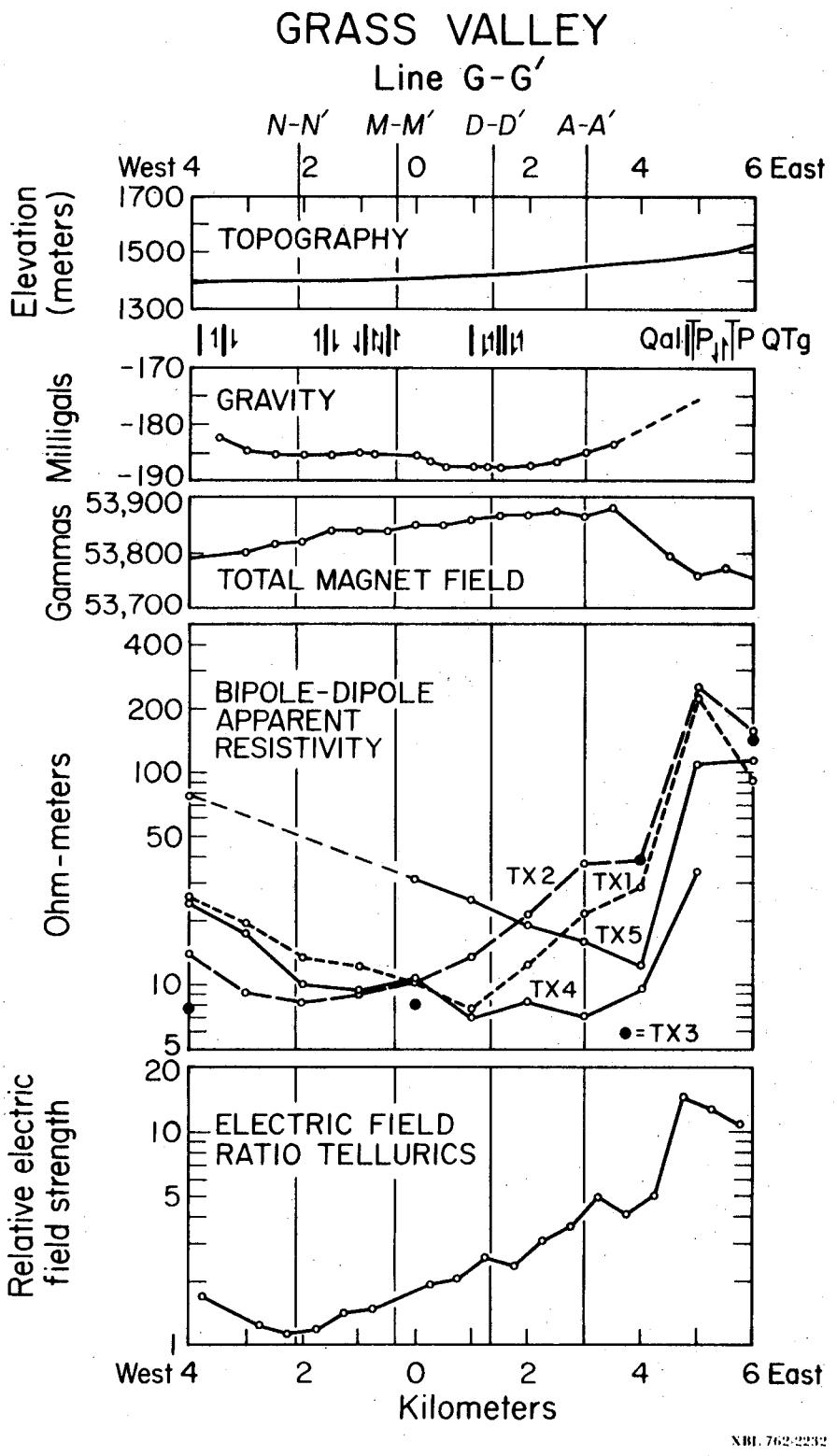

Figure A7: Geophysical Data Profile Composite for line G-G'

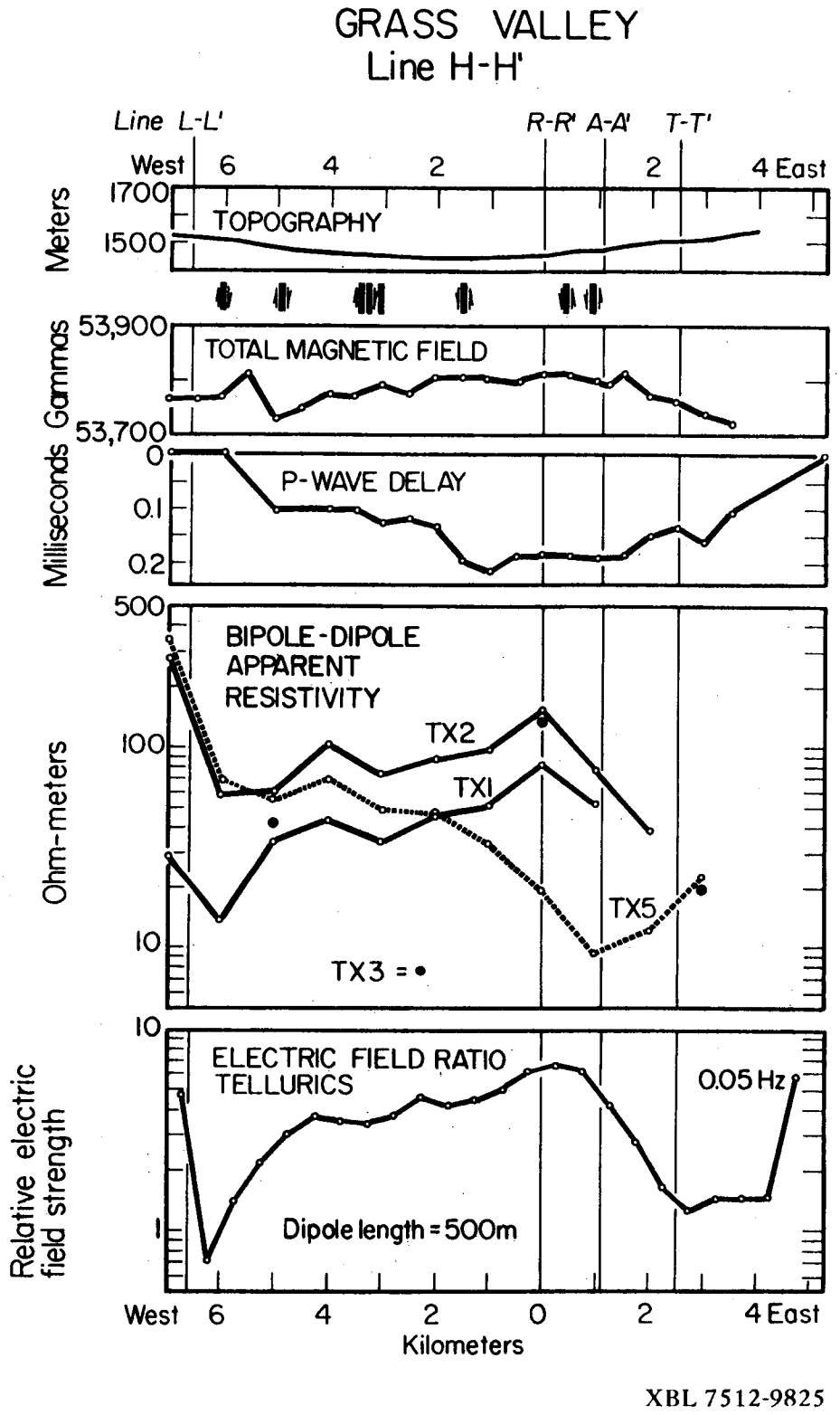

Figure A8: Geophysical Data Profile Composite for line H-H'

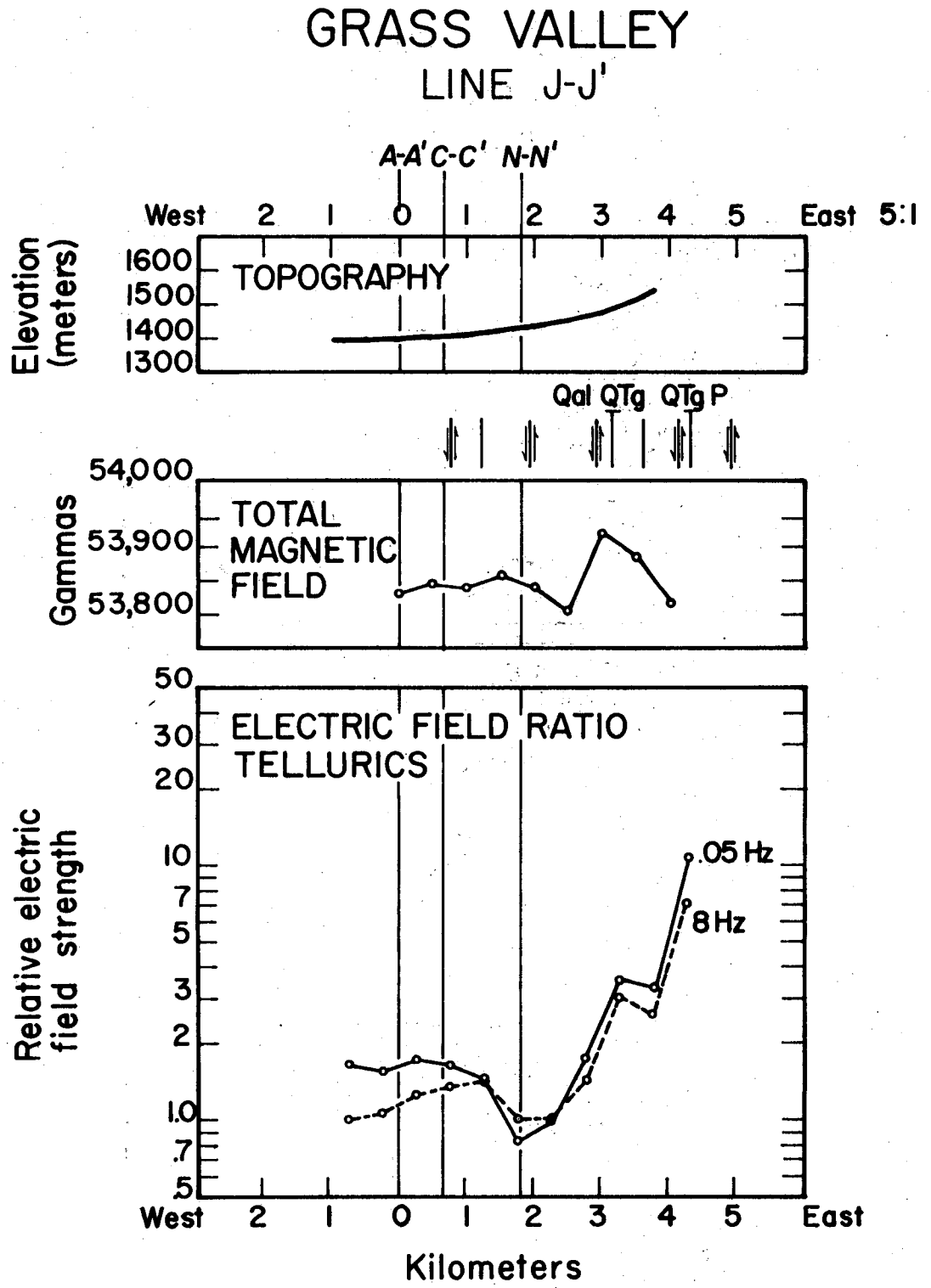

Figure A9: Geophysical Data Profile Composite for line J-J'

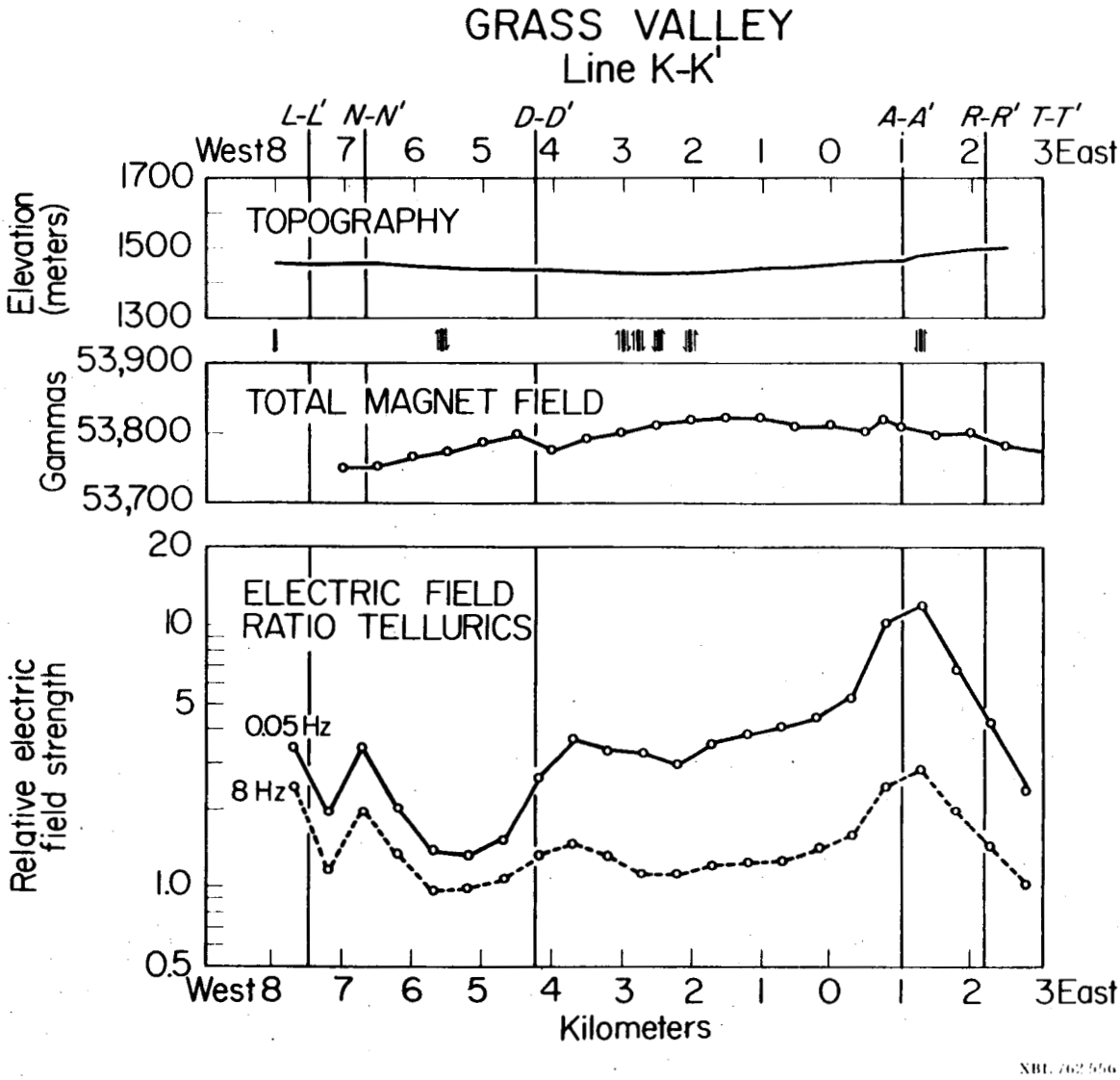

Figure A10: Geophysical Data Profile Composite for line K-K'

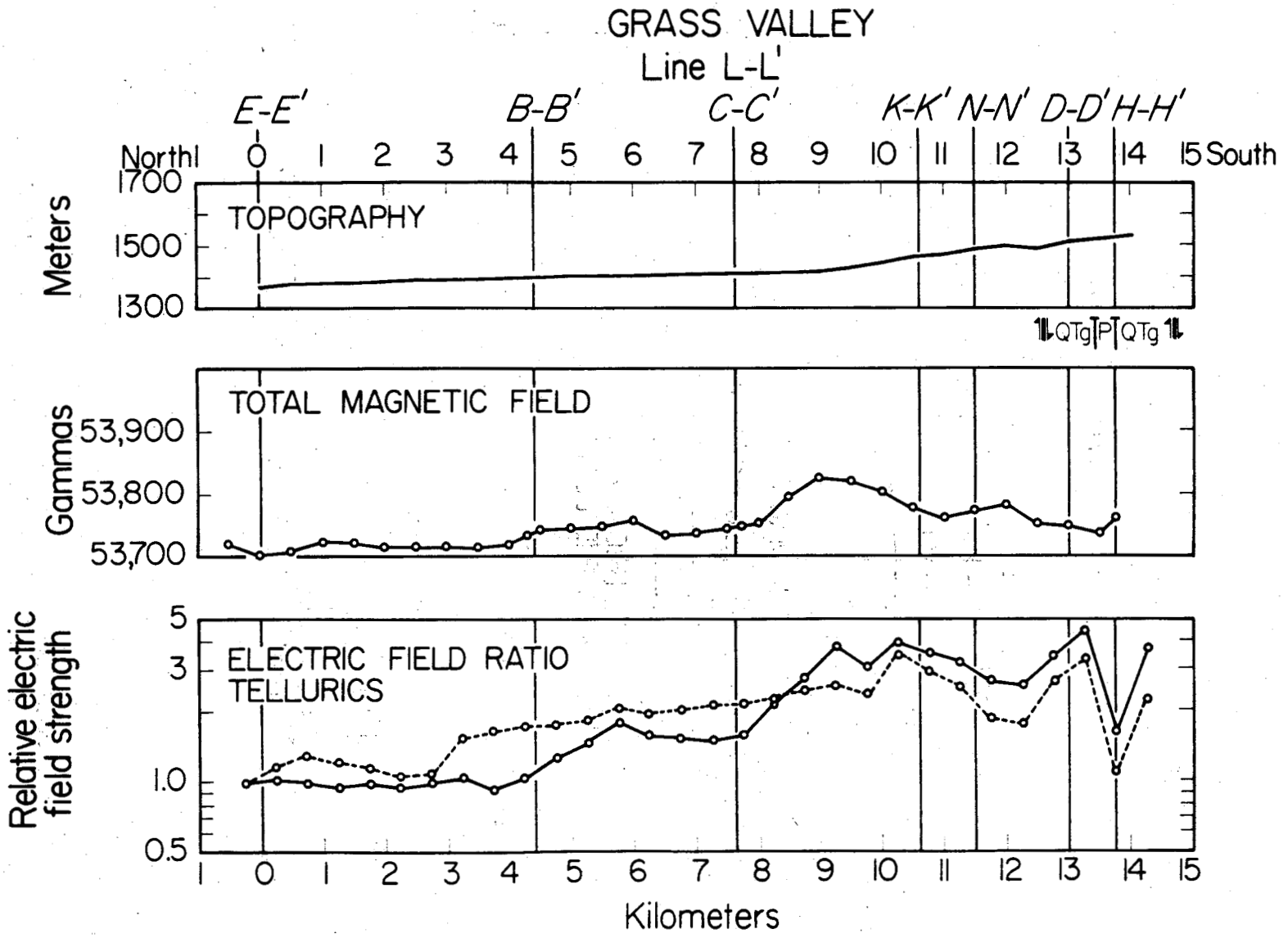

Figure All: Geophysical Data Profile Composite for line L-L'

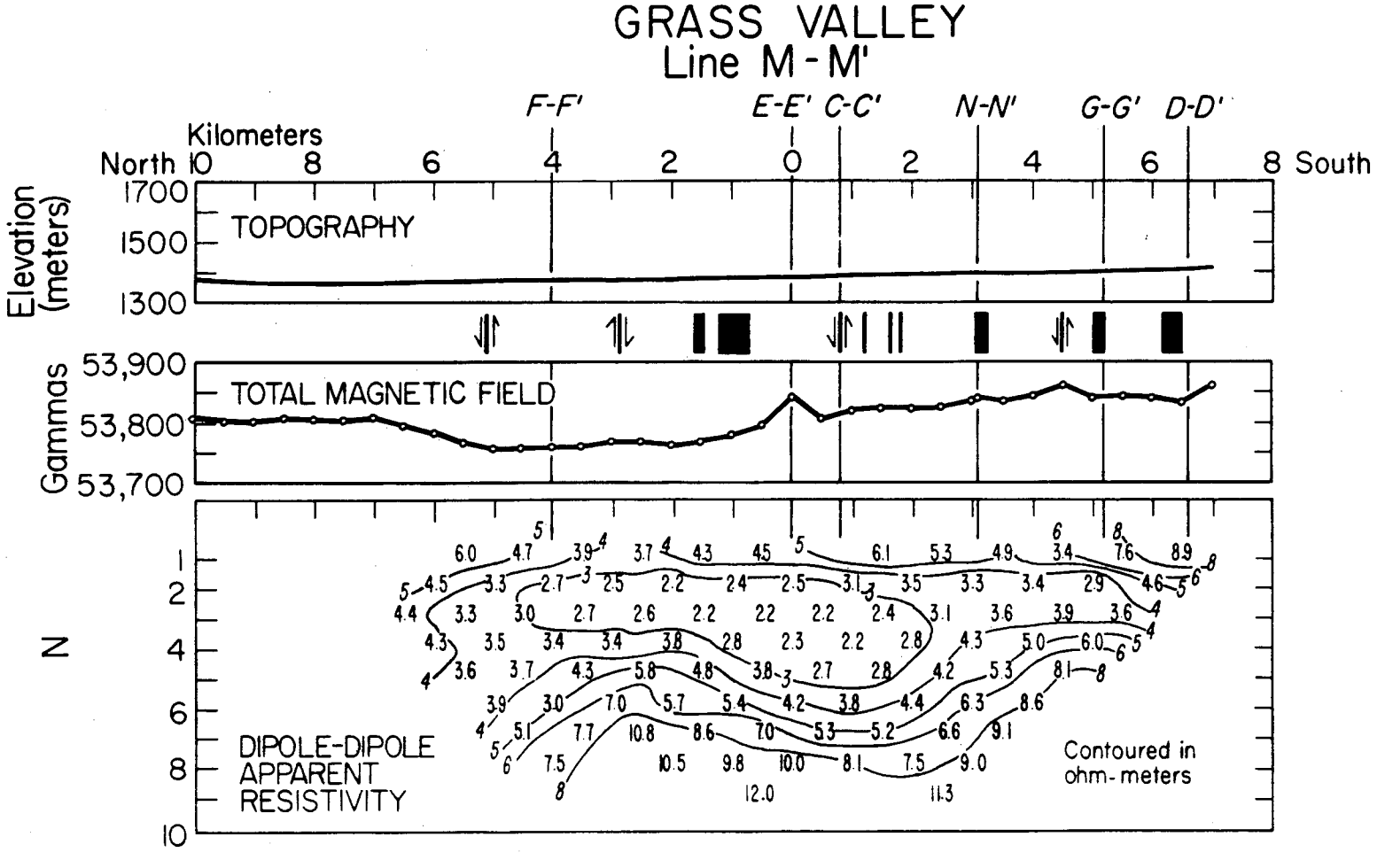

Figure A12: Geophysical Data Profile Composite for line M-M'

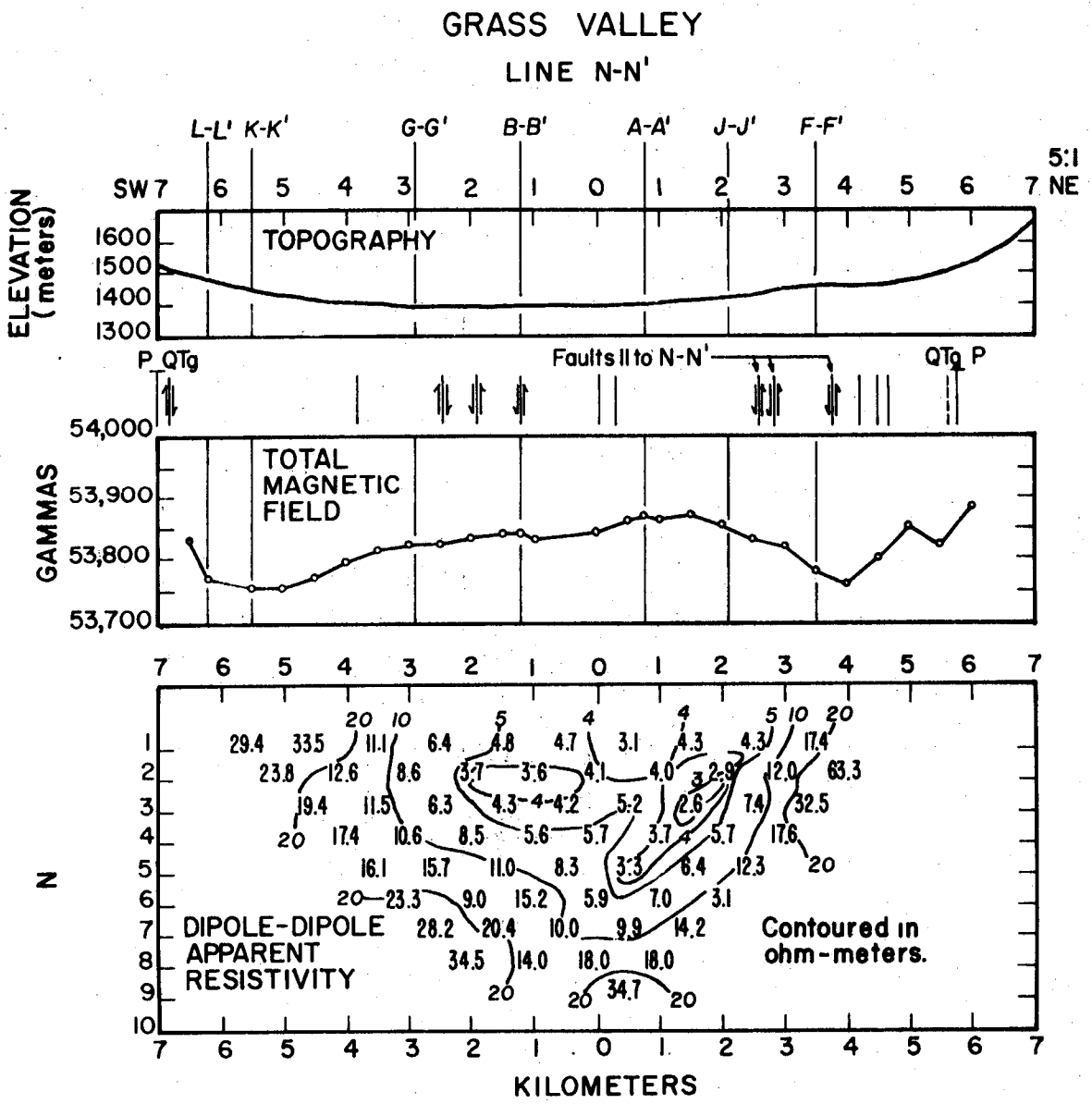

Figure A13: Geophysical Data Profile Composite for line N-N'

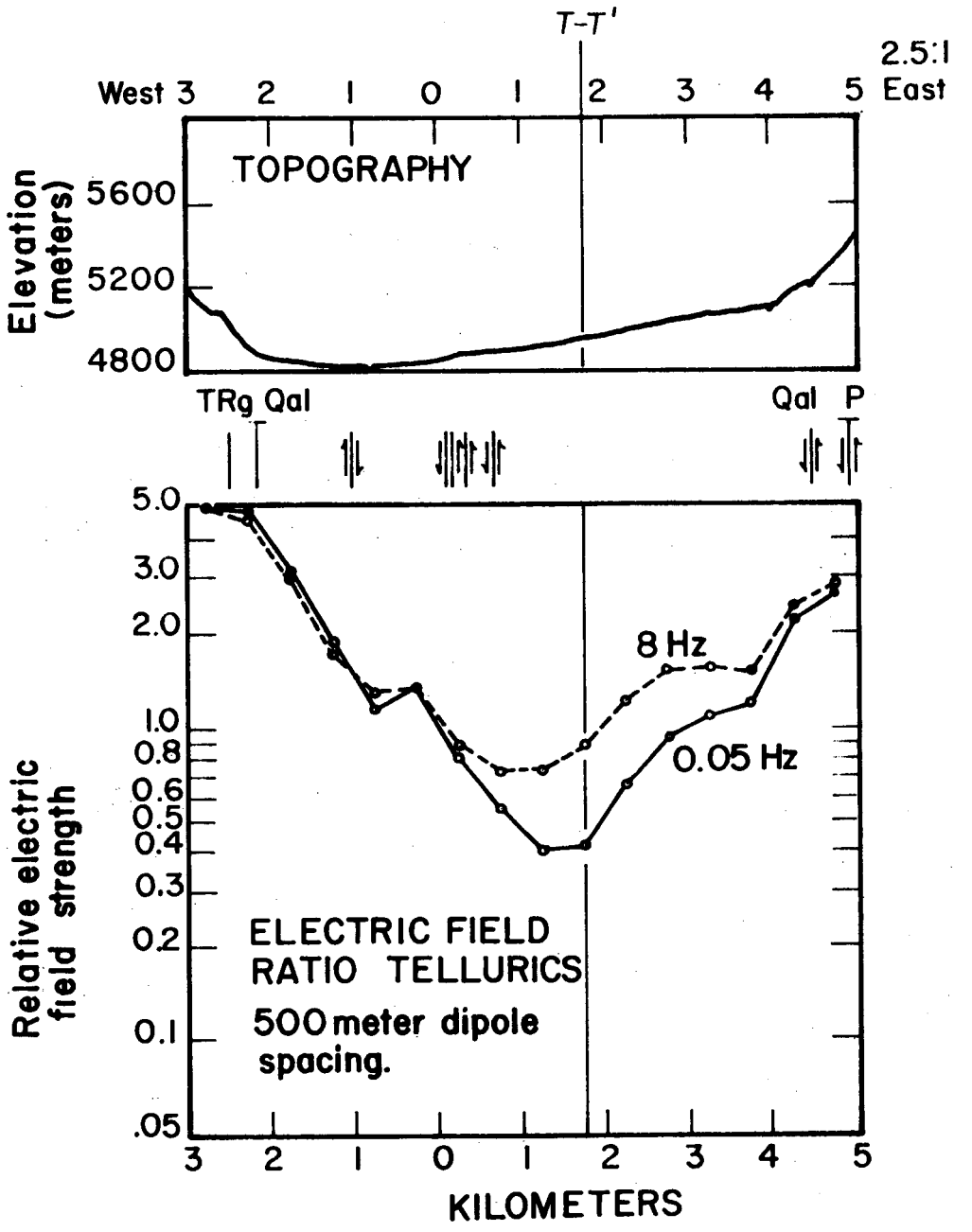

XBL 763-617

Figure A14: Geophysical Data Profile Composite for line P-P'

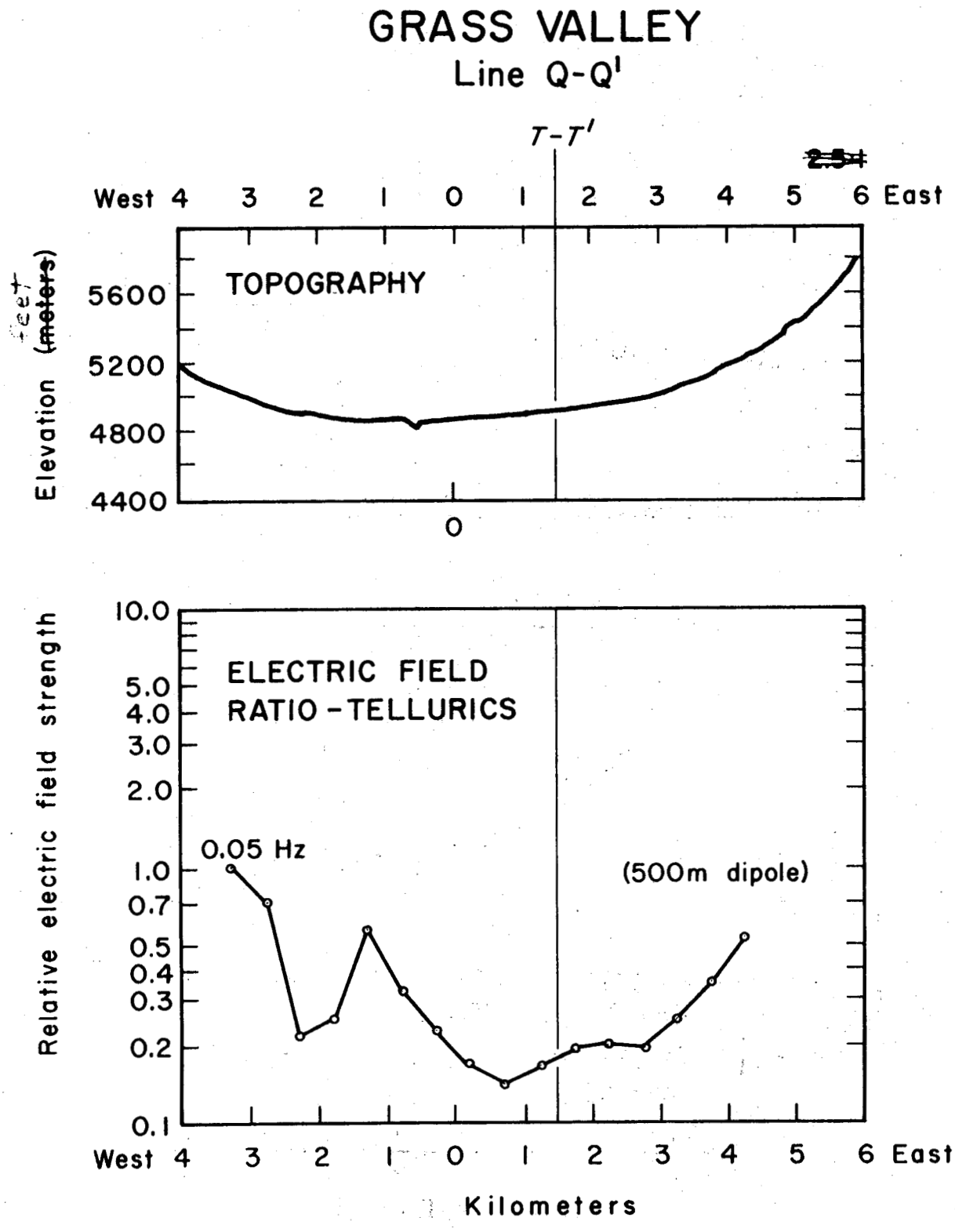

Figure A15: Geophysical Data Profile Composite for line Q-Q'

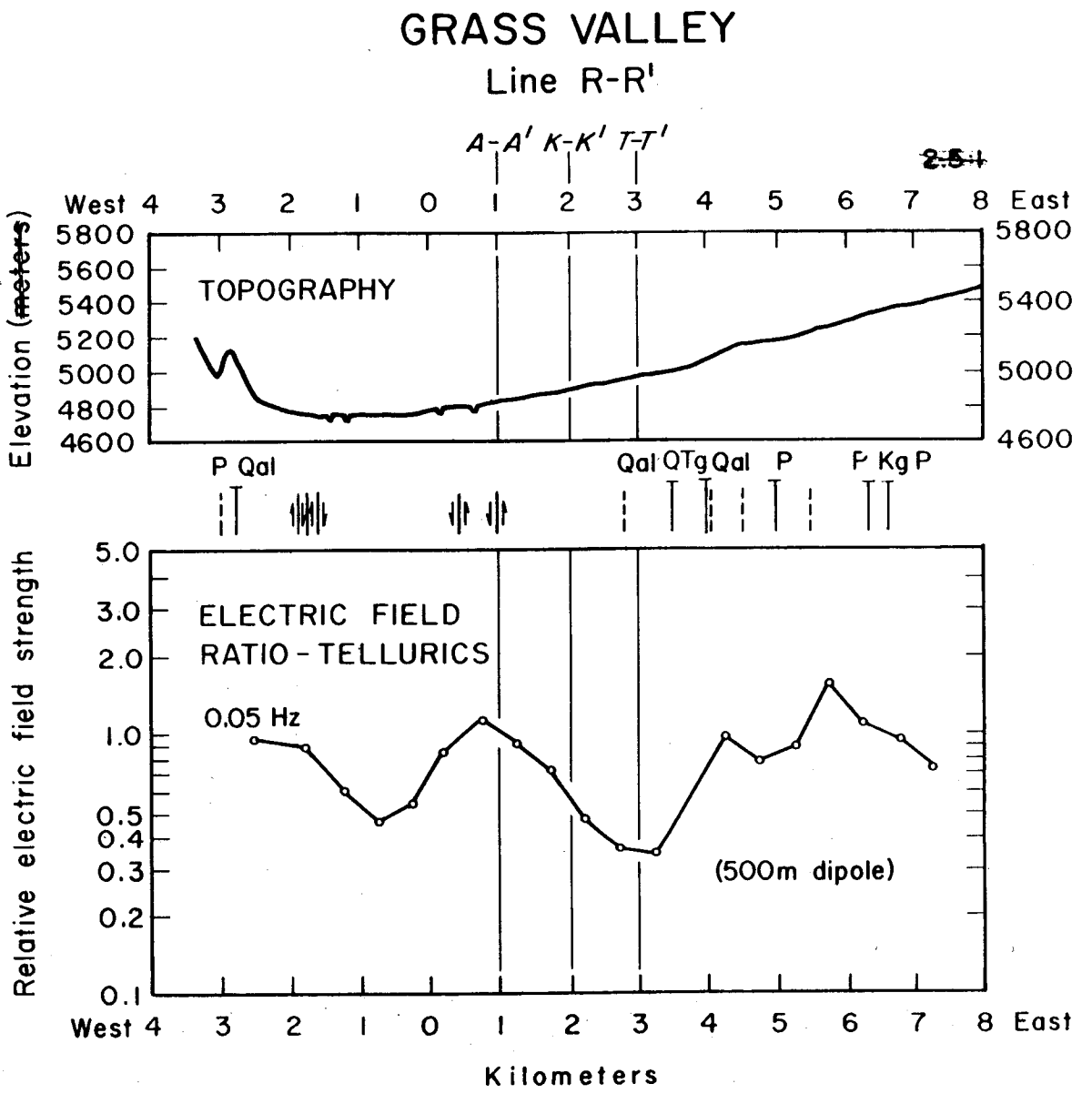

XBL 763-634

Figure A16: Geophysical Data Profile Composite for Line R-R'

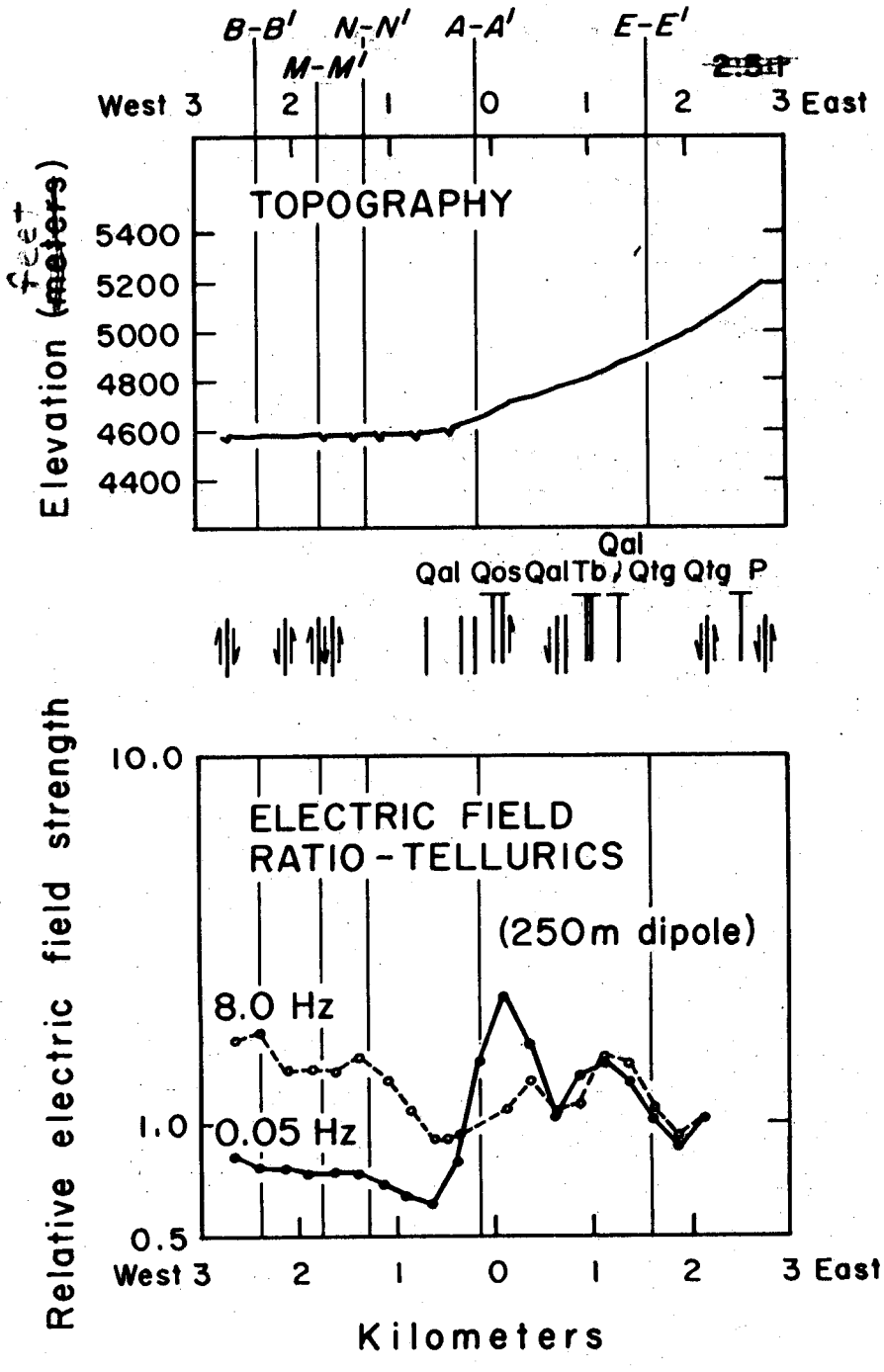

XBL 763-635

Figure A17: Geophysical Data Profile Composite for line S-S'